

# **A Probabilistic Approach to Improving the Stability of Meshed Power Networks with Embedded HVDC Lines**

A thesis submitted to The University of Manchester for the Degree of

**Doctor of Philosophy**

in the Faculty of Engineering and Physical Sciences

**2013**

**Mr Robin Preece**



# Table of Contents

---

List of Figures.....	8
List of Tables.....	12
Nomenclature.....	14
Abstract .....	19
Declaration.....	20
Copyright Statement.....	21
Acknowledgements .....	22
1 Introduction .....	24
1.1 Power System Stability .....	25
1.1.1 Stability Issues .....	25
1.1.2 Power System Oscillations .....	26
1.1.3 Wide Area Measurement Systems.....	29
1.2 HVDC Development.....	30
1.2.1 HVDC Technology.....	30
1.2.2 LCC-HVDC.....	31
1.2.3 VSC-HVDC.....	31
1.2.4 Offshore Development.....	32
1.2.5 Future HVDC Systems .....	33
1.3 Past Research on Damping of Power Oscillations.....	34
1.3.1 Power Oscillation Damping Control .....	34
1.3.2 Probabilistic Small-Disturbance Stability Assessment.....	42
1.3.3 Summary of Past Research .....	45
1.4 Research Aims and Objectives .....	46
1.5 Main Contributions of this Research .....	47
1.6 Thesis Overview .....	48
2 Power System Modelling and Analysis Techniques .....	51
2.1 Modelling Power System Components.....	52
2.1.1 Synchronous Generators.....	52
2.1.2 Generator Excitation Systems.....	53
2.1.3 Power System Stabilisers.....	55
2.1.4 Transmission Lines.....	56
2.1.5 Transformers.....	56
2.1.6 Loads.....	57
2.1.7 Network .....	57
2.1.8 Modelling of Signal Time Delays.....	58
2.2 Modelling HVDC Systems .....	59
2.2.1 HVDC Converters .....	59
2.2.2 LCC-HVDC Modelling .....	60

2.2.3	VSC-HVDC Modelling .....	62
2.2.4	Interface with AC System.....	64
2.2.5	Multi-Terminal HVDC Grid Modelling.....	64
2.2.6	HVDC Model Summaries .....	65
2.3	Power System Analysis Techniques .....	69
2.3.1	Power System Linearisation .....	69
2.3.2	Modal Analysis.....	70
2.4	Damping Controller Design.....	72
2.4.1	PSS-based POD Control.....	72
2.4.2	Modal Linear Quadratic Gaussian Control.....	73
2.5	Test Networks .....	77
2.5.1	Two Area Network .....	77
2.5.2	New England Test System and New York Power System (NETS-NYPS).....	78
2.6	Summary .....	79
3	The Effects of HVDC Lines on Power System Stability .....	81
3.1	Introduction of HVDC lines into AC Networks .....	83
3.1.1	Modifications to the Test Network.....	83
3.1.2	HVDC Line Power Flow Variations .....	83
3.1.3	Results and Discussion .....	84
3.2	VSC-HVDC POD Control on a Small Test System .....	88
3.2.1	Modifications to the Test Network.....	88
3.2.2	POD Controller Designs .....	89
3.2.3	Small-Disturbance Analysis .....	91
3.2.4	Large Disturbance Analysis.....	91
3.3	VSC-HVDC POD Control on a Large Test System.....	94
3.3.1	Modifications to the Test Network.....	95
3.3.2	POD Controller Designs.....	96
3.3.3	Small-Disturbance Analysis .....	97
3.3.4	Large Disturbance Analysis.....	98
3.3.5	Wide Area Signal Delay .....	102
3.3.6	Loss of Wide Area Signals .....	104
3.3.7	Effect of Reactive Power Modulation .....	106
3.3.8	Limiting Modulation Capacity .....	107
3.4	POD Control with Multi-Terminal HVDC Grids .....	109
3.4.1	Modifications to the Test Network.....	109
3.4.2	WAMS-Based POD Control .....	110
3.4.3	Large Disturbance Analysis.....	111
3.4.4	Blocking Modulating Signals .....	113
3.5	Summary .....	114
4	Assessing the Robustness of Controllers.....	117
4.1	Robust Probabilistic Evaluation of Controller Performance.....	118
4.1.1	Establishing the Probabilistic Operating Conditions.....	119
4.1.2	Modelling Contingencies.....	120
4.1.3	Identification of Critical Oscillatory Modes.....	120
4.2	Test System Details.....	122
4.2.1	Modifications to the Test Network.....	122

4.2.2	WAMS-Based POD Control .....	122
4.3	Evaluation of Controller Robustness .....	126
4.3.1	Establishing the Probabilistic Operating Conditions.....	126
4.3.2	Uncertain Parameter Reduction.....	127
4.3.3	Modelling Contingencies.....	128
4.4	Results and Discussion.....	129
4.4.1	Comparison of Controller Designs .....	129
4.4.2	Mitigating for Inadequate Controller Peformance.....	130
4.4.3	Predicting Inadequate Performance with Multiple System Variables.....	133
4.5	Summary .....	136
5	Modal Estimation using the Probabilistic Collocation Method .....	139
5.1	The Probabilistic Collocation Method .....	141
5.1.1	The PCM Model Function.....	141
5.1.2	Selection of Probabilistic Operating Points.....	143
5.1.3	Using the PCM Model Function.....	144
5.2	Case Study on a Small Test Network.....	144
5.2.1	Modifications to the Test Network .....	144
5.2.2	Application of the PCM with Test System .....	145
5.2.3	Errors of the Produced PCM Models .....	147
5.2.4	Results and Discussion .....	148
5.2.5	Incorporating POD Control .....	152
5.3	Reduction in Modelled Uncertainties .....	154
5.3.1	Eigenvalue Sensitivity .....	154
5.3.2	The Effect of Parameter Reduction on Model Error .....	155
5.3.3	Results and Discussion .....	156
5.4	Case Study on Large Test Network .....	157
5.4.1	Modifications to the Test Network.....	157
5.4.2	Uncertain Network Parameters.....	158
5.4.3	Reduced System Uncertainties .....	158
5.4.4	Results and Discussion .....	159
5.4.5	Inclusion of Optimal Power Flow .....	160
5.5	Summary .....	161
6	Probabilistic Tuning of Damping Controllers .....	163
6.1	Probabilistic Controller Tuning Methodology.....	164
6.1.1	Determining Probabilistic Mode Locations.....	164
6.1.2	Probabilistic System Representation .....	165
6.2	Test System Details.....	166
6.2.1	Modifications to the Test Network .....	166
6.2.2	WAMS-Based POD Control .....	167
6.3	Application of Probabilistic Controller Tuning .....	170
6.3.1	Variation in System Operating Conditions.....	170
6.3.2	Identification of Electromechanical Modes.....	171
6.3.3	Results and Discussions.....	171
6.4	Application of the Probabilistic Collocation Method .....	175
6.4.1	Reduction in Modelled Uncertainties .....	176
6.4.2	Discontinuities in Wind Farm Power Output .....	177

6.4.3	PCM-Based Probabilistic Modal Estimation.....	177
6.4.4	Results and Discussions.....	179
6.5	Summary .....	182
7	Conclusions and Future Work.....	184
7.1	Conclusions.....	184
7.2	Future Work .....	187
8	References .....	191
Appendix A : Network Data.....		204
A.1	Two-Area Test Network Data.....	204
8.1.1	Line Impedances.....	204
A.1.1	Load Flow Data .....	204
A.1.2	Generator Dynamic Data .....	205
A.2	NETS-NYPS Test Network Data.....	205
A.2.1	Line Impedances.....	205
A.2.2	Load Flow Data .....	207
A.2.3	Generator Dynamic Data .....	208
A.3	HVDC System Details .....	209
A.3.1	LCC-HVDC Line Embedded in Two-Area Network (Section 3.1) .....	209
A.3.2	VSC-HVDC Line Embedded in Two-Area Network (Section 3.1) .....	209
A.3.3	VSC-HVDC Line Embedded in Two-Area Network (Section 3.2) .....	210
A.3.4	VSC-HVDC Line Embedded in Five-Area Network (Section 3.3) .....	210
A.3.5	VSC-MTDC Grid Embedded in Five-Area Network (Section 3.4) .....	210
A.3.6	Two VSC-HVDC Lines Embedded in Five-Area Network (Section 4.2) .....	211
A.3.7	VSC-HVDC Line Embedded in Two-Area Network (Section 5.2) .....	211
A.3.8	VSC-MTDC Grid Embedded in Five-Area Network with Additional Wind Farm (Section 6.2) .....	212
A.4	Data for Optimal Power Flow.....	213
Appendix B : Eigenvalue Sensitivity Rank Values.....		214
B.1	Numerical Example of Rank Calculation .....	214
B.2	Five-Area Test Network (Section 4.3).....	215
B.3	Two-Area Test Network (Section 5.3).....	216
Appendix C : PCM Model Functions.....		217
Appendix D : PCM Model Uncertain Parameter Details .....		218
D.1	Two-Area Test Network (Section 5.2).....	218
D.1.1	Normally Distributed Parameters .....	218
D.1.2	Uniformly Distributed Parameters.....	218
D.2	Five-Area Test Network with Standard Power Flow Solution (Section 5.4).....	219
D.2.1	Normally Distributed Parameters .....	219
D.3	Five-Area Test Network with Optimal Power Flow Solution (Section 5.4.5).....	219
D.3.1	Normally Distributed Parameters .....	219
D.3.2	Uniformly Distributed Parameters.....	219
Appendix E : Modal System Representation.....		221

Appendix F : Publications from the Thesis .....	223
F.1 International Journal Publications.....	223
F.2 Submitted International Journal Publications .....	223
F.3 International Conference Publications .....	223

*Word Count: 51,454*

# List of Figures

---

Figure 1-1: Line power flow through one of the three AC lines in the COI on 10 August 1996 – adopted from [2].	28
Figure 1-2: Growth in global HVDC capacity (projected up to 2016) – adopted from [41].	30
Figure 2-1: Relationship and signals between the synchronous generator, excitation system, and power system stabiliser.	54
Figure 2-2: Simplified block diagram for the IEEE Type ST1A static exciter.	55
Figure 2-3: Simplified block diagram for the IEEE Type DC1A DC exciter.	55
Figure 2-4: Block diagram of a PSS.	56
Figure 2-5: Equivalent $\pi$ -representation of a two winding transformer.	56
Figure 2-6: Injection model for one HVDC converter station connected to an AC network.	59
Figure 2-7: Injection model for an HVDC transmission system in parallel with an existing AC line.	60
Figure 2-8: LCC-HVDC injection model controller for (a) rectifier converter station, and (b) inverter converter station.	61
Figure 2-9: LCC-HVDC line model.	61
Figure 2-10: VSC-HVDC injection model controller for (a) DC voltage, (b) active power, and (c) reactive power.	63
Figure 2-11: VSC-HVDC line model based on power injection.	63
Figure 2-12: Generic MTDC converter node line model.	65
Figure 2-13: Example of a four-node VSC-MTDC grid.	68
Figure 2-14: PSS-based POD controller structure.	73
Figure 2-15: Standard LQG controller structure.	76
Figure 2-16: Kundur two-area test network diagram.	78
Figure 2-17: NETS-NYPS five-area test network diagram.	79
Figure 3-1: Two-area test network including VSC-HVDC line.	83
Figure 3-2: Movement of local mode 1 with varying connection point and power flow with (a) VSC-HVDC, and (b) LCC-HVDC technology.	84
Figure 3-3: Movement of local mode 2 with varying HVDC technology, connection point and power flow.	85
Figure 3-4: Movement of inter-area mode with varying VSC-HVDC connection point and power flow.	86
Figure 3-5: AC power flow from bus 7 to bus 9 following a disturbance with varying power flow through the VSC-HVDC line.	87
Figure 3-6: Two-area test network including embedded VSC-HVDC line.	88

Figure 3-7: General control scheme for the Kundur two-area test network including a VSC-HVDC line with supplementary POD control.....	89
Figure 3-8: Modal placement of electromechanical modes with POD controllers installed.....	91
Figure 3-9: For the <i>base case</i> : (a) Active power injected at bus 9 from bus through the AC infeeds, and (b) Active power injected at bus 9 by the VSC-HVDC line.....	92
Figure 3-10: For the <i>increased power transfer case</i> : (a) Active power injected at bus 9 from bus through the AC infeeds, and (b) Active power injected at bus 9 by the VSC-HVDC line.....	94
Figure 3-11: Five-area test network with VSC-HVDC line installed. ....	95
Figure 3-12: General control scheme for the five-area test network including a VSC-HVDC line with supplementary POD control.....	96
Figure 3-13: Modal placement of inter-area modes with POD controllers installed.....	97
Figure 3-14: Settling times for the NYPS inter-area AC infeeds for the <i>base case</i> . ....	99
Figure 3-15: For the <i>base case</i> : (a) Active power injected at bus 9 from bus 8 through an AC infeed, and (b) Active power injected at bus 50 by the VSC-HVDC converter station. ....	100
Figure 3-16: Settling times for the NYPS inter-area AC infeeds for the <i>outage case</i> . ....	101
Figure 3-17: For the <i>outage case</i> : (a) Active power injected at bus 9 from bus 8 through an AC infeed, and (b) Active power injected at bus 50 by the VSC-HVDC converter station. ....	102
Figure 3-18: Deterioration in damping factors of low frequency modes with increasing wide area signal delays to the MLQG controller.....	104
Figure 3-19: Active power injected at bus 9 from bus 8 for the <i>base case</i> operating point with the loss of input signals $y_1$ and $y_2$ for the MLQG controller. ....	105
Figure 3-20: Active power injected at bus 9 from bus 8 for the <i>base case</i> operating point with and without reactive power modulation. ....	106
Figure 3-21: For the <i>base case</i> operating point with differing modulation capacity limits: (a) Active power injected at bus 9 from bus 8 and (b) Active power injected at bus 50 by VSC-HVDC inverter station. ....	107
Figure 3-22: Availability of spare capacity on the Britned HVDC line.....	108
Figure 3-23: Five-area test network with VSC-MTDC grid installed.....	110
Figure 3-24: Control overview for the five-area test network including a VSC-MTDC grid with supplementary MLQG POD control.....	111
Figure 3-25: Settling times for the NYPS inter-area AC infeeds with MLQG POD control through the VSC-MTDC grid. ....	112
Figure 3-26: System stabilisation demonstrated by (a) Active power injected at bus 9 from bus 8 and (b) Active power injected into the NYPS area from the MTDC grid at nodes 3–5.....	113
Figure 4-1: Flowchart of complete robust evaluation procedure. ....	121
Figure 4-2: Five-area test network including two additional VSC-HVDC lines. ....	122

Figure 4-3: Control overview for the five-area network including two VSC-HVDC lines, showing both centralised and decentralised POD control schemes.....	125
Figure 4-4: For differing POD schemes: (a) Active power injected at bus 9 from bus 8 and (b) Active power injected at bus 40 by the VSC-HVDC-2 converter station.....	126
Figure 4-5: Residual values between the distributions of $\sigma_i$ with increasing numbers of uncertain system parameters, and all uncertain parameters, modelled with the centralised controller in place. Highlighted bars represent 16 uncertain parameters...	128
Figure 4-6: Absolute improvement in damping factor across all contingencies for the low frequency modes with different controller structures.....	130
Figure 4-7: Boundaries for classification of centralised controller effect on Mode 3 with VSC-HVDC-1 out of service.....	132
Figure 4-8: Classification tree for controller effect on Mode 3 with VSC-HVDC-1 out of service.....	133
Figure 4-9: Visualisation of the classification tree with two system variables. ....	134
Figure 4-10: For an example case with the <i>initial</i> and <i>redesigned centralised controller</i> structures in place: (a) Active power injected at bus 9 from bus 8 and (b) Active power injected at bus 40 by the VSC-HVDC-2 converter station.....	135
Figure 4-11: Absolute improvement in damping factor with line 40–41 out of service with the <i>initial</i> and <i>redesigned centralised controller</i> structures in place. ....	136
Figure 5-1: Two-area test network including embedded VSC-HVDC line. ....	145
Figure 5-2: $\varepsilon_{RSSH}$ error values with varying PCM model order for (a) the real, and (b) the imaginary parts of the electromechanical mode locations.....	148
Figure 5-3: Plots of probabilistic electromechanical mode locations based on system uncertainties. Plots (a)–(c) have been produced using the MC approach with full system linearisations. Plots (d)–(f) have been produced using the MC approach with the 3rd order PCM models.....	149
Figure 5-4: Overlap plots of the 90% contours for (a) local Modes 1 and 2, and (b) the inter-area Mode 3.....	150
Figure 5-5: Probability distributions for $\zeta_{crit}$ derived using MC runs with linearisation of the full system and using the third order PCM model.....	151
Figure 5-6: Probability distributions for $\zeta_{crit}$ with PSS-based POD controller installed. ....	153
Figure 5-7: Plots of PCM-based $\zeta_{crit}$ values against linearisation-based $\zeta_{crit}$ values with (a) no POD controller, and (b) a PSS-based POD controller installed.....	153
Figure 5-8: $\varepsilon_{RSSH}$ for increasing numbers of modelled uncertain parameters. ....	156
Figure 5-9: <i>Pdfs</i> for $\zeta_{crit}$ with the full and reduced sets of uncertain parameters.....	157
Figure 5-10: <i>Pdfs</i> for $\zeta_{crit}$ with the PCM model using a reduced set of uncertain parameters and the full linearisation-based approach.....	159
Figure 5-11: <i>Pdfs</i> for $\zeta_{crit}$ with the PCM model using a reduced set of uncertain parameters and the full linearisation-based approach with an OPF solution. ....	161

Figure 6-1: Five-area test network with VSC-MTDC and wind generation installed..	167
Figure 6-2: Control overview for the five-area network including VSC-MTDC grid and wind farm, with MLQG POD controller. ....	168
Figure 6-3: Transient performance of the <i>nominal</i> controller at the nominal operating point demonstrated by the stabilisation of power flow through (a) line 8–9, (b) line 2–1, and (c) line 18–50. ....	169
Figure 6-4: (a) Weibull distribution of wind speed, and (b) Vestas V-80 2 MW turbine power curve. ....	171
Figure 6-5: Closed loop low frequency model locations with <i>nominal</i> controller installed. Dashed lines signify damping factors of 0%, 5%, and 15%. ....	172
Figure 6-6: Open loop low frequency mode locations, including the nominal and probabilistic values. The dashed line signifies a damping factor 5%. ....	173
Figure 6-7: <i>Pdfs</i> for the open loop damping factors of the low-frequency modes. ....	174
Figure 6-8: Damping factors for the low frequency modes with the <i>nominal</i> and <i>probabilistic</i> controllers installed. ....	175
Figure 6-9: PCM-based probabilistic values for Mode 2 with increasing numbers of modelled uncertain parameters. ....	178
Figure 6-10: Damping factors for the low frequency modes with the MC-based and PCM-based probabilistic controllers installed. ....	179
Figure 6-11: <i>Pdfs</i> for the damping factor of Mode 2 with different controller designs in place. ....	180

# List of Tables

---

Table 2-1: Electromechanical mode properties for the two area test system at the nominal operating point.....	78
Table 3-1: Electromechanical mode properties for the two area test system with an embedded VSC-HVDC line. ....	89
Table 3-2: Damping factors of electromechanical modes with POD controllers installed. ....	91
Table 3-3: Settling times for the parallel AC tie lines with different POD control schemes installed. ....	94
Table 3-4: Inter-area mode details for five-area test network with VSC-HVDC line....	95
Table 3-5: Damping factors of inter-area modes with POD controllers installed. ....	98
Table 3-6: MLQG controller delay tolerances. ....	104
Table 3-7: Damping factors of inter-area modes with loss of input signals.....	105
Table 3-8: Inter-area mode details for the five-area network with embedded VSC-MTDC grid with and without an MLQG POD controller in place. ....	111
Table 3-9: Effect of blocking MLQG controller output signals on NYPS AC infeed settling times.....	114
Table 4-1: Inter-area mode details for the five-area network with two embedded VSC-HVDC lines with various POD control schemes.....	125
Table 4-2: Proportion of operating conditions for given contingencies leading to poor controller performance. ....	131
Table 5-1: Electromechanical mode properties for the two area test system with an embedded VSC-HVDC line. ....	144
Table 5-2: Number of coefficients for PCM models with six uncertain parameters....	147
Table 5-3: Percentage of under-representation for electromechanical modes at the 90% contour level. ....	150
Table 5-4: Times taken to complete MC uncertainty studies on the two-area system. ....	152
Table 5-5: 95% confidence range for the PCM model function estimate of $\zeta_{crit}$ .....	153
Table 5-6: Times taken to complete MC uncertainty studies on the five-area system. ....	160
Table 6-1: Inter-area mode details for the five-area network with embedded VSC-MTDC grid and wind farm with and without an MLQG POD controller in place. ....	168
Table 6-2: Risk of poor damping for low frequency modes.....	180
Table 6-3: Computational process times for the Probabilistic Collocation Method. ...	181
Table 6-4: Time taken and probability of poor damping for Mode 2 with each controller design.....	182
Table A-1: Line data for the Kundur two area test network.....	204
Table A-2: Load flow data for the Kundur two area test network. ....	204

Table A-3: Generator dynamic data for the Kundur two area test network. ....	205
Table A-4: Line data for the NETS-NYPS test network. ....	205
Table A-5: Load flow data for the NETS-NYPS test network. ....	207
Table A-6: Generator dynamic data for the NETS-NYPS test network (1). ....	208
Table A-7: Generator dynamic data for the NETS-NYPS test network (2). ....	208
Table A-8: VSC-MTDC line data .....	211
Table A-9: VSC-MTDC line data .....	212
Table A-10: Data for optimal power flow solution with five-area test network. ....	213
Table B-1: Normalised rank values with the centralised controller installed. ....	215
Table B-2: Normalised rank values with the decentralised controller installed. ....	216
Table B-3: Normalised rank values with and without the PSS-based POD controller. ....	216
Table D-1: Normal distribution details for uncertain parameters in the Kundur two area network. ....	218
Table D-2: Recursive coefficients for orthogonal polynomials representing the uniform distribution of the VSC-HVDC line power flow. ....	218
Table D-3: Normal distribution details for uncertain parameters in the five-area network with standard PF solution. ....	219
Table D-4: Normal distribution details for uncertain parameters in the five-area network with OPF solution. ....	219
Table D-5: Recursive coefficients for orthogonal polynomials representing the uniform distributions of $P_{dc}^{VSC-1}$ and $P_{dc}^{VSC-2}$ .....	220

# Nomenclature

---

## *List of Symbols*

$a$	Recursive coefficient
$B$	Susceptance
$b$	Recursive coefficient
$C$	Capacitance
$c$	Calculation constant
$D$	Generator damping constant
$E$	Voltage
$f(\bullet), g(\bullet)$	A function
$G$	Active power output from a generator
$H$	Generator inertia constant
$H_o(\bullet)$	Orthogonal polynomial of order $o$
$I$	Current
$K$	Controller gain/Vector of PCM function coefficients
$k$	Weibull shape parameter
$L$	Inductance/Active power demand at a load
$m$	Number of power system inputs
$n$	Converter transformer turns ratio/Number of/Power system order
$o$	PCM model order
$P_2(s)$	Second order Padé approximation
$P$	Active power
$p$	Number of power system outputs
$R$	Resistance/system transfer function residue
$r$	Rank index
$T$	Time constant
$t$	Time
$u$	Controller output signal (power system input)
$V$	Voltage
$X$	Reactance
$x$	System state
$Y$	Admittance
$y$	Controller input signal (power system output)
$Z$	Impedance
$z$	Modal system state

$\alpha$	Firing angle
$\beta$	Inverter angle
$\Gamma$	Set of uncertain system parameters
$\gamma$	Extinction angle/Uncertain system parameter
$\delta$	Generator rotor angle
$\varepsilon$	Error
$\zeta$	Modal damping factor
$\theta$	Voltage angle
$\lambda$	Complex eigenvalue
$\mu$	Mean
$\sigma$	Modal damping (real part)/Standard deviation
$\tau$	Signal transmission delay
$\varphi$	Power angle/Weibull scale parameter
$\phi$	Right eigenvector
$\psi$	Generator flux linkage/Left eigenvector
$\omega$	Speed/Modal frequency (imaginary part)

### **Subscripts**

$1, 2, 3, 4$	Various controller constants
$1d$	Effective $d$ -axis (mathematically defined parameter)
$2q$	Effective $q$ -axis (mathematically defined parameter)
$0$	Initial values/equilibrium point
$A, B, C, E$	Various controller constants
$C$	Shunt capacitor (load flow)/commutating
$c$	Complex eigenvalue pairs
$comp$	Compensation
$conv$	HVDC converter
$D$	$D$ -axis (system reference frame)
$d$	$d$ -axis (machine reference frame)
$dc$	DC system parameter
$e$	Generator electrical output
$eq$	Equivalent
$ex$	Excitation system
$f$	Excitation field
$G$	Generation (load flow)
$I$	Integral
$i$	Index value, where $i = 1, 2, 3 \dots$
$inv$	Inverter

$j$	Index value, where $j = 1, 2, 3 \dots$
$L$	Load (load flow)
$l$	Lines (or branches)
$lk$	Leakage
$m$	Generator mechanical input
$margin$	Margin
$N$	Number of buses within a power system
$o$	Open-circuit
$P$	Proportional
$POD$	Power oscillation damping controller
$PSS$	Power system stabiliser
$Q$	$Q$ -axis (system reference frame)
$q$	$q$ -axis (machine reference frame)
$R$	Transducer delay
$RSSR$	Relative sum-squared-root
$r$	Generator rotor/real eigenvalues
$rect$	Rectifier
$s$	Generator stator
$syn$	Synchronous
$t$	Generator terminal
$W$	Washout
$\gamma$	Uncertain system parameter

### **Superscripts**

$\cdot$	Derivative
$\hat{\phantom{x}}$	Estimate
$'$	transient
$''$	Sub-transient
$conv$	HVDC converter
$ex$	Excitation system
$Idc$	DC current
$inv$	Inverter
$load$	Load
$MLQG$	Modal linear quadratic Gaussian controller
$max$	Maximum limit
$min$	Minimum limit
$Pdc$	DC active power injection
$POD$	Power oscillation damping controller

<i>PSS</i>	Power system stabiliser
<i>Q<sub>dc</sub></i>	DC reactive power injection
<i>rect</i>	Rectifier
<i>red</i>	Reduced
<i>ref</i>	Reference set-point
<i>sys</i>	AC power system
<i>T</i>	Matrix transpose
<i>TGR</i>	Transient gain reduction
<i>T<sub>x</sub></i>	Transformer
<i>V<sub>dc</sub></i>	DC voltage
<i>VSC</i>	Voltage source converter

### **Acronyms**

AC	Alternating Current
ARE	Algebraic Riccati Equation
AVR	Automatic Voltage Regulator
COI	California-Oregon AC Intertie
CPU	Central Processing Unit
DC	Direct Current
FACTS	Flexible AC Transmission System
GPS	Global Positioning System
HVDC	High Voltage Direct Current
IEEE	Institute of Electrical and Electronic Engineers
IGBT	insulated gate bipolar transistor
INELFE	Interconnexion Électrique France Espagne
LCC	line commutated converter
LDS	Low Discrepancy Sequences
LMI	Linear Matrix Inequality
LQG	Linear Quadratic Gaussian
LQR	Linear Quadratic Regulator
LTR	Loop Transfer Recovery
MC	Monte Carlo
MIMO	Multiple-Input-Multiple-Output
MIS	Mexican Interconnected System
MISO	Multiple-Input-Single-Output
MLQG	Modal Linear Quadratic Gaussian
MTDC	Multi-Terminal Direct Current
NB	Naïve Bayes
NETS- NYPS	New England Test System and New York Power System

NGET	National Grid Electricity Transmission plc
ODIS	Offshore Development Information Statement
OPF	Optimal Power Flow
PC	Personal Computer
PCM	Probabilistic Collocation Method
PDC	Phasor Data Concentrator
PDF	Probability Density Function
PI	Proportional-Integral (Control)
PLF	Probabilistic Load Flow
PMU	Phasor Measurement Unit
POD	Power Oscillation Damping
PSS	Power System Stabiliser
PV	(Active) Power–Voltage
RAM	Random Access Memory
RSSR	Relative Sum-Squared-Root (Error)
SISO	Single-Input-Single-Output
SSR	Sub-Synchronous Resonance
SVC	Static Var Compensator
TCSC	Thyristor Controlled Series Capacitor
TGR	Transient Gain Reduction
TPE	Two Point Estimate
UK	United Kingdom
USA	United States of America
VDCOL	Voltage Dependent Current Order Limiter
VSC	Voltage Source Converter
WAC	Wide Area Controller
WAMS	Wide Area Measurement System
WSCC	Western Systems Coordinating Council

# Abstract

---

*A Probabilistic Approach to Improving the Stability of Meshed Power Networks with Embedded HVDC Lines*

**Mr Robin Preece, The University of Manchester, December 2012**

This thesis investigates the effects of High Voltage Direct Current (HVDC) lines and multi-terminal grids on power system small-disturbance stability in the presence of operational uncertainties. The main outcome of this research is the comprehensive probabilistic assessment of the stability improvements that can be achieved through the use of supplementary damping control applied to HVDC systems.

Power systems are increasingly operated closer to stability boundaries in order to improve their efficiency and economic value whilst a growing number of conventional controlled power plants are being replaced by stochastic renewable generation sources. The resulting uncertainty in conditions can increase the risk of operational stability concerns and should be thoroughly evaluated. There is also a growing necessity to explore the potential improvements and challenges created by the introduction of new equipment, such as HVDC systems. In recent years, HVDC systems have become more economically competitive and increasingly flexible, resulting in a proliferation of projects. Although primarily installed for power transmission purposes, their flexibility and controllability can provide further benefits, such as the damping of persistent oscillations in the interconnected networks.

This work contributes to a number of areas of power systems research, specifically surrounding the effects of HVDC systems on the small-disturbance stability of transmission networks. The application and comprehensive assessment of a Wide Area Measurement System (WAMS) based damping controller with various HVDC systems is completed. The studies performed on a variety of HVDC technology types and configurations – as well as differing AC test networks – demonstrate the potential for HVDC-based Power Oscillation Damping (POD). These studies include examinations of previously unexplored topics such as the effects of available modulation capacity and the use of voltage source converter multi-terminal HVDC grids for POD. Following these investigations, a methodology to probabilistically test the robustness of HVDC-based damping controllers is developed. This methodology makes use of classification techniques to identify possible mitigation options for power system operators when performance is sub-optimal. To reduce the high computational burden associated with this methodology, the Probabilistic Collocation Method (PCM) is developed in order to efficiently identify the statistical distributions of critical system modes in the presence of uncertainties. Methods of uncertain parameter reduction based on eigenvalue sensitivity are developed and demonstrated to ensure accurate results when the PCM is used with large test systems. Finally, the concepts and techniques introduced within the thesis are combined to probabilistically design a WAMS-based POD controller more robust to operational uncertainties. The use of the PCM during the probabilistic design results in rapid and robust synthesis of HVDC-based POD controllers.

# Declaration

---

No portion of the work referred to in this thesis has been submitted in support of an application for another degree or qualification of this or any other university or institute of learning.

# Copyright Statement

---

The author of this thesis (including any appendices and/or schedules to this thesis) owns certain copyright or related rights in it (the “Copyright”) and s/he has given The University of Manchester certain rights to use such Copyright, including for administrative purposes.

Copies of this thesis, either in full or in extracts and whether in hard or electronic copy, may be made only in accordance with the Copyright, Designs and Patents Act 1988 (as amended) and regulations issued under it or, where appropriate, in accordance with licensing agreements which the University has from time to time. This page must form part of any such copies made.

The ownership of certain Copyright, patents, designs, trade marks and other intellectual property (the “Intellectual Property”) and any reproductions of copyright works in the thesis, for example graphs and tables (“Reproductions”), which may be described in this thesis, may not be owned by the author and may be owned by third parties. Such Intellectual Property and Reproductions cannot and must not be made available for use without the prior written permission of the owner(s) of the relevant Intellectual Property and/or Reproductions.

Further information on the conditions under which disclosure, publication and commercialisation of this thesis, the Copyright and any Intellectual Property and/or Reproductions described in it may take place is available in the University IP Policy<sup>1</sup>, in any relevant Thesis restriction declarations deposited in the University Library, The University Library’s regulations<sup>2</sup> and in The University’s policy on presentation of Theses.

---

<sup>1</sup> See <http://www.campus.manchester.ac.uk/medialibrary/policies/intellectual-property.pdf>

<sup>2</sup> See <http://www.manchester.ac.uk/library/aboutus/regulations>

# Acknowledgements

---

I would like to express my gratitude to my supervisor Prof Jovica V. Milanović for his guidance, advice and encouragement throughout this research. His commitment to excellence and the enthusiasm with which he has reviewed this thesis and the work contained within it has been inspirational.

A special acknowledgement must also go to the Engineering and Physical Sciences Research Council (EPSRC) and National Grid Electrical Transmission plc (NGET) who have sponsored this project. I would particularly like to thank Mr Paul Coventry of NGET who has provided valuable insight and helped to strengthen my knowledge of the industrial context into which this research is placed.

I am extremely appreciative of the support provided to me by the Power Quality and Power Systems Dynamics group at The University of Manchester, as well as many other members of the Electrical Energy and Power Systems department. The opportunities to discuss and develop ideas have been instrumental in ensuring the success of this research. Special thanks go to Dr Nick Woolley, Dr Manuel Avendaño-Mora and Dr Muhammad Ali for the hours of entertaining discussion and debate they have provided.

I would also like to congratulate my dad and my sister for recently completing their PhDs. The ambition that they have shown and the support provided to me by my whole family throughout this period has been invaluable.

Most importantly, I would like to thank Kaylee Jenkinson for her patience throughout this research – and particularly during the writing of this thesis. Without her support and encouragement this period would have been far more stressful, and far less enjoyable.

*To Kaylee, and my family*

# **1 Introduction**

---

This research has been conducted in order to gain a greater understanding of how High Voltage Direct Current (HVDC) systems, which are becoming increasingly integrated within modern power networks, can be exploited to improve system stability. HVDC systems have historically been very expensive and reserved only for those situations when power transmission through traditional Alternating Current (AC) systems is unfeasible – such as transmission over extremely long distances, subsea interconnections, and transmission between asynchronous networks. As the technology has developed, HVDC systems have become more economically competitive and increasingly flexible, resulting in a proliferation of projects.

Power systems are increasingly being operated closer to the boundaries of stability in order to increase the efficiency and economics of their use. Stochastic renewable generation sources such as wind and solar are replacing conventional controlled power sources, resulting in more uncertain operating conditions. It is important to fully explore the effects of these uncertainties, and the risks that they introduce with respect to power system stability. Furthermore, there is a growing necessity to explore the potential improvements and challenges that new equipment, such as HVDC lines, can make. Although these systems are almost unilaterally installed for the sole purpose of power

transmission, their flexibility and controllability can provide further benefits with respect to power system operations – including power system stability.

## **1.1 Power System Stability**

Power system stability describes the ability of an electrical power system to maintain stable operation during normal conditions and to return to an acceptable stable operating point following disturbances [1]. Power systems are continually subjected to small disturbances as loads are connected or disconnected and the system must be capable of responding to these changes without failure. As power systems grow in size there is also an increasing likelihood that the network will be subjected to large disturbances due to faults or the sudden loss of major components, such as transmission lines, transformers or generating units. In these circumstances, following the operation of protection devices to remove the faulty component from the network, the remaining power system equipment must regain stable operation quickly to restore the supply of power to affected loads.

### **1.1.1 Stability Issues**

Power system stability issues can be broadly classified as follows [1]:

- ***Rotor Angle Stability*** is concerned with the ability of the interconnected generators within the power system to maintain synchronous operation at the same frequency. The manner in which rotor angle stability is maintained is a complex process, dependent not only on the inherent properties of the rotating machines themselves, but also the myriad of controllers which are used to regulate their operation.
- ***Voltage Stability*** refers to the ability to maintain acceptable voltages at all system buses. A system can be considered to be voltage unstable if an increase in reactive power injection at any system bus yields a drop in the voltage at the same bus. Voltages may collapse if a sequence of system events accompanies underlying unknown voltage instability, resulting in unacceptably low voltages for significant parts of the power system.
- ***Mid and Long-Term Stability*** refers to the slow system dynamics following severe system disturbances and significant frequency deviations. Study periods typically range from minutes to tens of minutes and incorporate the thermal

properties of boilers and generating equipment in addition to electromechanical components.

This thesis focuses on rotor angle stability. The electromechanical oscillations inherent to power system operation which can lead to wide-spread problems and even system collapse are of particular interest in this research.

### 1.1.2 Power System Oscillations

In a stable system, if the rotor of one machine deviates from its synchronous speed, the distribution of power generation amongst the remaining generators and the installed system controllers will act to reduce this deviation [2]. As synchronous generators are large rotating machines with inertia, returning to equilibrium can lead to oscillations as the rotor angle and speed of one or many machines settle. These mechanical oscillations are seen as variations in the electrical output of the machine in terms of electrical power and voltage. Ensuring that these oscillations are well damped is the main problem surrounding the *small-disturbance* rotor angle stability of modern power systems [1].

Small-disturbance (or small-signal) stability analysis is defined as the ability of the system to maintain stability following the small changes which continuously occur in practical power systems. These studies typically have timeframes of tens of seconds to one or two minutes in very large systems [1]. Small-disturbance stability is often treated separately to *transient* (or large disturbance) stability analysis, which is concerned with the response of the power system following large transient disturbances and time scales of milliseconds to a few seconds at most [1]. The work presented within this thesis is primarily focussed on small-disturbance rotor angle stability analysis of power systems. Large transient disturbances are also used though to investigate the time-varying performance of the network in the presence of the HVDC lines and controllers.

Electromechanical oscillations within power systems have varying causes, and require different techniques to improve their damping. These oscillatory modes can be classified as follows [1]:

- **Torsional Modes** ( $f \approx 5 - 50$  Hz) are associated with oscillations present within the rotational components in the turbine-generator shaft system. These can become problematic due to interactions with high speed controllers of generators, HVDC systems, and Flexible AC Transmission Systems (FACTS) devices – particularly when high levels of series compensation are installed.

Most famously, sub-synchronous resonance (SSR) between the system and turbine-generator shaft led to a catastrophic failure at Southern California Edison's Mojave Power Plant in 1970 [3].

- **Control Modes** ( $f$  typically  $< 0.1$  Hz) are associated with controllers installed within the system. These can include generator controllers such as Automatic Voltage Regulators (AVRs) or turbine speed governors, as well as the controllers of HVDC systems or FACTS devices.
- **Local Modes** ( $f \approx 1-2.5$  Hz) are associated with the machines at one generating station oscillating (or swinging) with respect to the rest of power system. These local oscillations can typically be damped sufficiently by installing power system stabilisers (PSSs) on the affected machines.
- **Inter-Area Modes** ( $f \approx 0.1-1$  Hz) are associated with many machines within an area of the power system oscillating against machines in other areas of the network. They occur when tightly coupled groups of generators exist within a large power system. They are traditionally harder to damp than *local modes* due to the number, dispersion, and varying levels of participation of the machines involved.

If any of these oscillatory modes present within a power system become unstable then they will lead to growing oscillations and eventually the disconnection of equipment, possibly leading to further cascading failures.

This thesis investigates inter-area oscillations which are increasingly causing concern as power system operators seek to transfer progressively larger amounts of power through long transmission lines.

### **1.1.2.1 Inter-Area Oscillations**

Low-frequency inter-area oscillations have become more prevalent as power systems have grown larger and look to achieve greater reliability and economy through interconnection with neighbouring systems. In many cases, the high values of generator exciter gain which have been used to improve the transient recovery of power systems following disturbances are resulting in small-disturbance stability concerns [2].

It has been shown that inter-area oscillations are an inherent property of large interconnected power systems [4]. Monitoring the flow of power through any tie-line

will reveal the presence of underlying oscillations, but provided that they are not large, they do not cause problems for the operation of the power system [5]. Unfortunately, as complex conditions evolve within power systems, it is possible for these underlying oscillations to become unstable and to increase in magnitude. Eventually this can lead to system collapse, potentially leaving millions of customers without electricity.

### 1.1.2.2 Consequences of Unstable Oscillations

On 10 August 1996, a series of events took place which led to the splitting of the Western Systems Coordinating Council (WSCC) grid in the USA into four islanded regions, disconnecting over 30 GW of load and affecting 7.5 million customers [6]. A number of transmission paths were tripped due to the sagging of lines in hot weather and faulty protection relays. The resulting system conditions meant that an inter-area oscillatory mode present between the north and south of the WSCC grid became unstable and growing oscillations were seen on the key California-Oregon AC Intertie (COI). These oscillations, see Figure 1-1 below, were sustained for almost a minute before they became so large that they caused all three lines that make up the COI to trip [7]. At this point, system collapse became inevitable and a series of cascading failures resulted in the islanding and loss of supply described above.

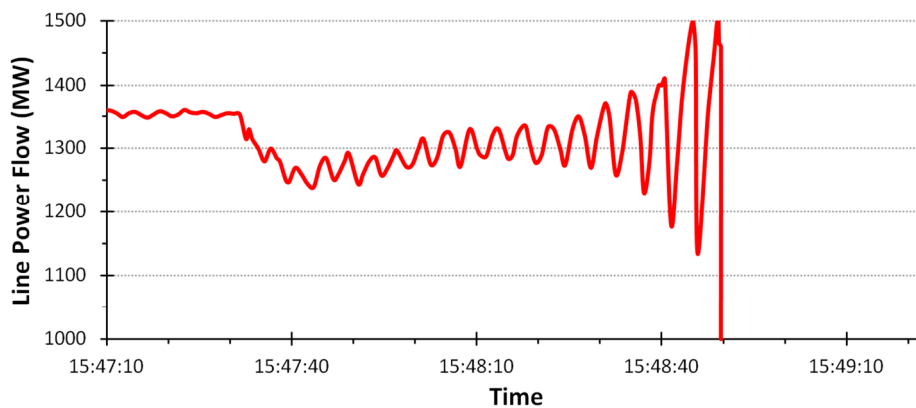


Figure 1-1: Line power flow through one of the three AC lines in the COI on 10 August 1996 – adopted from [2].

Further analysis of this disturbance and consequent recommendations have concluded that the system could have maintained stability had the inter-area oscillations been sufficiently damped [6-8]. Regrettably, the existing controllers had not been suitably designed and despite existing knowledge of the persistent low-frequency mode, no coordinated controller tuning effort had been made to stop unstable situations arising [6].

This is merely one of many examples, with power oscillations causing further issues in a variety of power systems, including:

- The interconnection of the Columbian and Venezuelan power systems in 1993 due to an unstable oscillatory mode with a frequency of roughly 0.20 Hz [9].
- The integration of the Turkish Grid into the European Network of Transmission System Operators for Electricity (ENSTO-E) network due to a poorly damped 0.15 Hz mode [10].
- Within the Mexican Interconnected System (MIS), where on 31 July 2008 a number of system events led to wide-spread power oscillations with a frequency of 0.40 Hz. These increased in magnitude for roughly two minutes before lines were tripped and system stability was restored [11].

### **1.1.3 Wide Area Measurement Systems**

Complex controller designs are increasingly being used to help provide crucial damping to inter-area modes. This has been largely facilitated in recent years by the development of Wide Area Measurement Systems (WAMS) which can collect data from various points within a large interconnected network to provide greater observability of any inter-area oscillations. These measurement systems use Phasor Measurement Units (PMUs) to collect time-stamped data which can be used to significantly improve the damping of inter-area oscillations [12-14].

PMUs were first developed at Virginia Polytechnic Institute and State University (Virginia Tech) in 1988 and use signals from the Global Positioning System (GPS) in order to achieve a synchronisation accuracy of 1  $\mu$ s [15]. The format of the data files created and transmitted by commercially available PMUs is presently governed by an Institute of Electrical and Electronic Engineers (IEEE) standard [16], and the OpenPMU, open source, platform exists to encourage research into further synchronophasor algorithm development [17]. PMUs must sample voltage and current measurements with sufficient incidence to ensure accurate calculation of phasor quantities and are required to report measurements at the system frequency (typically 50 Hz or 60 Hz) [16] – though faster reporting rates are encouraged.

The synchronised signals produced by the PMUs are collected at Phasor Data Concentrators (PDCs) and can be used to evaluate time-stamped variations in voltage, current and power flows at various points within the network – providing crucial

information to monitoring and control applications. Transmitting these signals from the remote locations to controllers incurs some time delays. These can vary based on the distances involved as well as the communications links used and have been reported as ranging from 7–185 ms for fibre optics cables [18-20] and between 100–500 ms for satellite communications [20-23]. Despite the delays involved, the use of these global signals can significantly improve the effectiveness of power oscillation damping (POD) controllers specifically designed and installed to reduce inter-area oscillations. These POD controllers typically act by varying the output of generators [24-29], FACTS devices [30-34], or HVDC systems [35-39].

## 1.2 HVDC Development

Despite the fact that the overwhelming majority of installed electrical transmission networks worldwide use AC, HVDC systems often emerge as the better power delivery solution in a number of situations. The recent proliferation of HVDC systems is so great that despite taking forty-seven years from the first commercial installation in 1954 to reach a worldwide installed capacity of 50 GW in 2001, it took just nine further years for this to double to 100 GW by 2010 [40]. Based on currently planned projects, it is expected that this will have doubled again to 200 GW by 2016. This growth in worldwide HVDC capacity is presented in Figure 1-2.

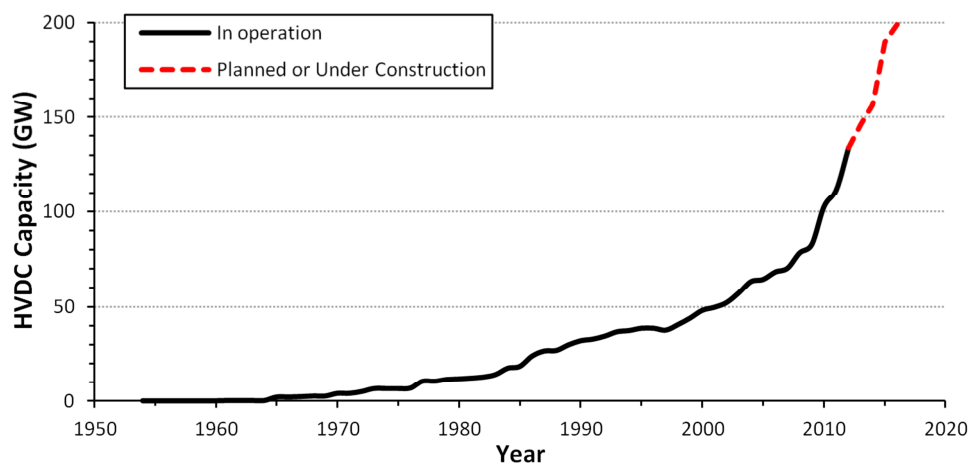


Figure 1-2: Growth in global HVDC capacity (projected up to 2016) – adopted from [41].

### 1.2.1 HVDC Technology

There are currently two converter technologies available commercially for use in HVDC transmission:

- **Line Commutated Converter** (LCC-HVDC) which began with the use of mercury valves and now utilises high power thyristors.

- **Voltage Source Converter** (VSC-HVDC) which uses insulated gate bipolar transistors (IGBTs).

Full details of the converter technologies and their associated control and protection schemes can be found in [42, 43]. The following sections present a brief overview of both LCC-HVDC and VSC-HVDC.

### 1.2.2 LCC-HVDC

LCC-HVDC was the first (and until relatively recently the only) practical HVDC conversion technology to be developed. Although the most widely used HVDC technology, LCC-HVDC is limited by its use of thyristor switching. The lack of turn off controllability leads to:

- **Poor power factors** – reactive power can only be consumed with thyristor control schemes and will be in the order of 50-60% active power flow under normal operation [43].
- **Considerable waveform distortion** – this leads to large filtering requirements, considerably increasing the physical footprint of the converter stations.

Line commutated conversion is fundamentally simple – it is the external plant required for reactive power compensation and filtering, which is elaborate and expensive. LCC-HVDC is used for the largest power transmission projects, capable of operating at 800 kV and delivering up to 8000 MW [44, 45].

### 1.2.3 VSC-HVDC

VSC-HVDC has seen rapid development in recent years and overcomes many of the shortcomings of LCC-HVDC [43, 46, 47]:

- VSC-HVDC is presently competitive in terms of converter station losses and costs. Until recently this was not the case and VSC-based systems would rarely be selected for HVDC projects due to high costs.
- The VSCs display very low harmonic content, in some cases removing the need for filters entirely.
- VSC-HVDC systems are capable of providing reactive power support at each converter station – whereas LCC-HVDC demands reactive power support.
- VSC-HVDC lines can be connected to weak or even passive AC networks, supporting black start situations.

- Point-to-point VSC-HVDC lines can be easily extended into multi-terminal HVDC grids due to the constant voltage polarity during bidirectional power flow.
- The development of VSC-HVDC systems into modular designs has also meant that converter stations can be delivered fully assembled to site allowing fast installation and testing [48].
- VSC-HVDC systems however cannot operate at the same power levels as the more mature LCC-HVDC and are currently limited to 500 kV and 1500 MW [44, 45].
- The smaller footprint of VSC-HVDC converter stations, as well as the ability to provide reactive power support, enables their offshore placement.

#### **1.2.4 Offshore Development**

Offshore development represents a large and growing area of demand for VSC-HVDC systems, particularly in Europe. As of 30 June 2011, there were 1,247 offshore wind turbines connected to transmission grids across nine European countries with a total capacity of 3.3 GW. The United Kingdom (UK) is making a huge investment in offshore turbines – installing 93.5% of all the European offshore turbines which were connected between January and June 2011 [49]. An examination of the Offshore Development Information Statement (ODIS) of 2011 produced by National Grid Electricity Transmission plc (NGET) reveals that the UK's installed offshore wind generation capacity will increase from the present value of 1.5 GW to between 25 GW and 59 GW by 2030 [50]. On a European scale, 40 GW of installed offshore capacity is expected by 2020, rising considerably to 150 GW by 2030 [51].

For large wind farm connections of roughly 500 MW or more, capacitive charging current limitations significantly reduce the useable capacity of AC cables and many lines, or large-core cables, are required, as well as reactive power compensating devices. The expense of the AC solution means that HVDC provides the only feasible connection option when the turbines are located further than 50 km offshore [50]. This means that a large number of VSC-HVDC lines will be required in order to bring power to shore. There is however currently very little operational experience with respect to offshore VSC-HVDC systems.

Despite the fact that there are ample examples of HVDC lines being used for subsea inter-connections, the technology has only seen two constructed projects with offshore terminations – though many more are planned. Of these two VSC-HVDC lines, only one is currently operational, delivering up to 88 MW of power to the Norwegian Troll A offshore gas compressor station [45]. The second system, which is significantly behind schedule and not operational as of October 2012, will be a 125 km subsea VSC-HVDC line, bringing 400 MW of power onshore to Germany from the BorWin1 wind farm [45]. Despite these few examples, many offshore projects for wind farm connections have been secured with commissioning expected between 2013–15 and capacities ranging from 576 MW to 900 MW [44, 45].

### **1.2.5 Future HVDC Systems**

Electrical transmission systems worldwide are seeing growing changes and development. In many developing countries this is due to increasing industrialisation and growing demand for electrical power. Worldwide demand is expected to reach 34 trillion ( $34 \times 10^{12}$ ) kWh by 2035, an increase of 84% since 2008 [52]. Economically developed countries are increasingly looking to exploit more remote sources of power. Whether these are previously unexploited hydro-power reserves or offshore wind farms, interconnection to load centres is often only possible using HVDC. This can be especially true for densely populated countries where securing right-of-way permission for new transmission pylons is simply no longer possible. An example of this is the UK Western HVDC Line where the unavailability of an AC transmission path has resulted in a submarine cable route for the 2 GW reinforcement between Scotland and England [53]. Furthermore, the desire for increased interconnection between transmission systems to improve security and energy trading options (particularly in Europe) is resulting in the gradual installation of high capacity embedded HVDC lines which will operate in parallel with existing AC infrastructure. This is illustrated by the Interconnexion Électrique France Espagne (INELFE), a €700 million VSC-HVDC line between France and Spain which will dramatically increase the possible energy transfer capabilities between these countries from its present value of 1400 MW to 2800 MW [54].

HVDC systems have traditionally been used as point-to-point transmission schemes, often between asynchronous power networks [42]. As embedded HVDC lines become more prevalent, there is growing interest in the unique opportunities that they provide to

improve system stability. If used correctly, the converters can rapidly vary power flow to improve the damping of existing inter-area oscillation and provide additional value to the projects. In the following sections a review of the existing work into this and other related areas is presented.

### **1.3 Past Research on Damping of Power Oscillations**

Power oscillation damping has traditionally fallen under the remit of PSSs installed at generating units within power systems. Although years of experience have demonstrated these to be effective at damping local modes, performance with respect to inter-area modes is much poorer and sometimes inadequate – as shown by the examples previously presented. This is primarily due to the complexities of coordinated tuning and the sacrifice in local mode damping that must be made [55-57]. As such, PSSs are often tuned for local modes when the generators are installed, and settings are rarely altered unless issues arise.

The need for improved inter-area mode damping has led to widespread research into the field of power oscillation damping. Over the years, many different controller designs have been shown to be effective at damping power oscillations with various technologies, though very few have been implemented in real systems.

#### **1.3.1 Power Oscillation Damping Control**

A number of factors must be considered when assessing POD controllers. The *performance* of the controller is clearly important in terms of the extent to which the damping of power system oscillations is improved. In addition to this, the *robustness* of the controller is increasingly of concern. As system conditions become more variable, and the number of model and operating condition uncertainties increase, POD controllers which are robust with respect to these changes and maintain their designed performance are essential. Additional factors such as the *simplicity* of the control design and its *scalability* to large power systems will also factor when determining if a control design is appropriate for practical installations.

##### **1.3.1.1 Generator-Based Control**

Many approaches which have attempted to improve the damping of inter-area oscillations within power systems have sought to do so through the improved control of the existing generators within the network. This work has taken the form of both coordinated tuning of existing PSSs within the system, for example [57-62], and the use

of advisory controllers which send supplementary control signals to appropriate generators, as in [24-29].

Despite the fact that coordinated PSS tuning is often constrained by the use of existing local input signals, results reported in [59] demonstrate that high damping factors of more than 20% can be achieved for all electromechanical modes. The coordinated tuning is typically completed using optimisation approaches with evolutionary techniques such as genetic algorithms and particle swarm optimisation proving popular and effective [57-60]. An alternative approach is the use of Linear Matrix Inequalities (LMIs) to form a set of robust decentralised controllers which replace traditional PSSs [61]. In [62], Prony analysis is used to produce a reduced order model of a single generator connected to a large system. These models, produced for each generator in turn, incorporate the system inter-area oscillations to ensure that adequate damping factors are achieved for all power system oscillations.

Advisory controllers are able to send supplementary signals to the generators in addition to the local stabilising control actions which are governed by traditional PSSs. The hierarchical nature of these controllers maintains a level of decentralised control within the PSSs, whilst inter-area oscillation damping is achieved using a single centralised Wide Area Controller (WAC) which exploits global signals sourced from a WAMS. The use of LMIs to incorporate the mixed sensitivities of  $H_2$  and  $H_\infty$  criteria has proved a popular method for the development of supplementary WACs as demonstrated in [24-26] and also in [27] where a fuzzy logic switch is used to enable the controller when inter-area oscillations are detected.  $H_\infty$  controllers are optimised to achieve a desired balance of performance and robustness with respect to the effects of system uncertainties. Although they are capable of exhibiting good robustness properties, this is reliant on accurate modelling of both the system and all considered uncertainties. The problem formulation is vital as the final controller is only robust for this formulated system. If the uncertainties are poorly formalised then the controller's practical efficacy may not match its intended mathematical performance.

Linear Quadratic Gaussian (LQG) control is used successfully in both [28] and [29], effectively incorporating WAMS-based signal delays. The novel use of a modal formulation in [29] removes many of the difficulties experienced in [28] such as the requirement for participation factor analysis. This Modal Linear Quadratic Gaussian

(MLQG) design, therefore, allows targeted control action on inter-area modes whilst leaving sufficiently damped locally controlled modes unaffected. The simplicity of the controller synthesis technique presented in [29] makes it suitable for a wide range of POD purposes, although only generator-based implementation has currently been investigated.

### **1.3.1.2 FACTS-Based Control**

There has been extensive research into the use of POD controllers installed with FACTS devices, for example [12, 23, 30-34, 63-71]. The scope of this work is broad, covering a wide variety of device types and controller design techniques.

FACTS devices are most effective at power oscillation damping when connected in series with the AC network and capable of modulating active power flow, such as Thyristor Controlled Switched Capacitors (TCSCs) [31, 34, 63, 67, 70, 71] or other series-connected devices [33, 69, 72]. Nevertheless, due to the existence of shunt-connected devices such as Static Var Compensators (SVCs) which have been installed within many power systems to provide voltage support, POD applications for these devices [12, 23, 64, 66] and combinations of both series and shunt-connected devices [30, 32, 65, 68] have also been researched extensively.

In much of the previous work into FACTS-based POD control, WAMS-based global signals are exploited to improve system observability and improve modal damping [12, 23, 31, 32, 34, 70, 71]. Research has also been conducted into which signals are most suitable for POD in [73-75], considering not only the signal content but also the reliability and robustness of the content. However, many studies cite the need for robust decentralised control utilising only those signals locally available at the FACTS installation [30, 33, 63-69, 72]. In these instances, good damping factors can be achieved, but the performance becomes heavily dependent on the location of the installed device and those signals which are available. These factors may not be controllable in practical installations when devices are not primarily installed for POD purposes.

Controller synthesis techniques are varied, ranging from extensions of traditional linearisation-based residue techniques which incorporate global signals [12, 70], to the novel use of fuzzy control laws [33]. Lyapunov energy functions have been used for control design purposes in [68] and [69], demonstrating robust designs which are

independent of system modelling techniques. Such designs do however have complex formulations (especially for large power systems) which may prove prohibitive in practical installations.  $H_\infty$  designs which attempt to guarantee robustness to system variations are proposed in [23, 65, 66], as well as LMI formulations in [30, 31]. The final designs are nominally robust; however the performance of the controllers is tested only for a very small set of operating conditions and the practical limits of the considered uncertainties are not evaluated.

LQG control is used in [34, 67, 71] to improve the damping of inter-area modes, with improved modal damping maintained following a significant reduction of the final controller order. As with the previously discussed LQG implementations, the complexities surrounding the need for participation factor analysis and complex weight tuning limit the practicality of the standard approach on large systems when high numbers of generating units participate in the poorly damped power oscillations. There are also approaches such as [32, 63, 64] which utilise non-linear control theory in an attempt to remove the assumptions implicit in the use of linearised power system models. Complex feedback is used to produce controllers which are not adversely affected by significant variations in network conditions. However, as with the robust  $H_\infty$  controllers previously discussed, no thorough assessment of the controller performance across wide ranging conditions has been completed.

FACTS devices are very expensive, so much so that in 2006 it was estimated that there were just ten TCSC installations worldwide [76]. It is therefore unlikely that these devices will be installed specifically to damp power system oscillations. By complementing the steady state system improvements they provide with dynamic POD controllers, such projects can become more economically feasible. Furthermore, the POD action of FACTS devices can be coordinated with that of existing PSSs in an attempt to improve performance and robustness. This coordination has been demonstrated using both traditional residue-based techniques in [77] and using non-linear optimisation in [56, 78-80]. As with all design techniques, care must be taken to ensure that the robustness of the resulting controllers to system changes is assessed. The coordinated control schemes created in [56, 77-80] are only simulated at a few *close-to-nominal* operating scenarios and it is acknowledged in [56] that performance will deteriorate if system conditions vary from those used during the optimisation procedure.

### 1.3.1.3 HVDC-Based Damping Control

The need to model HVDC systems correctly for small-disturbance stability studies has long been stated. Modelling techniques which display the correct level of dynamic behaviour are vital to ensure the accuracy of the produced results [81, 82]. In [83], a model is presented for use when assessing stability concerns in the range of 2–200 Hz; system dynamics faster than typical electromechanical oscillations. General small-disturbance HVDC models are presented in [84, 85], and [86] proposes a standardised VSC-HVDC model for such studies. This is based on injection modelling and permits varying degrees of model complexity.

An early study into the effects that the location of HVDC systems can have on small-disturbance stability is presented in [87], and developed further in [88] to identify the optimal connection points and desired power flow to improve the stability of the connected AC system. This approach assumes that the HVDC system can be installed in any location and can be controlled purely to improve system stability. In practical installations however, not only are possible points of connection likely to be extremely limited based on logistical considerations, but HVDC systems are operated to maximise their economic value – typically through maximising power flow. There have also been converter controller designs which attempt to improve the inherent stabilising action of the HVDC system, such as [89] and [90] which utilise sliding mode control. These are not active modulation-based controllers; rather the steady-state operation and response of the converters is altered to provide some stability improvements. It must be noted that the majority of research into the use of HVDC for oscillation damping has focussed on the use of supplementary controllers.

As LCC-HVDC systems have been available and operational for longer than VSC-HVDC systems, it is unsurprising that more research has been published into the use of the classic converter technology to damp power oscillations. Fundamentally, any techniques proposed for active power modulation through LCC-HVDC systems could be readily applied to VSC-HVDC systems as this modulation can be accomplished with fewer reactive power concerns. The most recent publications in the area, however, are primarily focussed on VSC-HVDC applications.

Controlled modulation of the active power flow through LCC-HVDC lines was proposed over thirty-five years ago in 1976 as a means to improve the transmission capacity of parallel AC tie lines [91]. Traditional PSS-based controls were tuned

following standard linearisation-based methods using the power flow through the AC tie as an input signal. The scheme's success at suppressing oscillations was sufficient to enable an upgrade of the AC tie-line capacity from 2100 MW to 2500 MW [92] – though the controller could not be relied upon following severe disturbances which would cause significant oscillations.

Studies into single or double-machine systems connected to an infinite-bus through single LCC-HVDC lines [93, 94] and parallel AC/DC lines [95, 96] have demonstrated frequency stabilisation benefits. The use of local generator speed or frequency signals has been combined with fuzzy controllers [93, 94] and non-linear energy function-based techniques [95], as well as traditional linearisation-based approaches [96], to improve the small-disturbance stability of the test systems. The investigations presented in [93] and [94] are concerned with isolated HVDC infeeds into synchronous AC networks and are not typical of this research area, which primarily focuses on AC/DC systems. Although modulation of an infeed is possible, and can improve the stability of the connected AC system significantly, this improvement will come at the expense of induced oscillations in the AC network which is connected to the other end of the HVDC line. The second system must be sufficiently stable to cope with this; otherwise such schemes should not be attempted.

Studies such as [97] demonstrate the effect that LCC-HVDC POD control can have on more radial transmission networks, such as the Australian power system. Both LQG-based state feedback techniques and particle swarm optimisation of control parameters are compared and shown to demonstrate similar performance – significantly improving the post-disturbance response of the network.

In recent years China has installed a greater number of LCC-HVDC lines than any other nation, with a current operational HVDC transmission capacity of over 45 GW. These large transmission corridors have been installed to help transfer power from extensive hydro-power sources such as the Three Gorges Dam in the western mountainous regions to the densely populated load centres in the south and east of the country. There are also further lines between these load centres to ensure good interconnectivity and redundancy. This large investment in HVDC systems has encouraged significant research specifically concerned with POD within the Chinese grid [38, 39, 90, 98-101]. This work has been wide ranging, including both POD controllers for single lines [90, 98, 99, 101] and coordinated schemes such as [38, 39, 100]. The simulation-based

studies using these coordinated schemes have displayed improvements in low frequency mode damping factors of over 10%. This is a significant increase which is facilitated in part by the use of WAMS-based global signals and ensures power oscillations are quickly settled. Numerous control design strategies have been studied, including standard linearisation and residue techniques using local [98] and wide area [99] signals, sliding mode controls [90], relative gain array [38], non-linear optimisation of PSS-based designs using local [100] and global [39] signals, and adaptive controllers which self-tune using the Prony method [101]. All approaches demonstrate good nominal performance. However, as has been noted for other POD research with generator and FACTS implementations, the robustness of the controllers is poorly assessed (if at all). The control schemes will often only be simulated at the operating conditions used during the design process. Occasionally increased loading conditions are considered, but investigations across wide ranging conditions are not forthcoming in the available literature.

VSC-HVDC systems have received greater attention recently as the number of planned installations has increased. Investigations using small study networks have demonstrated that a number of control designs can be applied, such as pole placement techniques [102], non-linear control strategies [103], model predictive control [104], and energy function formulations [105]. These approaches have focussed on the use of WAMS-based signals, specifically generator frequency measurements [102-104], though local measurement of the frequency at the VSC-HVDC point of connection can also serve as a suitable controller input [105]. The comparison of local and global signals presented in [106] demonstrates that local signals can provide suitably high information content to effectively damp oscillations. It is however acknowledged that this is highly dependent on the location of the installed line. In [106], the location of the VSC-HVDC line has been selected based on the controllability of the inter-area mode that requires additional damping. If this flexibility is not available then global signals may be required to ensure optimum POD performance.

Investigations on larger multi-area test networks such as the interconnected New England Test System and New York Power Systems (NETS-NYPS) [107], the Nordic thirty-two bus network [108], and the Australian equivalent system [37] have shown VSC-HVDC-based POD damping to be extremely effective. VSC-HVDC systems provide the option of utilising not only active power modulation, but also variation in

reactive power injection for stabilising purposes. The benefits of this are briefly investigated within [37] and [107] where it is found that active power modulation is much more effective at damping power oscillations within the AC system. In [107] it is suggested that a more effective use of reactive power modulation would be for the stabilisation of AC system voltages.

The level of active power deviation permitted, or the modulation capacity, varies throughout the wide range of HVDC-based POD studies. The early investigations presented in [91] and [92] used a variation of just  $\pm 3\%$  of rated power flow. However as confidence in the capabilities and reliability of the converter technology has grown, so too has the willingness to exploit greater modulation capacities with values of 10–25% commonly seen within the research. Within [38] it is stated that power transmission of 20% above rated power is acceptable for long-term overload, and that 40% greater than rated power can be used for short-term overload in emergency situations. No study into the effects that varying modulation capacity has on the damping controller performance has been reported.

#### **1.3.1.4 Multi-Terminal HVDC Systems**

Point-to-point LCC-HVDC lines do not easily extend to multi-terminal systems as power reversal is facilitated by a reversal in voltage polarity. This results in the need for complex configurations in order to tap off power at terminals along the line, and limited power flow options. As such, only two Multi-Terminal LCC-HVDC (LCC-MTDC) systems exist, the largest being the 2 GW Quebec – New England Transmission system. VSC-HVDC with constant voltage polarity makes multi-terminal systems easily realisable and although no VSC-MTDC systems currently exist, it is expected they will in the future [109, 110].

Despite the complexities and broad lack of LCC-MTDC systems in operation, research into the application of POD for MTDC systems was first completed in the 1980s [111–114]. This work identified the benefits that multiple controlled power injection points could offer, whilst also acknowledging the complexities in implementing such schemes with LCC-based systems. Since the advent of VSC-HVDC systems there has been very little research into the feasibility and practicality of VSC-MTDC-based POD, despite the demonstrated abundance of various control methods which can be used for oscillation damping control design. As no VSC-MTDC systems have been constructed, the majority of work within this area is focussed on steady-state control and operation –

for example [115-118] – rather than the additional possible stability benefits. A brief discussion can be found in [119] which identifies that VSC-MTDC grids could present opportunities for AC system stabilisation, although no studies or control methods are proposed.

### 1.3.1.5 Signal Delays in WAMS-Based Damping Controllers

Wide area signals are subject to transmission delays which can vary according to the distances and transmission method used. The effects of signal latency and mitigation techniques for WAMS-based damping controllers have received much research interest.

Control designs based on linearised power system models typically include the signal delays as part of this state space representation. This is often achieved using a Padé rational approximation of the true exponential Laplace-domain representation, as in [28, 120, 121]. It has been demonstrated in [28] and [29] that a second order Padé representation provides a good approximation of long delays.

Further comprehensive analyses of the effects of signals delays and novel mitigation techniques are proposed in [22, 23, 122-124]. The effects of time delay uncertainty on the closed loop stability of power systems incorporating a generator PSS-based advisory WAC are examined in [22] where gain scheduling is shown to improve the controller's robustness to varying time delays. In [23] and [122], Smith predictors are incorporated into LMI formulated  $H_\infty$  damping controller designs. These predictors estimate the current state of the network based on the delayed signals they receive in order to effectively damp oscillations using FACTS devices. Adaptive controllers are demonstrated in [123] and [124] in which self-tuning phase compensation blocks are utilised to negate the effects of any variation in the transmission delay experienced by the global signals. These approaches have been demonstrated using generator and FACTS-based WAMS-based POD controllers. The proposed techniques could also be applied to POD controllers installed for use with HVDC systems.

### 1.3.2 Probabilistic Small-Disturbance Stability Assessment

The deterministic approaches traditionally used when assessing power system stability do not account for the variability and true stochastic nature of modern power systems. As these variations increase, for example due to rising numbers of intermittent renewable energy sources and new types of loads such as electric vehicles, there is a growing need for probabilistic stability assessments.

The aim of any probabilistic small-disturbance stability assessment is to determine the probability distribution for a given critical system mode of interest, based on the variation in the considered system uncertainties. The resultant probability density function (*pdf*) can then be used to assess probabilistic risk measures, such as the probability of system instability. A number of techniques have been used to perform such studies, many of which were first established for use with Probabilistic Load Flow (PLF) [125, 126].

### **1.3.2.1 Numerical Method**

The numerical method involves Monte Carlo (MC) simulation of a wide range of operating scenarios which are based on pseudo-random sampling from the *pdfs* of stochastic sources of system uncertainty. For each computational scenario, the standard deterministic small-disturbance stability assessment can be completed. Once sufficient scenarios have been simulated, the critical mode *pdf* can be generated.

This method is a commonly used approach for probabilistic studies and has been implemented in [127] and [128] to assess the stochastic effects of generation and load on inter-area mode damping for a large power system. The MC method is simple and can be relied upon to produce accurate results. However, for large systems containing many uncertainties, the total number of scenarios that must be considered to ensure that full variation of all parameters is captured can be extremely large – limiting the feasibility of the MC method with such systems.

### **1.3.2.2 Analytical Methods**

Analytical methods for probabilistic small-disturbance stability assessment attempt to remove the need for vast numbers of simulations through direct calculation of the effects of the system uncertainties on the critical modes of interest. Initial approaches were based on generalised tetrachoric series, using a multivariate Gaussian distribution to include multiple independent stochastic sources [129]. This is developed further in [130] and implemented on a ten-machine network, although the presented research assumes that the critical modes follow a Gaussian distribution – which is not necessarily the case in practical power systems [131].

The Gram-Charlier expansion-based method removes the assumption of Normally distributed parameters and has been effectively applied to probabilistic stability studies in [132]. Accurate solutions are reported, however this method requires complex

mathematical analysis to establish the moments and cumulants of both the stochastic system variables and the critical eigenvalues. It is also often necessary to include approximations within the calculations in order to converge on a solution within an acceptable length of time.

### 1.3.2.3 Efficient Sampling Methods

Efficient sampling methods can be viewed as a combination of both numerical and analytical techniques. An initial method is used to determine a set of specified sampling points, based on the known distributions of the stochastic system parameters. The numerical approach is then used to evaluate the critical mode value at each of the specified sample points. Following this, a further method is used to reconstruct the modal distribution from the sampled values. The use of various techniques to efficiently sample the whole search-space means that vast savings can be made compared to the full MC approach, without the need for the complexities of a fully analytical approach.

One such approach is the Two Point Estimate (TPE) method, used in [133] to assess probabilistic stability. This approach requires just  $2m$  samples for a system with  $m$  uncertain parameters. However it assumes a pre-determined distribution for the measured output (typically Gaussian), which is not necessarily true in practical power systems and was seen to be a limiting factor for the tetrachoric series based analytical approach in [129].

A further example of an efficient sampling method includes the use of Low Discrepancy Sequences (LDS) in [134] to robustly tune system PSSs. The PSS parameters are optimally tuned using sample points which are selected to evenly cover the whole search-space, demonstrating clear improvements when compared to a standard MC-based optimisation. In [135],  $\Lambda\Pi_r$  sequence based sampling is applied in a similar way to evenly cover the search-space in order to accomplish the robust ranking of loads with respect to their sensitivity to system uncertainties. The accuracy of reduced numbers of MC runs for PLF has been improved with the use of Latin hypercube sampling with Cholesky decomposition in [136].

The techniques described in [134-136] all use even search-space covering in their efficient sampling methods. A further promising approach is proposed in [137] where the Probabilistic Collocation Method (PCM) is used to analyse the effect of fault clearing time uncertainty on the transient response of system voltages. The PCM

approach also uses a small number of efficiently selected samples, but their selection is weighted to represent the most probable regions of the uncertain parameter *pdfs* in the greatest detail. In this way, the PCM estimation accuracy is focussed in the regions of operation most likely to occur. This method does not require any assumptions about the shape of the output distribution and has subsequently demonstrated accurate results. It has seen limited application within power systems with only load model uncertainties considered with respect to variations in small-disturbance stability [137-139]. The method has potential limitations, as the number of required samples increases quickly with the number of considered uncertainties. However, eigenvalue sensitivity approaches (suggested in [137] but not applied) may allow a reduction in the number of modelled uncertainties, facilitating application for large power system studies.

Further development of these efficient sampling techniques is required in order to provide methods for fast probabilistic power system stability analysis which are not encumbered by the disadvantages of the purely numerical and analytical approaches.

### **1.3.3 Summary of Past Research**

Having reviewed the past research in the field, several areas have been identified which need to be addressed. These are summarised as follows:

- The effect of a WAMS-based POD controller for VSC-HVDC lines on the small-disturbance stability of mixed AC/DC networks requires thorough investigation. Studies to date have shown various controllers to be effective for power oscillation damping, however a thorough investigation of a single wide area controller design structure for VSC-HVDC based POD is not available.
- An assessment into the effects of varying the modulation capacity available for HVDC-based POD control should be completed. Previously published research in this area has used a variety of modulation capacities but the change in system stability caused by these variations has not been investigated.
- No studies concerning the use of VSC-MTDC grids for POD control to improve system small-disturbance stability have been completed. The existing research into POD with multi-terminal HVDC was published prior to the development of VSC-HVDC and before many of the recent publications on wide area control.

- A comprehensive assessment of the robustness of VSC-HVDC POD controllers is currently lacking. Many nominally robust control schemes have been published but these have not been thoroughly tested across the wide ranging operating conditions that are typical of modern power systems.
- The Probabilistic Collocation Method requires development for implementation on large power systems to efficiently assess probabilistic power system small-disturbance stability with respect to uncertain operating conditions.
- Current robust control designs are mathematically complex and are currently not implemented within practical power systems where simple *Single-Input-Single-Output* (SISO) linear controllers have been favoured. A straightforward and logical method to improve the robustness of WAMS-based POD controllers with respect to the uncertainty of power systems would be extremely beneficial.

#### **1.4 Research Aims and Objectives**

This thesis aims to address many of the issues which have been identified within the current body of research. The main aims of this research are to undertake a thorough evaluation of the improvement in power system small-disturbance stability that HVDC-based POD control can achieve, and to use probabilistic methods to produce a supplementary WAMS-based POD controller which is more robust to the uncertainties inherent in modern power systems. In order to achieve these aims, the following research objectives have been defined:

1. To summarise and critically evaluate existing methods for improving the small-disturbance stability of power systems using POD controllers.
2. To select and develop appropriate LCC-HVDC, VSC-HVDC and VSC-MTDC models within MATLAB/Simulink for integration with AC network models in order to produce supplementary POD controllers and perform power system small-disturbance stability analysis and transient studies.
3. To thoroughly investigate a suitable WAMS-based supplementary POD controller design for HVDC systems within meshed AC/DC power systems. This study should include multiple AC system topologies, different VSC-HVDC system configurations, variable signal transmission delay, signal loss, the effects

of reactive power modulation, varying active power modulation capacity, and comparison with traditional controller designs.

4. To assess the applicability of VSC-MTDC systems for POD purposes within meshed AC/DC networks using global signals and an appropriate supplementary control structure.
5. To develop a methodology to probabilistically evaluate the robustness of WAMS-based supplementary POD controllers for HVDC systems with respect to uncertain power system conditions.
6. To develop appropriate measures which allow the application of the PCM for critical mode estimation within large power systems. This will allow fast and accurate calculation of system risk indices such as the probability of instability.
7. To develop a methodology to improve the robustness of HVDC-based POD controllers by probabilistically accounting for the operating uncertainties within power systems.

## **1.5 Main Contributions of this Research**

The work within this thesis contributes to a number of areas of power systems research, specifically surrounding the effects of HVDC systems on the small-disturbance stability of transmission networks. The main outcome of this research is the comprehensive probabilistic assessment of the improvement to power system small-disturbance stability that can be achieved through the use of supplementary damping control applied to HVDC systems. Assessment of the robustness of these controllers has in turn guided the controller synthesis procedure, resulting in improved system performance in the presence of operational uncertainties.

References prefixed with the letter 'F' refer to publications which have arisen from the work completed during this research. A full list of international journal and conference publications is included in Appendix F at the end of the thesis. The contributions found within this thesis can be summarised as follows:

- The application and comprehensive assessment of a WAMS-based damping controller with various HVDC systems. The application of the MLQG controller synthesis approach (previously unused with HVDC applications) has extended the existing research within this field to comprehensively demonstrate the

potential for HVDC-based power oscillation damping in wide range of mixed AC/DC networks. [F1, F2, F6, F7].

- An investigation into the effects of variable modulation capacity on the effectiveness of HVDC-based POD controllers has been performed. This concluded that the use of flexible modulation limits is required to effectively exploit the damping capabilities of installed HVDC lines [F2].
- WAMS-based control of VSC-MTDC grids has been shown to effectively damp power oscillations within complex meshed AC/DC systems. The work carried out in this previously unexplored area has highlighted the AC system stability benefits and innate redundancy afforded by the presence of multiple points of controllable power injection [F4, F10].
- The development of a methodology to probabilistically test the robustness of HVDC based damping controllers, using classification techniques to identify possible mitigation options for power system operators when performance is sub-optimal [F1, F4, F8].
- The Probabilistic Collocation Method has been developed for use in large power system to identify the statistical distributions of critical electromechanical modes within power systems in the presence of multiple operational uncertainties [F3, F9].
- The use of a probabilistic system representation is proposed improve POD controller performance, yielding more robust controllers when considering the effects of system uncertainties. The use of the Probabilistic Collocation Method to establish the probabilistic system representation results in rapid and robust design of HVDC based damping controllers [F4].

## **1.6 Thesis Overview**

This thesis consists of seven chapters in total. The six chapters which follow this introduction are outlined below:

### ***Chapter 2 – Power System Modelling and Analysis Techniques***

This chapter provides the basis of the power system modelling and analysis techniques used within this thesis. It further presents the mathematical descriptions of power system components and HVDC systems. Following this, the way in which power systems are linearised in order to facilitate small-disturbance analysis is explained. Brief

descriptions of the damping controller designs that are later used with the HVDC systems to improve stability are then presented, alongside the test networks utilised throughout this thesis.

### ***Chapter 3 – The Effects of HVDC Lines on Power System Stability***

An extensive analysis of the effects of HVDC systems on the small-disturbance stability of power systems is presented within this chapter. Initial comparisons are made between LCC and VSC-based systems, assessing the impact of their placement and power transfer on the electromechanical modes within a small test network. Following this, POD controllers are designed and their effects are investigated for a variety of AC/DC system configurations. This comprehensive analysis of the supplementary POD control includes VSC-MTDC studies, demonstrating the effectiveness of DC grids for oscillation damping control. For a wide range of operating configurations, the use of WAMS-based global signals and a multivariable control structure is shown to outperform traditional POD controller designs.

### ***Chapter 4 – Assessing the Robustness of Controllers***

The need for a thorough evaluation of supplementary POD controllers is outlined at the start of this chapter. Following this, a methodology for the robust probabilistic evaluation of damping controller performance is presented. This method considers not only the statistical uncertainty in system operating conditions based on the variability of loading and generation, but also outages of key system equipment. The problem formulation is simplified by a reduction in number of considered uncertainties based on critical eigenvalue sensitivity measures. Furthermore, classification techniques are exploited throughout the procedure to improve the accuracy of the assessment. The methodology proposed within this chapter enables the calculation of risk indices and the identification of operational regions which may increase the risk of system instability and should, therefore, be avoided through appropriate system control.

### ***Chapter 5 – Modal Estimation using the Probabilistic Collocation Method***

This chapter presents the PCM for probabilistic small-disturbance analysis. The PCM significantly reduces the number of simulations required to complete a probabilistic system assessment whilst still accurately producing the statistical distributions of critical system modes. The method is demonstrated on a small test network where it is shown to accurately produce the statistical distributions of critical modes. Following this, techniques for reduction in the number of considered uncertainties based on

eigenvalue sensitivity are established. Following their demonstration on a small test network, the reduction techniques are then applied to a large network and shown to produce accurate results. An illustrative example on the large network incorporating an optimal power flow solution further demonstrates the practical applicability of the efficient sampling method.

### ***Chapter 6 – Probabilistic Tuning of Damping Controllers***

Within this chapter the idea of a probabilistic power system representation is introduced as a method to more accurately account for the statistical variation in critical system modes. This probabilistic model is then used during the design of a supplementary WAMS-based POD controller which is demonstrated to be more robust to the operational uncertainty of the power system. The PCM is also utilised as an efficient means to obtain this probabilistic system representation, allowing fast and robust design of POD controllers for HVDC systems. The technique is demonstrated using a case study representative of a possible future grid scenario – a large test system incorporating a multi-node meshed VSC-MTDC grid with interconnected stochastic wind generation.

### ***Chapter 7 – Conclusions and Future Work***

In this chapter the main conclusions of the research are discussed and suggestions are made for the future development and improvement of the presented methodologies.

# 2 Power System Modelling and Analysis Techniques

---

Various well documented tools are available to engineers for power system modelling and analysis. This chapter will describe the fundamental techniques required to complete studies on the stability of power systems including HVDC systems. Within this chapter, models are presented for all of the main components of electrical power systems, including synchronous generators, excitation systems, power system stabilisers, power transformers, transmission lines, systems loads and the electrical network. The modelling technique used to handle the time delays associated with wide area signals is also given. Following this, the techniques used to represent the HVDC system for power system stability analysis are presented, including relevant control schemes and converter controllers. The methods of modelling HVDC lines and multi-terminal HVDC grids are also provided.

In addition to the modelling techniques presented, tools for power system stability analysis based on system linearisation are also described. Once this framework has been established, the damping controller designs utilised within this thesis are thoroughly

discussed. Finally, a description of the various test networks used whilst completing this research is presented.

Throughout this thesis, all modelling has been completed using the MATLAB/Simulink environment (version 7.9.0, R2009b) with direct implementation of the mathematical component descriptions outlined within this chapter.

## 2.1 Modelling Power System Components

Within this section, the models of all main power system components are presented. These models have been used throughout the research to provide the simulation results presented later. The power system, and all included components, are modelled using an orthogonal phase representation, under the assumption that all three phases are balanced [140].

### 2.1.1 Synchronous Generators

The synchronous generator is the fundamental source of energy within modern electrical power networks, and can be modelled with varying levels of complexity. Two different synchronous generator models are used within this thesis, a sixth order model including leakage reactance, and a fifth order model neglecting leakage reactance.

#### 2.1.1.1 Sixth Order Model with Leakage Reactance

The first order differential equations for the sixth order synchronous generator model including leakage reactance are given by (2.1)–(2.6) with notation consistent with [141].

$$\frac{d}{dt} E_d' = \frac{1}{T_{qo}'} \left[ -E_d' + (X_q - X_q') \left\{ I_q - \frac{X_q' - X_q''}{(X_q' - X_{lk,s})^2} (\psi_{2q} + (X_q' - X_{lk,s}) I_q + E_d') \right\} \right] \quad (2.1)$$

$$\frac{d}{dt} E_q' = \frac{1}{T_{do}'} \left[ -E_q' - (X_d - X_d') \left\{ I_d - \frac{X_d' - X_d''}{(X_d' - X_{lk,s})^2} (\psi_{1d} + (X_d' - X_{lk,s}) I_d - E_q') \right\} + E_{fd} \right] \quad (2.2)$$

$$\frac{d}{dt} \psi_{1d} = \frac{1}{T_{do}''} \left[ -\psi_{1d} + E_q' - (X_d' - X_{lk,s}) I_d \right] \quad (2.3)$$

$$\frac{d}{dt} \psi_{2q} = \frac{1}{T_{qo}''} \left[ -\psi_{2q} - E_d' - (X_q' - X_{lk,s}) I_q \right] \quad (2.4)$$

$$\frac{d}{dt} \Delta\omega_r = \frac{1}{2H} [P_m - P_e - D\Delta\omega_r] \quad (2.5)$$

$$\frac{d}{dt}\delta = (\omega_r - \omega_{syn}) = \Delta\omega_r \quad (2.6)$$

The algebraic equations defining the stator voltages and generator electrical real power are given by (2.7)–(2.10), assuming the generator armature resistance is negligible.

$$E_d = \frac{X_q'' - X_{lk,s}}{X_q' - X_{lk,s}} E_d' - \frac{X_q' - X_q''}{X_q' - X_{lk,s}} \psi_{2q} + X_q'' I_q \quad (2.7)$$

$$E_q = \frac{X_d'' - X_{lk,s}}{X_d' - X_{lk,s}} E_q' + \frac{X_d' - X_d''}{X_d' - X_{lk,s}} \psi_{1d} - X_d'' I_d \quad (2.8)$$

$$E_t = \sqrt{E_d^2 + E_q^2} \quad (2.9)$$

$$P_e = E_d I_d + E_q I_q \quad (2.10)$$

### 2.1.1.2 Fifth Order Model Neglecting Leakage Reactance

In the fifth order model it is assumed that  $E_d' = 0$  and that  $X_q' = X_q$ . The leakage reactance is also neglected, resulting in the use of (2.11)–(2.13) for the generator voltage state equations and (2.5) and (2.6) representing the mechanical dynamics of the generator [140].

$$\frac{d}{dt} E_q' = \frac{1}{T_{do}''} [E_{fd} - E_q' + I_d (X_d - X_d')] \quad (2.11)$$

$$\frac{d}{dt} E_d'' = \frac{1}{T_{qo}''} [-E_d'' - I_q (X_q' - X_q'')] \quad (2.12)$$

$$\frac{d}{dt} E_q'' = \frac{1}{T_{do}''} [E_q' - E_q'' + I_d (X_d' - X_d'')] \quad (2.13)$$

The algebraic equations describing the  $d$ - and  $q$ -axis stator voltages are given as (2.14) and (2.15) with the generator stator terminal voltage and electrical power output defined as (2.9) and (2.10) respectively.

$$E_q = E_q'' - X_d'' I_d \quad (2.14)$$

$$E_d = E_d'' - X_q'' I_q \quad (2.15)$$

## 2.1.2 Generator Excitation Systems

Generators are reliant on excitation systems to provide direct current to the synchronous machine field winding [1]. Furthermore, through controlling the field voltage  $E_{fd}$  (and therefore the field current), the excitation system is able to contribute towards

maintaining power system stability. This control is provided by the AVR, which manipulates the field voltage in order to reach the generator stator terminal voltage reference set-point,  $E_t^{ref}$ , and to ensure the *first-swing* stability of the machine. A power system stabiliser may also be included in order to reduce rotor speed variations following disturbances. The functional relationship between the synchronous generator, excitation system, and PSS (if included) is shown in Figure 2-1.

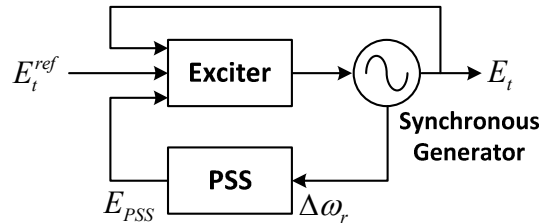


Figure 2-1: Relationship and signals between the synchronous generator, excitation system, and power system stabiliser.

Various excitation systems are used in practice, with comprehensive details found in [142]. Descriptions of the excitation systems used within this thesis are provided in the following sections.

### 2.1.2.1 Manual Excitation

Manual excitation is the simplest excitation scheme, with the field voltage  $E_{fd}$  maintained at a constant value determined during the synchronous generator parameter initialisation. No AVR is used and therefore the generator terminal voltage may vary from the desired value if operating conditions change.

### 2.1.2.2 Static Excitation (IEEE Type ST1A)

Static excitation systems supply direct current to the generator field winding through rectifiers which are fed by either transformers or auxiliary machine windings [142]. A simplified version of the IEEE Type ST1A static exciter is shown in Figure 2-2, consisting of voltage transducer delay, exciter, and Transient Gain Reduction (TGR). The signal  $E_{PSS}$  is a stabilising signal from the PSS, if one is used in conjunction with the exciter.

Two versions of this controller are used within this thesis, referred to as ST1A\_v1 and ST1A\_v2.

**ST1A\_v1** treats the transducer delay as negligible ( $T_R = 0$ ).

ST1A\_v2 has no time constant in the exciter block ( $T_A^{ex} = 0$ ), and no transient gain reduction block ( $T_B^{TGR} = T_C^{TGR} = 0$ ).

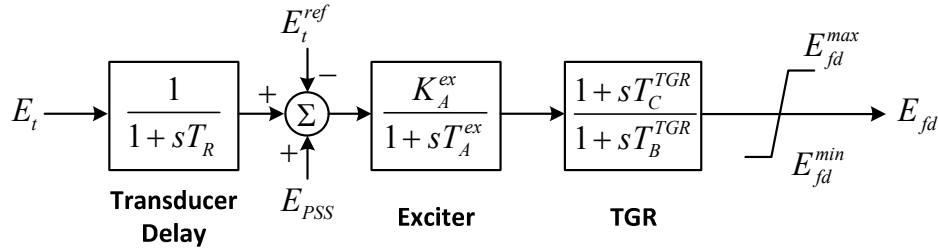


Figure 2-2: Simplified block diagram for the IEEE Type ST1A static exciter.

### 2.1.2.3 DC Excitation (IEEE Type DC1A)

Excitation systems which use a DC current generator and commutator are referred to as DC exciters and typically respond more slowly than static systems [142]. Figure 2-3 presents a simplified version of the IEEE Type DC1A DC excitation system used within this thesis.

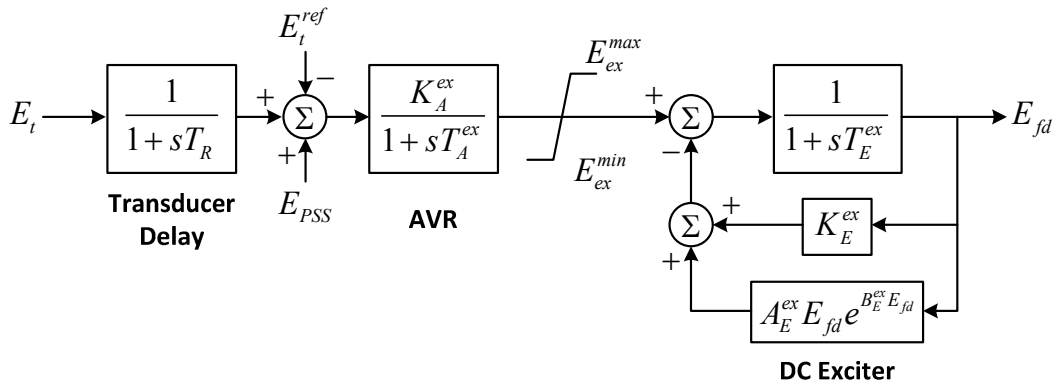


Figure 2-3: Simplified block diagram for the IEEE Type DC1A DC exciter.

### 2.1.3 Power System Stabilisers

A power system stabiliser will act to add damping to generator rotor oscillations through a supplementary control signal sent to the excitation system. The most common [1] and logical signal to use to monitor generator rotor oscillations is the rotor speed deviation  $\Delta\omega_r$  and this is used within this thesis.

Due to the phase characteristics of the excitation system through which the stabilising signal  $E_{PSS}$  must act, the PSS must include suitable phase compensation blocks to ensure the introduced electrical damping torque component is in phase with the rotor speed variation. This phase compensation is created by a number of phase lead/lag blocks which are combined with a washout filter so that steady state changes are

ignored, and a gain  $K_{PSS}$  in order to maximise damping. The PSS block diagram is shown in Figure 2-4. Limits on the supplementary control signal  $E_{PSS}$  are sometimes asymmetric to allow a large positive contribution during large swings, but limiting the negative output to reduce the risk of an under-voltage unit trip if the stabiliser fails [143]. The inclusion of a low-pass filter may be required to reduce the high-frequency output of the PSS in order to avoid potential interactions with the torsional mechanical modes of large steam-turbines – which can be as low as 7–8 Hz [1]. As these mechanical systems are not modelled within this work, there is no requirement to include the low-pass filter.

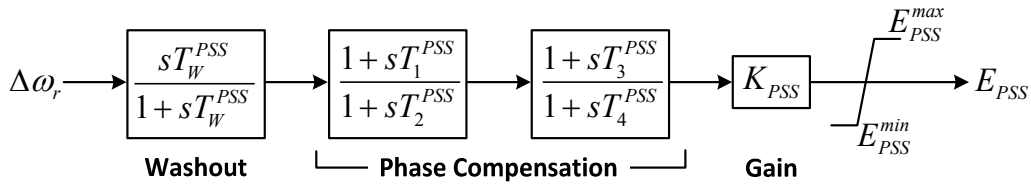


Figure 2-4: Block diagram of a PSS.

### 2.1.4 Transmission Lines

Throughout the work presented within this thesis, transmission lines are modelled using a lumped parameter model and the common  $\pi$ -representation [1]. The lines are assumed to be short enough that this approach is applicable and that more complex  $\pi$ -section or distributed parameter representation is not required [5].

### 2.1.5 Transformers

With orthogonal phase representation of the power system, an equivalent  $\pi$ -representation of a two-winding transformer can be used, as shown in Figure 2-5 [1]. In this representation,  $Y_{eq}^{Tx} = 1/Z_{eq}^{Tx}$  where  $Z_{eq}^{Tx}$  is the equivalent leakage reactance of the transformer, and  $c^{Tx} = 1/\text{ONR}$  where ONR is the Off-Nominal turns Ratio of the transformer.

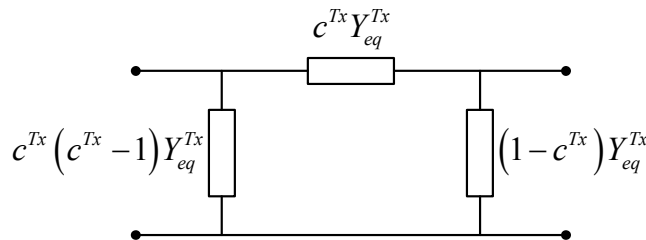


Figure 2-5: Equivalent  $\pi$ -representation of a two winding transformer.

### 2.1.6 Loads

The way in which power system loads are modelled can have a significant effect on the results obtained from simulations [144]. Electromechanical oscillations can affect voltage magnitude and frequency across the network and loads which are sensitive to these changes may require more detailed models to ensure accurate results. Further examples of the effects of load modelling can be found in [145]. Within this thesis, a constant impedance load model is used, represented as a shunt admittance  $Y_i^{load}$  connected to the  $i^{\text{th}}$  load bus as in (2.16). This model is considered adequate for stability studies [140], although further studies involving more complex load models could be used in order to more accurately establish the system dynamic response. The modelling of system loads is not critical for the methodologies developed within this research and the use of a constant impedance representation is fully adequate for all the studies which have been performed.

$$Y_i^{load} = \frac{P_i^{load} - jQ_i^{load}}{V_i} \quad (2.16)$$

### 2.1.7 Network

The power system network is modelled simply as a combination of all transmission lines, transformers, and constant impedance loads. The nodal network equation formed, shown in (2.17) for a network with  $N$  buses, describes the relationship between system voltages  $V$  and points of current injection  $I$  [140].

$$\begin{bmatrix} I_1 \\ \vdots \\ I_i \\ \vdots \\ I_N \end{bmatrix} = \begin{bmatrix} Y_{11} & \cdots & Y_{1i} & \cdots & Y_{1N} \\ \vdots & \ddots & \vdots & & \vdots \\ Y_{i1} & \cdots & Y_{ii} & \cdots & Y_{iN} \\ \vdots & & \vdots & & \vdots \\ Y_{N1} & \cdots & Y_{Ni} & \cdots & Y_{NN} \end{bmatrix} \begin{bmatrix} V_1 \\ \vdots \\ V_i \\ \vdots \\ V_N \end{bmatrix} \quad \text{or} \quad \mathbf{I} = \mathbf{YV} \quad (2.17)$$

In (2.17), subscripts  $i$  and  $j$  are bus numbers such that  $Y_{ii}$  is the self-admittance of bus  $i$ , and  $Y_{ij}$  is the mutual- admittance between buses  $i$  and  $j$ .

Reduction of the network model is possible so that all zero-injection buses are neglected and the *nodal network equation* has much smaller dimension [5]. This lowers the computational burden during simulations and power system analysis.

### 2.1.7.1 Network Reference Frames

The network is modelled in the common system reference frame ( $D$ - $Q$ ), however each machine is modelled using its own individual machine reference frame ( $d$ - $q$ ). Both of these orthogonal reference frames are rotating; the system reference frame at synchronous speed  $\omega_{syn}$ , and each machine reference frame with the generator rotor, at  $\omega_r$ , offset by the rotor angle  $\delta$ . Transformations between reference frames for voltages are completed using (2.18) and (2.19), with transformations applied similarly for system current injections.

$$\begin{bmatrix} V_D \\ V_Q \end{bmatrix} = \begin{bmatrix} \sin \delta & \cos \delta \\ -\cos \delta & \sin \delta \end{bmatrix} \begin{bmatrix} V_d \\ V_q \end{bmatrix} \quad (2.18)$$

$$\begin{bmatrix} V_d \\ V_q \end{bmatrix} = \begin{bmatrix} \sin \delta & -\cos \delta \\ \cos \delta & \sin \delta \end{bmatrix} \begin{bmatrix} V_D \\ V_Q \end{bmatrix} \quad (2.19)$$

### 2.1.7.2 Network Disturbances

With a single phase representation of the network, only balanced faults can be simulated when assessing the non-linear transient response of the network. These are readily simulated by adding a large shunt admittance (a value of  $10^9$  pu is used within this thesis) to the *self-admittance*  $Y_{ii}$  of the faulted bus  $i$  in the *nodal admittance matrix*.

### 2.1.8 Modelling of Signal Time Delays

As wide area signals are often used as controller inputs for oscillation damping, the time delays associated with their transmission must be considered. The standard Laplace domain representation of the time-based function  $f(t-\tau)$  subject to the signal transmission delay  $\tau$  is given as  $F(s) = e^{-\tau s}$ . This must be approximated by a rational function for inclusion within a linearised power system model.

Padé approximations of time delays are commonly used with WAMS-based damping controllers where they have been shown to provide good results [28, 29, 120, 121].

Within this thesis a second order approximation  $P_2(s)$  is used, given by (2.20) [146].

$$P_2(s) = \frac{\tau^2 s^2 - 6\tau s + 12}{\tau^2 s^2 + 6\tau s + 12} \quad (2.20)$$

## 2.2 Modelling HVDC Systems

The technique used within this work to model HVDC systems for stability studies is injection modelling [86, 117, 147, 148]. It is a flexible approach which can be used to model both LCC-HVDC and VSC-HVDC with varying levels of detail.

### 2.2.1 HVDC Converters

An HVDC converter station is modelled as a voltage source with variable magnitude  $V^{conv}$  and angle  $\theta^{conv}$  connected to an AC bus across a reactance  $X_{eq}^{conv}$ , as shown in Figure 2-6. Practically, this reactance represents the equivalent reactance between the converter station terminals and the point of common coupling with the AC system and is dominated by the leakage reactance of the converter transformer. By varying  $V^{conv}$  and  $\theta^{conv}$  it is possible to produce the desired flow of active and reactive power from the DC system to the AC network or vice versa.

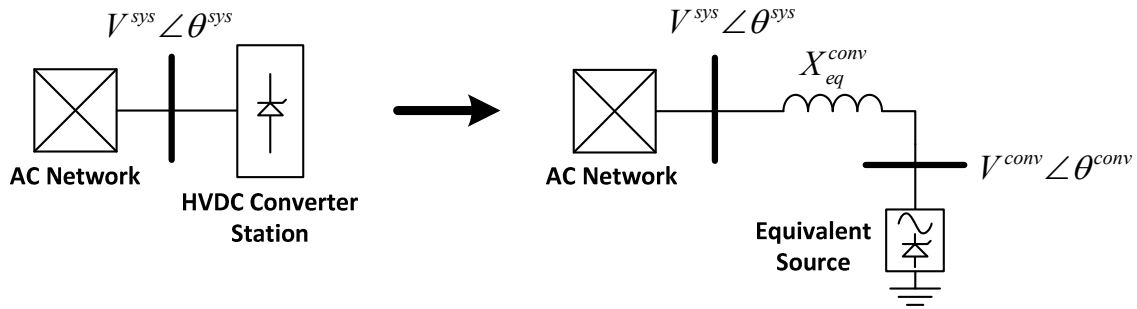


Figure 2-6: Injection model for one HVDC converter station connected to an AC network.

When an HVDC line is connected in parallel with an existing AC transmission line, the equivalent representation is therefore given by Figure 2-7. The line shown between buses  $i$  and  $j$  represents the pre-existing AC line. The voltage and angle at the equivalent source buses can be varied to produce the desired converter power injection into the AC network. The injections of active and reactive power are dictated by (2.21) and (2.22) respectively.

$$P^{conv} = \frac{V^{conv} V^{sys} \sin(\theta^{conv} - \theta^{sys})}{X_{eq}^{conv}} \quad (2.21)$$

$$Q^{conv} = \frac{V^{conv} [V^{conv} - V^{sys} \cos(\theta^{conv} - \theta^{sys})]}{X_{eq}^{conv}} \quad (2.22)$$

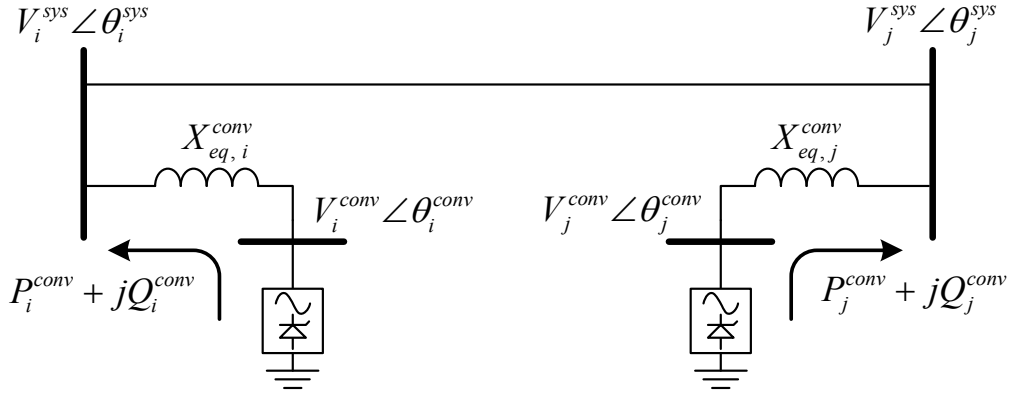


Figure 2-7: Injection model for an HVDC transmission system in parallel with an existing AC line.

Converter controls and DC line dynamics can be modelled to varying degrees of complexity, and the model can be extended for use with multi-terminal HVDC systems. This injection model can be easily integrated with existing AC network models as the interface point is the equivalent source bus voltage.

## 2.2.2 LCC-HVDC Modelling

LCC-HVDC systems cannot provide independent control of active and reactive power. They are controlled through variation of the converter firing angle  $\alpha$ . From this single controllable parameter, the HVDC converter voltage can be calculated at the rectifier and inverter stations as in (2.33) and (2.24) respectively – assuming a generalised six-pulse converter [42].

$$V_{dc}^{rect} = \frac{3\sqrt{2}}{\pi} n V^{sys} \cos \alpha - \frac{3X_C}{\pi} I_{dc}^{rect} \quad (2.23)$$

$$V_{dc}^{inv} = \frac{3\sqrt{2}}{\pi} n V^{sys} \cos \beta + \frac{3X_C}{\pi} I_{dc}^{inv} \quad (2.24)$$

In (2.33) and (2.24),  $\beta = 180^\circ - \alpha$ ,  $n$  is the converter transformer ratio,  $V^{sys}$  is the AC system voltage at the bus connected to the HVDC system, and  $X_C$  is the commutating reactance.

### 2.2.2.1 LCC-HVDC Converter Controls

Control of  $\alpha$  is provided by Proportional-Integral (PI) controllers with clamped anti-windup as shown in Figure 2-8. The rectifier controller maintains constant current with the current reference subjected to a standard Voltage Dependent Current Order Limiter (VDCOL) [1]. At the inverter the primary control aim is to maintain the DC system voltage. However current support is provided for situations when the DC current drops

below a threshold equal to  $I_{dc}^{ref} - I_{marg}$  (where  $I_{marg}$  is the current margin). Furthermore, at the inverter there is an added constraint on  $\alpha$  in that it cannot be set such that the extinction angle  $\gamma$  as calculated in (2.25) falls below  $\gamma^{\min}$  (required to ensure full extinction of valves and avoid commutation failures) [42].

$$\gamma = \cos^{-1} \left[ \left( V_{dc}^{inv} + \frac{3X_C}{\pi} I_{dc}^{inv} \right) / \frac{3\sqrt{2}}{\pi} nV^{sys} \right] \quad (2.25)$$

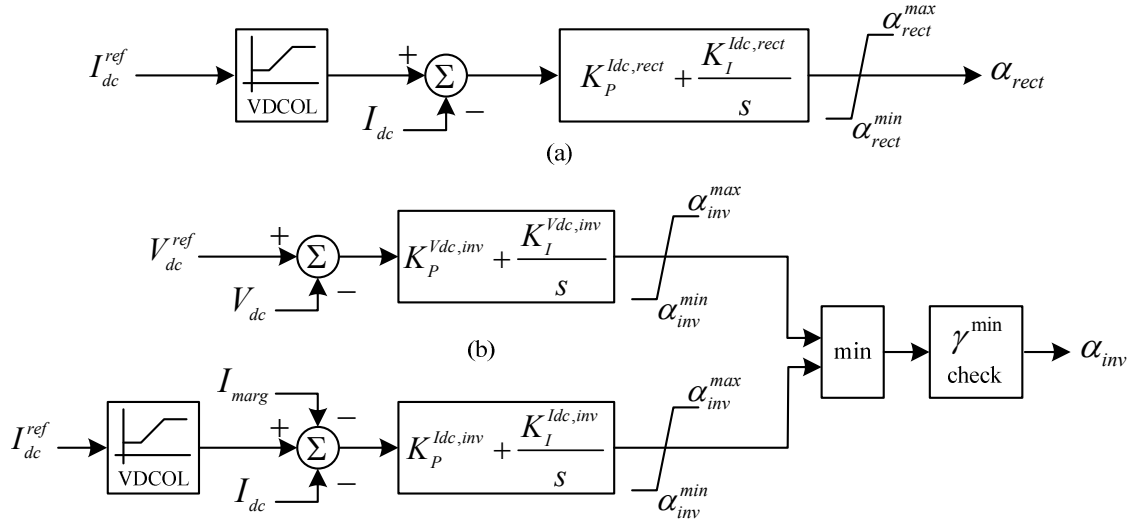


Figure 2-8: LCC-HVDC injection model controller for (a) rectifier converter station, and (b) inverter converter station.

### 2.2.2.2 LCC-HVDC Line Modelling

For LCC-HVDC systems, a  $T$ -model is used to represent the DC system dynamics. Figure 2-9 illustrates this model, with the DC capacitance voltage and line currents described mathematically by (2.26)–(2.28) where  $C_{dc}$ ,  $L_{dc}$  and  $R_{dc}$  are representative of the capacitance, inductance and resistance of the HVDC line [1]. This allows for simple calculation of the instantaneous power flow from the HVDC line to each converter station as (2.29). The convention that power flow from the DC system to the AC system is considered positive is maintained throughout this work.

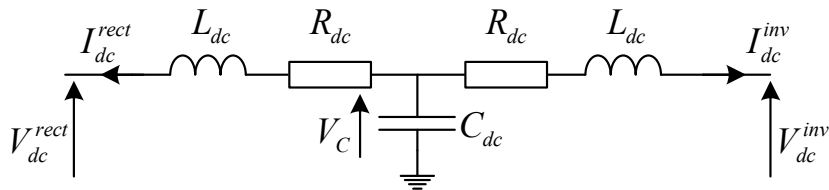


Figure 2-9: LCC-HVDC line model.

$$\frac{d}{dt} I_{dc}^{rect} = \frac{1}{L_{dc}} (V_C - V_{dc}^{rect} - R_{dc} I_{dc}^{rect}) \quad (2.26)$$

$$\frac{d}{dt} I_{dc}^{inv} = \frac{1}{L_{dc}} (V_C - V_{dc}^{inv} - R_{dc} I_{dc}^{inv}) \quad (2.27)$$

$$\frac{d}{dt} V_C = \frac{1}{C_{dc}} (-I_{dc}^{rect} - I_{dc}^{inv}) \quad (2.28)$$

$$P_{dc} = I_{dc} V_{dc} \quad (2.29)$$

All symbols used in (2.26)–(2.29) are in accordance with Figure 2-9. If converter stations are considered to be lossless then  $P^{conv} = P_{dc}$ , otherwise losses must be accounted for when calculating  $P^{conv}$ .

### 2.2.2.3 Reactive Power Compensation

The reactive power consumed by the LCC-HVDC converter is then given by (2.30), assuming reactive compensation is provided by a shunt susceptance  $B_{comp}$  [1].

$$Q^{conv} = -P^{conv} \tan \varphi + B_{comp} (V^{sys})^2 \quad (2.30)$$

In (2.30),  $\varphi$  is given by (2.31) at the rectifier and by (2.32) at the inverter.

$$\varphi^{rect} = \cos^{-1} \left( \cos \alpha - \frac{X_C I_{dc}^{rect}}{\sqrt{2} n V^{sys}} \right) \quad (2.31)$$

$$\varphi^{inv} = \cos^{-1} \left( \cos \beta + \frac{X_C I_{dc}^{inv}}{\sqrt{2} n V^{sys}} \right) \quad (2.32)$$

The active and reactive power injections to the AC network ( $P^{conv}$  and  $Q^{conv}$ ) for an LCC-HVDC line are fully defined.

### 2.2.3 VSC-HVDC Modelling

VSC-HVDC is capable of providing four-quadrant power control consisting of any combination of positive or negative active and reactive power [43]. This is achieved through control of the converter bus voltage magnitude and angle. For point-to-point transmission systems a common and realistic control solution is used with one converter station maintaining DC voltage and the other regulating active power flow. Reactive power control is independent at each converter station [43].

### 2.2.3.1 VSC-HVDC Converter Controls

Controllers are PI or integral regulators with clamped anti-windup as shown in Figure 2-10 [149]. Signals  $\Delta P_{dc}^{ref}$  and  $\Delta Q_{dc}^{ref}$  are to be used for auxiliary stabilising control action [147, 150].

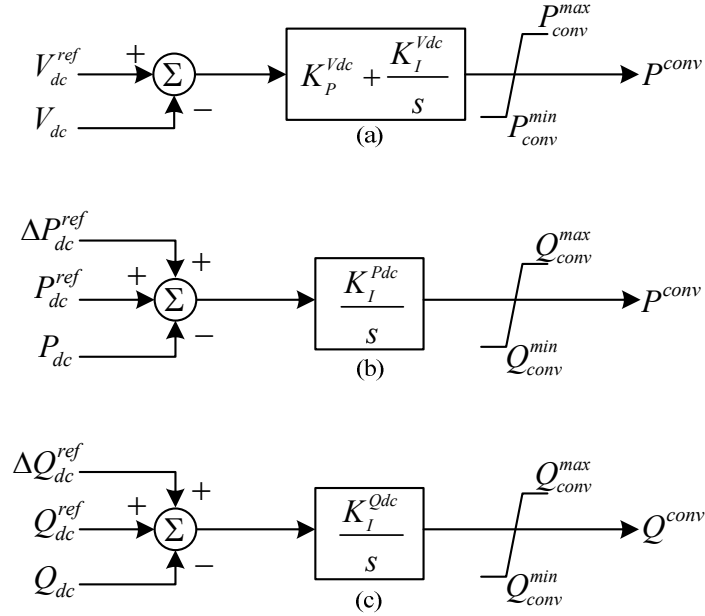


Figure 2-10: VSC-HVDC injection model controller for (a) DC voltage, (b) active power, and (c) reactive power.

### 2.2.3.2 VSC-HVDC Line Modelling

VSC-HVDC line dynamics are represented by a simple  $\pi$ -model within this research, as in Figure 2-11. The DC line voltages and current are described mathematically by (2.33)–(2.35). As with the LCC-HVDC model, power flow from the DC system to the AC system is considered positive.

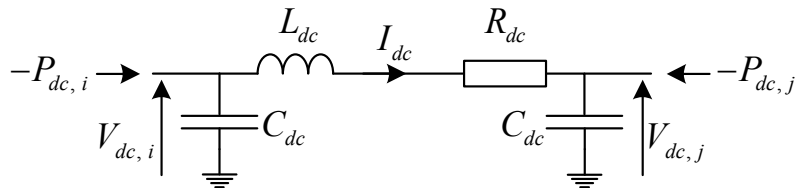


Figure 2-11: VSC-HVDC line model based on power injection.

$$\frac{d}{dt} V_{dc,i} = \frac{1}{C_{dc}} \left( -\frac{P_{dc,i}}{V_{dc,i}} - I_{dc} \right) \quad (2.33)$$

$$\frac{d}{dt} V_{dc,j} = \frac{1}{C_{dc}} \left( -\frac{P_{dc,j}}{V_{dc,j}} + I_{dc} \right) \quad (2.34)$$

$$\frac{d}{dt} I_{dc} = \frac{1}{L_{dc}} (-I_{dc} R_{dc} + V_{dc,i} - V_{dc,j}) \quad (2.35)$$

All symbols used in (2.33)–(2.35) are in accordance with Figure 2-11. As with LCC-HVDC lines, if converter stations are considered to be lossless then  $P^{conv} = P_{dc}$ .

### 2.2.4 Interface with AC System

As electromechanical oscillations with a typical frequency in the range of 0.2–2.5 Hz are being investigated within this research, the fast time constants associated with the switching operations of the power electronics can be neglected [147, 150]. It is therefore assumed that the converters are able to instantaneously reach the controller set-points  $P^{conv}$  and  $Q^{conv}$  in Figure 2-10. Interface with the AC system requires setting the equivalent source voltage to ensure that these powers are injected into the AC network using (2.36) and (2.37).

$$V^{conv} = \sqrt{a^2 + b^2} \quad (2.36)$$

$$\theta^{conv} = \theta^{sys} + \tan^{-1}(a/b) \quad (2.37)$$

In (2.36) and (2.37),  $a = V^{conv} \sin(\theta^{conv} - \theta^{sys})$  and  $b = V^{conv} \cos(\theta^{conv} - \theta^{sys})$  are calculated using (2.38) and (2.39).

$$a = \frac{X_{eq}^{conv} P^{conv}}{V^{sys}} \quad (2.38)$$

$$b = \frac{1}{2} \left[ V^{sys} + \sqrt{(V^{sys})^2 - 4 \left( \frac{(X_{eq}^{conv} P^{conv})^2}{(V^{sys})^2} - X_{eq}^{conv} Q^{conv} \right)} \right] \quad (2.39)$$

### 2.2.5 Multi-Terminal HVDC Grid Modelling

Extension of the point-to-point VSC-HVDC injection model to a multi-terminal grid is easily performed. The converter controls and interface equations remain the same. However the DC line equations require modification in order to represent a network, rather than a single line. As described fully in [117], the DC capacitance is lumped at the converter station terminals, and the lines are represented as purely resistive and inductive.

Using the generic MTDC converter node shown in Figure 2-12, converter node equations (2.40) and (2.41) can be used to describe the DC voltages and currents within the grid. The convention that power flow is positive when injected into the AC system from the DC system is still maintained. For the purposes of the local converter node equations, it is also assumed that all outgoing current flows from the node are positive.

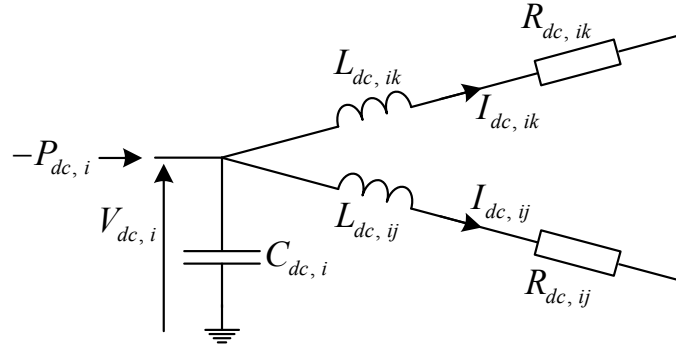


Figure 2-12: Generic MTDC converter node line model.

$$\frac{d}{dt}V_{dc,i} = \frac{1}{C_{dc,i}} \left( -\frac{P_{dc,i}}{V_{dc,i}} - \sum_{j \neq i}^{n_{conv,i}} I_{dc,ij} \right) \quad (2.40)$$

$$\frac{d}{dt}I_{dc,ij} = \frac{1}{L_{dc,ij}} \left( -I_{dc,ij}R_{dc,ij} + V_{dc,i} - V_{dc,j} \right) \quad (2.41)$$

In (2.40) and (2.41),  $n_{conv,i}$  is the number of converters connected to the  $i^{\text{th}}$  converter through DC lines, and the subscript  $ij$  refers to the line connecting the  $i^{\text{th}}$  and  $j^{\text{th}}$  converters.

Within this thesis a simple extension of the point-to-point control schemes is used. One converter station within the MTDC grid will maintain the DC voltage – referred to as the slack DC bus. The remaining converter stations regulate active power flow with reactive power flow independently controlled at all converter stations. The controls presented previously in Figure 2-10 are used. Use of more complex DC voltage droop characteristics are only of importance when studying the effects of transient events and outages, such as the loss of a converter station [151]. As these transient studies are not investigated as part of this research, the use of a slack DC bus is a suitable simplification.

## 2.2.6 HVDC Model Summaries

The equations which constitute the complete HVDC models are repeated for completeness in the following summary sections.

### 2.2.6.1 LCC-HVDC

A complete LCC-HVDC line is modelled as follows. The rectifier converter station is modelled using (2.42) with control from Figure 2-8(a).

$$V_{dc}^{rect} = \frac{3\sqrt{2}}{\pi} nV^{sys} \cos \alpha - \frac{3X_C}{\pi} I_{dc}^{rect} \quad (2.42)$$

The inverter converter station is modelled using (2.43)–(2.44) with control from Figure 2-8(b).

$$V_{dc}^{inv} = \frac{3\sqrt{2}}{\pi} nV^{sys} \cos \beta + \frac{3X_C}{\pi} I_{dc}^{inv} \quad (2.43)$$

$$\gamma = \cos^{-1} \left[ \left( V_{dc}^{inv} + \frac{3X_C}{\pi} I_{dc}^{inv} \right) / \frac{3\sqrt{2}}{\pi} nV^{sys} \right] \quad (2.44)$$

The LCC-HVDC line currents and respective power flows are found using (2.45)–(2.48).

$$\frac{d}{dt} I_{dc}^{rect} = \frac{1}{L_{dc}} (V_C - V_{dc}^{rect} - R_{dc} I_{dc}^{rect}) \quad (2.45)$$

$$\frac{d}{dt} I_{dc}^{inv} = \frac{1}{L_{dc}} (V_C - V_{dc}^{inv} - R_{dc} I_{dc}^{inv}) \quad (2.46)$$

$$\frac{d}{dt} V_C = \frac{1}{C_{dc}} (-I_{dc}^{rect} - I_{dc}^{inv}) \quad (2.47)$$

$$P_{dc} = I_{dc} V_{dc} \quad (2.48)$$

$P^{conv}$  is determined from  $P_{dc}$  considering the losses of the converter stations, with reactive power consumption calculated using (2.49) and (2.50) at the rectifier, and (2.49) and (2.51) at the inverter.

$$Q^{conv} = -P^{conv} \tan \phi + B_{comp} (V^{sys})^2 \quad (2.49)$$

$$\phi^{rect} = \cos^{-1} \left( \cos \alpha - \frac{X_C I_{dc}^{rect}}{\sqrt{2} nV^{sys}} \right) \quad (2.50)$$

$$\phi^{inv} = \cos^{-1} \left( \cos \beta + \frac{X_C I_{dc}^{inv}}{\sqrt{2} nV^{sys}} \right) \quad (2.51)$$

Finally, the equivalent source voltages to ensure the correct injections of  $P^{conv}$  and  $Q^{conv}$  at each converter station are calculated using (2.52)–(2.73).

$$V^{conv} = \sqrt{a^2 + b^2} \quad (2.52)$$

$$\theta^{conv} = \theta^{sys} + \tan^{-1}(a/b) \quad (2.53)$$

$$a = \frac{X_{eq}^{conv} P^{conv}}{V^{sys}} \quad (2.54)$$

$$b = \frac{1}{2} \left[ V^{sys} + \sqrt{(V^{sys})^2 - 4 \left( \frac{(X_{eq}^{conv} P^{conv})^2}{(V^{sys})^2} - X_{eq}^{conv} Q^{conv} \right)} \right] \quad (2.55)$$

### 2.2.6.2 VSC-HVDC

The model requirements for a point-to-point VSC-HVDC line are presented within this section. One converter operates with control schemes (a) and (c) from Figure 2-10, and the other with control schemes (b) and (c) from Figure 2-10. The VSC-HVDC system currents and voltages are determined by the line model which is defined using (2.56)–(2.58).

$$\frac{d}{dt} V_{dc,i} = \frac{1}{C_{dc}} \left( -\frac{P_{dc,i}}{V_{dc,i}} - I_{dc} \right) \quad (2.56)$$

$$\frac{d}{dt} V_{dc,j} = \frac{1}{C_{dc}} \left( -\frac{P_{dc,j}}{V_{dc,j}} + I_{dc} \right) \quad (2.57)$$

$$\frac{d}{dt} I_{dc} = \frac{1}{L_{dc}} (-I_{dc} R_{dc} + V_{dc,i} - V_{dc,j}) \quad (2.58)$$

The converters are assumed to reach the power injection controller set-points instantaneously [147, 150]. Therefore as with the LCC-HVDC line, the equivalent source voltages to ensure the correct injections of  $P^{conv}$  and  $Q^{conv}$  at each converter station are calculated using (2.59)–(2.62).

$$V^{conv} = \sqrt{a^2 + b^2} \quad (2.59)$$

$$\theta^{conv} = \theta^{sys} + \tan^{-1}(a/b) \quad (2.60)$$

$$a = \frac{X_{eq}^{conv} P^{conv}}{V^{sys}} \quad (2.61)$$

$$b = \frac{1}{2} \left[ V^{sys} + \sqrt{(V^{sys})^2 - 4 \left( \frac{(X_{eq}^{conv} P^{conv})^2}{(V^{sys})^2} - X_{eq}^{conv} Q^{conv} \right)} \right] \quad (2.62)$$

### 2.2.6.3 VSC-MTDC

A VSC-MTDC system is modelled as an extension of a point-to-point VSC-HVDC line. One *slack* converter station uses control schemes (a) and (c) from Figure 2-10 (to regulate voltage and reactive power). All other converter stations use control schemes (b) and (c) from Figure 2-10. An example is presented the VSC-MTDC grid shown in Figure 2-13 below, for which the mathematical model has been explicitly stated.

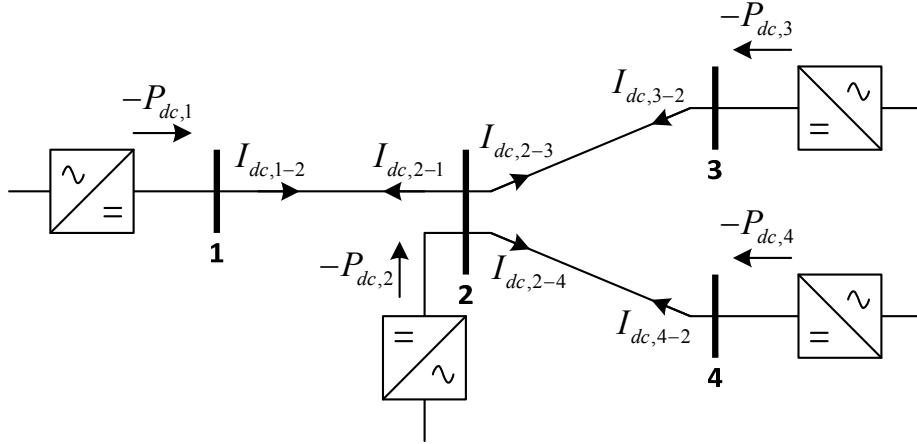


Figure 2-13: Example of a four-node VSC-MTDC grid.

For clarity,  $C_{dc}$ ,  $L_{dc}$  and  $R_{dc}$  have not been included in the diagram. At each converter station  $i$  there exists a capacitance  $C_{dc,i}$ . Each line between the  $i^{\text{th}}$  and  $j^{\text{th}}$  converter stations consists of a resistance  $R_{dc,ij}$  and an inductance  $L_{dc,ij}$ .

The voltages at converter stations 1–4 are defined by (2.63)–(2.66), with all line currents calculated using (2.67)–(2.69) considering the identities (2.70)–(2.72).

$$\frac{d}{dt}V_{dc,1} = \frac{1}{C_{dc,1}} \left( -\frac{P_{dc,1}}{V_{dc,1}} - I_{dc,1-2} \right) \quad (2.63)$$

$$\frac{d}{dt}V_{dc,2} = \frac{1}{C_{dc,2}} \left( -\frac{P_{dc,2}}{V_{dc,2}} - I_{dc,2-1} - I_{dc,2-3} - I_{dc,2-4} \right) \quad (2.64)$$

$$\frac{d}{dt}V_{dc,3} = \frac{1}{C_{dc,3}} \left( -\frac{P_{dc,3}}{V_{dc,3}} - I_{dc,3-2} \right) \quad (2.65)$$

$$\frac{d}{dt}V_{dc,4} = \frac{1}{C_{dc,4}} \left( -\frac{P_{dc,4}}{V_{dc,4}} - I_{dc,4-2} \right) \quad (2.66)$$

$$\frac{d}{dt}I_{dc,1-2} = \frac{1}{L_{dc,1-2}} \left( -I_{dc,1-2}R_{dc,1-2} + V_{dc,1} - V_{dc,2} \right) \quad (2.67)$$

$$\frac{d}{dt}I_{dc,2-3} = \frac{1}{L_{dc,2-3}}(-I_{dc,2-3}R_{dc,2-3} + V_{dc,2} - V_{dc,3}) \quad (2.68)$$

$$\frac{d}{dt}I_{dc,2-4} = \frac{1}{L_{dc,2-4}}(-I_{dc,2-4}R_{dc,2-4} + V_{dc,2} - V_{dc,4}) \quad (2.69)$$

$$I_{dc,1-2} = -I_{dc,2-1} \quad (2.70)$$

$$I_{dc,2-3} = -I_{dc,3-2} \quad (2.71)$$

$$I_{dc,2-4} = -I_{dc,4-2} \quad (2.72)$$

## 2.3 Power System Analysis Techniques

The various AC and DC components that make up the complete non-linear power system model have been described according to their differential and algebraic equations. This section will describe the further tools which are often used to assess power system small-disturbance stability and which facilitate the design of power system oscillation damping controllers.

### 2.3.1 Power System Linearisation

As described in Chapter 1, small-disturbance stability is the ability of a power system to maintain synchronous operation when subjected to small disturbances [1]. A disturbance is considered to be small if the power system equations can be linearised for the purpose of the analysis.

The power system is described by the compact vector-matrix representation of (2.73) and (2.74).

$$\dot{\mathbf{x}} = \mathbf{f}(\mathbf{x}, \mathbf{u}) \quad (2.73)$$

$$\mathbf{y} = \mathbf{g}(\mathbf{x}, \mathbf{u}) \quad (2.74)$$

In (2.73) and (2.74),  $\mathbf{x}$  is a vector of  $n$  state variables,  $\mathbf{u}$  is a vector of  $m$  system inputs,  $\mathbf{y}$  is a vector of  $p$  system outputs, and  $\mathbf{f}$  and  $\mathbf{g}$  are vectors of non-linear equations.

An equilibrium point can be defined at which  $\mathbf{x} = \mathbf{x}_0$  and  $\mathbf{u} = \mathbf{u}_0$  such that (2.73) is equal to zero. By making a small perturbation ( $\Delta$ ) from this point, (2.75) can be established.

$$\dot{\mathbf{x}}_0 + \Delta\dot{\mathbf{x}} = \mathbf{f}(\mathbf{x}_0 + \Delta\mathbf{x}, \mathbf{u}_0 + \Delta\mathbf{u}) \quad (2.75)$$

As only small perturbations are considered, a first order Taylor's series expansion of (2.75) can be used as a suitable approximation [1]. This can be similarly completed for (2.74) with respect to system outputs, and simplified, to provide the linearised *state space* power system model consisting of (2.76) and (2.77).

$$\Delta \dot{\mathbf{x}} = \mathbf{A}\Delta \mathbf{x} + \mathbf{B}\Delta \mathbf{u} \quad (2.76)$$

$$\Delta \mathbf{y} = \mathbf{C}\Delta \mathbf{x} + \mathbf{D}\Delta \mathbf{u} \quad (2.77)$$

In (2.76) and (2.77), the following definitions are used:

$$\mathbf{A} = \begin{bmatrix} \frac{\partial f_1}{\partial x_1} & \dots & \frac{\partial f_1}{\partial x_n} \\ \vdots & \ddots & \vdots \\ \frac{\partial f_n}{\partial x_1} & \dots & \frac{\partial f_n}{\partial x_n} \end{bmatrix}, \mathbf{B} = \begin{bmatrix} \frac{\partial f_1}{\partial u_1} & \dots & \frac{\partial f_1}{\partial u_m} \\ \vdots & \ddots & \vdots \\ \frac{\partial f_n}{\partial u_1} & \dots & \frac{\partial f_n}{\partial u_m} \end{bmatrix}, \mathbf{C} = \begin{bmatrix} \frac{\partial g_1}{\partial x_1} & \dots & \frac{\partial g_1}{\partial x_n} \\ \vdots & \ddots & \vdots \\ \frac{\partial g_p}{\partial x_1} & \dots & \frac{\partial g_p}{\partial x_n} \end{bmatrix}, \mathbf{D} = \begin{bmatrix} \frac{\partial g_1}{\partial u_1} & \dots & \frac{\partial g_1}{\partial u_m} \\ \vdots & \ddots & \vdots \\ \frac{\partial g_p}{\partial u_1} & \dots & \frac{\partial g_p}{\partial u_m} \end{bmatrix}.$$

### 2.3.2 Modal Analysis

By Lyapunov's first method, the small-disturbance stability of a system is given by the roots of the characteristic equation of the system first order approximations [152]. With respect to the linearised state space model of the power system, calculation of the eigenvalues of the system matrix  $\mathbf{A}$  is required.

The eigenvalues of  $\mathbf{A}$  are given by the values of the scalar  $\lambda$  for which there are non-trivial solutions to (2.78), where  $\boldsymbol{\phi}$  is an  $n \times 1$  vector and  $\boldsymbol{\phi} \neq 0$ . There are  $n$  solutions to (2.78), forming the set of  $n$  eigenvalues (or modes)  $\lambda = \lambda_1, \lambda_2 \dots \lambda_n$ .

$$\mathbf{A}\boldsymbol{\phi} = \lambda\boldsymbol{\phi} \quad (2.78)$$

The column vector  $\boldsymbol{\phi}_i$  which satisfies (2.78) for the  $i^{\text{th}}$  eigenvalue  $\lambda_i$  is referred to as the *right eigenvector* of  $\mathbf{A}$  associated with  $\lambda_i$ . Similarly there exists a *left eigenvector*, a  $1 \times n$  row vector  $\boldsymbol{\psi}_i$  which satisfies (2.79) for  $\lambda_i$ .

$$\boldsymbol{\psi}\mathbf{A} = \boldsymbol{\psi}\lambda \quad (2.79)$$

As both right and left eigenvectors are unit-less, it is common practice to normalise them such that  $\boldsymbol{\phi}_i\boldsymbol{\psi}_i = 1$ .

The modal matrices are often used to succinctly express the eigenproperties of a system. These  $n \times n$  matrices are defined by (2.80)–(2.82).

$$\Phi = [\phi_1 \quad \phi_2 \quad \cdots \quad \phi_n] \quad (2.80)$$

$$\Psi = [\psi_1^T \quad \psi_2^T \quad \cdots \quad \psi_n^T]^T \quad (2.81)$$

$$\Lambda = \text{diag}[\lambda_1 \quad \lambda_2 \quad \cdots \quad \lambda_n] \quad (2.82)$$

In (2.80)–(2.82),  $\Phi$  is the matrix of right eigenvectors,  $\Psi$  is the matrix of left eigenvectors, and  $\Lambda$  is a diagonal matrix of system eigenvalues.

Within this thesis, the MATLAB/Simulink environment is used to provide linearised system models and perform eigenvalue analysis.

### 2.3.2.1 Modal Stability

The time-based behaviour of a mode  $\lambda_i$  is given by  $e^{\lambda_i t}$  [140]. It can therefore be easily established that purely real eigenvalues are non-oscillatory. Negative real eigenvalues will result in a time response which decays, whereas positive real eigenvalues will lead to an aperiodically increasing time response. If  $\mathbf{A}$  is real, complex eigenvalues occur only in conjugate pairs ( $\lambda = \sigma \pm j\omega$ ). These oscillatory modes are described by their *damping*  $\sigma$  and *frequency*  $\omega$ . The *damping factor*  $\zeta$  of a mode is defined as in (2.83) and provides the rate of decay of the amplitudes of oscillation associated with the mode. If a complex eigenvalue has positive real part, these oscillations will grow and lead to system instability.

$$\zeta = \frac{-\sigma}{\sqrt{\sigma^2 + \omega^2}} \quad (2.83)$$

It can be concluded that if any single eigenvalue has a positive real part, the system is unstable. Furthermore, in practical power system applications, it is desirable to restore steady state operation as quickly as possible following disturbances. High damping factors for electromechanical modes are therefore desired, with a typical threshold of  $\zeta > 5\%$  often implemented for control design purposes [2].

### 2.3.2.2 Modal System Representation

The state space power system model given by (2.76) and (2.77) can be rewritten in the modal canonical form of (2.84) and (2.85) by means of a modal transformation of the state variables  $\Delta \mathbf{x}$  to the modal variables  $\mathbf{z}$  as in (2.86).

$$\dot{z} = \Lambda z + B_M \Delta u \quad (2.84)$$

$$\Delta y = C_M z + D \Delta u \quad (2.85)$$

$$z = M \Delta x \quad (2.86)$$

In (2.84)–(2.86), the modal transformation matrix  $M = \Phi^{-1}$ , and the modal state matrices are defined as  $\Lambda = MAM^{-1}$ ,  $B_M = MB$ , and  $C_M = CM^{-1}$ .

The  $n \times m$  matrix  $B_M$  is the *mode controllability matrix* and defines how controllable a mode is through a given input. If the element  $B_M(i, j)$  is equal to zero, then the  $j^{\text{th}}$  input will have no effect on the  $i^{\text{th}}$  mode [1].

The  $p \times n$  matrix  $C_M$  is the *modal observability matrix* which defines how observable a mode is in a given output. If the element  $C_M(k, i)$  is equal to zero, then the  $i^{\text{th}}$  mode cannot be observed in the  $k^{\text{th}}$  output [1].

Residue values contain information about both modal observability in a given output, and controllability through a given input. The open loop residue of the system transfer function between the  $j^{\text{th}}$  input and  $k^{\text{th}}$  output, with respect to the  $i^{\text{th}}$  mode, is given by (2.87). The complex entries in  $R_i$  also contain information about the phase delay between system inputs and outputs which is useful for control purposes [1].

$$R_i(j, k) = C_M(k, i) B_M(i, j) \quad (2.87)$$

## 2.4 Damping Controller Design

It was shown in Chapter 1 that HVDC systems can be exploited for POD purposes. This section will briefly present the POD controller designs that have been used within this thesis. It should be noted that these are not the only POD controller methodologies available, and many alternative schemes have been discussed further in Section 1.3.1. The two controllers described below are the PSS structure, and modal linear quadratic Gaussian control. These two controller forms offer different advantages and vary significantly in complexity.

### 2.4.1 PSS-based POD Control

A simple supplementary POD controller design commonly used with HVDC systems follows the conventional structure of a PSS incorporating washout, phase compensation, gain, and limits as shown in Figure 2-14. This design has been used numerous times in

previous studies, for example [97, 101, 153, 154]. The control structure is simple, effective, and easily tuned; it can however only be optimally tuned for a single mode.

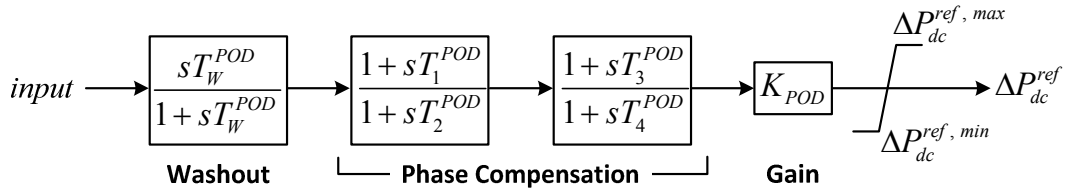


Figure 2-14: PSS-based POD controller structure

Input to the controller is usually selected as a local input, although PSS designs incorporating wide area signals also exist [12, 70, 99]. Throughout this thesis, signal selection will be specified for each case study presented.

Controller parameters are specified using the residue-based tuning approach [155-157]. Once the controller output ( $\Delta P_{dc}^{ref}$ ) and the controller input are known, the open loop transfer function residues for each electromechanical mode requiring additional damping can be determined using (2.87). POD controller tuning is carried out for the mode with the greatest residue magnitude  $|R_i|$  as it will be most affected by the controller [155, 156].

Having established the mode to be damped, the residue angle  $\angle R_i$  is determined. The phase compensation required within the PSS-based POD controller is then calculated as  $180^\circ - \angle R_i$ . This will move the target eigenvalue further into the left half of the complex plane with no change in frequency [156, 157]. Parameters for the lead-lag blocks are determined according to the required phase compensation. Phase compensation is limited to approximately  $60^\circ$  per block to reduce sensitivity to noise at high frequencies as well as due to the physical limitations of  $RLC$  circuits [158, 159]. Following this, controller gain  $K_{POD}$  is increased until a sufficient amount of damping is achieved for the target mode, taking care to avoid causing detrimental effects to the other system eigenvalues and ensuring a suitable PSS gain margin [158, 159]. Final controller parameters will be presented for each case study throughout this thesis.

## 2.4.2 Modal Linear Quadratic Gaussian Control

A control approach capable of using multiple wide area signals to improve the damping of a number of targeted modes has also been studied. This controller structure can also

be extended to a multiple-output configuration. This is necessary when coordinated damping using more than one VSC-HVDC line or an MTDC grid is considered.

The linear quadratic Gaussian control design is a cornerstone of modern optimal control theory and its advantages have led to widespread research into its use in power system damping [28, 34, 71, 160, 161]. However, the design approach is rarely straightforward, especially within large power systems where many generators participate in the critical modes which require additional damping. In these situations, the controller tuning process can become prohibitively complex.

Participation factor analysis is required in order to identify the electromechanical states involved in critical system modes [1]. Weightings can then be assigned to these states. However, if these states are involved in other targeted modes or modes that do not require altering, the damping of these modes will also be affected, sometimes adversely. This results in a complex and time consuming tuning process in which it is often not possible to obtain exact target damping factors. These complexities and problems can be overcome through the novel use of a modal representation of the control design problem. The formulation of this control structure and extensive studies are presented in [29]. A brief description is presented below.

The power system model is linearised to (2.88) and (2.89), where  $\mathbf{w}$  and  $\mathbf{v}$  are assumed to be uncorrelated zero-mean Gaussian stochastic noise processes with constant power spectral density matrices  $\mathbf{W}$  and  $\mathbf{V}$  respectively [162]. Note that  $\mathbf{D}$  from (2.85) is neglected as it is typically equal to zero for all power system applications.

$$\dot{\mathbf{x}} = \mathbf{A}\mathbf{x} + \mathbf{B}\mathbf{u} + \mathbf{\Gamma}\mathbf{w} \quad (2.88)$$

$$\mathbf{y} = \mathbf{C}\mathbf{x} + \mathbf{v} \quad (2.89)$$

The standard LQG feedback control law can be written simply as (2.90).

$$\mathbf{u}(t) = -\mathbf{K}\hat{\mathbf{x}}(t) \quad (2.90)$$

The Linear Quadratic Regulator (LQR) gain  $\mathbf{K}$  is determined by solving the associated Algebraic Riccati Equation (ARE) to minimise the cost function (2.91). In this modal formulation, the real matrix  $\mathbf{M}$  is the modal transformation matrix described previously in Section 2.3.2.2, obtained using real Schur decomposition [163]. This transformation to the modal variables, as in (2.86), allows targeted damping on specific system modes through appropriate, commonly diagonal, setting of the weighting matrices  $\mathbf{Q}_M$  and  $\mathbf{R}$ .

$$\mathbf{J}_K = \lim_{T \rightarrow \infty} \mathbf{E} \left\{ \int_0^T (\mathbf{x}^T (\mathbf{M}^T \mathbf{Q}_M \mathbf{M}) \mathbf{x} + \mathbf{u}^T \mathbf{R} \mathbf{u}) dt \right\} \quad (2.91)$$

Values of  $\mathbf{R}$  are set in order to penalise the corresponding controller's outputs from high actions. Values of  $\mathbf{Q}_M$  are set in order to effect a higher effort by the controller to stabilise the corresponding modal variables  $z_i$ , and hence  $e^{\lambda_i t}$ . Non-zero weights are given only to modes of interest in  $\mathbf{Q}_M$ , thus targeting the control effort of the LQR while keeping the locations of other modes unaltered.

With respect to (2.90)  $\hat{\mathbf{x}}$  is an estimate of the states  $\mathbf{x}$  obtained using a Kalman filter as described by (2.92).

$$\dot{\hat{\mathbf{x}}}(t) = \mathbf{A}\hat{\mathbf{x}} + \mathbf{B}\mathbf{u} + \mathbf{L}(\mathbf{y} - \mathbf{C}\hat{\mathbf{x}}) + \mathbf{L}\mathbf{v} \quad (2.92)$$

The optimal choice of the constant estimation error feedback matrix  $\mathbf{L}$  minimises  $\mathbf{E} \{ [\mathbf{x} - \hat{\mathbf{x}}]^T [\mathbf{x} - \hat{\mathbf{x}}] \}$ . It is calculated by solving the ARE associated with the cost function (2.93). The weighting matrices  $\mathbf{W}$  and  $\mathbf{V}$  are calculated as in (2.94) and (2.95) and tuned according to the Loop Transfer Recovery (LTR) procedure at plant input [162].

$$\mathbf{J}_L = \lim_{T \rightarrow \infty} \mathbf{E} \left\{ \int_0^T (\mathbf{x}^T \mathbf{W} \mathbf{x} + \mathbf{u}^T \mathbf{V} \mathbf{u}) dt \right\} \quad (2.93)$$

$$\mathbf{W} = \mathbf{\Gamma} \mathbf{W}_o \mathbf{\Gamma}^T + q \mathbf{B} \mathbf{\Theta} \mathbf{B}^T \quad (2.94)$$

$$\mathbf{V} = \mathbf{V}_o \quad (2.95)$$

In (2.94) and (2.95),  $\mathbf{W}_o$  and  $\mathbf{V}_o$  are estimates of the nominal model noise, and  $\mathbf{\Theta}$  is any positive definite matrix.

Full recovery of robustness is achieved as  $q \rightarrow \infty$ . Care should be taken though, as full recovery would lead to excessively high gains and the nominal performance of the controller with respect to the true noise problem would therefore deteriorate. For non-minimum phase systems, which is commonly the case in power systems, only partial recovery can be achieved [162].

The MLQG controller has the structure shown in Figure 2-15. The closed-loop dynamics of the LQG controller are described by (2.96). The transfer function for the complete LQG controller from  $y$  to  $u$  is given by (2.97).

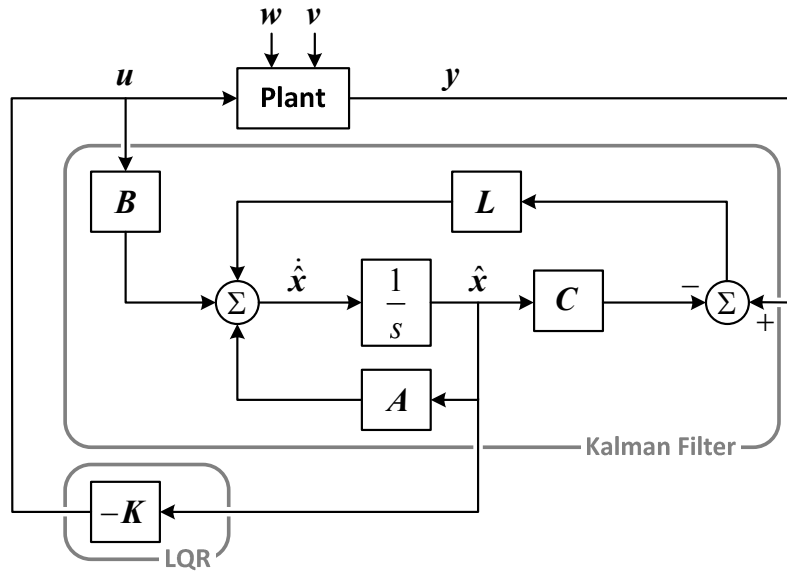


Figure 2-15: Standard LQG controller structure.

$$\frac{d}{dt} \begin{bmatrix} \mathbf{x} \\ \hat{\mathbf{x}} \end{bmatrix} = \begin{bmatrix} \mathbf{A} & -\mathbf{BK} \\ \mathbf{LC} & \mathbf{A} - \mathbf{LC} - \mathbf{BK} \end{bmatrix} \begin{bmatrix} \mathbf{x} \\ \hat{\mathbf{x}} \end{bmatrix} + \begin{bmatrix} \mathbf{\Gamma} \mathbf{w} \\ \mathbf{L} \mathbf{v} \end{bmatrix} \quad (2.96)$$

$$\mathbf{K}_{LQG}(s) = \begin{bmatrix} \mathbf{A}_c & \mathbf{B}_c \\ \mathbf{C}_c & \mathbf{D}_c \end{bmatrix} = \begin{bmatrix} \mathbf{A} - \mathbf{BK} - \mathbf{LC} & \mathbf{L} \\ -\mathbf{K} & 0 \end{bmatrix} \quad (2.97)$$

Input signal selection is very important in order to capture as much information as possible regarding the critical modes that require improved damping. The methods used for signal selection and details of any signal delays will be discussed when specific case studies are presented throughout the thesis.

#### 2.4.2.1 Model Reduction

As can be seen from (2.97), the final MLQG controller is of the same order as the plant model on which it is designed. It is often desirable to obtain a lower order controller in order to ensure that it is not too complex for practical implementation [162]. The possibility exists to reduce the order of the final controller at various stages of the design process. This reduction can occur:

- **On the plant model** prior to commencing the design procedure. When designing LQG controllers, it is sometimes necessary to perform initial model order reduction to avoid ill conditioning when solving high order matrix Riccati

equations [71]. Following this reduction, signal delays are introduced where appropriate on inputs and outputs. The reduced plant model including delays is then used during the control design process.

- ***On the final controller design*** after completion of the design process. This will lessen the online computational burden of the controller whilst still maintaining the improved critical mode damping.
- ***Both on the plant model and the final controller design*** in order to minimise the final controller size.

Throughout this research, the *Schur Balanced Truncation Method* [164] has been used to perform model reduction – implemented within MATLAB. The rigorous comparison of the frequency response of the singular values of the full and reduced order systems is used to ensure that only system states having little effect on the *input-output* behaviour of the system are discarded [165].

In order to ensure clarity, the model reduction details for individual case studies within this thesis will be explicitly stated.

The research methods and results presented throughout this thesis are not dependent on the controller designs or tuning methods employed and further techniques, such as those previously discussed in Section 1.3.1, could also be used.

## 2.5 Test Networks

Throughout this thesis two standard test networks are used. The standard AC networks are presented in the following sections. When HVDC modifications are made for the various studies conducted (such as the addition of point-to-point lines or an MTDC grid) they will be detailed on a case-by-case basis to avoid ambiguity.

All system details including line parameters, standard loading, and dynamic machine data is included in Appendix A. In all cases, initial load flows are performed using modified MATPOWER functions [166].

### 2.5.1 Two Area Network

A small four-machine, two-area network is introduced in [1] for use with small-disturbance stability studies. The network diagram is shown in Figure 2-16. This system requires significant transmission of power from bus 7 to bus 9 through a long

transmission corridor, with the left and right areas of the network prone to post-disturbance inter-area oscillations. All generators are modelled as fifth order neglecting leakage reactance, and controlled by type ST1A\_v1 static exciters with PSSs installed. All power system loads are modelled as constant impedance.

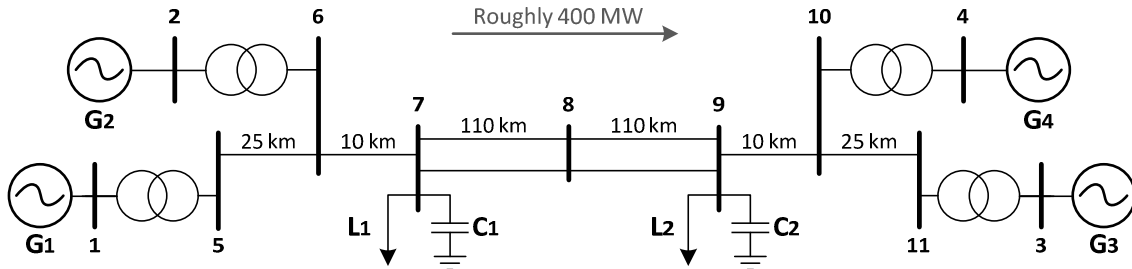


Figure 2-16: Kundur two-area test network diagram.

The power system exhibits three electromechanical oscillatory modes. At the nominal operating point given in Appendix A, these modes have the properties which are given in Table 2-1.

Table 2-1: Electromechanical mode properties for the two area test system at the nominal operating point.

Mode	Description	Eigenvalue, $\lambda = \sigma + j\omega$ (pu)	Frequency, $f$ (Hz)	Damping Factor, $\zeta$ (%)
Mode 1	Local mode between G1 and G2	$-0.332 \pm j6.022$	0.958	5.50
Mode 2	Local mode between G3 and G4	$-0.349 \pm j6.232$	0.992	5.58
Mode 3	Inter-area mode between all generators	$-0.137 \pm j3.472$	0.553	3.94

## 2.5.2 New England Test System and New York Power System (NETS-NYPS)

A larger sixteen-machine, sixty-eight-bus, five-area network is also utilised throughout this thesis to investigate oscillatory behaviour. The network is shown in Figure 2-17 and was introduced in [2] and used extensively in [165] for damping controller design studies. The network represents a reduced order equivalent model of the New England Test System (NETS) and the New York Power System (NYPS). Five separate areas are present: NETS consisting of G1-G9, NYPS consisting of G10-G13, and three further infeeds from neighbouring areas are represented separately by G14, G15 and G16. Flows of active power across inter-area ties are shown in Figure 2-17, demonstrating the heavy import of power into the NYPS area, due to a generation shortfall of roughly 2.7 GW.

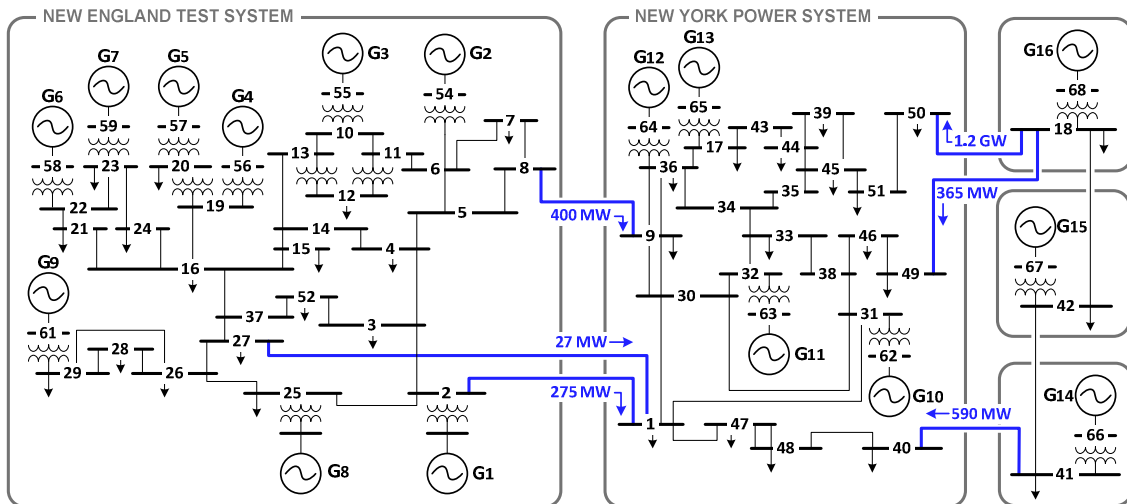


Figure 2-17: NETS-NYPS five-area test network diagram.

All generators are represented by full sixth order models. Generators G1-G8 use the slow DC1A exciter, whilst G9 is equipped with a fast acting ST1A\_v2 static exciter and PSS. The remaining generators (G10-G16) are under constant manual excitation. Power system loads are modelled as constant impedance.

The network exhibits four inter-area modes with a frequency of less than 1 Hz and poor damping factors of less than 5%. The remaining eleven local modes have frequencies between 1–1.6 Hz and damping factors between 5.6–16.0% and are all suitably damped.

## 2.6 Summary

This chapter has presented the fundamental modelling and analysis techniques which will be used throughout this thesis.

The chapter began by presenting the mathematical models of the components that form power systems. These included traditional AC apparatus including synchronous generators and their associated controls, transformers, transmission lines and loads, as well as describing the modelling of VSC-HVDC systems.

The way in which non-linear power system models can be linearised in order to conduct small-disturbance stability analysis was then discussed. The modal analysis techniques introduced then formed the basis of the linear POD controller designs. The two controller structures described in this chapter will be used throughout the thesis and their impact on system stability and performance in the presence of uncertainties will be assessed. Finally, the test networks used throughout this research have been introduced.

The following chapters will utilise these models, controller designs, and analysis techniques to perform a thorough investigation into the effects of HVDC on system stability.

# **3 The Effects of HVDC Lines on Power System Stability**

---

HVDC lines are primarily installed within power systems to provide transmission paths. These may be for bulk transmission over long distances, or they may be used when other transmission options are infeasible such as for subsea interconnections. Traditionally these lines have been installed between asynchronous networks, and this has often been one of the main reasons for selecting DC, rather than AC, solutions. However, a number of projects have been confirmed [50, 167] which will make use of HVDC lines operating in parallel with traditional AC paths within synchronous networks. For these situations especially, it is important to explore the effects that this new HVDC line will have on system stability. Furthermore, the introduction of a transmission solution which can provide fast, controllable power injection at new points within the network provides multiple options for improving any pre-existing stability issues within the network.

There has been much interest into the effects of HVDC on system stability and methods of utilising these points of controllable power flow to improve system stability. A

review of this work has been presented in Section 1.3.1. A wide variety of methods have been proposed for POD control with generators and FACTS devices, as well as with HVDC systems. A thorough examination of suitable control methods considering a wide variety of operational concerns is required – particularly surrounding the use of VSC-MTDC grids for POD stabilising control action.

Within this chapter, a comprehensive analysis of the effects of HVDC lines on the small-disturbance stability of mixed AC/DC networks is presented. This begins with a discussion of the effects that converter technology, topological variations and changes in HVDC power flow can have on electromechanical modal frequency and damping. These studies, performed on the small two-area test network, demonstrate that there may be occasions when further oscillation damping control may be required.

An investigation into the use of the installed VSC-HVDC lines for POD purposes is then presented. Both the traditional PSS-based POD controller and the multi-input MLQG controller are synthesised and demonstrated as having a significant effect on the stability of the mixed AC/DC networks. The PSS-based controller displays deteriorating performance at off-nominal operating conditions. These limitations are overcome using the multivariable complex MLQG controller.

Having established the applicability of the MLQG controller on the small test system, this controller design approach is extensively tested on the large five-area test network. The effects of varying delay on input signals and the loss of one or more input signals are assessed and it is shown that good performance can be maintained for extreme contingencies. Following this the modulation of reactive power injection at each converter station is included into the controller design approach but shown to offer little benefit over modulating only the active power flow to damp power oscillations. An investigation into the effects of limited modulation capacity being available for POD purposes suggests that flexible limits may be desirable to achieve the maximum benefit from the stabilising action of the VSC-HVDC line. The comprehensive evaluation of this WAMS-based controller for VSC-HVDC implementation and subsequent investigation into the effects of modulation capacity on damping improvement represent the first and second original contributions of this thesis.

The third original contribution is a further study in which a VSC-MTDC grid is installed within the large five-area network, demonstrating the benefits that multiple

points of controllable power injection provide when stabilising mixed AC/DC networks following a disturbance. The level of control afforded is such that modulation signals can be blocked if desired with little degradation to the stabilisation of the network as a whole.

### 3.1 Introduction of HVDC lines into AC Networks

An HVDC line is introduced into the two-area test network in order to establish how the electromechanical modes are affected. The converter technology, the points of connection to the AC network, and the operational power flow through the HVDC line are varied to establish the extent to which the system mode values vary.

#### 3.1.1 Modifications to the Test Network

The two-area network is modified to introduce an HVDC line in parallel with the long transmission corridor to the load L2. Both LCC-HVDC and VSC-HVDC lines are investigated, with the line feeding power directly to the loaded bus 9. The other converter station can be connected to bus 5, bus 6, or bus 7, in order to investigate the differences that the point of connection may have on modal stability. The modified network is shown in Figure 3-1, with HVDC parameters and control settings given in Appendix A.

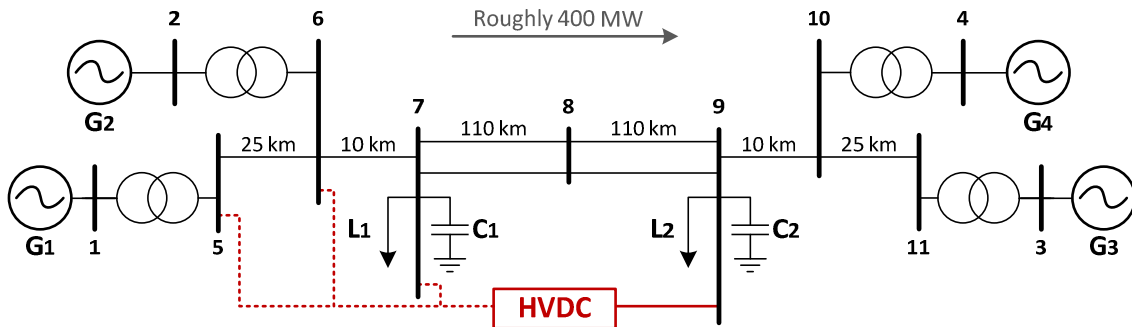


Figure 3-1: Two-area test network including VSC-HVDC line.

#### 3.1.2 HVDC Line Power Flow Variations

In addition to altering the technology type and the point of connection of one converter station, the power carried through the HVDC line is also varied. These variations are from 50 MW to 350 MW in 50 MW steps. In all cases, reactive power injection at both converter stations is maintained at zero. For the LCC-HVDC line this is achieved through appropriate setting of the compensating shunt susceptance  $B_{comp}$ . When transferring just 50 MW, most of the power transfer from G1 and G2 to L2 is through

the AC lines. When the HVDC line carries 350 MW, almost no power flows through the AC transmission corridor.

### 3.1.3 Results and Discussion

The variation of the local modes – Mode 1 and Mode 2 which were previously detailed in Table 2-1 – is shown in Figure 3-2 and Figure 3-3 respectively. The arrows show the movement of the modes as power transfer through the HVDC line ( $P_{DC}$ ) is increased from 50 MW to 350 MW in 50 MW steps. Note that the horizontal axis in these figures is the mode *damping*  $\sigma$  and not the *damping factor*  $\zeta$  (as defined previously in Section 2.3.2.1).

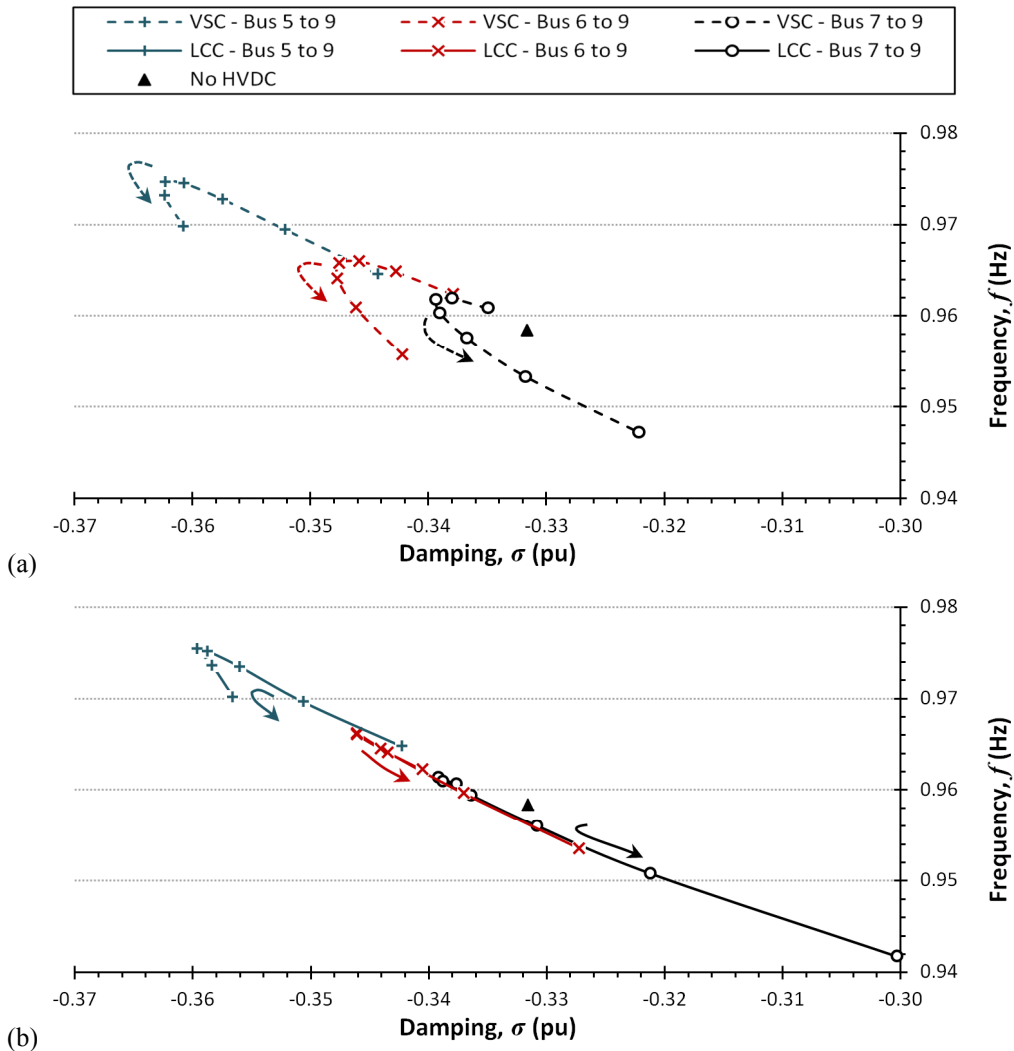


Figure 3-2: Movement of local mode 1 with varying connection point and power flow with (a) VSC-HVDC, and (b) LCC-HVDC technology.

Mode 1 (between G1 and G2) shown in Figure 3-2 is subject to some minor variation. Damping factor values lie in the range  $[5.41, 5.92]\%$  for the VSC-HVDC line, and

[5.07, 5.86]% for the LCC-HVDC line, with higher damping seen as the connection point for the converter station is moved closer towards G1 and G2.

This variation can be explained by considering the effect on the generators. Increasing the transmission through the VSC-HVDC line reduces the reactive power requirements on the generators. Furthermore, moving the point of connection closer to G1 and G2 increases the length of the parallel DC transmission path and further reduces the reactive power requirement caused by power transfer through the AC line. As the left-hand area is affected by the variation in the HVDC configuration, movement of this local mode is seen. This variation is small however and the damping factor remains above 5% in all cases.

The precise values for the location of Mode 2 (between G3 and G4) are unclear in Figure 3-3 as little change is seen. The damping factor for this local mode only varies in the small range of [5.57, 5.67]% with the VSC-HVDC technology used, and [5.45, 5.65]% with the LCC-HVDC, and in both cases is largely unaffected by the HVDC line. The variations explored do not significantly change the operation of the right-hand area of the network. The output of generators G3 and G4 remain roughly constant for all operating points considered and so it would be expected that the electromechanical interaction between these generators would remain largely unchanged as is shown.

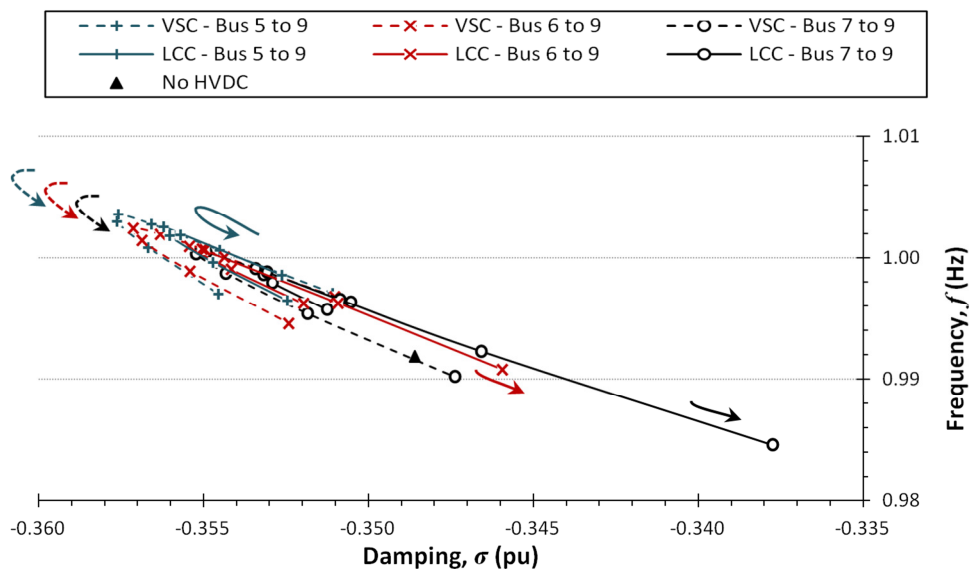


Figure 3-3: Movement of local mode 2 with varying HVDC technology, connection point and power flow.

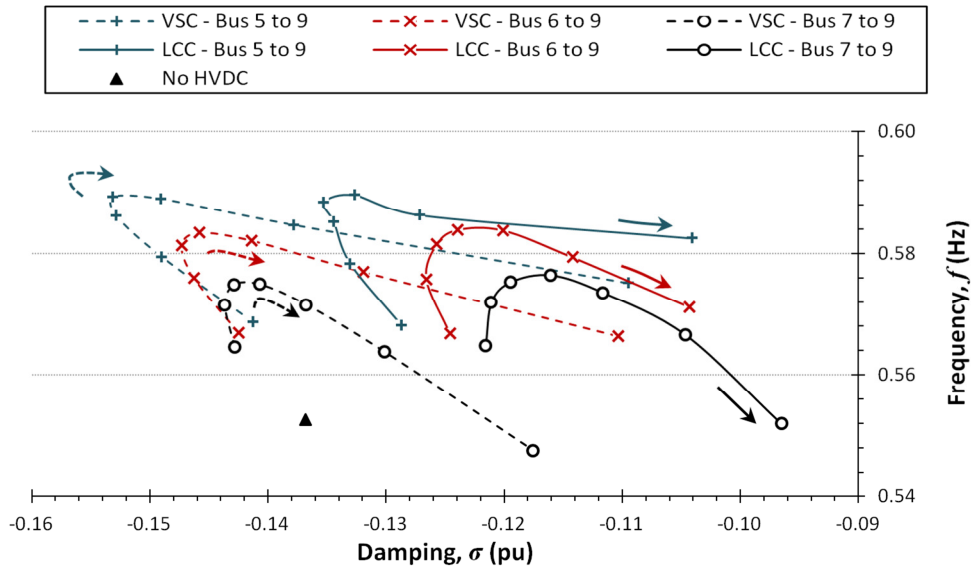


Figure 3-4: Movement of inter-area mode with varying VSC-HVDC connection point and power flow.

With the HVDC line affecting the power flow between the two areas to such a large extent, the inter-area mode (Mode 3 from Table 2-1) is subject to the greatest variations. With all three points of connection, the damping factor of the mode is highly variable, as shown in Figure 3-4. With the use of the LCC-HVDC technology, the damping factors vary in the range  $[2.78, 3.66]\%$ . With the VSC-HVDC line installed, the greatest variation is seen for connections directly at bus 5 when damping factors vary in the range  $[3.03, 4.15]\%$ . Compared with the value when no HVDC is installed (3.94%), it can be seen that in some cases inter-area modal damping is improved with the addition of the supporting VSC-HVDC line. It is, however, also evident that the inclusion of the LCC-HVDC line results in a reduction of the damping factor of the inter-area mode for all conditions. For all configurations and operating points and configurations, the use of LCC-HVDC results in a lower damping factor for each electromechanical mode than an equivalent VSC-HVDC line.

The shape of the curves seen in Figure 3-4 suggests an optimum operating point at which the damping of the inter-area mode is maximised. With a VSC-HVDC line installed between buses 5 and 9, the maximum value of damping occurs when  $P_{DC} = 200 \text{ MW}$ .

The transient responses seen following a large system disturbance when a VSC-HVDC line is transferring different levels of power is shown in Figure 3-5. The disturbance is a 100 ms self-clearing three-phase fault at bus 10 at a time of 2 s. Two HVDC power

levels are considered, 200 MW when damping is greatest, and 350 MW when damping is at its lowest value for this technology. Also included for comparison is the system response with no HVDC line installed. The active power oscillations seen on the tie lines between the two areas in the network have been normalised for comparison.

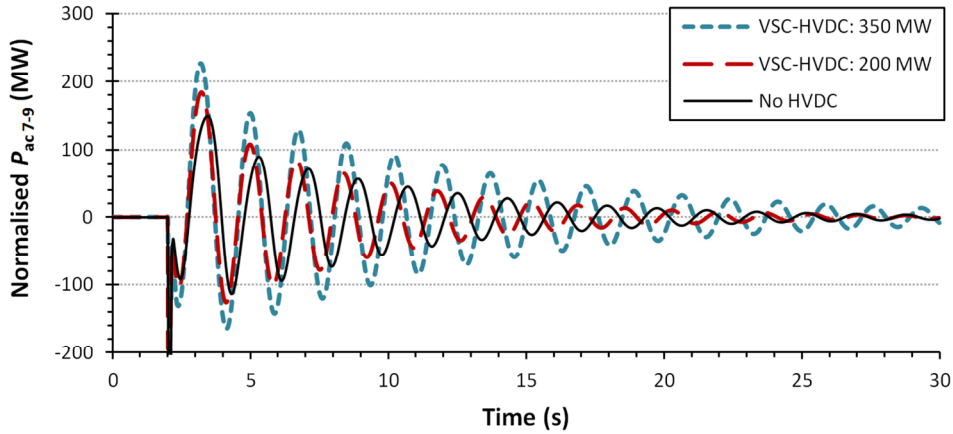


Figure 3-5: AC power flow from bus 7 to bus 9 following a disturbance with varying power flow through the VSC-HVDC line.

The transient results clearly confirm the findings of the small-disturbance analysis: damping of the inter-area mode is greatest for the case when  $P_{DC} = 200$  MW. The damping at this operating condition demonstrates a marginal improvement over the system response with no HVDC installed, however this is very slight. It is clear that the oscillations are more persistent when  $P_{DC} = 350$  MW and the power flow through the AC system is reduced. This operating point clearly shows a reduction in the damping of the inter-area mode.

It has been clearly shown that there are connection options and operating conditions for an additional HVDC line which can have a detrimental effect on the damping of electromechanical modes within the power system. With sufficiently low initial damping, the introduction of an HVDC line may in fact introduce sufficient negative modal damping to lead to small-disturbance instability. It is advisable to control the power flow through the HVDC line based partly on the stability of the system. However, in practical installations, the operation of HVDC lines will be primarily determined based on economic dispatch concerns. Modal damping can however be improved with supplementary control, ensuring that inherent negative effects are counteracted and that the system stability is improved.

POD control based on the modulation of the active power flow within HVDC lines can improve the stability of power systems. Within this research, the limitations of a common PSS-based controller are highlighted and improved performance using a more complex MLQG controller structure is demonstrated.

It has been demonstrated in Section 3.1 that the inclusion of an LCC-HVDC line will cause negative modal damping compared to an equivalent VSC-HVDC system connected between the same buses and transferring the same power. With VSC-HVDC systems, reactive power is controlled independently of active power and can be maintained at a constant value throughout all investigations if desired. This is not the case with LCC-HVDC where it is more difficult to modulate the active power flow due to complex reactive power compensation requirements. In addition to this, it has been identified in Chapter 1 that the number of VSC-HVDC systems in planning and production is presently rapidly increasing, including the proposal of multi-terminal grid solutions. For these reasons, all studies involving the controlled modulation of active power for oscillation damping will be performed using VSC-HVDC lines.

### 3.2 VSC-HVDC POD Control on a Small Test System

Within this section, the POD controllers which have been outlined previously in Chapter 2 will be designed and tested using a small test system incorporating an embedded VSC-HVDC line. The aim of this initial study is to demonstrate the benefits of utilising pre-installed HVDC lines for POD purposes and to compare the two different controller design structures.

#### 3.2.1 Modifications to the Test Network

A VSC-HVDC line is embedded within the two-area test network between buses 5 and 9 to support power flow to the load L2. The modified network is shown in Figure 3-12, with VSC-HVDC parameters and control settings given in Appendix A.

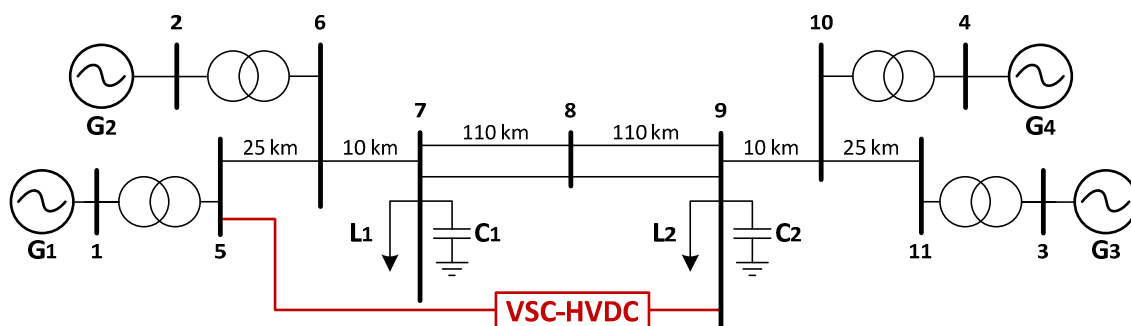


Figure 3-6: Two-area test network including embedded VSC-HVDC line.

With the VSC-HVDC line installed and operating at a nominal active power set-point of 200 MW, the mode details are changed slightly from the purely AC network. The new values are presented in Table 3-1. It can be seen that both local modes are adequately damped (with  $\zeta > 5\%$ ). The inter-area mode would benefit from additional damping. The installed VSC-HVDC link can be utilised for POD control in order to achieve this.

Table 3-1: Electromechanical mode properties for the two area test system with an embedded VSC-HVDC line.

Mode	Eigenvalue, $\lambda = \sigma + j\omega$ (pu)	Frequency, $f$ (Hz)	Damping Factor, $\zeta$ (%)
Mode 1	$-0.361 \pm j6.124$	0.975	5.88
Mode 2	$-0.362 \pm j6.304$	1.003	5.73
Mode 3	$-0.155 \pm j3.697$	0.588	4.20

### 3.2.2 POD Controller Designs

A diagram of the general control overview for the two-area network including the VSC-HVDC line is shown in Figure 3-7 below. POD control through the modulation of the active power flow through the VSC-HVDC line is the subject of the investigation. Therefore the POD controller output is limited to a single signal ( $u_1 : \Delta P_{dc}^{ref}$ ) which is fed to the converter station regulating active power injection. Within this study, this is the converter station connected to bus 9.

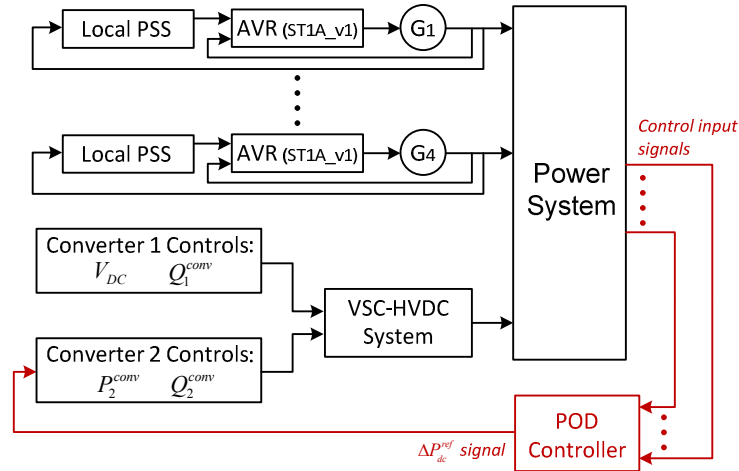


Figure 3-7: General control scheme for the Kundur two-area test network including a VSC-HVDC line with supplementary POD control.

#### 3.2.2.1 PSS-based POD Controller Details

The PSS-based controller design uses a locally available signal, selected as the active power injected into bus 9 through one of the parallel AC lines,  $y_1^{PSS} : P_{ac, 8-9}^{(l \text{ line})}$ . As a local

input signal is selected, it is assumed that there is no associated transmission delay. Similarly, it is assumed that the POD controller is located at the VSC-HVDC converter station controlling active power regulation, and no output signal transport delays are modelled. Residue based tuning is completed for the inter-area mode, resulting in the final controller settings given in Appendix A.

### 3.2.2.2 MLQG POD Controller Details

The MLQG POD controller can use multiple global signals to improve inter-area oscillation damping. Construction of the state observability matrix shows that the active power flow into bus 9 through one of the parallel AC lines displays high modal content for all three electromechanical modes. This input is retained for use with the MLQG controller. Supplementary signals are also selected from voltage angles at all buses, representing the placement of PMUs throughout the network.

These extra signals are limited in number to two, in part to reflect the expense and current scarcity of PMUs within a network and in part to reduce controller complexity. Again, from the state observability matrix, angles at buses 2 and 4 are selected. The controller, therefore, has three inputs: active power flow into bus 9 ( $y_1^{MLQG} : P_{ac, 8-9}^{(l \text{ line})}$ ), the voltage angle at bus 2 ( $y_2^{MLQG} : \theta_2^{sys}$ ), and the voltage angle at bus 4, ( $y_3^{MLQG} : \theta_4^{sys}$ ).

In this preliminary study assessing the relative performance of the PSS-based and MLQG POD control structures with VSC-HVDC, no signal transmission delays are considered. It is acknowledged that this is not representative of a practical system and that the use of wide area signals will introduce both time delays and additional cost to the proposed solution. In order to reduce complexity for the purposes of this initial assessment into the feasibility of using MLQG control with VSC-HVDC, wide area signal transmission delays are not included. In the further studies presented within this chapter completed on the five-area test network, signal delays are included as appropriate.

The MLQG controller is designed using the full plant model, with equal weighting values assigned to all three electromechanical modes in the matrix  $\mathbf{Q}_M$ . The final controller is left unreduced for this initial study and is of 73<sup>rd</sup> order.

### 3.2.3 Small-Disturbance Analysis

Small-disturbance analysis is completed on the two-area test network with both POD controllers installed. The resulting modal positions can be seen in Figure 3-8, where the dashed line represents the  $\zeta = 5\%$  threshold. Final closed loop mode damping factors presented in Table 3-2.

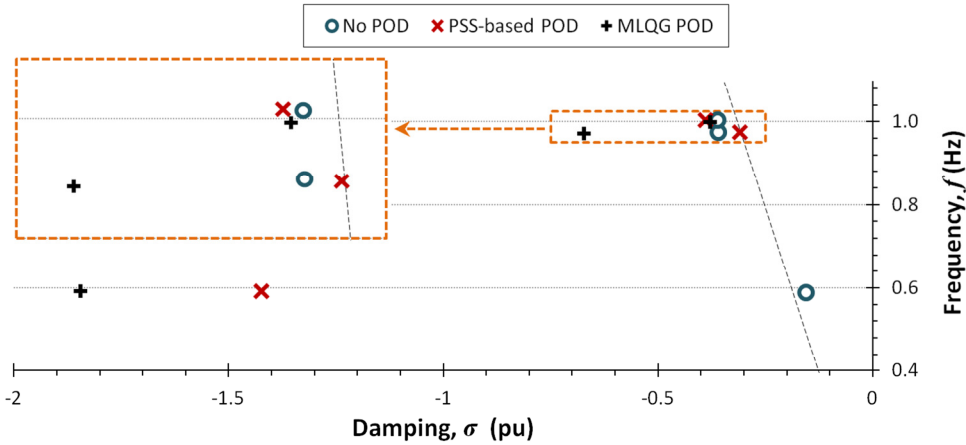


Figure 3-8: Modal placement of electromechanical modes with POD controllers installed.

With both controllers installed, the inter-area mode achieves very good damping, with  $\zeta$  values greater than 35%. With either controller installed, the high damping factor is sufficient to ensure good damping of the inter-area mode. Also shown in Table 3-2 are the damping factors for the local modes. It is evident that the damping of Mode 2 is largely unaffected by either controller. Mode 1, however, sees the introduction of some negative damping with the PSS-based POD controller – reducing its damping factor to 5.06%. In contrast, the MLQG controller improves the damping factor of Mode 1 to 10.95%.

Table 3-2: Damping factors of electromechanical modes with POD controllers installed.

Mode	No POD	PSS-based POD	MLQG POD
Mode 1	5.88	5.06	10.95
Mode 2	5.73	6.16	6.02
Mode 3	4.20	35.72	44.46

### 3.2.4 Large Disturbance Analysis

Large disturbance analysis is required in order to identify the true non-linear behaviour of the power system with the supplementary POD controllers in order to assess their performance. By subjecting the test system to a transient fault, the damping of the post-

disturbance oscillations can be observed and the small-disturbance analysis can be validated.

Large disturbance transient studies have been performed for two cases: the *base case* with the nominal operating conditions for which the controllers were designed, and an *increased power transfer case* when the system is more stressed. By testing with off-nominal conditions, knowledge about the robustness of the controller can be gained.

### 3.2.4.1 Base Case Scenario

For the *base case*, system generation and loading are at the standard nominal operating point and all transmission lines are in service. The VSC-HVDC line operates at 200 MW power flow from bus 5 to bus 9 to support L2. Reactive power output at both converter stations is regulated at zero. The system is subjected to a 100 ms self-clearing three-phase fault at bus 8 at a time of 0.5 s. VSC-HVDC modulation is limited to  $\pm 50$  MW.

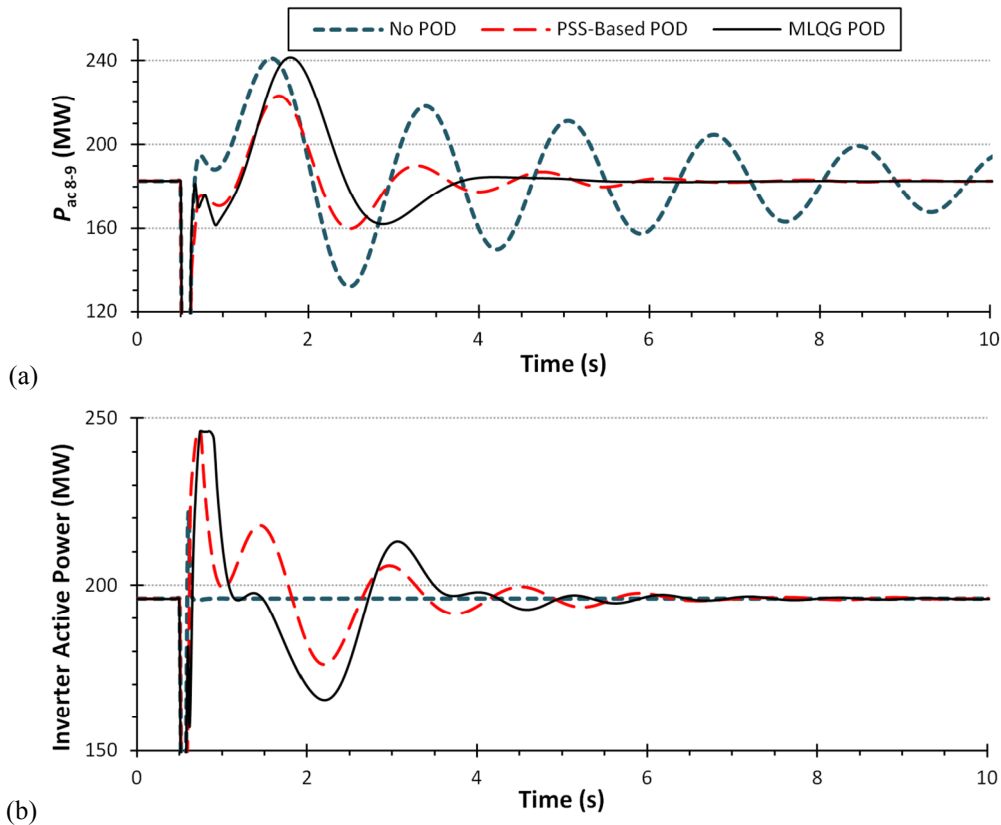


Figure 3-9: For the *base case*: (a) Active power injected at bus 9 from bus through the AC infeeds, and (b) Active power injected at bus 9 by the VSC-HVDC line.

Figure 3-9 displays the transient plots of the power flow through the AC tie-lines between the two areas of the network, and the active power injected at bus 9 by the VSC-HVDC line. It is evident from Figure 3-9(a) that both POD controllers are very

effective at damping power oscillations for the *base case*. The power flow through the parallel AC tie lines is settled (to less than 1% deviation from steady state values) within 5.09 s with the PSS-based controller, and within just 3.77 s with the MLQG design. For comparison, with no POD controller installed the system continues to oscillate for 21.58 s. The level of modulation of  $P_{DC}$  is shown in Figure 3-9(b) where it can be seen that following the initial swing after the disturbance, only small levels of modulation are required to effectively stabilise the AC network.

#### **3.2.4.2 Increased Power Transfer Scenario**

The designed POD controllers are also assessed at an operating point different to the one used during their designs. This provides some indication of the robustness of the controllers – their ability to perform well for a wide range of operating conditions. For this small system study, an *increased power transfer case* is considered in which a higher power demand in the right hand side of the network must be supported by generators G1 and G2 on the left hand side.

The active power load at L2 (bus 9) is increased by 100 MW. In addition to this, the output of G4 is reduced by 250 MW, with this shortfall met by G1 and G2. To help facilitate the increased power flow required, the operating capacity of the VSC-HVDC link is increased to 350 MW. The same transient disturbance is used – a 100 ms self-clearing three-phase fault at bus 8 at a time of 0.5 s. VSC-HVDC modulation is again limited to  $\pm 50$  MW.

The transient plots of AC power flow and VSC-HVDC injected power at bus 9 are shown for this *increased power transfer case* in Figure 3-10 below. With these stressed operating conditions, the improved response with the MLQG controller installed can clearly be seen. The PSS-based POD controller is not robust to the changes in operating conditions and takes 8.47 s to settle the power flow through the parallel AC lines. This is however still an improvement compared to when no POD controller is installed when it requires 11.62 s for the system to stabilise. The MLQG controller, utilising multiple global signals, is still able to perform very well despite the different operating conditions with all oscillations damped within 3.34 s.

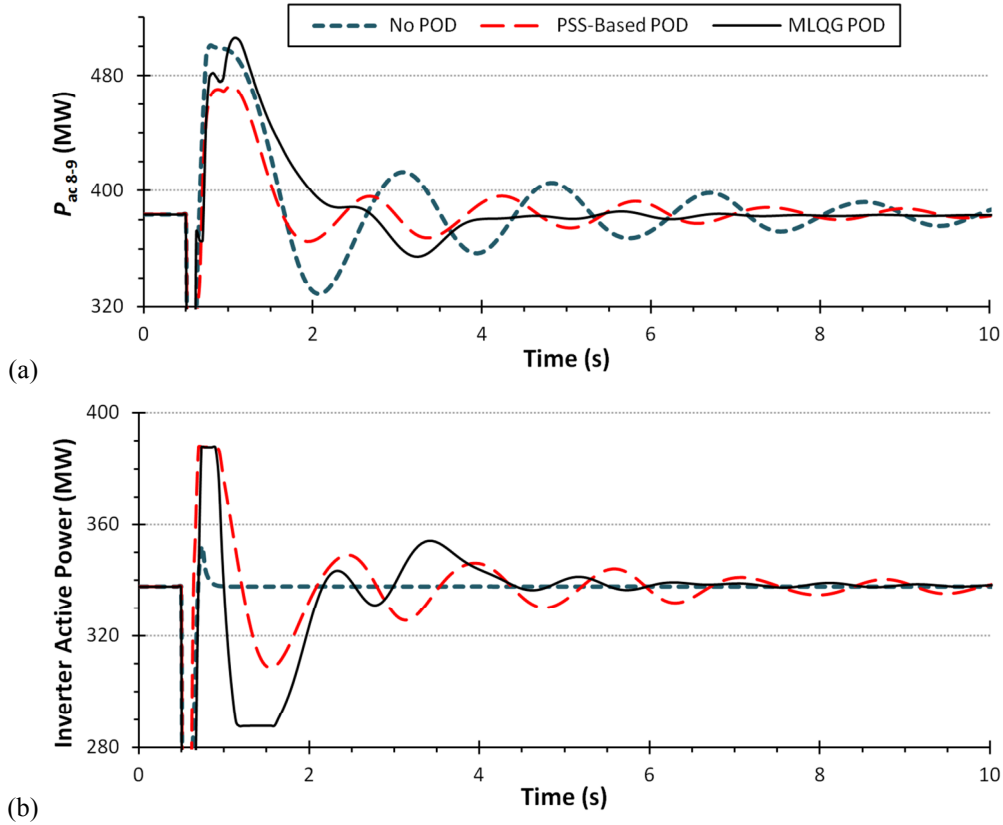


Figure 3-10: For the *increased power transfer case*: (a) Active power injected at bus 9 from bus through the AC infeeds, and (b) Active power injected at bus 9 by the VSC-HVDC line.

A summary of the settling times for the two case studies is presented in Table 3-3 where the improved performance of the MLQG controller design is clearly evident. This study has not only demonstrated the effectiveness of VSC-HVDC systems at damping power oscillations, but also the applicability of the MLQG design approach to VSC-HVDC-based POD control.

Table 3-3: Settling times for the parallel AC tie lines with different POD control schemes installed.

Controller Type	Settling Time for Parallel AC Tie-Line (s)	
	Base Case	Increased Power Transfer Case
No POD	21.58	11.62
PSS-based POD	5.09	8.47
MLQG POD	3.77	3.34

### 3.3 VSC-HVDC POD Control on a Large Test System

The small test system used in Section 3.2 provided a useful basis on which to test the potential of VSC-HVDC at damping power oscillations. It also presented an indication of how the MLQG design is able to improve the performance and robustness of a supplementary POD controller compared with a traditional PSS-based approach. Within

this section, this initial study is developed further to more comprehensively assess the performance of these controllers on a test network which is more representative of practical multi-area power systems.

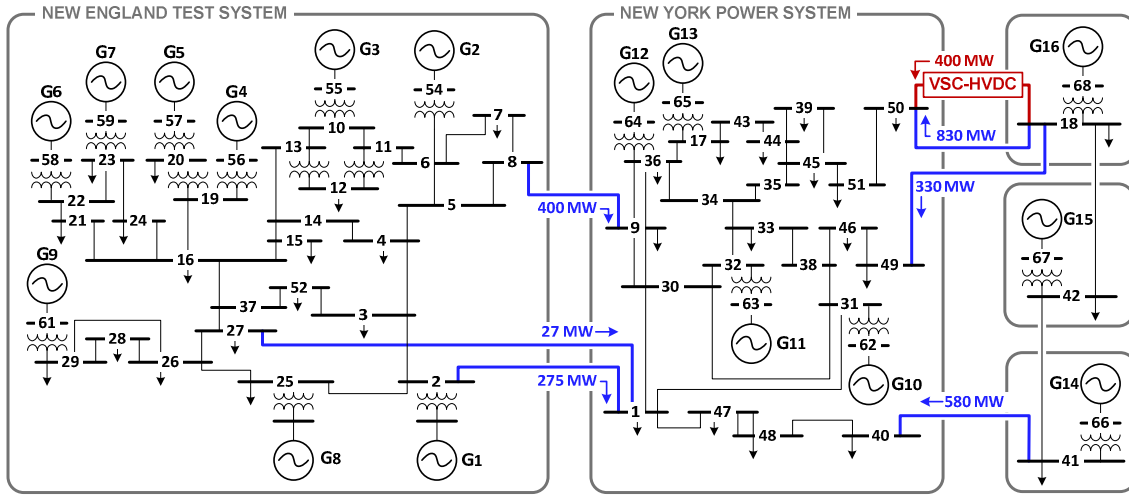


Figure 3-11: Five-area test network with VSC-HVDC line installed.

### 3.3.1 Modifications to the Test Network

These studies are performed using a modified version of the large five-area power system. With standard loading, the NYPS region of the network is heavily importing power – with the majority of this coming from the G16 area. To support this infeed, a VSC-HVDC line is installed from bus 18 to bus 50, with a nominal operating power of 400 MW. All VSC-HVDC line parameters and controller settings are given in Appendix A. The network (including this reinforcement) is shown in Figure 3-11 above, including updated inter-area power flows.

With this VSC-HVDC line in place, the system displays four low frequency inter-area modes with poor damping, detailed in Table 3-4. All local electromechanical modes are adequately damped with  $\zeta > 5\%$ .

Table 3-4: Inter-area mode details for five-area test network with VSC-HVDC line.

Mode	Description	Eigenvalue, $\lambda = \sigma + j\omega$ (pu)	Frequency, $f$ (Hz)	Damping Factor, $\zeta$ (%)
Mode 1	(NETS & NYPS) <i>against</i> (G14 & G15 & G16)	$-0.117 \pm j2.512$	0.400	4.66
Mode 2	(NETS & G14 & G15) <i>against</i> (NYPS & G16)	$-0.134 \pm j3.207$	0.510	4.18
Mode 3	(NETS & G16) <i>against</i> (NYPS & G14)	$-0.167 \pm j3.953$	0.629	4.21
Mode 4	G15 <i>against</i> (G14 & G16)	$-0.243 \pm j4.977$	0.792	4.87

### 3.3.2 POD Controller Designs

The general control overview for the five-area network is shown in Figure 3-12. For both supplementary POD controllers (PSS-based and MLQG), output is limited to a single signal ( $u_1 : \Delta P_{dc}^{ref}$ ) which is fed to the converter station regulating active power injection. Within this study, this is the station acting as the inverter at bus 50.

#### 3.3.2.1 PSS-based POD Controller Details

The input to the PSS-based controller is selected as a local signal, the active power injected into bus 50 from bus 18 through the parallel AC transmission line,  $y_1^{PSS} : P_{ac, 18-50}$ . As a local input signal is selected, it is assumed that there is no transport delay associated with receiving it. Similarly, it is assumed that the POD controller is located at the VSC-HVDC converter station controlling active power regulation, and no output signal transport delays are modelled. Residue analysis suggests that the lowest frequency Mode 1 is most controllable given the selection of controller input and output. Tuning is completed for this mode, with final controller settings given in Appendix A.

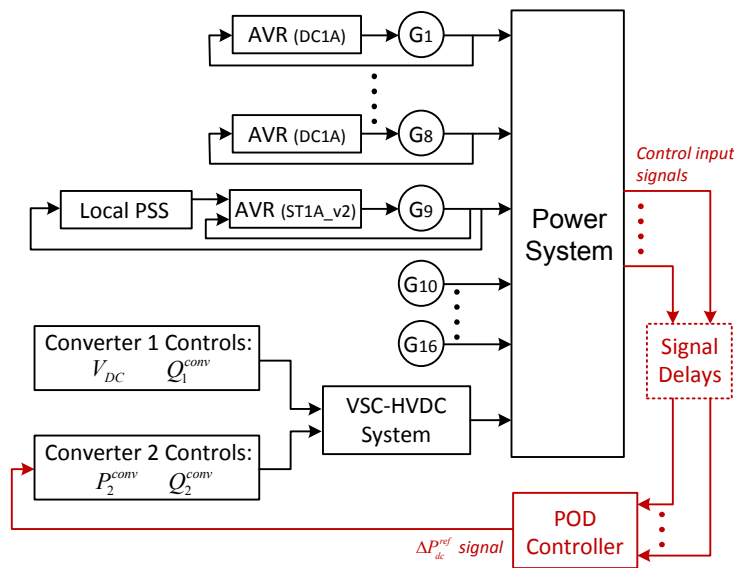


Figure 3-12: General control scheme for the five-area test network including a VSC-HVDC line with supplementary POD control.

#### 3.3.2.2 MLQG POD Controller Details

The MLQG controller structure can utilise multiple wide area signals to target multiple critical oscillatory modes. Practical networks containing a large number of PMUs will be able to exploit these available signals to gain a highly accurate representation of the network's oscillatory nature following disturbances. Within this study, a full modal

observability assessment initially carried out determined that four active power flow signals contained the greatest information about Modes 1–4. These signals are the active power flow along line 45–51 ( $y_1^{MLQG} : P_{ac, 45-51}$ ), line 68–18 ( $y_2^{MLQG} : P_{ac, 68-18}$ ), line 65–17 ( $y_3^{MLQG} : P_{ac, 65-17}$ ), and line 67–42 ( $y_4^{MLQG} : P_{ac, 67-42}$ ). It is assumed that pre-existing communications channels are used as opposed to dedicated optical fibre cables, meaning that the wide area signals are subject to a transmission delay of 500 ms [20–23]. It is also assumed that this supplementary controller is located at the converter station regulating active power flow, therefore output signal delays are not considered.

The MLQG controller is designed using the full plant model (182<sup>nd</sup> order) with weights  $Q_M$  set to achieve good damping across the four inter-area modes, whilst local modes are left unaffected. The final controller is then reduced, constrained by the degradation seen in the closed loop inter-area mode damping factors. A maximum allowable variation of 5% (in relative terms) is considered acceptable whilst completing the reduction. The final controller is of 28<sup>th</sup> order.

### 3.3.3 Small-Disturbance Analysis

Small-disturbance analysis is performed on the test system with each of the designed POD controllers installed. The position of the modes is shown in Figure 3-13, where the dashed line represents the  $\zeta = 5\%$  threshold. Final damping factor values are presented in Table 3-5.

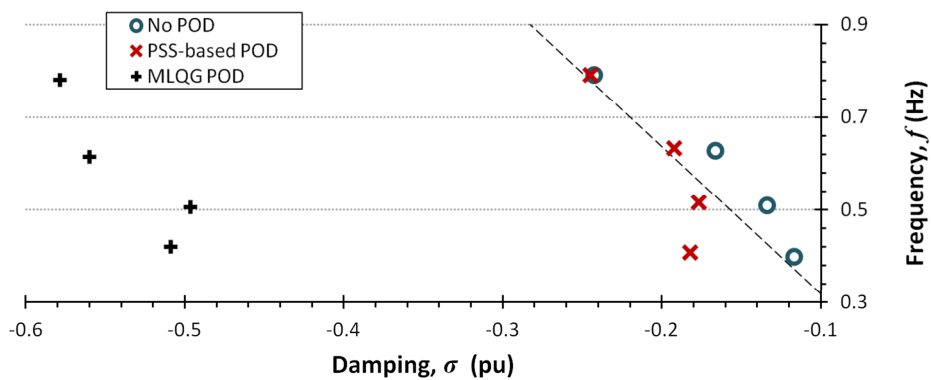


Figure 3-13: Modal placement of inter-area modes with POD controllers installed.

The data presented proves that with the PSS-based POD controller installed, some improvement is seen. This improvement is greatest for the tuned Mode 1. Although all modes do see an increase in damping factors, it is very slight and only Modes 1 and 2

cross the 5% threshold. It is clear that the use of a single local input severely limits the extent to which damping improvement is possible.

Table 3-5: Damping factors of inter-area modes with POD controllers installed.

Mode	No POD	PSS-based POD	MLQG POD
Mode 1	4.66	7.08	18.90
Mode 2	4.18	5.44	15.43
Mode 3	4.21	4.82	14.34
Mode 4	4.87	4.92	11.70

Figure 3-13 displays the improvement that is made by utilising the MLQG controller design and multiple wide area signals, even though they are subject to delays. The modes are moved further to the left-half complex plane, improving damping factors considerably for all modes. Table 3-5 reveals that  $\zeta$  values are greater than 10% for all modes, and should ensure quick recovery to steady state conditions following a system disturbance.

### 3.3.4 Large Disturbance Analysis

The small-disturbance analysis is dependent on the linearisation of the non-linear power network and approximations of the signal transmission delays. By subjecting the test network to large disturbances, the true non-linear behaviour of the power system can be seen and the performance of the supplementary POD controllers can be assessed accordingly.

Large disturbance transient studies have been performed for two cases: the *base case* with the conditions for which the controllers were designed, and an *outage case* with a key AC tie-line removed from service.

#### 3.3.4.1 Base Case Scenario

System generation and loading are at the standard nominal operating point with all transmission lines in service. The VSC-HVDC line operates at 400 MW import to NYPS with zero reactive power output at both converter stations. The system is subjected to a 100 ms self-clearing three-phase fault at bus 38 at a time of 0.5 s. VSC-HVDC modulation is limited to  $\pm 100$  MW.

Settling times are recorded from the point of fault clearance to the time at which the power deviation is within  $\pm 1\%$  of the steady state value (or  $\pm 1$  MW, whichever is greatest). These times are shown for the NYPS inter-area AC infeeds in Figure 3-14.

The PSS-based POD controller improves the settling time of all AC infeeds, having the greatest effect on the line 18–50 – the local signal source for the POD controller. However, the remaining AC infeeds still require more than 15 s to settle, and the line from bus 2–1 takes longer than 22 s to stabilise. This represents an improvement over having no POD controller installed, when all lines take between 20–30 s to settle, but further improvement is possible.

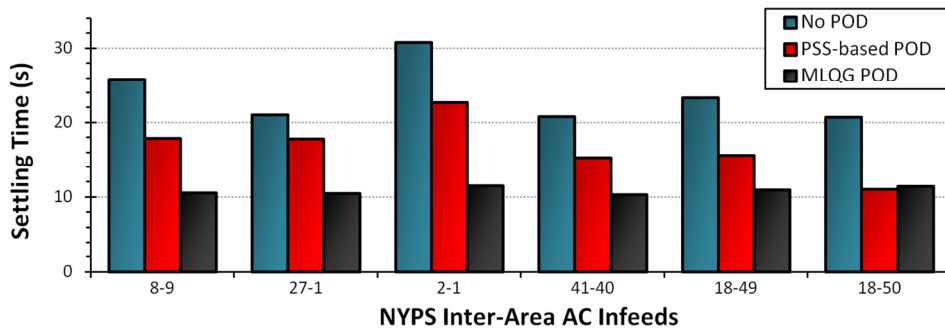


Figure 3-14: Settling times for the NYPS inter-area AC infeeds for the *base case*.

The improved performance of the MLQG controller suggested by the earlier small-signal analysis is evident in the results of the transient simulation. All AC tie-lines are stabilised in less than 12 s, a clear improvement over the PSS-based POD controller. The MLQG controller takes marginally longer than the PSS-based controller to ensure that the AC line in parallel with the VSC-HVDC system (line 18–50) is stabilised. However this takes just 0.4 s longer, and is a minor cost to ensure that all AC infeeds regain steady state operation much faster.

It can be seen from the network diagram (Figure 3-11) that many of these NYPS infeed tie-lines are some distance from the VSC-HVDC line, the location of the supplementary damping control action. Nevertheless, by utilising wide area signals to gain a full picture of the oscillatory state of the whole network, all NYPS infeeds are settled quickly – not only those closest to the line as is seen with the PSS-based controller.

The transient plots of the AC power flow along the tie-line 8–9, and the active power injected at bus 50 by the VSC-HVDC line are given in Figure 3-15. The damping of the power oscillations in this tie-line between the NETS and NYPS areas is shown to be much larger with the MLQG controller installed. The modulated active power flow injected by the VSC-HVDC line shows that with no POD controller in place, steady state operating is quickly achieved following the fault. This is comfortably maintained by the VSC-HVDC controllers despite the heavily oscillating AC network. A close-up

plot is provided in Figure 3-15(b) to clarify events surrounding the fault occurrence. At  $t_1 = 0.5$  s the fault occurs, at  $t_2 = 0.6$  s the fault is cleared and PSS-based POD controlled power modulation is evident, and at  $t_3 = 1.0$  s the delayed wide area signals reach the MLQG controller and POD power modulation begins.

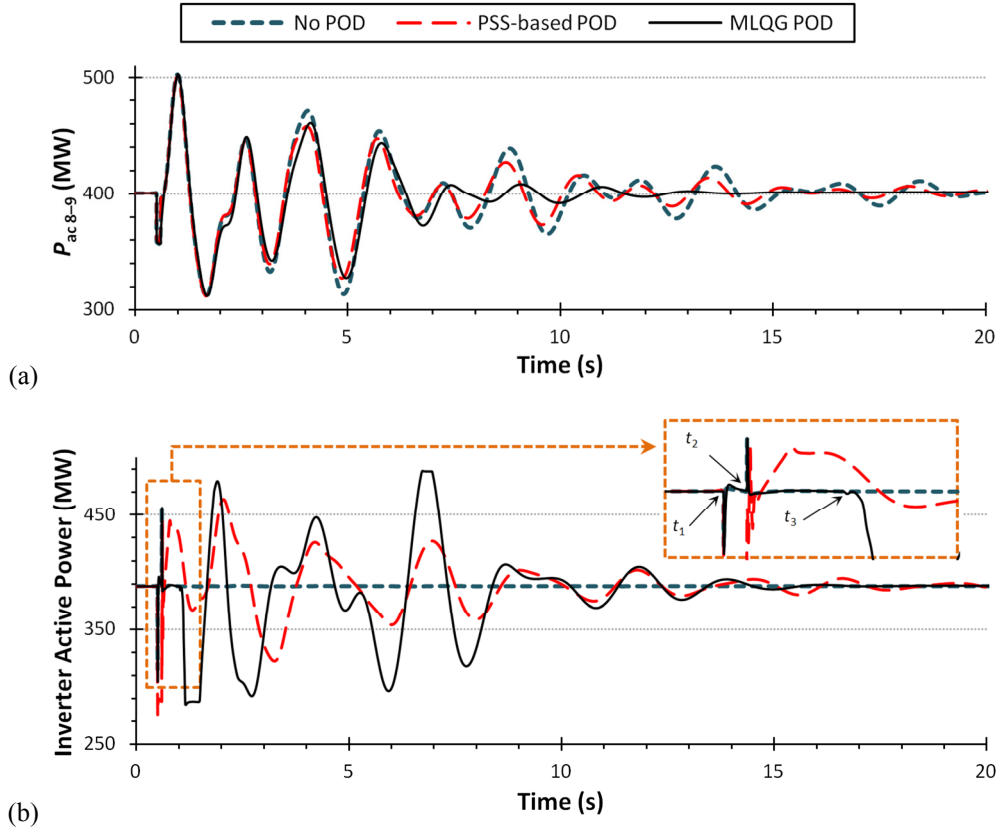


Figure 3-15: For the *base case*: (a) Active power injected at bus 9 from bus 8 through an AC infeed, and (b) Active power injected at bus 50 by the VSC-HVDC converter station.

For this *base case* scenario, the MLQG controller has outperformed the PSS-based controller by ensuring the entire network regains steady state operation within 12 s (compared to 22 s), with a slight sacrifice in local performance on the parallel AC tie-line 18–50. This is achieved despite the 500 ms delays experienced on all wide area signals.

### 3.3.4.2 Outage Case Scenario

To test the controllers with conditions different to those which they were designed for, an *outage case* is considered. The system is still operating with standard loading, but the AC line 18–49 is removed from service. This line provided a path for power flow from the G16 area to NYPS. As a consequence, power flow through the line 18–50 is increased. VSC-HVDC operational capacity is increased slightly to 450 MW to aid this transmission, still with zero reactive power injection. The system is subjected to a 100

ms fault near to bus 1 on the line from bus 1 to bus 30, at a time of 0.5 s. The fault is cleared by disconnecting the line, resulting in a final topology with two lines out of service. VSC-HVDC modulation is limited to  $\pm 100$  MW.

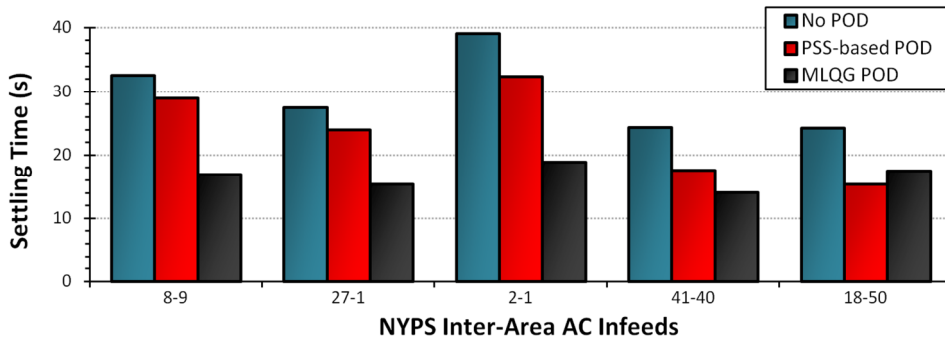


Figure 3-16: Settling times for the NYPS inter-area AC infeeds for the *outage case*.

As for the *base case*, the dismal performance of the AC network (taking up to 40 s to stabilise) is improved with the addition of the POD controllers. The increased strain that the two line outages place on the network is evident, with the PSS-based controller requiring 15–29 s before each NYPS infeed returns to steady state operation. This is improved on by using the MLQG controller which ensures stable power flow through the tie-lines in 14–19 s. Again, the MLQG controller is slower to settle the oscillations in the parallel AC line 18–50. This is however balanced by the network-wide improvement seen.

Figure 3-17(a) displays the power flow through the tie-line 8–9. The PSS-based POD controller with only local signals is shown to be moderately ineffective at damping oscillations in lines far from the VSC-HVDC line. A clear improvement is seen with the MLQG controller installed. A close-up plot is provided in Figure 3-17(b) which shows events around the time of the fault occurrence more clearly. At  $t_1 = 0.5$  s the fault occurs, at  $t_2 = 0.6$  s the fault is cleared and PSS-based modulation starts, and at  $t_3 = 1.0$  s the MLQG-based POD modulation begins. The strained power system experiences much larger power swings in the tie-line 8–9: roughly  $\pm 200$  MW swings compared to  $\pm 100$  MW swings for the *base case*. As a result, the MLQG controller's modulation of the injected VSC-HVDC active power is greater for a longer period of time in order to stabilise the network.

The large disturbance study involving the *outage case* has shown that the MLQG controller displays greater robustness than the PSS-based POD controller. It is able to

maintain more effective damping of the entire network with operating conditions different to those for which it was designed.

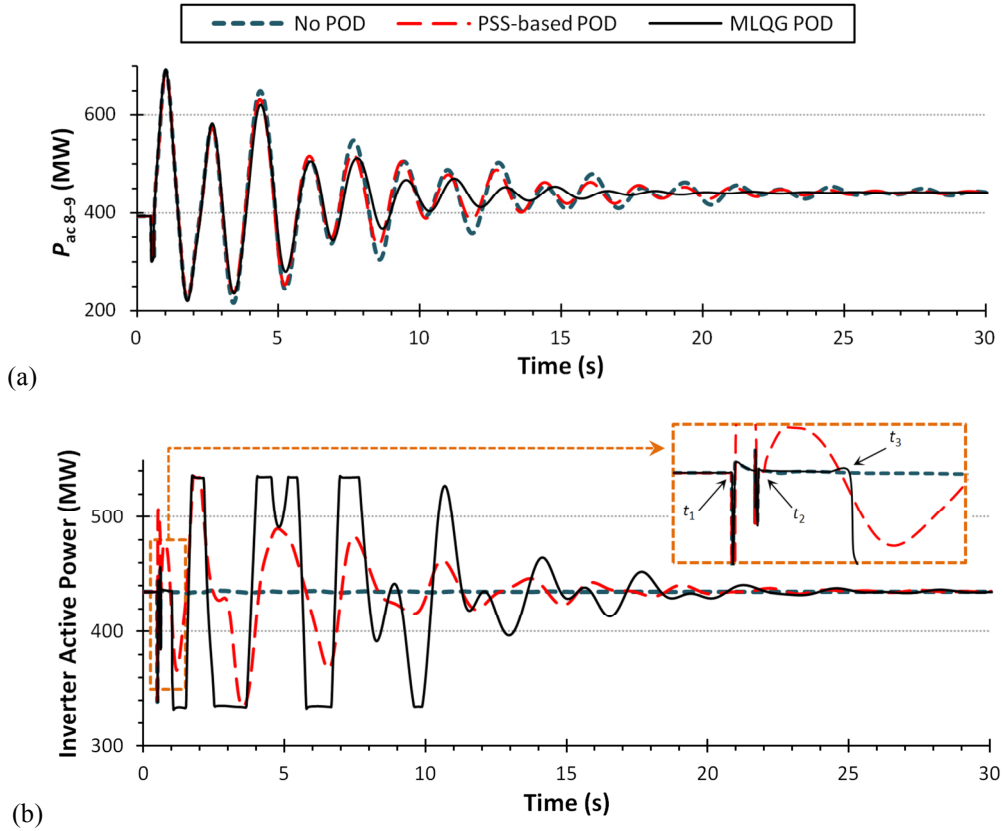


Figure 3-17: For the *outage case*: (a) Active power injected at bus 9 from bus 8 through an AC infeed, and (b) Active power injected at bus 50 by the VSC-HVDC converter station.

Although these transient simulations can reveal a lot about the performance of the designed controllers, a more thorough assessment of controller robustness is required in order to test the effectiveness of the supplementary POD control at a wide range of feasible operating conditions. This will be thoroughly addressed in the following chapter.

### 3.3.5 Wide Area Signal Delay

The use of wide area measurements enables a higher performing and more robust controller design. These signals are becoming more prevalent and increasingly available in modern power systems, providing reliable real-time data which can improve many aspects of system performance. However, these signals will often be sent through pre-existing satellite communication links as dedicated hard-wired links may prove prohibitively expensive. As such, they could potentially be subject to increased delay or even complete loss.

If faster communication channels (for example, fibre optic links) are available then the shorter associated delays should be included in the controller design stage. It has however been shown in [29] that the performance of the MLQG controller will improve as signal delays shorten, provided they are suitably modelled during controller synthesis.

The effects of signal latency and mitigation techniques for use with WAMS based controllers have been a topic of much interest, as discussed previously in Section 1.3. For the MLQG controller, the effects of increased signal delays and the complete loss of signals have been investigated in order to demonstrate the controller's robustness to these problems.

### 3.3.5.1 Variable Delays

The controller's local signal to the VSC-HVDC converter station is assumed to be hard-wired and not subject to these issues. The MLQG controller is designed with a (relatively pessimistic) delay of 500 ms on all wide area signals ( $y_1^{MLQG}, \dots, y_4^{MLQG}$ ). Small-disturbance analysis has been completed with increasing values of signal delay to establish the effect on the damping factor values for each mode.

The designed MLQG controller is very robust to delay increases in one input channel. For example, increasing the delay of signal  $y_1^{MLQG}$  to 2500 ms (five times its original value) results in damping factors for Modes 1–4 of 9.29%, 11.33%, 9.97%, and 9.94% respectively. These values are considerably higher than those achieved with the PSS-based controller when no delays were considered. Similar results are seen if delays are extended for any other single input channel.

In order to test the worst-case scenario, delays are increased for all four input channels of the MLQG controller simultaneously. The deterioration in the damping factors of the four inter-area modes can be seen in Figure 3-18 as delays are increased to 1100 ms at the previously defined *base case* operating scenario. There is a gradual degradation in controller performance as the signals are delayed for longer than the 500 ms assumed during the controller synthesis.

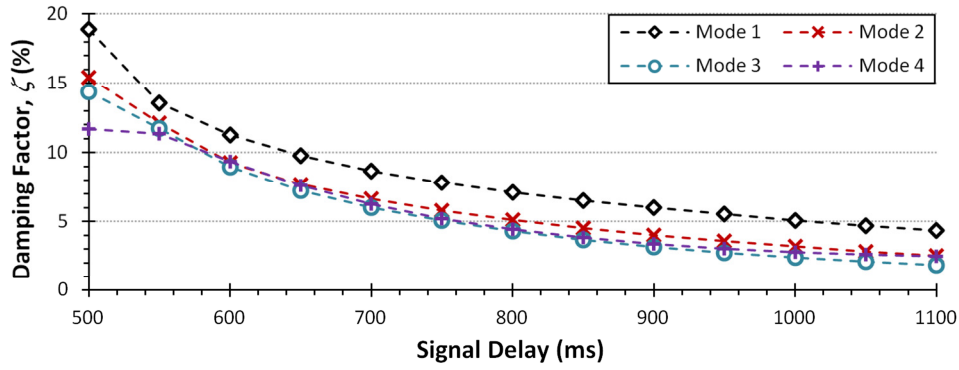


Figure 3-18: Deterioration in damping factors of low frequency modes with increasing wide area signal delays to the MLQG controller.

Table 3-6 details the maximum permissible delay tolerances beyond which the MLQG controller will exhibit a worse performance than the PSS-based POD controller. It is evident that these delays can increase to 766 ms (53.2% higher the 500 ms assumed) before the modal damping is lower than with the PSS-based controller receiving non-delayed local signals. Tolerances are also provided in Table 3-6 for the delay lengths at which the MLQG controller’s effect on modal damping becomes detrimental with respect to the system with no POD controller installed. In practical installations, if delays of this length were detected, the controller would be blocked. This would remain the case until the wide area signals arrived at the controller quickly enough to ensure a positive effect on the damping of the system oscillations.

Table 3-6: MLQG controller delay tolerances.

<i>MLQG damping worse than:</i>	<i>Signal Delay (ms)</i>			
	<i>Mode 1</i>	<i>Mode 2</i>	<i>Mode 3</i>	<i>Mode 4</i>
<i>PSS-based POD</i>	804	776	766	767
<i>No POD installed</i>	1058	887	809	771

### 3.3.6 Loss of Wide Area Signals

Complete signal loss should also be considered alongside increases in signal delays. This has been tested for the loss of up to two of the four inputs signals. All of the signals selected contain information about all the critical modes, therefore some redundancy is provided within them. The damping factors of the inter-area Modes 1–4 for the various cases are shown in Table 3-7.

The shaded cells represent the cases when the modal damping factor drops below that seen with the local PSS-based POD controller installed. It is evident, for example, that the loss of input signal  $y_3^{MLQG}$  always results in the damping factor of Mode 3 being

heavily reduced to less than 5%. This signal was initially selected for the high observability of Mode 3, therefore this result is not a surprise. Damping factors remain higher than with the PSS-based POD installed for the majority of cases when signals fail.

Table 3-7: Damping factors of inter-area modes with loss of input signals

Case	Signals Lost	Damping Factor, $\zeta$ (%)			
		Mode 1	Mode 2	Mode 3	Mode 4
–	None	18.90	15.43	14.34	11.70
1	$y_1^{MLQG}$	12.29	12.87	11.34	10.58
2	$y_2^{MLQG}$	12.78	5.90	9.83	9.95
3	$y_3^{MLQG}$	7.27	11.73	<b>4.62</b>	9.70
4	$y_4^{MLQG}$	13.87	9.87	13.26	5.28
5	$y_1^{MLQG}, y_2^{MLQG}$	9.60	<b>5.43</b>	8.87	9.38
6	$y_1^{MLQG}, y_3^{MLQG}$	<b>5.65</b>	11.32	<b>4.37</b>	9.30
7	$y_1^{MLQG}, y_4^{MLQG}$	10.88	9.10	10.87	5.25
8	$y_2^{MLQG}, y_3^{MLQG}$	<b>5.82</b>	5.65	<b>4.27</b>	8.82
9	$y_2^{MLQG}, y_4^{MLQG}$	11.37	<b>4.66</b>	9.64	5.03
10	$y_3^{MLQG}, y_4^{MLQG}$	7.54	9.26	<b>4.73</b>	5.01

Even with the unlikely loss of two input signals, the MLQG controller is often able to maintain high damping factors on some modes. Using Case 5 from Table 3-7 as an example, it can be seen that despite the fact that damping of Mode 2 has dropped to lower than PSS POD levels, the  $\zeta$  values of the remaining low frequency modes are still in the range of 8.87–9.60%. Due to this, the transient performance of the controller is highly competitive, with all infeeds settling within 16 s for the *base case* scenario when signals  $y_1$  and  $y_2$  are lost.

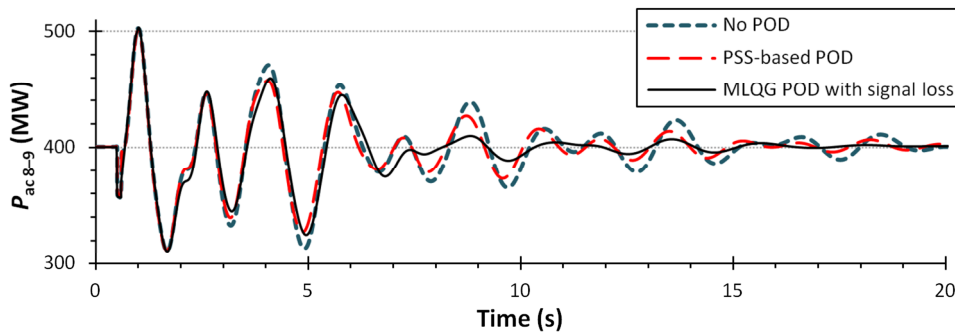


Figure 3-19: Active power injected at bus 9 from bus 8 for the *base case* operating point with the loss of input signals  $y_1$  and  $y_2$  for the MLQG controller.

The oscillations present on the tie-line 8–9 are shown in Figure 3-19. The robustness of the MLQG controller to the failure of wide area signals is clearly visible with the oscillations quickly damped.

### 3.3.7 Effect of Reactive Power Modulation

The VSC-HVDC POD studies presented have demonstrated the modulation of active power flow through parallel VSC-HVDC lines in order to stabilise post-disturbance system oscillations. One of the advantages of using VSC-HVDC over classic LCC-HVDC systems is the availability of *four-quadrant* operation of the converters, allowing the generation or consumption of reactive power at each converter station.

The MLQG design approach can be readily extended to include multiple controller outputs into a *Multiple-Input-Multiple-Output* (MIMO) structure. In addition to the single  $\Delta P_{dc}^{ref}$  signal,  $\Delta Q_{dc}^{ref}$  signals at each converter station were incorporated and the MLQG controller design was completed once more. The MLQG synthesis was performed using the same modal weightings, with the final controller reduced to 28<sup>th</sup> order as before.

Figure 3-20 shows the oscillations present on the tie-line 8–9 for the *base case* operating scenario, both with and without reactive power modulation included. It can be seen that the additional reactive power modulation provides very limited improvement in the system response: just 0.4 s reduction in settling time.

With little benefit added, it is unlikely that VSC-HVDC reactive power output would be modified for POD purposes, particularly when active power modulation is being exploited. It may be more advantageous to use fast reactive power modulation to ensure that bus voltages at the points of interconnection with the VSC-HVDC line are quickly stabilised during post-disturbance system oscillations.

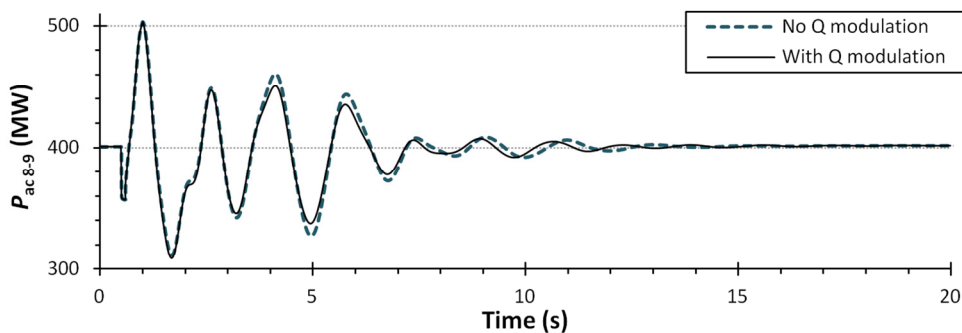


Figure 3-20: Active power injected at bus 9 from bus 8 for the *base case* operating point with and without reactive power modulation.

### 3.3.8 Limiting Modulation Capacity

The simulations presented, involving POD control, have assumed a generous allowance of  $\pm 100$  MW for power oscillation damping. This equates to 25% of the operating capacity for the nominal *base case* scenario discussed, and has been the same for both the PSS-based and MLQG controllers.

In a practical installation, the limit of available modulation capacity will be determined by the system operator. The benefits of reserving capacity (or temporarily using overload capacity) for modulating purposes following system disturbances must be compared with the costs of reducing the power transfer capability through the HVDC line. As the frequency of inter-area oscillations is usually below 1 Hz, this rate of change of current flow can easily be accommodated by the converters which are capable of responding to much faster dynamic changes. Furthermore, DC voltage violations should not present an issue provided the converter regulating DC voltage has been designed to be suitably fast.

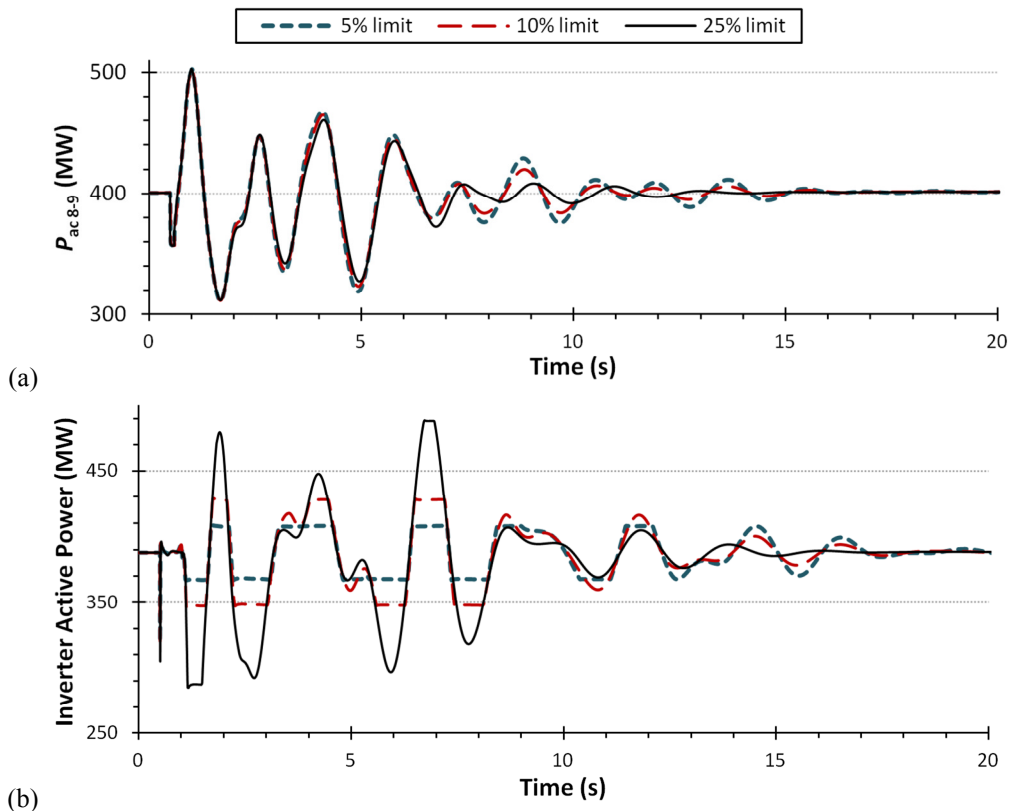


Figure 3-21: For the *base case* operating point with differing modulation capacity limits: (a) Active power injected at bus 9 from bus 8 and (b) Active power injected at bus 50 by VSC-HVDC inverter station.

The effect of limiting the modulation capacity (from the previously considered 25%) to 10% and 5% has also been investigated. Figure 3-21 shows the oscillations on the AC

tie-line 8–9 and the controlled variations in the power injected by the inverter station. These are presented for the *base case* operating scenario previously described with varying limits on modulation capacity. Only active power modulation is considered.

The settling time for this line increases slightly as less capacity is reserved for POD action. The same result is true if the PSS-based controller is used. In these studies, use of the PSS-based controller has been found to consistently result in faster settling of the oscillations in the line 18–50 than the MLQG controller – due to the local signal selection. However, all other inter-area AC ties stabilise quicker with the MLQG controller heavily restricted to just  $\pm 5\%$  modulation compared with the PSS-based controller operating with the full  $\pm 25\%$  modulation capacity.

For the MLQG controller, 10% modulation capacity results in key tie-line settling times increasing by 1.9–2.7 s (to a maximum of 14.1 s) and 5% modulation capacity results in settling times increasing by 2.7–4.7 s (to a maximum of 16.1 s) when compared with the initial 25% modulation capacity. These settling times are a vast improvement over the non-damped system, and demonstrate that VSC-HVDC based POD should be utilised even if the available modulation capacity is limited.

An estimate of the likely availability of this modulation capacity can be sourced from the publicly available data on the usage of the 1 GW Britned HVDC line between July and December 2011 [168]. This data is taken for an HVDC line which does not reserve capacity for modulation. However this line is an interconnection between two asynchronous power grids, and does not operate in parallel with AC transmission lines as considered in the test studies.

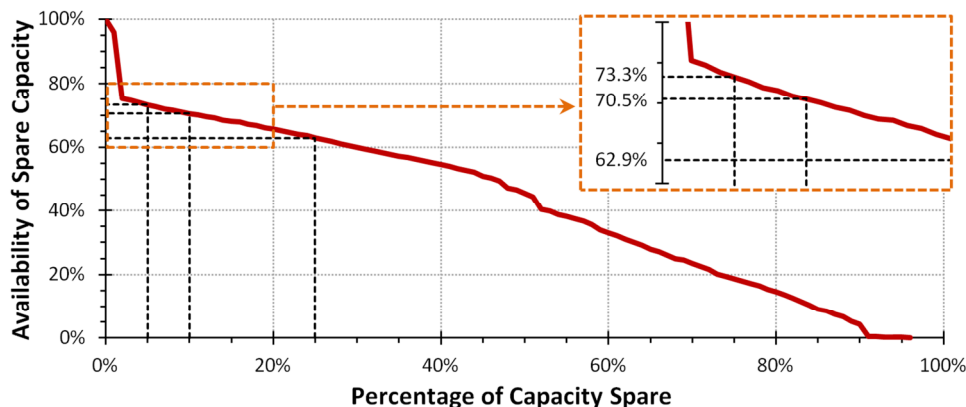


Figure 3-22: Availability of spare capacity on the Britned HVDC line.

The availability of spare capacity on this Britned line for the six month period is shown in Figure 3-22. It has been assumed that during periods when more than 95% of the rated capacity of 1000 MW is spare, the line is out of operation. These periods are not included in the brief availability analysis presented in Figure 3-22. From this plot it can be seen that 73.3% of the time at least 5% line capacity was spare, 70.5% of the time at least 10% line capacity was spare, and 62.9% of the time at least 25% line capacity was spare.

It is clear that there will be periods when large amounts of HVDC line capacity may be available for active power modulation for system stabilising purposes. At these times it would be advisable to fully exploit the damping capabilities of the HVDC line as higher modulation capacities result in faster system settling times. This may require flexible modulation limits dependent on system operating conditions.

### **3.4 POD Control with Multi-Terminal HVDC Grids**

A single VSC-HVDC line, implementing POD control, can have a significant effect on the stability of an AC power system. If this single line is extended to form a VSC-MTDC grid, then the POD control scheme can also be suitably extended to provide damping control at multiple points within the network. Within this research, this has been investigated and shown to be extremely effective at damping post-disturbance oscillations. Furthermore, with multiple control points, the total POD solution has greater redundancy and the loss (or blocking) of control signals can still result in vastly improved system stability.

#### **3.4.1 Modifications to the Test Network**

A modified version of the five-area test network is used for these studies. To support NYPS area power imports and represent a possible future network including a VSC-MTDC grid, the system connections between NYPS and areas G14 and G16 have been modified. The original network contained two inter-area ties between area G16 and NYPS; only the largest capacity line has been kept with the other removed completely. The original network also included one inter-area tie-line between area G14 and NYPS; this has also been removed. In place of these removed AC lines, a five-bus, six-line VSC-MTDC grid has been installed, as shown in Figure 3-23. Points of connection with the AC network have been selected as the same buses which previously fed inter-area ties. DC lines have been chosen to create a feasible meshed grid with reasonable

redundancy (it is capable of maintaining transfer between all converter stations with the loss of any DC line). The converter station at MTDC node 1 is the DC *slack* bus. Data and controller settings for the VSC-MTDC grid are provided in Appendix A.

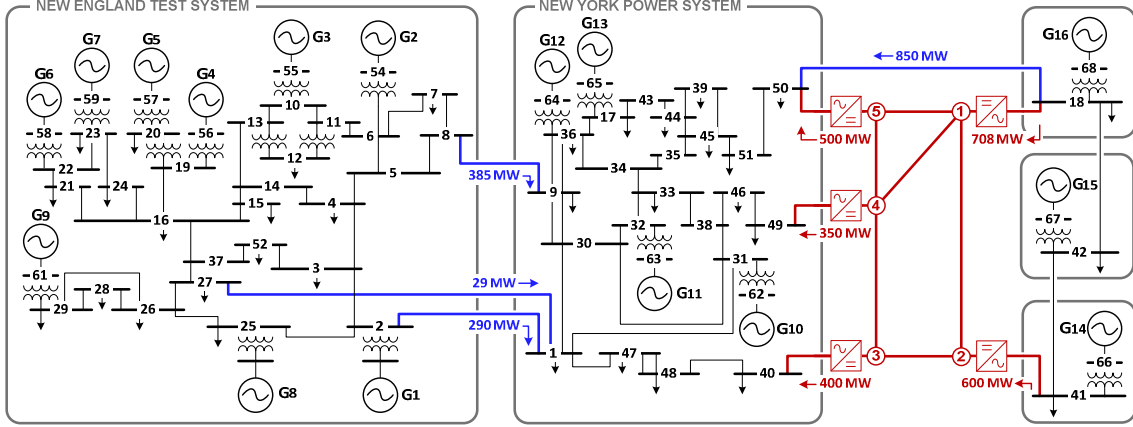


Figure 3-23: Five-area test network with VSC-MTDC grid installed.

### 3.4.2 WAMS-Based POD Control

The test network continues to display four inter-area modes which require additional damping, although frequencies and damping factors have changed slightly from the previous study case due to the modifications made. The MLQG controller design was previously extended to a MIMO structure to include modulation of reactive power injection at converter stations (see Section 3.3.7). It can also be readily extended to control multiple  $\Delta P_{dc}^{ref}$  signals for use with a VSC-MTDC grid POD solution.

#### 3.4.2.1 MLQG Controller Synthesis Details

The mixed AC/DC linearised power system model is reduced from 221<sup>st</sup> order to 45<sup>th</sup> order whilst preserving the system response in the frequency range of interest (tested by interrogation of the system singular values). Controller inputs are selected by modal observability as the same AC power flows previously used in Section 3.3:

$$y_1^{MLQG} : P_{ac, 45-51}, y_2^{MLQG} : P_{ac, 68-18}, y_3^{MLQG} : P_{ac, 65-17}, \text{ and } y_4^{MLQG} : P_{ac, 67-42}.$$

These four wide area signals are subject to delays of 350 ms [20-23]. Controller output signals  $(u_1^{MLQG}, \dots, u_4^{MLQG} : \Delta P_{dc, 2}^{ref}, \dots, \Delta P_{dc, 5}^{ref})$  are available at MTDC nodes 2–5 (with the exception of the slack node), and also subject to 350 ms transmission delays. The total considered controller delay is therefore 700 ms.

Table 3-8: Inter-area mode details for the five-area network with embedded VSC-MTDC grid with and without an MLQG POD controller in place.

Mode	No POD		MLQG POD	
	Frequency (Hz)	Damping Factor (%)	Frequency (Hz)	Damping Factor (%)
Mode 1	0.265	4.09	0.266	25.44
Mode 2	0.457	4.32	0.486	24.38
Mode 3	0.629	4.28	0.603	24.13
Mode 3	0.782	4.82	0.777	25.19

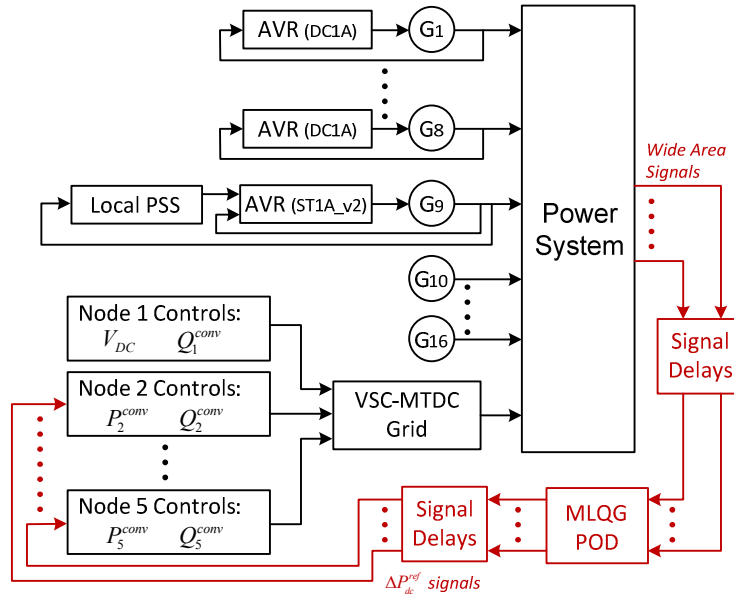


Figure 3-24: Control overview for the five-area test network including a VSC-MTDC grid with supplementary MLQG POD control.

The reduced plant model including delays (61<sup>st</sup> order) is used during the controller design process. Fine tuning of the modal weightings matrix  $\mathbf{Q}_M$  allows precise modal damping factors to be achieved. All four critical inter-area modes achieve damping factors of 25%, whilst leaving all other modes unaffected. The final controller structure is then reduced further (to 45<sup>th</sup> order) to lessen the online computational burden of the controller whilst maintaining the improved critical mode damping. The final low frequency modal details (with the reduced order controller and full order plant model) are shown in Table 3-8. Reactive power injection at each MTDC connection point is maintained at zero throughout the study. The full system control overview is presented in Figure 3-24 including the POD controller.

### 3.4.3 Large Disturbance Analysis

The system is subjected to a 100 ms self-clearing three-phase fault at bus 43 in the middle of the NYPS area with post disturbance oscillations easily observed. VSC-

MTDC converter station active power modulation is limited to  $\pm 100$  MW at nodes 2–5 controlling active power flow.

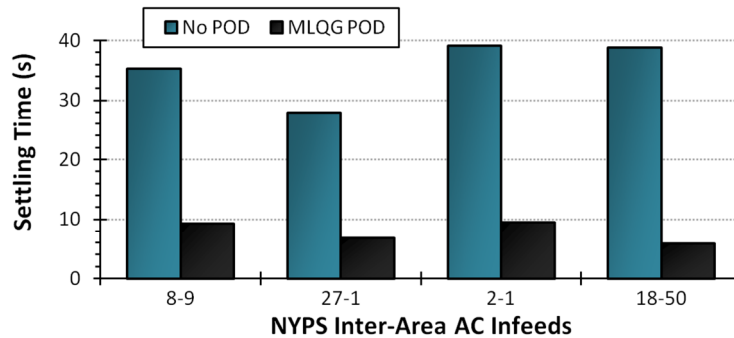


Figure 3-25: Settling times for the NYPS inter-area AC infeeds with MLQG POD control through the VSC-MTDC grid.

The settling times are recorded from the point of fault clearance to the time at which the power deviation is within  $\pm 1\%$  of the steady state value (or  $\pm 1$  MW, whichever is greatest). Figure 3-25 shows these settling times for the active power flows through the inter-area AC tie-lines. It is clearly shown that system performance without the POD controller installed is unsatisfactory with oscillations lasting 40 s. In stark contrast, with the MLQG POD controller in place all AC ties are stabilised within just 10 s. These settling times are faster than the case when a single VSC-HVDC line is used for POD purposes (see Section 3.3.4). It is evident that utilising multiple points of modulated power injection leads to a greater improvement in system stability.

The transient plots in Figure 3-26 display the response of the system. Figure 3-26(a) shows the active power flow through the inter-area tie-line 8–9. This AC line is distant from the VSC-MTDC grid but is still stabilised rapidly following the disturbance, demonstrating the ability of the MTDC POD solution to stabilise the entire network.

The stabilising modulation of the active power injected into the NYPS area of the AC test network is shown in Figure 3-26(b). It can be seen that relatively little modulation is required in order to significantly enhance the stability of the network – much less than the limits of  $\pm 100$  MW. The effect of the time delays associated with the control input and output signals can also be seen. The VSC-MTDC converter controls recover quickly following the large disturbance and return to their steady state operating conditions. It is not until the signal delays have passed (700 ms after the start of the disturbance) that the active power modulation begins.

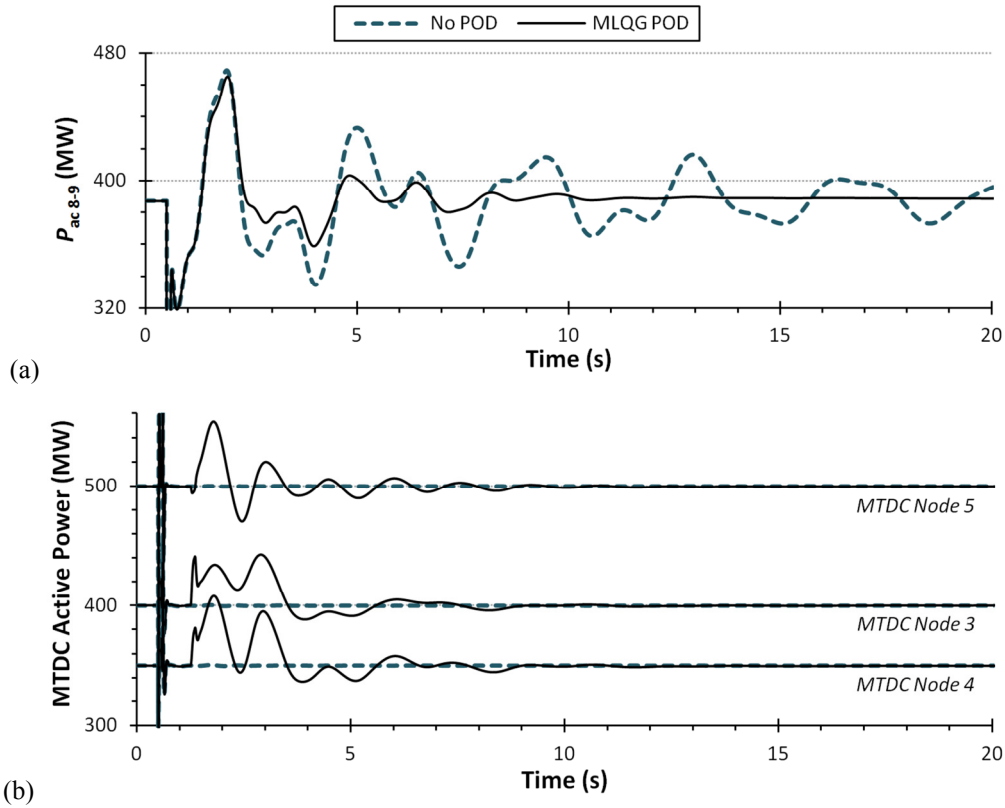


Figure 3-26: System stabilisation demonstrated by (a) Active power injected at bus 9 from bus 8 and (b) Active power injected into the NYPS area from the MTDC grid at nodes 3–5.

The VSC-MTDC grid has been demonstrated to provide an effective POD solution in conjunction with the MLQG controller. WAMS-based signals combined with the MLQG controlled modulation of active power injection at multiple MTDC converter nodes leads to a more stable power system.

### 3.4.4 Blocking Modulating Signals

VSC-MTDC grids may have points of connection with potentially weak AC grids. For example, if a point of connection is to a wind farm, there may be times when the generation conditions are not suitable to permit power modulation and allowing such action would risk the stability of the connected AC grid. Alternatively, the VSC-MTDC grid may be a major supply point for a weak section of an AC network and there may be times when it would be detrimental to the AC system to allow active power modulation at the point of injection.

For these fault instances, the converter station may wish to temporarily block the power modulation signal and recover to steady state active power injection as quickly as possible following the disturbance. These blocking signals have been applied to each system input (each  $\Delta P_{dc}^{ref}$  signal) one at a time in order to establish how well the system

recovers and if such signals may be permissible or whether full controller redesign would be required for these cases.

The settling times for the NYPS area AC infeeds with the various controller signals blocked are detailed in Table 3-9. Increases in settling times range from 0.1–6.8 s dependent on the tie-line and the blocked signal, however in all cases infeeds are settled in less than 13 s. This is a vast improvement over the situation with no POD controller installed where it takes up to 40 s for the power oscillations within the AC ties to stop.

Table 3-9: Effect of blocking MLQG controller output signals on NYPS AC infeed settling times.

AC Tie-Line	Settling times with blocked MLQG controller outputs (s)				
	No blocking	$u_1^{MLQG}$ blocked	$u_2^{MLQG}$ blocked	$u_3^{MLQG}$ blocked	$u_4^{MLQG}$ blocked
8–9	9.32	12.61	12.63	12.56	9.43
27–1	6.80	7.92	9.17	9.23	9.23
2–1	9.45	12.77	12.88	12.74	12.60
18–50	5.90	8.97	12.66	12.45	8.58

It has been shown that such a WAMS-based controller with multiple points of control within a large meshed VSC-MTDC grid can provide significant oscillation damping improvement to the AC network. This additional study suggests that this is may be true in circumstances when specific points of connection block the controller signals, or if such signals are lost. This highlights the effectiveness of using VSC-MTDC grids for POD purposes. The large number of AC connection points allows rapid damping and also provides redundancy in terms of the number of nodes where power modulation is required to enhance system stability.

### 3.5 Summary

An extensive analysis into the effects that HVDC systems can have on the small-disturbance stability of power systems has been completed. This has involved investigations using a number of case studies consisting of a single HVDC line installed in a small two-area network, a single VSC-HVDC line installed within a large five-area network, and a five-node VSC-MTDC grid embedded within a large five-area network. It has been clearly demonstrated that there exists a large potential to exploit these new lines, not only for power transfer but also for stabilising action within power systems.

The initial studies presented have shown that in installations where supplementary POD control is not considered, the operating conditions, connection points, and technology

type of the HVDC line can all affect the damping of oscillatory modes. It was seen that LCC-HVDC systems introduce negative damping with respect to equivalent VSC-HVDC lines. These details may require careful analysis and real-time monitoring, especially if critical modes are near the stability margin prior to the addition of the HVDC line.

Where additional POD control is to be used with VSC-HVDC systems, it has been shown that use of WAMS-based control and a multivariable control structure can provide improved performance over more traditional PSS-based designs using local input signals. This has been demonstrated first using a small two-area network where indications of the improved robustness to changes in operating conditions were seen. A further comparative investigation into the PSS-based design and the MLQG structure using the large five-area network confirmed the initial findings. Furthermore, the MLQG controller is resilient to increases in the delays on the wide area signals it receives, and even complete signal loss. Modulation of reactive power injection was shown to offer little benefit with respect to the damping of power oscillations and may be more usefully applied to the stabilisation of voltages during periods of post-disturbance system oscillation.

A study into the effects of limiting the modulation capacity available for POD action has shown that system stabilisation is quickest when large capacity is available. Reduction from  $\pm 25\%$  (of operational capacity) to just  $\pm 5\%$  resulted in an increase in system settling time from 12 s to 16 s. This is however an improvement compared to the system with no POD controller installed, where post-disturbance stabilisation would take longer than 30 s. A brief availability study based on the Britned HVDC line has shown that there is relatively high availability of spare operational capacity which could be used for POD purposes, without the need to specifically reserve it (potentially at great expense). A flexible limit on modulation capacity dependent on operating conditions would enable greater exploitation of the damping capabilities of the HVDC systems.

Finally, an examination of POD with VSC-MTDC grids has been completed. It has been demonstrated that the MLQG controller makes effective use of the multiple points of controlled power injection available to provide an excellent method of stabilising system oscillations. The inherent redundancy within the VSC-MTDC POD solution is such that single controller output signals can be blocked without a serious detrimental

effect on system performance. This may be desirable to specific converter stations connected to potentially vulnerable sections of AC networks which may momentarily require a return to steady state operation (i.e., constant power flow) as soon as possible following disturbances.

The following chapter will build on these findings in order to develop a methodology which can be utilised to assess the robustness of supplementary damping controllers. It has been shown that a wide range of factors should be considered, and the transient analyses performed at various operating conditions have gone some way to demonstrate the improved robustness of the WAMS-based MLQG controller. However, the studies completed do not fully represent the uncertain and variable operating conditions expected of future power systems, and a more thorough assessment is required.

# 4 Assessing the Robustness of Controllers

---

The uncertainties surrounding the operation of future power networks are wide ranging and increasing. They encompass not only load demand and generation capacity across a network but also the availability of generating units as the penetration of wind power increases. The previous chapter demonstrated the positive effects that supplementary POD control using VSC-HVDC systems can have on the stability of power networks. This was particularly true when the WAMS-based MLQG controller was implemented. This is one of many wide area controller designs which can be used to improve system stability. With variations in generation size and even location expected in the future, the robustness of POD controllers is of vital importance.

Many controller structures claim inherent mathematical robustness, for example  $H_\infty$  approaches. However, these synthesis techniques must first accurately model the uncertainties to ensure the practical robustness of the designed controller. If these uncertainties are poorly formalised then the controller's practical efficacy may not match its intended mathematical performance. An LQG controller synthesis approach,

on the other hand, cannot intrinsically guarantee any robustness properties (as demonstrated in [169]), although robust performance can be achieved. For all controller designs it is clear that the performance and stability of the final structure must be thoroughly assessed in order to establish its true robustness.

Typically, tests for robustness are limited to a few reasonable and expected operating conditions. Although these *close-to-nominal* conditions will represent the vast majority of operating points experienced in practice, it is the rare *far-from-nominal* conditions, often incorporating  $n-1$  or  $n-2$  situations which invariably lead to the worst operating scenarios and greatest chance of system maloperation.

This chapter will present the fourth original contribution of this thesis: a methodology for the robust probabilistic evaluation of supplementary damping controller performance within power systems. The methodology considers not only the statistical uncertainty in system operating conditions, but also outages of key equipment (including generators, lines, and VSC-HVDC lines). Techniques to reduce the number of modelled uncertainties are used in order to simplify the problem formulation, and classification tools are exploited to improve accuracy during the assessment. A demonstrative example is presented on the five-area power system into which two VSC-HVDC lines are embedded.

The method enables the assessment of the risk indices, most readily the risk of system instability for a given outage contingency. These measures can be used in order to assess the robustness of the controller and assess whether it meets the requirements for practical implementation within a power system. Furthermore, the wealth of data collected facilitates the classification of operational regions in which controller performance is unsatisfactory. These regions can then be avoided through correct generator dispatch, especially when system plant outages are planned (for example, for maintenance).

#### **4.1 Robust Probabilistic Evaluation of Controller Performance**

Damping controllers are typically designed for a specified system operating point and, unless adaptive, the controller design will remain fixed. However, the power network will rarely operate with these assumed conditions. Many factors including system maintenance, generator availability, load variation and economics will contribute towards the true operating point. By generating a diverse range of system operating

points in a probabilistic manner (including outage contingency situations), a more thorough evaluation of a controller's performance can be established.

The volume of data collected during such an evaluation will allow a power system engineer to identify the situations when controller performance is unacceptable and to develop appropriate mitigation techniques (discussed in detail in Section 4.4.2). The proposed methodology could further lead to operational guidance tools for system control engineers, flagging up the possibility of undesirable system behaviour and suggesting effective means of improvement.

#### **4.1.1 Establishing the Probabilistic Operating Conditions**

To start with, the probabilistic distribution of system operating points must be defined. In this study a normal distribution of power generation and load demand around the nominal operating point is chosen to represent the expected variation in system operating conditions. In practice any other distributions including conditional loading, optimal power flow solutions, historical data, or forecast data could be used if known.

Feasible operating points with converged load flows and stable open loop eigenvalues are selected from the given parameter distributions. The controller performance at each operating point is then assessed using small-disturbance analysis in order to analyse the controller robustness across wide ranging conditions.

Practical power systems contain many sources of variability with respect to operating conditions, including generating units, loads, HVDC lines and FACTS devices. When investigating the effects of these uncertainties on a controller's performance, it is desirable to reduce the number of uncertainties considered. This will allow the studies to be more simply and easily defined, especially if uncertain parameters are subject to more complex distributions or constraints. Furthermore, it will ease the analysis of the results. Having identified the parameters most critical in determining the controller performance, important correlations between parameters and performance can be readily identified. This will, in turn, allow simple development of operational constraints if desired, so poor POD controller performance can be avoided.

##### **4.1.1.1 Eigenvalue Sensitivity to System Uncertainties**

Within this research, eigenvalue sensitivity analysis is used to rank the uncertain system parameters based on their importance to the behaviour of the critical system modes. The

effect that each uncertain parameter,  $\gamma_j \in \Gamma$ , has on each critical oscillatory mode,  $\lambda_i = \sigma_i \pm j\omega_i$ , is established using the rank given in (4.1) [170].

$$\text{Rank} = \left| \frac{\partial \lambda_i}{\partial \gamma_j} \right| \left| \frac{\gamma_j}{\lambda_i} \right| \left| \frac{\sigma_{\gamma_j}}{\mu_{\gamma_j}} \right| \quad (4.1)$$

In (4.1),  $\mu_{\gamma_j}$  and  $\sigma_{\gamma_j}$  are the mean and standard deviation of the uncertain parameter  $\gamma_j$ . Note that care should be taken to distinguish between the eigenvalue real part  $\sigma$  and the uncertain parameter standard deviation  $\sigma_\gamma$ . As the main measure of performance with respect to the critical eigenvalue is its damping, the rank is calculated using only the real part  $\sigma_i$  substituted for  $\lambda_i$  in (4.1). Within this research, ranks are evaluated using a 1% deviation in  $\gamma_j$ . These rank values are then normalised for each critical mode, before being summed for each parameter.

These normalised-summed rank values can be used to identify which critical parameters should be modelled when determining the controller's performance. For practical applications, the final decision on the number of modelled variables required is made at the discretion of the power system engineer.

#### 4.1.2 Modelling Contingencies

It is important to include system outage contingencies when completing a robustness assessment for a POD controller. These situations may represent the points at which the network is operating at its limits and guaranteed satisfactory damping performance is required. These contingencies could include (but are not limited to) generator outages, line outages, HVDC line outages, and the loss of controller signals.

As this procedure would most likely be performed during the offline design stages of a system controller, the number of contingencies considered should be set as high as is permissible based on time and computational constraints.

#### 4.1.3 Identification of Critical Oscillatory Modes

The performance of the damping controllers is assessed through small disturbance analysis. Depending on the controller structure in use, some complexity may exist in accurately identifying the electromechanical modes of interest – particularly if their locations vary widely as the system conditions change. Classification tools can be used

to aid the accurate identification of the critical system modes of interest based on system state participation factors. Within this research, a Naïve Bayes (NB) classifier [171] was used to identify critical system modes for later evaluation.

An NB classifier will return the probability that a feature set belongs to a given group based on training data provided. The feature set consists of the eigenvalue real and imaginary parts, as well as participation factors for all system states. Training data is created through user-classification of data sets including varying operating points across all contingencies. From the probabilities returned, the most likely eigenvalue for each critical mode is selected. If any mode has zero probability of existing in the shortlisted set, the classification is deemed to have failed and a new operating point is selected.

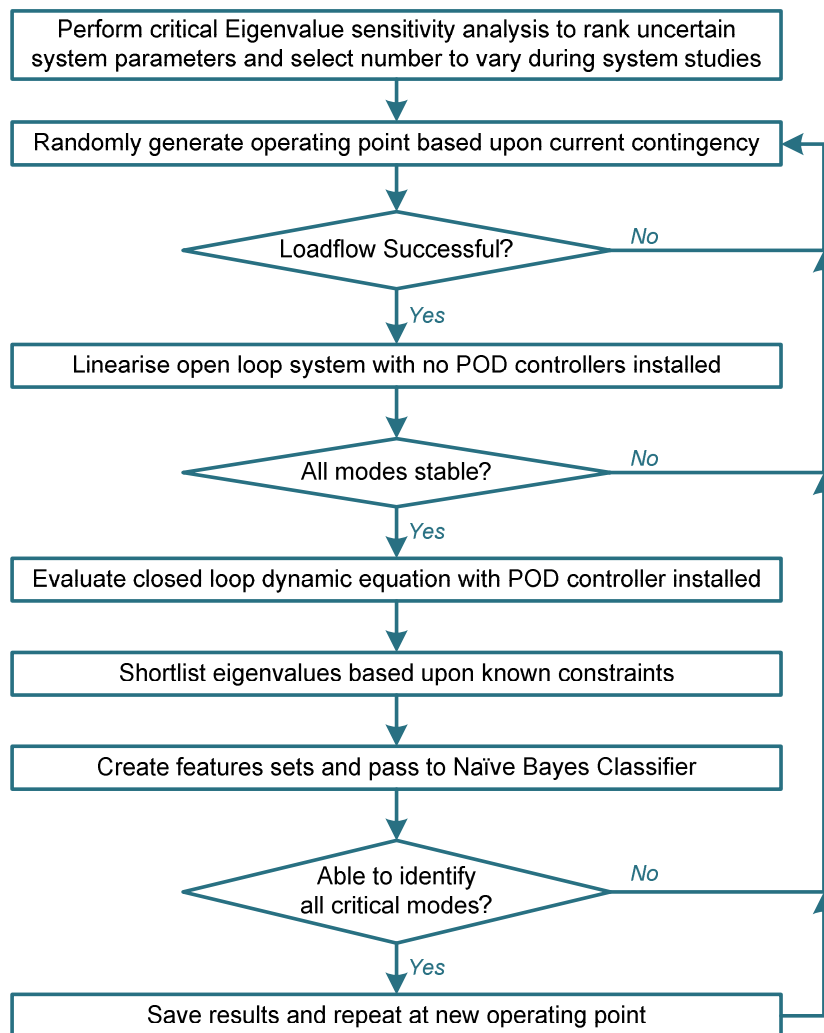


Figure 4-1: Flowchart of complete robust evaluation procedure.

#### 4.1.3.1 Overview of Methodology

A summary flowchart of the complete robust evaluation procedure is presented in Figure 4-1. This process has been used to produce the results presented in this chapter.

## 4.2 Test System Details

The robustness assessment methodology is most clearly outlined through application on a test system, wherein the requirements when applying the method can be thoroughly detailed. The results obtained will be discussed with relation to how this methodology can allow more secure operation of future networks.

### 4.2.1 Modifications to the Test Network

This study is performed using a modified version of the large five-area power system. To represent future reinforcement of the transmission corridors, VSC-HVDC lines are installed in parallel with the two most heavily loaded inter-area tie lines: (1) line 18–50 and (2) line 41–40. VSC-HVDC nominal operating capacities are set as 400 MW and 300 MW respectively). Locations of the VSC-HVDC lines and resulting inter-area active power flows into the NYPS area are shown in Figure 4-2. Data and controller settings for the two VSC-HVDC lines are provided in Appendix A.

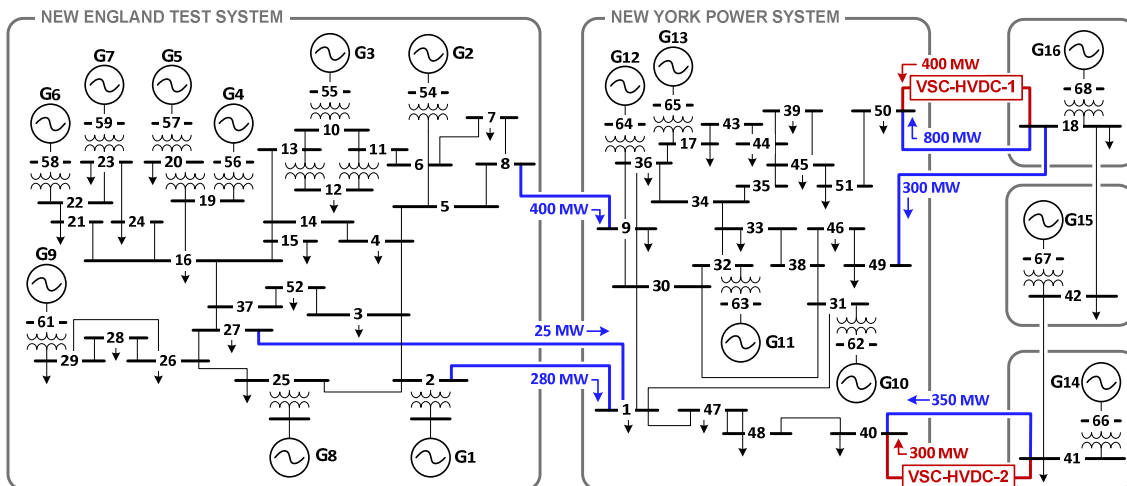


Figure 4-2: Five-area test network including two additional VSC-HVDC lines.

### 4.2.2 WAMS-Based POD Control

The network, including the stated modifications, continues to display four poorly damped inter-area oscillatory modes with  $\zeta$  values below 5%. Supplementary POD control acting through active power modulation at both VSC-HVDC lines is selected as the means to improve modal damping. The WAMS-based MLQG controller structure is utilised within this study. It would, however, be possible to test any POD controller design using the methodology presented as the approach is not dependent on the type of POD controller used.

The MLQG controller structure has been applied in both centralised and decentralised forms. This approach not only provides a point of comparison for the robust evaluation of controller performance, but also demonstrates plausible future control methodologies.

#### 4.2.2.1 MLQG Controller Synthesis Details

The full open loop plant model is of 193<sup>rd</sup> order. This is reduced to 30<sup>th</sup> order whilst preserving the eigenvalue locations and frequency response in the frequency-range of interest. The reduced plant model including delays on appropriate signals is then used during the control design process. The final control design is reduced further to lessen the online computational burden of the controller whilst still maintaining the improved critical mode damping.

Controller inputs are selected using a modal observability study and are the same AC power flows used in previous example case studies on the five-area test network:

$$y_1^{MLQG} : P_{ac, 45-51}, \quad y_2^{MLQG} : P_{ac, 68-18}, \quad y_3^{MLQG} : P_{ac, 65-17}, \quad \text{and} \quad y_4^{MLQG} : P_{ac, 67-42}.$$

Both the centralised and the decentralised controllers receive all four signals in order to obtain maximum information about the critical system modes. Practically, once a measurement device has been installed at a location, it is expected that transmission of this wide-area signal through pre-existing communication links will be comparatively inexpensive.

#### 4.2.2.2 Centralised MLQG POD Control

With a centralised scheme, only one MLQG controller is designed. This MIMO controller takes the inputs specified from the power system and sends  $\Delta P_{dc}^{ref}$  control signals to both VSC-HVDC lines. In practical terms, this could represent a situation in which both VSC-HVDC lines are owned and operated by one organisation wishing to develop POD through coordinated active power modulation. This approach can be readily extended to any number of HVDC lines or other points of control such as FACTS devices if they are also available for a coordinated POD approach.

Remote input signals are sent through pre-existing communications systems with constant transmission delays of 375 ms [20-23]. The MLQG controller is located at one VSC-HVDC converter station (in this study a converter station of VSC-HVDC-1 is selected). Output controller signal delays are therefore only experienced for the  $\Delta P_{dc}^{ref}$  signal sent to the other line. This delay is again constant at 375 ms.

### 4.2.2.3 Decentralised MLQG POD Control

A decentralised scheme involves the design of two individual MLQG controllers. These *Multiple-Input-Single-Output* (MISO) controllers will both receive the delayed wide area signals from the network and will locally control active power modulation at the VSC-HVDC line where they are installed. As the controllers are individually installed at each VSC-HVDC line, no controller output delays are considered. The controller inputs still experience constant transmission delays of 375 ms.

For practical systems, this decentralised methodology could be representative of a situation in which the VSC-HVDC lines are operated by two different organisations, both wishing to coordinate their POD control but also wanting to retain ownership and maintenance of controllers acting on their equipment. In this study the controllers are to be designed sequentially (first at VSC-HVDC-1, then at VSC-HVDC-2), possibly representing a staged implementation process.

Unlike the centralised structure, mode allocation is required in this case as the controllers should not act on the same inter-area modes. VSC-HVDC-1, installed between the NYPS and G16 areas, is allocated the modes which cause these two regions to oscillate against each other – Modes 1 and 3 (see Table 3-4). The second line, VSC-HVDC-2, is allocated the remaining Modes 2 and 4. A modal controllability assessment for the  $\Delta P_{dc}^{ref}$  signals at each line supports these mode allocations.

### 4.2.2.4 Controller Tuning and Small-Disturbance Analysis

The modal weighting matrix  $\mathbf{Q}_M$  is tuned during the design process for both the centralised and decentralised controllers to achieve target damping of 20% for each inter-area mode. The designed controllers are then reduced in order whilst preserving the closed loop damping of the critical inter-area modes. The final centralised controller is of 35<sup>th</sup> order. The decentralised controllers are of 29<sup>th</sup> and 53<sup>rd</sup> order at VSC-HVDC-1 and VSC-HVDC-2 respectively.

The final low frequency mode details (with reduced order controllers acting on the full order plant model) are shown in Table 4-1. The full system control overview is presented in Figure 4-3 and includes both the centralised and decentralised POD control schemes.

Table 4-1: Inter-area mode details for the five-area network with two embedded VSC-HVDC lines with various POD control schemes.

Mode	No POD		Centralised MLQG POD		Decentralised MLQG POD	
	Frequency (Hz)	Damping Factor (%)	Frequency (Hz)	Damping Factor (%)	Frequency (Hz)	Damping Factor (%)
Mode 1	0.409	4.35	0.422	19.49	0.417	19.58
Mode 2	0.519	4.07	0.537	19.43	0.561	20.39
Mode 3	0.631	4.21	0.613	17.89	0.629	17.38
Mode 3	0.796	4.86	0.783	19.83	0.782	19.03

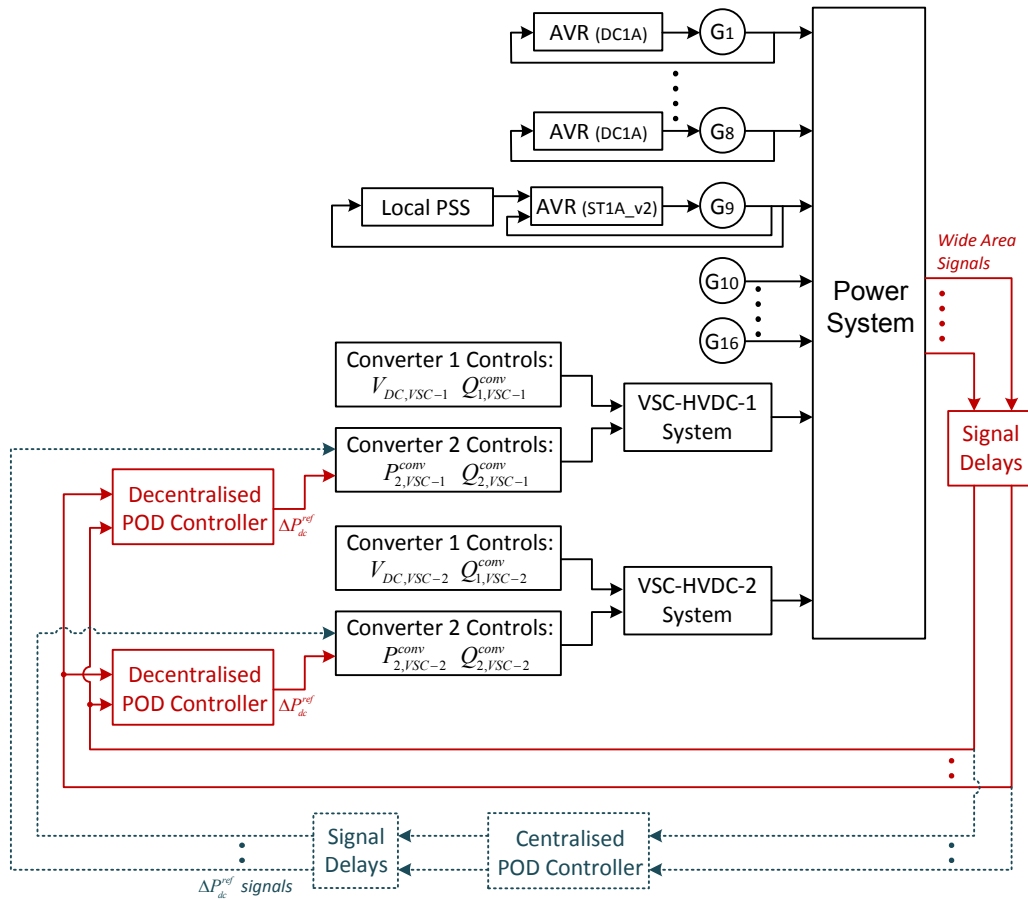


Figure 4-3: Control overview for the five-area network including two VSC-HVDC lines, showing both centralised and decentralised POD control schemes.

#### 4.2.2.5 Nominal Controller Performance

Both of the designed control schemes are tested at the nominal operating point to ensure that large-disturbance studies confirm the level of oscillation damping suggested by the small-disturbance analysis. The transient performance of the designed controllers following a large disturbance is demonstrated by simulating a 100 ms self-clearing three-phase fault at bus 38 at a time of 0.5 s. The system is at the nominal operating point at which the controllers were designed with all lines in service. VSC-HVDC active power modulation is limited to  $\pm 100$  MW.

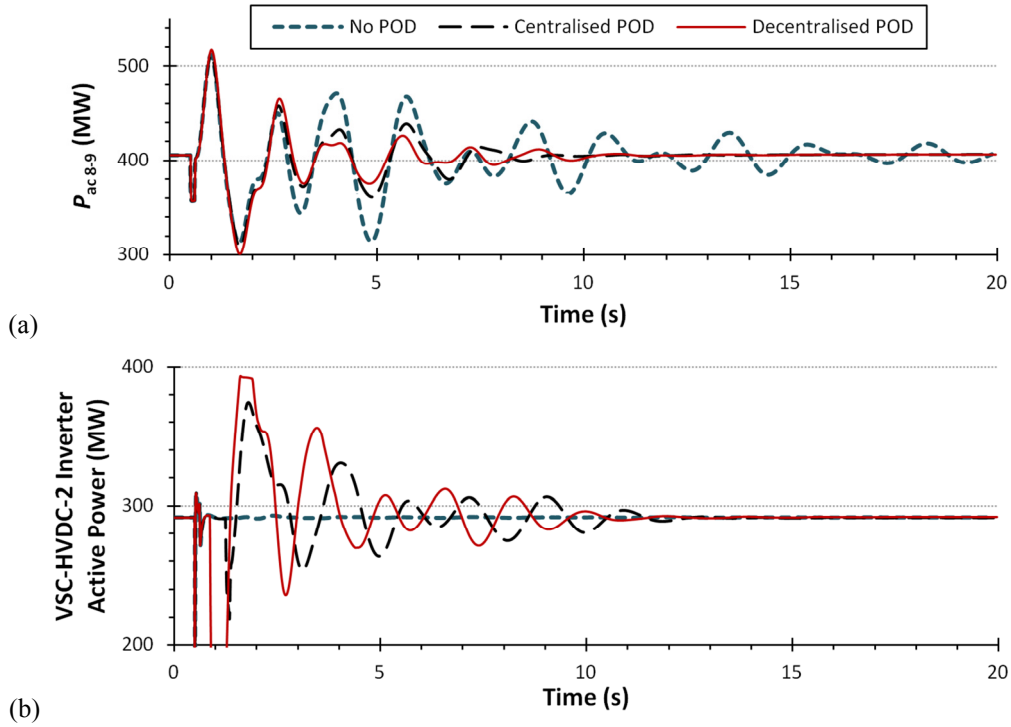


Figure 4-4: For differing POD schemes: (a) Active power injected at bus 9 from bus 8 and (b) Active power injected at bus 40 by the VSC-HVDC-2 converter station.

Figure 4-4 shows the system response and demonstrates the improved damping of the active power flow through the inter-area tie-line 8–9. It can be seen that with both the centralised and decentralised POD the system is stabilised within 10 s, demonstrating the damping suggested by the small-disturbance analysis. The active power modulation through VSC-HVDC-2 is also shown. The delays in modulation caused by the signal transmission delays can clearly be seen and are more severe for the centralised case, when VSC-HVDC-2 experiences both input and output signal delays.

It is clear that the controllers perform well for their designed operating conditions and that the transient simulations confirm the small-disturbance analysis results. The robustness of the controllers can be assessed using the proposed methodology.

### 4.3 Evaluation of Controller Robustness

Within this section the details relating to the application of the robustness evaluation methodology on the outlined test system are presented.

#### 4.3.1 Establishing the Probabilistic Operating Conditions

The given nominal operating point (as described in Appendix A) is assumed to represent 80% of maximum system loading, with full loading representing a  $+3\sigma_\gamma$  increase from the mean nominal values  $\mu_\gamma$ . Generators are represented as *PV* (active

*power-voltage*) buses during load flow with non-varying voltage and normally distributed active power output as described. Loads are also normally distributed and assumed to have constant power factor equal to the nominal power factor.

Both VSC-HVDC lines are considered to have unidirectional power flow with operating capacity varying uniformly between 200 and 500 MW at VSC-HVDC-1 and between 150 and 400 MW at VSC-HVDC-2 (in 50 MW steps).

### 4.3.2 Uncertain Parameter Reduction

The test system consists of fifteen generators (excluding the slack G13), two VSC-HVDC lines and thirty-four loads – in total a set of fifty-one uncertain network variables,  $\Gamma$ . The sensitivity analysis was completed using (4.1). A numerical example of this rank calculation is provided in Appendix B. The resulting normalised rank values suggested that a reduced set of 16 variables,  $\Gamma^{red}$ , may represent the system variation adequately. This ranking analysis was completed for both the centralised and decentralised controllers in place with final values included in Table B-1 and Table B-2 in Appendix B. Although the individual ranked orders contain slight differences, the top sixteen parameters are the same for both controllers.

The validity of this choice is demonstrated by assessing the error introduced into the distributions of the inter-area modes. Sets of 500 randomly selected operating points are created, with increasing numbers of modelled uncertainties. With the centralised controller installed, the distributions of eigenvalue real parts  $\sigma_i$  for each critical mode are calculated and then subtracted from the distributions created with the full set  $\Gamma$  of uncertain parameters modelled. These residual values are plotted for each low frequency mode in Figure 4-5 against the number of uncertain parameters modelled.

With the inclusion of sixteen variables (highlighted in black in Figure 4-5 below), the residual values for each mode can be seen to have reached the level of background error associated with the Monte Carlo process.

It is not statistically possible to show that two distributions are the same. It is possible, however, to show that they are not sufficiently different to suggest that the two distributions are distinct. A Kolmogorov-Smirnov two sample test [172] can be used to test whether distributions are different by rejecting the null hypothesis that the sample values are consistent with being drawn from a single distribution. This test is completed

on the distributions of  $\sigma_i$  with the reduced set  $\Gamma^{red}$  and the full set  $\Gamma$  of uncertain parameters modelled. For each mode of interest, the result is the same: the null hypothesis cannot be rejected, and the values are consistent with being from the same distribution. Therefore, the choice of sixteen parameters is fully justified.

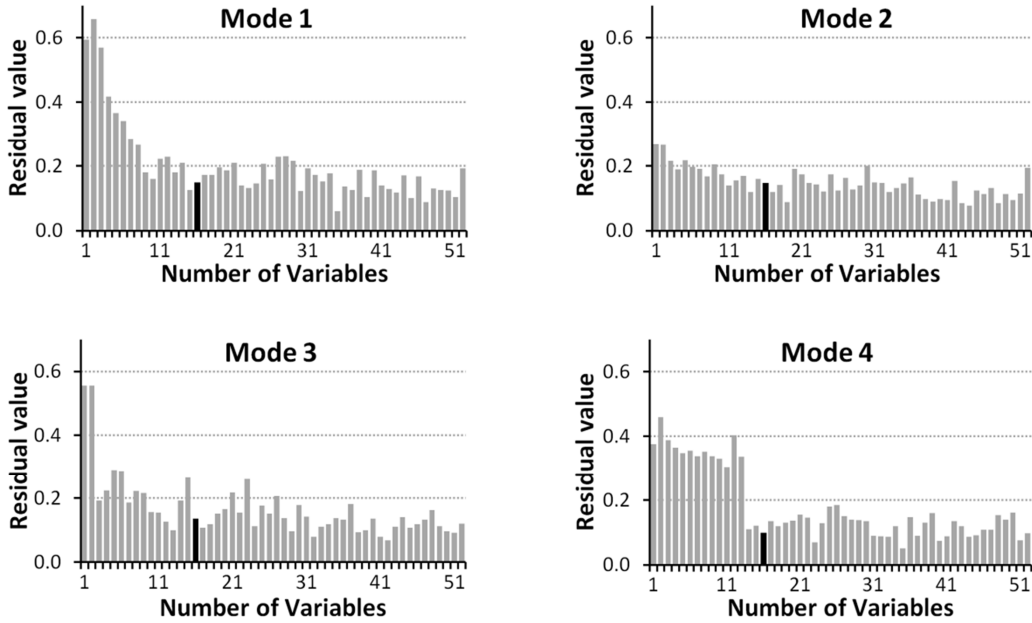


Figure 4-5: Residual values between the distributions of  $\sigma_i$  with increasing numbers of uncertain system parameters, and all uncertain parameters, modelled with the centralised controller in place. Highlighted bars represent 16 uncertain parameters.

### 4.3.3 Modelling Contingencies

The reduced set of uncertain parameters  $\Gamma^{red}$  consists of eleven generators (G2–9, G14–16), four loads (at buses 18, 20, 41 and 42), and the VSC-HVDC-2 line between buses 41 and 40. In addition to modelling these parameters with distributions as previously discussed, several  $n-1$  outage contingencies representing equipment failures are also considered.

Generators G1–12 outage contingencies are modelled by setting the power output to zero. Slack G13 experiences no outage condition. Outages of generators representing external areas, G14–16, are set accordingly at 50% their selected operating point to represent a limit in power available for import into NYPS. The VSC-HVDC lines each experience an outage by setting the power transfer to zero. During such situations, there is no POD facility at the VSC-HVDC lines.

Line outages are considered on four major NYPS inter-area AC ties: (i) line 8–9, (ii) line 2–1, (iii) line 40–41, and (iv) line 18–49. An outage on the major infeed line 18–50 is not considered as it results in an unsuccessful load flow solution.

Outages of wide area signals are not investigated within this study, although they could be included if required. It should be noted that the worst case scenario (in which all controller input signals are lost) will result in no controller action, and therefore the plant open loop response.

In total, twenty-two separate operating scenarios exist: all generators in service, fifteen generator contingencies, two VSC-HVDC outages, and four line outages. 1000 distinct operating points are created for each of these scenarios totalling 22,000 separate operating conditions used to assess controller performance. These represent only feasible steady state operating points with converged load flow solutions and stable open loop modes.

## **4.4 Results and Discussion**

This section describes not only the results of the simulations, but also how they can be used to aid power systems engineers in ensuring satisfactory system performance. A clear demonstration of the benefits associated with this methodology is presented.

### **4.4.1 Comparison of Controller Designs**

The centralised and decentralised control schemes can be assessed across the entire range of operating conditions and contingencies considered. A boxplot of the absolute improvement in damping factor ( $\Delta\zeta$ ) for each inter-area mode with both control designs is presented as Figure 4-6. The boxes represent the 25<sup>th</sup> and 75<sup>th</sup> percentiles, the bar within the box displays the median, the whiskers show the extents of the minimum and maximum values, and the notches on the whiskers display the 2.5<sup>th</sup> and 97.5<sup>th</sup> percentiles (i.e., 95% of the data is contained within these notches).

Figure 4-6 demonstrates that both the centralised and decentralised controllers display similar performance. For the vast majority of cases investigated, of which almost all represent an  $n-1$  outage contingency, both controllers provide a positive damping improvement to the critical inter-area modes. This would help to ensure a satisfactory system response is seen following a disturbance.

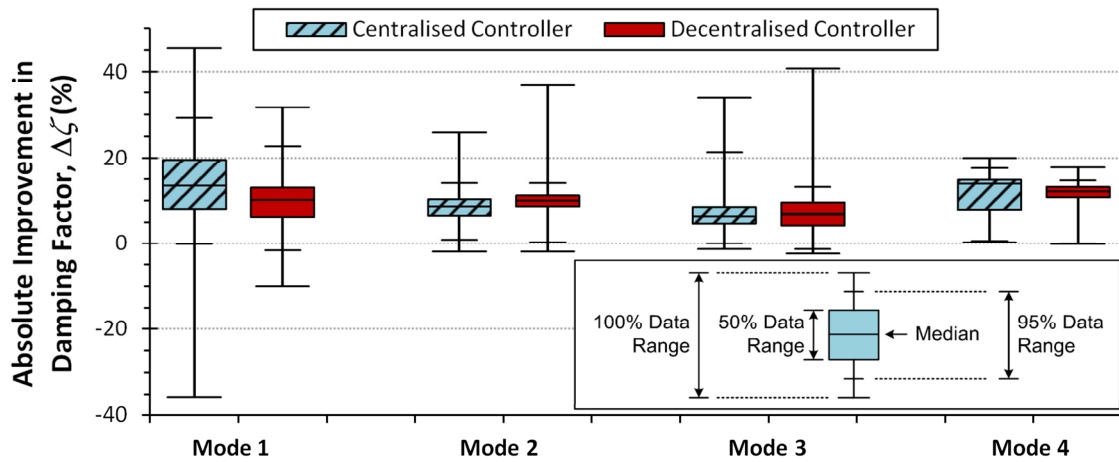


Figure 4-6: Absolute improvement in damping factor across all contingencies for the low frequency modes with different controller structures.

Comparing the 95% confidence range (between the notches on the whiskers), neither controller could justifiably claim to outperform the other. Therefore, if a centralised or decentralised approach is favoured based on external factors (such as cost or asset ownership), then the systems operator could be satisfied that the controller structure will not adversely affect system performance.

There are, however, some operating scenarios for which controller performance is reduced significantly and the controllers have a detrimental effect on the damping of the critical modes. Each mode experiences a detrimental effect at some point dependent upon the outage and controller structure. In some cases this is so severe as to lead to closed loop system instability, and should therefore be investigated further in order to be avoided. The conditions leading to poor performance vary for each mode and each controller design. By completing this full robustness assessment, it is possible to identify and mitigate for these circumstances.

#### 4.4.2 Mitigating for Inadequate Controller Performance

The key to being able to mitigate for poor controller performance is to identify the operating conditions that lead to this unsatisfactory behaviour. Once these conditions are known they can either be avoided, or the controller can be redesigned so that it can cope with this operating scenario and still exhibit good performance.

Table 4-2 below outlines the proportion of operating conditions for each of the investigated contingencies which lead to poor controller performance, or system instability. This table clearly shows that the two controllers experience substandard performance during different outage scenarios. For example, the decentralised scheme

experiences significant issues during VSC-HVDC outages. This is largely expected as modal damping is shared between lines 1 and 2. When a VSC-HVDC line is removed from service and its POD capacity is also removed, the damping for these modes is lost. Moreover, the action of the remaining VSC-HVDC POD controller can have a negative effect on the initial open loop damping. In the case of Mode 3 when VSC-HVDC-1 is out of service, this happens 100% of the time. Care should also be taken when VSC-HVDC lines are removed from service (for example, for maintenance) to avoid detrimental performance.

The wealth of data collected during this process allows for further action following the identification of contingencies which lead to poor controller performance. An illustrative example is taken for the situation when VSC-HVDC-1 is out of service with the centralised control structure in place. As can be seen from Table 4-2, in 44.4% of the wide ranging operating conditions considered the centralised controller had a detrimental effect on the damping factor of Mode 3.

Table 4-2: Proportion of operating conditions for given contingencies leading to poor controller performance.

<i>Centralised Control (%)</i>			<i>Decentralised Control (%)</i>		
<i>Mode   Outage</i>	<i>Detrimental</i>	<i>Unstable</i>	<i>Mode   Outage</i>	<i>Detrimental</i>	<i>Unstable</i>
Mode 1   Line 40–41	56.4	24.1	Mode 1   G14	1.3	–
Mode 2   Line 8–9	5.3	–	G16	29.3	1.8
Line 2–1	0.1	–	Line 8–9	2.3	1.2
Line 40–41	0.2	–	Line 2–1	0.7	0.4
HVDC–2	1.3	–	Line 40–41	1.1	0.4
Mode 3   HVDC–1	44.4	–	HVDC–1	79.0	5.8
			Mode 2   HVDC–2	36.6	–
			Mode 3   HVDC–1	100	–
			Mode 4   HVDC–2	68.4	–

#### 4.4.2.1 Predicting Inadequate Performance with One System Variable

Having already reduced the number of network variables which are modelled stochastically, it is much simpler to identify the possible correlations between modal damping and system parameter values. For the *centralised VSC-HVDC-1 outage case*, the conditions which lead to detrimental performance are analysed to determine if there are similarities. If these poor operating conditions can be classified, then this can be used as the first stage of mitigation against detrimental controller effects.

Plotting the uncertain parameter values against the improvement in damping suggests that there is some correlation between the improvement in damping factor of Mode 3 ( $\Delta\zeta_3$ ) and the values of both power output of G16, and the load at bus 18 (L18). Calculation of the correlation coefficients for both of these parameters suggests that G16 is the most important parameter and could be used to classify controller performance.

Figure 4-7 below shows the improvement in the damping factor of Mode 3 for the *centralised VSC-HVDC-1 outage case* plotted against the active power output of G16. *Good* performance is any positive effect on modal damping factor, *poor* performance covers negative values, and *unclassified* refers to those points which are not included within the defined operational boundaries.

The relationship between generator power production and the improvement in Mode 3 damping factor is clearly visible in the figure. The improvement seen in the  $\zeta$  value for Mode 3 reduces and become increasingly negative as the power output of G16 rises. By knowing the active power output from this key generator (and which operational boundary region this lies in), an operator can be confident as to whether they will see good or poor controller performance during oscillatory post disturbance situations. Practically this may allow a system operator to steer a network away from potentially poor conditions (with respect to POD damping) through appropriate generator dispatch.

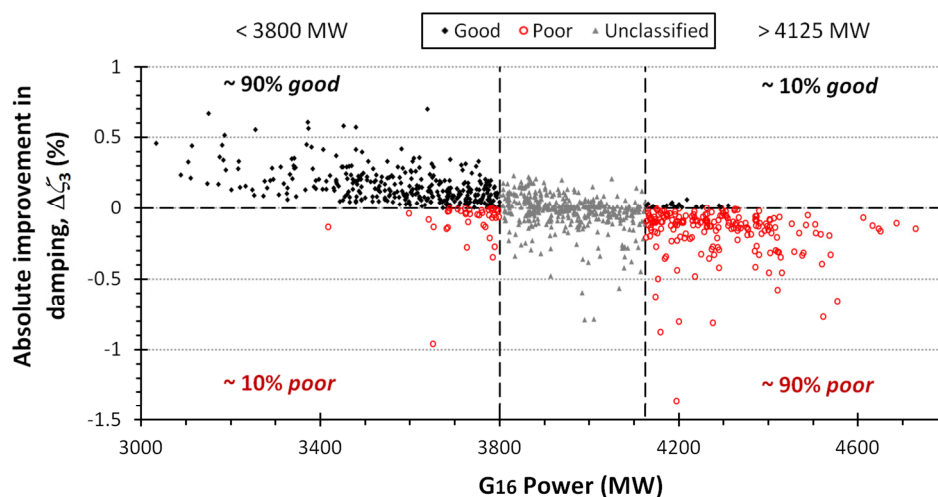


Figure 4-7: Boundaries for classification of centralised controller effect on Mode 3 with VSC-HVDC-1 out of service.

Boundaries have been defined for the *centralised VSC-HVDC-1 outage case* as shown in Figure 4-7. For operating conditions where the power output from G16 is less than 3800 MW, there is a 90% chance that the controller effect will be positive. Conversely,

when G16 is outputting more than 4125 MW, there is a 90% chance of poor controller performance. By re-dispatching generators, an operator may be able to move to a different operational zone, therefore improving system stability. With knowledge of these boundaries, it would be possible to ensure that if this contingency is planned in advance, the generators are dispatched accordingly to ensure good controller effects.

#### 4.4.3 Predicting Inadequate Performance with Multiple System Variables

This example of identification of system conditions leading to poor controller performance for the *centralised VSC-HVDC-1 outage case* can be extended to include more than one indicative parameter. More complex classification tools can be used to incorporate multiple system variables and to improve accuracy. This facilitates classification of all operating conditions and not merely probable regions of good or poor performance.

The introduction of more complex classification tools requires a compromise between the level of accuracy and the *visibility* of the classification technique; i.e., how easy it is to understand the decisions made by the classifier. A classification tree has been produced as shown in Figure 4-8 for the *centralised VSC-HVDC-1 outage case* to demonstrate a highly visible solution with good accuracy.

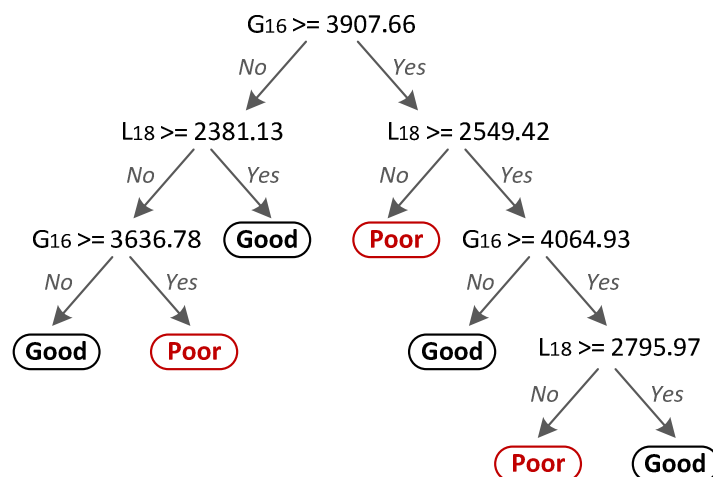


Figure 4-8: Classification tree for controller effect on Mode 3 with VSC-HVDC-1 out of service.

This classification tree was produced using the standard method of *over-fitting* the tree and then *pruning* it to ensure optimum performance against cross validation data sets [173]. This method produces a tree with just two parameters – the power output of G16 and the load at bus 18 (G16 and L18). Seven final nodes are optimum for classifying the

data, providing a *resubstitution accuracy* of 89.5%. This resubstitution error relates to the ability of the tree to correctly reclassify the training data used to generate it.

As the classification tree that has been produced contains decisions in just two parameters it is possible to visualise the classification rules on a plot, as shown in Figure 4-9 (where the shaded area is classified as *good* by the tree). From this visualisation, it can be seen that the decision tree in Figure 4-8 is performing well, although there is some misclassification at boundary regions. In many cases this misclassification is not a serious issue. With a binary classification of *good* or *poor* a very marginal improvement may be misclassified as poor. In these circumstances, the true improvement would be so slight that achieving a better controller performance would be welcomed.

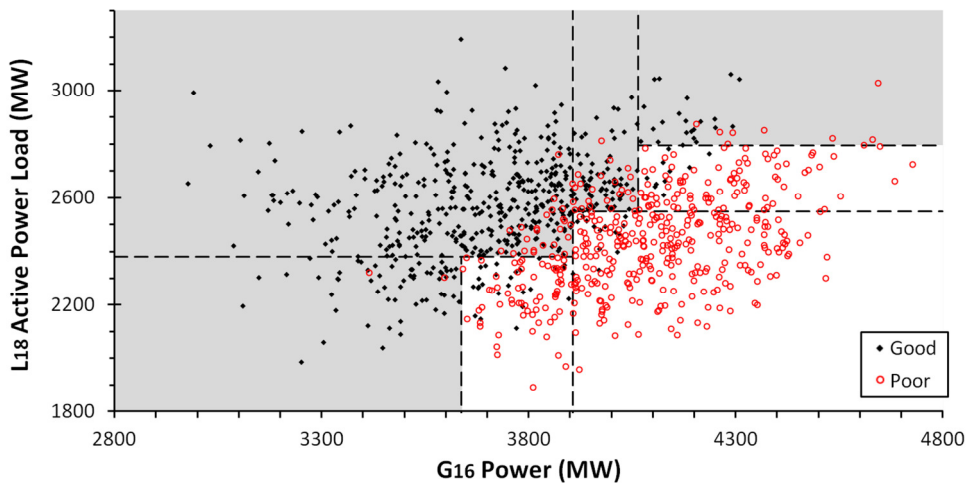


Figure 4-9: Visualisation of the classification tree with two system variables.

The classification-based methods of identifying the operating conditions that would lead to poor POD controller performance allow for some mitigation through avoidance of these conditions during system operation. More complex methods of classification are also available and can offer improved accuracy. For example, with the *centralised VSC-HVDC-1 outage case* data, use of a Functional Tree [174] or a Logistic Model Tree [175] can give classification accuracy of 93.4% and 94.3% respectively. However as previously mentioned, the visibility of such classification methods are much reduced and the rules and decisions implemented have less tangible equivalent meanings.

#### 4.4.3.1 Mitigation through Controller Redesign

A further mitigation option is available for situations when controller performance for a given contingency is unacceptable – that of contingency specific controller redesign.

From the contingency performance shown previously in Table 4-2, it is clear that the performance of the centralised controller when line 40–41 is out of service would not be acceptable. In 56.4% of the 1000 operating points generated with this outage, the controller reduces the damping factor of Mode 1. Moreover, this detrimental effect leads to closed loop instability of the power system in 24.1% of the 1000 cases – the risk of system instability  $P(\zeta < 0) = 24.1\%$ . This line outage is selected as a new case study, and the centralised controller is redesigned for this scenario in order to demonstrate the benefits of a contingency specific controller.

The centralised controller is redesigned following the same procedure as previously used (see Section 4.2.2 for details) with a linearised model of the system at the nominal operating point with line 40–41 out of service. This *redesigned centralised controller* is of 33<sup>rd</sup> order and has closed loop damping factor values for Modes 1–4 of 20.62%, 19.73%, 20.20% and 19.82% (at the operating point outlined above). These values are similar to those achieved using the initial centralised controller, but the system is now operating with line 40–41 out of service.

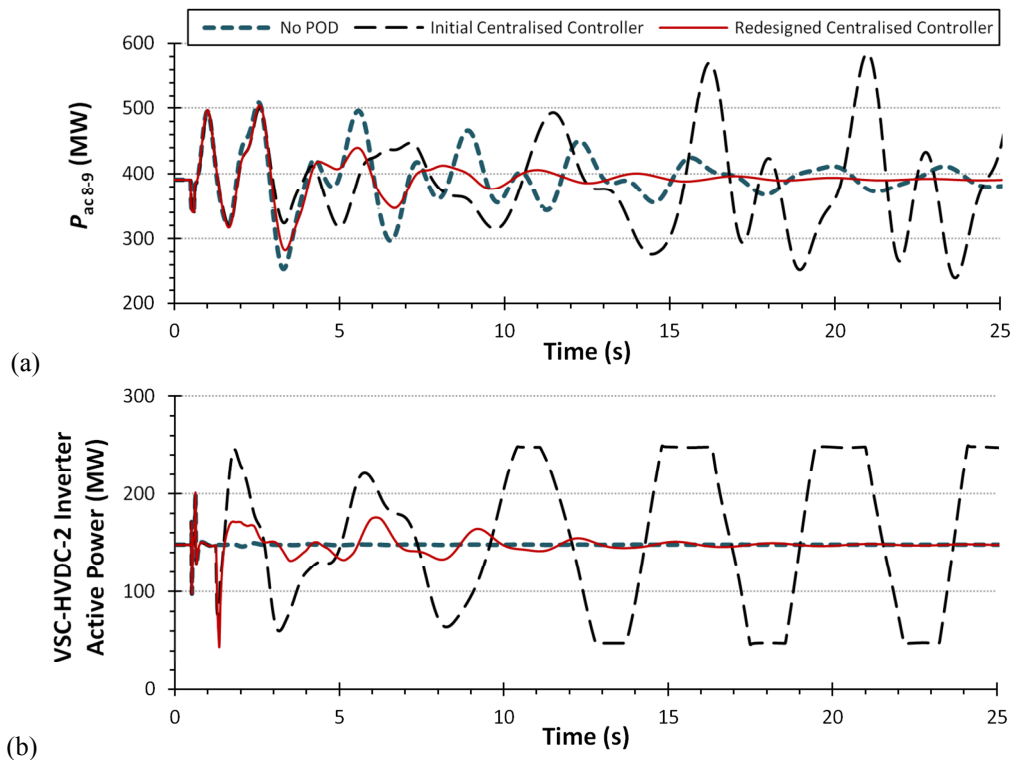


Figure 4-10: For an example case with the *initial* and *redesigned centralised controller* structures in place: (a) Active power injected at bus 9 from bus 8 and (b) Active power injected at bus 40 by the VSC-HVDC-2 converter station.

Figure 4-10 above demonstrates the improvement that can be achieved using the redesigned centralised controller, when compared to the *initial centralised controller*

(designed with all lines in service) and the system with no supplementary POD controller in place. The operating point selected is one for which the open loop response consists of poorly damped but stable oscillations. The initial centralised controller can be seen to cause closed loop instability within the network, with growing oscillations in the AC power flow in line 8–9. The redesigned centralised controller performs well for this stressed operating point with line 40–41 out of service, showing significant improvement over the *no POD* case.

Finally, a probabilistic robustness assessment is completed for this redesigned centralised controller considering only the contingency when line 40–41 is out of service. The results of this assessment are shown in the boxplot in Figure 4-11. The improvement in damping factor ( $\Delta\zeta$ ) for all modes is positive in all investigated cases and the risk of instability is reduced to zero. This is greatly improved over the previous centralised controller which has a negative effect on Mode 1 in the majority of cases. This result suggests that for some extreme system outage contingencies, *controller banks* with many predesigned controllers for various operating scenarios may be required in order to ensure truly robust performance across all possible conditions.

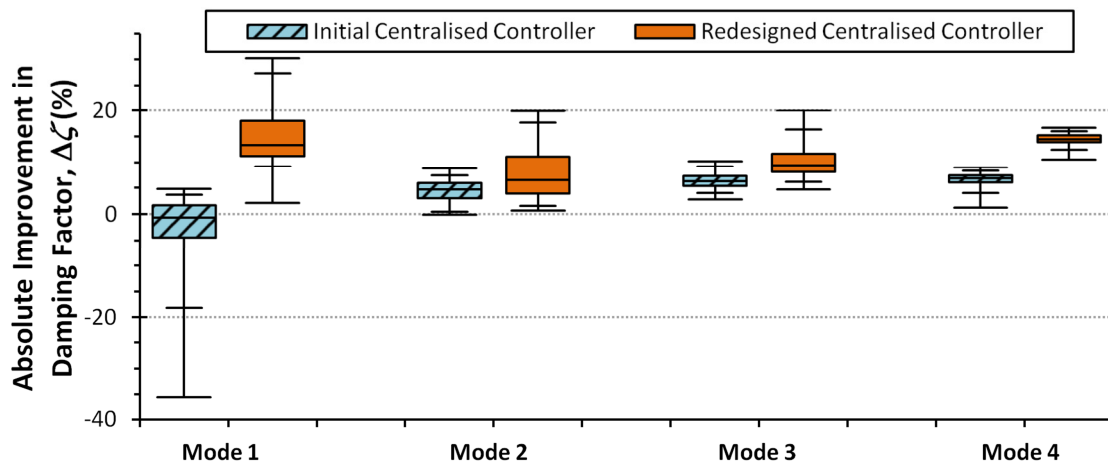


Figure 4-11: Absolute improvement in damping factor with line 40–41 out of service with the *initial* and *redesigned centralised controller* structures in place.

## 4.5 Summary

A methodology to assess the robustness of supplementary system damping controllers has been established and demonstrated using a large test system with multiple embedded VSC-HVDC lines. This methodology accounts for wide ranging operating conditions and system outage contingencies in order to fully assess the performance of supplementary controllers with any design structure. The proposed analysis is

completed based on small-disturbance analysis of the linearised power system. The results provide vital information which can be used for mitigation techniques in situations where system behaviour is unsatisfactory.

A study has been presented using a modified version of the five-area network containing two embedded VSC-HVDC lines. Within this network, system parameters were modelled as independent random variables, however other distributions could be used if known (for example, optimal power flow solutions, conditions distributions, or historical loading data). A technique to reduce the number of considered uncertainties based on eigenvalue sensitivity analysis has also been introduced in order to simplify the problem formulation, particularly for large power systems.

Classification tools were used throughout the procedure to improve the accuracy of the methodology and provide mitigation options to a systems engineer. A Naïve Bayes classifier was utilised in order to ensure correct identification of electromechanical modes based on system state participation factors during the robustness assessment. Following the data collection, classification trees were used to calculate regions of operation where good and poor controller performance would be expected with re-substitution accuracies of between 89.5–94.3% for the *centralised VSC-HVDC-1 outage case* (dependent on the classification algorithm). Accurate identification of these regions would allow systems operators to ensure that conditions which result in poor performance are avoided through appropriate generator dispatch, particularly in situations when outage contingencies are planned.

Finally, the demonstrative example within this chapter has shown the advantages of using a contingency specific controller design for an outage situation leading to unacceptable system performance. A controller designed for the full system with all units and lines in service leads to a 24.1% risk of system instability when the critical line 40–41 is removed from operation. However, a controller designed for this given outage ensures a positive effect on the damping factors of all low-frequency modes for all operating conditions, reducing the risk of instability to zero. Such contingency specific controller designs may be necessary to guarantee fully robust controller performance for all potential system conditions.

The method outlined within this chapter is reliant on the linearisation of the power system thousands of times using a MC approach in order to produce the distributions of

the oscillatory electromechanical system modes. The next chapter presents a technique which can be used to produce accurate distributions of the system modes using a greatly reduced number of system linearisations. This method enables the fast identification of modal distributions, subsequently allowing quick determination of the risk of instability.

# **5 Modal Estimation using the Probabilistic Collocation Method**

---

The previous chapter demonstrated the need for a probabilistic assessment of critical modes which considers the uncertainties that are inherent in the operation of future networks. However the numerical Monte Carlo approach used in Chapter 4 can be extremely computationally expensive. For studies taking place during planning or design stages, when results are not time critical, this may not prove to be problematic even though MC studies can be time and labour intensive, particularly as system size increases. When online applications such as the rapid assessment of the risk of system instability are considered, the computational demand of MC-based assessments is simply too great to reach an accurate decision in a suitably fast time.

The Probabilistic Collocation Method is a technique which significantly reduces the number of simulations that are required to complete a probabilistic system assessment, whilst still accurately producing the statistical distributions of system parameters. The PCM approximates the system response as a polynomial function of uncertain system

parameters, therefore replacing a computationally intensive study with a simple deterministic algorithm.

The PCM provides two clear benefits which make it suitable for power system uncertainty studies. Firstly, the method is designed to provide a statistical distribution for the system output. This is particularly important when considering stochastic variations in future operating points, and when calculating risk indices. With growth in renewable energy sources leading to an increase in future system uncertainty, methods which present the probabilistic nature of the network response are vital to ensure accurate system representation. Secondly, the PCM provides significant computational savings by reducing the number of full system studies required. This in turn increases the feasibility of incorporating uncertainty into online studies. As levels of stochastic and intermittent distributed generation and load increase, online statistical uncertainty studies will become a key element in coping with increasingly variable network conditions.

As discussed earlier in Section 1.3.2, alternative efficient sampling methods have investigated the use of techniques such as low discrepancy sequences,  $\Lambda\Pi_r$  sequences, and Latin hypercube sampling [134-136]. These methods all ensure that the full search-space is evenly sampled within fewer full simulations than required for traditional MC methods. The PCM uses a similar approach to these methods, building the model function from a small number of efficiently selected samples. However, unlike the approaches mentioned above, the samples are not selected to evenly cover the search space. Alternatively they are chosen to ensure that there is greatest coverage of the most probable operating points, based on the known probability distributions for the uncertain system parameters. The accuracy of the PCM estimation of the desired system outputs is therefore focused on the most probable values.

Further methods for probabilistic system stability studies include analytical solutions such as the Gram-Charlier expansion method and techniques based on generalised tetrachoric series [130, 132]. Such approaches have been shown to provide accurate solutions, but they require complicated mathematical analysis and often the inclusion of approximations is necessary in order to converge on a solution within an acceptable length of time. Other techniques which are similar to the PCM include the two point estimate method, which has been used in [133] to assess probabilistic stability. As with the PCM, a small number of simulations are used with the TPE method to estimate the

distribution of the desired system parameter. Although TPE requires just  $2m$  full simulations for a system with  $m$  uncertain parameters, it assumes a pre-determined distribution for the measured output (typically Normal). This is not necessarily the case in practical non-linear power systems, and is not a constraint on the PCM approach.

This chapter presents the use of the PCM for probabilistic small-disturbance stability studies and represents the fifth original contribution of the thesis. Techniques to reduce the number of modelled uncertainties based on eigenvalue sensitivity are established. Following their demonstration on a small test system, these reduction techniques are then applied to a large case study network and shown to produce accurate results when combined with the PCM. A brief illustrative example on a large power system incorporating an optimal power flow solution is also included, further demonstrating the applicability of the method for realistic power systems.

## 5.1 The Probabilistic Collocation Method

The PCM can be used to approximate the behaviour of a power system model with respect to changing parameters. This can be completed using a much smaller number of full simulations than is required for more traditional sampling techniques. More fully explained in [137, 176] and especially in [177], the approximated response  $\hat{Y}$  is modelled as a polynomial function of the uncertain parameter set  $\Gamma$ , as shown in (5.1).

$$\hat{Y} = g(\Gamma) \quad (5.1)$$

The PCM consists of two key aspects. These are:

1. The form of the model function.
2. The method used to specify the operating points at which full system simulations are required.

These aspects are discussed in the following sections, and a more detailed and thorough explanation can be found in [137, 176, 177].

### 5.1.1 The PCM Model Function

Orthogonal polynomials [178] of increasing order are derived for the known probability distributions of each uncertain parameter  $\gamma_j \in \Gamma$ . The PCM model function  $g(\Gamma)$  is formed as a sum of products of these polynomials, weighted by a set of coefficients  $\mathbf{K}$ .

The order of the orthogonal polynomials used is dependent on the desired order of the final model function.

### 5.1.1.1 Orthogonal Polynomials for Parameters with Normal Distributions

A set of orthogonal polynomials can be created for any known probability density function (*pdf*).

Normally distributed parameters are represented using the transformation given in (5.2).

$$\gamma_j = \mu_{\gamma_j} + \sigma_{\gamma_j} (H_1(\eta)) \quad (5.2)$$

In (5.2),  $\mu_{\gamma_j}$  and  $\sigma_{\gamma_j}$  are the mean and standard deviation of the uncertain parameter  $\gamma_j$ , and  $H_1(\eta)$  is the first order orthogonal polynomial of the standard normal distribution  $\eta$ .

The orthogonal polynomials  $H_o(\eta)$ , where  $o$  is the polynomial order, are given by the standard Hermite polynomials (5.3)–(5.7) (shown here up to 5<sup>th</sup> order).

$$H_1(\eta) = \eta \quad (5.3)$$

$$H_2(\eta) = \eta^2 - 1 \quad (5.4)$$

$$H_3(\eta) = \eta^3 - 3\eta \quad (5.5)$$

$$H_4(\eta) = \eta^4 - 6\eta^2 + 3 \quad (5.6)$$

$$H_5(\eta) = \eta^5 - 10\eta^3 + 15\eta \quad (5.7)$$

### 5.1.1.2 Orthogonal Polynomials for Parameters with Other Distributions

Orthogonal polynomials can be derived for other distributions using recursive methods [179]. Within this work, the *orthpol* set of functions for Matlab [180] is used to produce the recursive coefficients  $a$  and  $b$ . These coefficients are used in conjunction with the recursive formula (5.8) and the standard identities (5.9)–(5.10) to produce a set of monic orthogonal polynomials for any given *pdf*.

$$H_n(x) = (x - a)H_{n-1}(x) - bH_{n-2}(x) \quad (5.8)$$

$$H_{-1}(x) = 0 \quad (5.9)$$

$$H_0(x) = 1 \quad (5.10)$$

### 5.1.2 Selection of Probabilistic Operating Points

Linearisations of the full system model are required in order to produce a set of observed results. These results can then be used to fit the polynomial function using the set of coefficients  $\mathbf{K}$ . As the order of the PCM model increases, so too does the number of possible combinations of the orthogonal polynomials. An increased number of coefficients must therefore be deduced.

The number of coefficients  $c$  to calculate is dependent on both the number of uncertain parameters  $n_\gamma$  and the PCM model order  $o$ , as in (5.11).

$$c = \binom{n_\gamma + o}{n_\gamma} = \frac{(n_\gamma + o)!}{n_\gamma! o!} \quad (5.11)$$

In (5.11),  $n_\gamma!$  denotes the factorial of  $n_\gamma$ .

This number can increase rapidly as it is based on the binomial coefficients [181]. It is therefore beneficial to ensure that the model order and the number of modelled uncertainties are as small as possible.

A number of simulations must be run in order to provide points around which the set of coefficients  $\mathbf{K}$  can be solved in order to fit the model as shown in (5.12).

$$\mathbf{Y} = \mathbf{H}\mathbf{K} \quad (5.12)$$

In (5.12),  $\mathbf{Y}$  is a vector of observed system output values, and  $\mathbf{H}$  is a matrix with rows formed by the combinations of orthogonal polynomials for each uncertain parameter evaluated at the operating points resulting in the corresponding system output in  $\mathbf{Y}$ . The mathematical description for the combination of orthogonal polynomials is presented up to the 4<sup>th</sup> order as (C.1)–(C.4) in Appendix C.

The points at which simulation of the true plant model is required are called collocation points, and are selected based on the Gaussian quadrature technique of estimating integrals [179]. For each known parameter distribution, collocation points for a PCM function of a given order are chosen as the roots of the next higher order polynomial. Collocation points with the greatest probability of occurring are selected. By doing this, the accuracy of the PCM model is concentrated in the regions defined by the *pdfs* as most likely to occur.

The collocation points required are also independent of the system output which is to be modelled. Therefore only one set of full system simulations is required to build PCM functions for any number system outputs. Different outputs will require the calculation of a new set of polynomial coefficients  $K$ .

### 5.1.3 Using the PCM Model Function

Once the PCM function is known, it can be used as a computationally inexpensive substitute for running a full simulation of the power system during a standard MC-based uncertainty study. It is also possible to extract the *pdfs* directly from the PCM model functions. This method however requires the inversion of the function, which is not trivial for non-monotonic multi-dimensional functions. The numerical methods which would be required would often take so long to perform this inversion that they would negate the time benefits associated with using PCM.

## 5.2 Case Study on a Small Test Network

The first study presented within this thesis into the use of the PCM with small disturbance studies incorporating uncertainties is completed on the small two-area network. This case study is used to demonstrate the application of the PCM and to develop methods for the reduction of uncertain parameters that will allow further application for larger power systems.

### 5.2.1 Modifications to the Test Network

A VSC-HVDC line is embedded within the two-area network between buses 5 and 9 to support power flow to the load L2. The modified network is shown in Figure 5-1, with VSC-HVDC parameters and control settings given in Appendix A. With the VSC-HVDC line installed and operating at a nominal active power set-point of 200 MW, the mode details are changed slightly from the purely AC network. The new values are presented in Table 5-1.

Table 5-1: Electromechanical mode properties for the two area test system with an embedded VSC-HVDC line.

<i>Mode</i>	<i>Frequency,</i> $f$ (Hz)	<i>Damping Factor,</i> $\zeta$ (%)
Mode 1	0.975	5.88
Mode 2	1.003	5.73
Mode 3	0.588	4.20

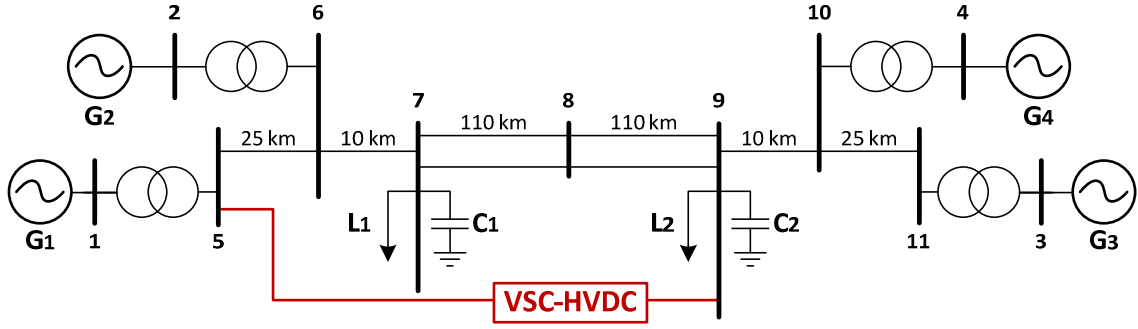


Figure 5-1: Two-area test network including embedded VSC-HVDC line.

## 5.2.2 Application of the PCM with Test System

Studies are initially performed without the use of any POD control. This will assess the effects of uncertainty in the network operating conditions on the locations of the identified electromechanical modes, with a specific focus on their damping.

### 5.2.2.1 Uncertain Network Parameters

The set of uncertain network parameters  $\Gamma$  consists of system generation, loading, and VSC-HVDC power transfer. This constitutes a set of six uncertain parameters (5.13).

$$\Gamma = \{G_2, G_3, G_4, L_1, L_2, P_{dc}\} \quad (5.13)$$

In (5.13),  $G_n$  is the active power output from generator  $n$ ,  $L_n$  is the active power demand at load  $n$ , and  $P_{dc}$  is the active power flow through the VSC-HVDC line.

Generators and loads are modelled with a normal distribution, where the mean  $\mu_\gamma$  is equal to nominal loading and the standard deviation  $\sigma_\gamma$  is equal to 20% at  $3\sigma_\gamma$ . Generators are modelled as  $PV$  buses with constant voltage output (as per nominal loading) and generator G1 is the slack bus. Loads are considered to have constant nominal power factor when producing their parameter values. Values for  $\mu_\gamma$  and  $\sigma_\gamma$  for these normally distributed parameters  $(\gamma_1, \gamma_2 \dots \gamma_5)$  are given in Table D-1 in Appendix D.

As previously stated, there is no requirement to model parameters with a Normal distribution when implementing the PCM and any other known distribution can be substituted as desired. This is illustrated within this study using the power flow through the VSC-HVDC line  $(\gamma_6 : P_{dc})$ . This parameter considered to be unidirectional (from left to right in Figure 5-1) and is modelled with a uniform probability distribution

between 100 and 300 MW. Reactive power injection at both converter stations is regulated at zero.

Within these given distributions of system parameters there exist potential operating conditions that are unstable. It is therefore desirable to determine the probabilistic locations of the system electromechanical modes in the presence of system operational uncertainties. If standard MC simulation is used it will require a large number of runs to ensure that the variation in all parameters had been captured. The use of the PCM can speed up the process while adequately covering the whole parameter search space.

### 5.2.2.2 Generation of Orthogonal Polynomials

As discussed in Section 5.1.1.1, the normally distributed parameters  $(\gamma_1 \dots \gamma_5)$  can utilise the standard Hermite polynomials (5.3)–(5.7) via the transformation (5.2). Orthogonal polynomials for the uniformly distributed  $\gamma_6 : P_{dc}$  are found using the recursive formula (5.8) described in Section 5.1.1.2. The recursive coefficients are given in Table D-2 in Appendix D and the final orthogonal polynomials are presented as (5.14)–(5.18).

$$H_1(\gamma_6) = \gamma_6 - 200 \quad (5.14)$$

$$H_2(\gamma_6) = \gamma_6^2 - 400\gamma_6 + 3.667 \times 10^4 \quad (5.15)$$

$$H_3(\gamma_6) = \gamma_6^3 - 600\gamma_6^2 + 1.14 \times 10^5 \gamma_6 - 6.80 \times 10^6 \quad (5.16)$$

$$H_4(\gamma_6) = \gamma_6^4 - 800\gamma_6^3 + 2.314 \times 10^5 \gamma_6^2 - 2.857 \times 10^7 \gamma_6 + 1.266 \times 10^9 \quad (5.17)$$

$$H_5(\gamma_6) = \gamma_6^5 - 1000\gamma_6^4 + 3.889 \times 10^5 \gamma_6^3 - 7.333 \times 10^7 \gamma_6^2 + 6.690 \times 10^9 \gamma_6 - 2.359 \times 10^{11} \quad (5.18)$$

### 5.2.2.3 Collocation Point Selection

The number of coefficients which must be calculated (and therefore the number of collocation points required) is shown in Table 5-2, calculated from (5.11). As previously explained, the PCM process is designed to be most accurate in the regions of the parameter *pdfs* which are most likely to occur. Previous research into the application of the PCM with power systems [137-139] has only considered one or two uncertain parameters. For these situations, the collocation points are most easily selected by hand. This cannot be achieved with larger numbers of uncertain parameters. For example, a 4<sup>th</sup> order model with six uncertain parameters has a possible  $5^6 (= 15,625)$  permutations of collocation points.

Table 5-2: Number of coefficients for PCM models with six uncertain parameters.

PCM Model Order	1 <sup>st</sup>	2 <sup>nd</sup>	3 <sup>rd</sup>	4 <sup>th</sup>
Number of Coefficients	7	28	84	210

In order to select the most probable sets of collocation points, all possible permutations are generated and then ranked by the joint probability density for the given set. Following this, the list of ordered sets is iterated through until the matrices to solve in (5.12) have sufficient rank to be invertible.

PCM models have been produced for the eigenvalue locations of all three electromechanical modes. This has been completed by taking the real ( $\sigma$ ) and imaginary ( $\omega$ ) parts for each electromechanical mode as the system outputs of interest. These PCM model functions have been produced up to the 4<sup>th</sup> order.

### 5.2.3 Errors of the Produced PCM Models

The standard measure of the Relative Sum-Squared-Root (RSSR) error can be used to assess the error of the different order PCM models and thus determine which should be selected for use in the uncertainty studies. The RSSR error  $\varepsilon_{RSSR}$  is defined by (5.19).

$$\varepsilon_{RSSR} = \frac{1}{E(\hat{Y})} \sqrt{\frac{\sum_{k=1}^m \left[ (\hat{Y}_k - Y_k)^2 f_{\Gamma}(\Gamma_k) \right]}{m f_{\Gamma}(\mu_{\Gamma})}} \quad (5.19)$$

In (5.19),  $\hat{Y}$  is the predicted value produced by the PCM model,  $Y$  is the extracted value from simulation for the same set of uncertain parameters,  $m$  is the total number of points used for error checking,  $f_{\Gamma}(\Gamma)$  is the joint probability density value for a given set of parameters  $\Gamma$ ,  $\mu_{\Gamma}$  is the set of uncertain parameter mean values, and therefore  $f_{\Gamma}(\mu_{\Gamma})$  is the joint probability density for the parameter mean values.

Values of  $\varepsilon_{RSSR}$  can be calculated using any values, but typically the roots of the next higher order orthogonal polynomial are selected (i.e., for a 4<sup>th</sup> order model, the 6<sup>th</sup> order polynomial roots are used) [176]. Again, this leads to a vast number of possible collocation point sets. The 100 most probable sets are, therefore, used within this work for error checking.  $\varepsilon_{RSSR}$  values for both the real and imaginary parts of each mode have been calculated for the various PCM models, as shown in Figure 5-2. These error values relate to the accuracy of the PCM model function when estimating the system outputs of

interest. The lowest possible model order which preserves accurate estimates of the true system output *pdfs* should be selected as it will be the quickest to produce and use.

It can be seen in Figure 5-2 that the  $\varepsilon_{RSSR}$  values decrease as the model order increases. Slight variations leading to higher error for higher order models are simply due to differences in the error checking points which are used. For both local modes, it can be seen that the  $\varepsilon_{RSSR}$  values have levelled off once a 2<sup>nd</sup> order model is used. A 3<sup>rd</sup> order PCM model is however required for the inter-area mode. As this is the critical mode with the lowest damping factor and is most likely to lead to system instability, it is paramount to ensure that accurate estimates for this modal placement are produced. All system outputs, the real and imaginary parts of each electromechanical mode, will therefore use 3<sup>rd</sup> order models. As previously stated all models will utilise the same set of full simulations and derive new sets of coefficients  $\mathbf{K}$ .

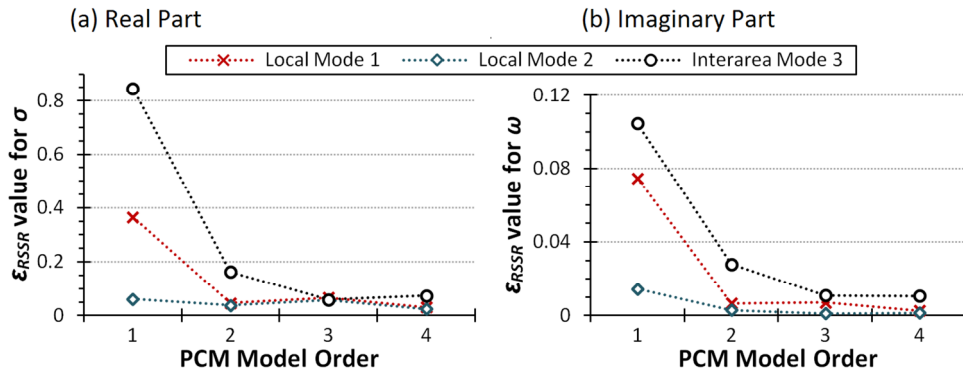


Figure 5-2:  $\varepsilon_{RSSR}$  error values with varying PCM model order for (a) the real, and (b) the imaginary parts of the electromechanical mode locations.

### 5.2.4 Results and Discussion

The PCM models can be used to predict the locations of the electromechanical modes at any distinct operating point. However this does not make the best use of the computationally inexpensive algorithm that can replace the process of full system linearisation. The PCM model functions can be used with a traditional MC pseudo-random sampling approach to quickly generate the probabilistic modal locations. By doing this, and avoiding the full linearisation process, vast time savings can be made.

Figure 5-3 below shows the probabilistic mode locations based on the uncertain network parameters. These have been produced using 10,000 MC runs. Plots (a)–(c) are based on the full automated process of load flow, linearisation, eigenvalue analysis and electromechanical mode identification. Plots (d)–(f) have been produced using the third

order PCM models. The contours shown (representing 10%, 30%, 50%, 70% and 90% of the data distributions) have been produced using a two-dimensional kernel smoothing density estimate [182].

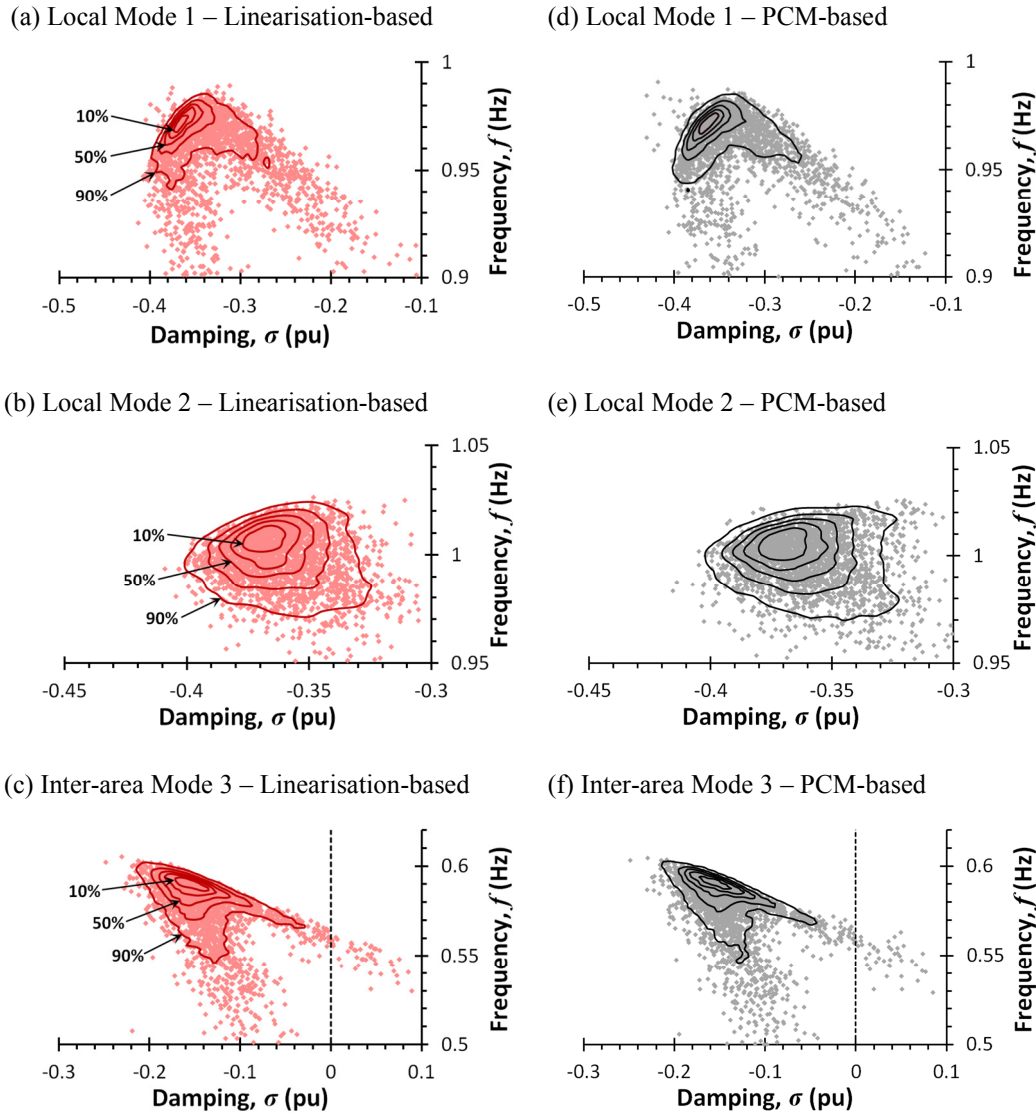


Figure 5-3: Plots of probabilistic electromechanical mode locations based on system uncertainties. Plots (a)–(c) have been produced using the MC approach with full system linearisations. Plots (d)–(f) have been produced using the MC approach with the 3rd order PCM models.

It is clear that the PCM model functions are able to reproduce the statistical modal locations produced by the full MC-based linearisation approach. In order to further assess the accuracy of the PCM-based distributions, the 90% contours have been reproduced as overlap plots in Figure 5-4.

It is clear from Figure 5-4 that the PCM-based contours accurately overlap those produced using the full linearisation-based MC approach. It should be noted that these contours are representative of three-dimensional distributions, and therefore is the

volume of overlap – and not the *area* – that corresponds to the accuracy. As this is not easily assessed, a simpler measure has been used.

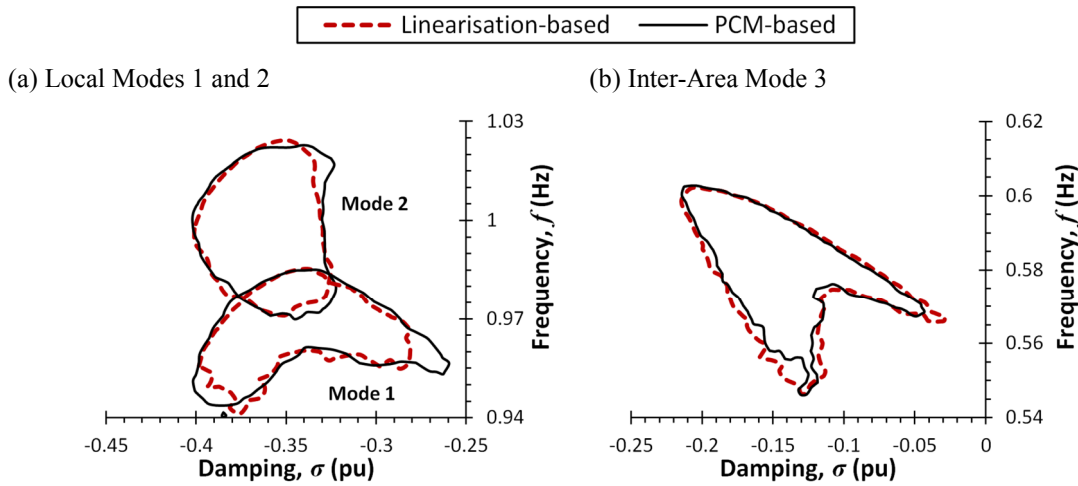


Figure 5-4: Overlap plots of the 90% contours for (a) local Modes 1 and 2, and (b) the inter-area Mode 3.

The number of data points from the set contained by the 90% linearisation-based contour ( $A^{90\%}$ ) that are not contained within the 90% PCM-based contour ( $B^{90\%}$ ) have been calculated. This is defined mathematically by (5.20), and represents the extent to which the true linearisation-based distribution is *under-represented* by the PCM distribution.

$$A^{90\%} - (A^{90\%} \cap B^{90\%}) \tag{5.20}$$

In (5.20), the symbol  $\cap$  represents the intersection of two sets.

These under-representation values for the 90% contour level are given in Table 5-3, expressed as a percentage. It can be seen that the produced distributions are highly accurate, although the inter-area mode, which sees the greatest level of variation, displays the greatest proportion of under-representation. For this inter-area mode, 5.79% of the data that should be included within the 90% contour would be outside the PCM-based contour.

Table 5-3: Percentage of under-representation for electromechanical modes at the 90% contour level.

Percentage of under-representation		
Mode 1	Mode 2	Mode 3
1.84%	0.86%	5.79%

Looking solely at the critical inter-area mode (which can be seen to be potentially unstable in certain situations), the data presented in Figure 5-3(c) and Figure 5-3(f) can be represented as shown in Figure 5-5. This displays the *pdfs* for the damping factor of this critical mode ( $\zeta_{crit}$ ), as produced using the full MC process and using the third order PCM model. The high degree of accuracy can clearly be seen from the almost perfectly overlapping *pdfs*.

The Risk of Instability (RoI) for the critical inter-area mode,  $P(\zeta_{crit} < 0\%)$ , can be assessed from the associated cumulative probability functions. This RoI is shown in Figure 5-5 as the area enclosed by the *pdfs* to the left of the  $\zeta_{crit} < 0\%$  boundary. The PCM-based predicted value is 1.89%, whereas the true linearisation-based value is 1.91%. For such a low probability event, this small difference could easily be due to the MC process itself. Similar plots can be produced for the other non-critical local modes.

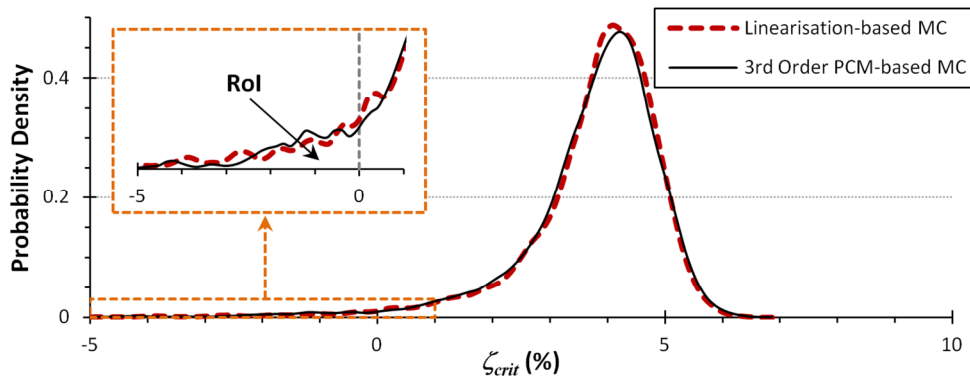


Figure 5-5: Probability distributions for  $\zeta_{crit}$  derived using MC runs with linearisation of the full system and using the third order PCM model.

The ability of the PCM to accurately produce statistical distributions for system parameters based on network uncertainties has been demonstrated effectively. The method also provides considerable time savings due to the vastly reduced number of (computationally intensive) full system linearisations required.

Table 5-4 shows the times taken to complete the studies which are required to produce the plots in Figure 5-3 and Figure 5-5. These are based on simulation using a PC with 2.66 GHz quad-core CPU and 4 GB RAM. The PCM-based studies are significantly faster, taking less than 1% of the time used by the full linearisation-based method. As the majority of time is taken when linearising the full power system, minimising the PCM model order or the number of considered uncertainties will further increase the time and computational savings.

Table 5-4: Times taken to complete MC uncertainty studies on the two-area system.

Task	PCM-based	Linearisation-based
Generate $\Gamma$ sets	0.08 s	N/A
Identify sets with unique rank	6.07 s	N/A
Run linearisations and build model	72.40 s	N/A
10,000 MC runs	3.4 s	~140 minutes
Total time taken	81.95 s	~140 minutes

## 5.2.5 Incorporating POD Control

This case study on the simple two-area network has been investigated further to examine the effects of the inclusion of a simple PSS-based POD controller acting through the VSC-HVDC line.

### 5.2.5.1 PSS-based POD Controller Details

The standard PSS-based design described in Section 2.4.1 is used. The input signal is selected as the active power flow injected at bus 9 from bus 8 through one AC power line. No signal delays are considered and the controller is tuned for the critical inter-area mode. The final POD controller parameters are given in Appendix A.

### 5.2.5.2 PCM Model Details

The PCM model is produced using the same procedure as before, when no POD controller was installed. The system output is selected directly as the damping of the critical inter-area mode,  $\zeta_{crit}$ . Error analysis suggests that a 3<sup>rd</sup> order model is again most suitable for the PCM function, as the 4<sup>th</sup> order model didn't show any further improvement in  $\varepsilon_{RSSR}$ .

### 5.2.5.3 Results and Discussion

The produced PCM model has been used to produce a *pdf* for the distribution of  $\zeta_{crit}$ . This is compared in Figure 5-6 with the distribution produced using a full linearisation-based approach.

Figure 5-6 shows that with the PSS-based POD controller installed, the two *pdfs* do not overlap to the same extent as seen with no POD controller. Despite this, they still show excellent coherency. In this case, the RoI is determined as 0.49% with the PCM while the true value from linearisation is 0%. This inconsistency can be explained by further investigating the accuracy of the produced PCM models.

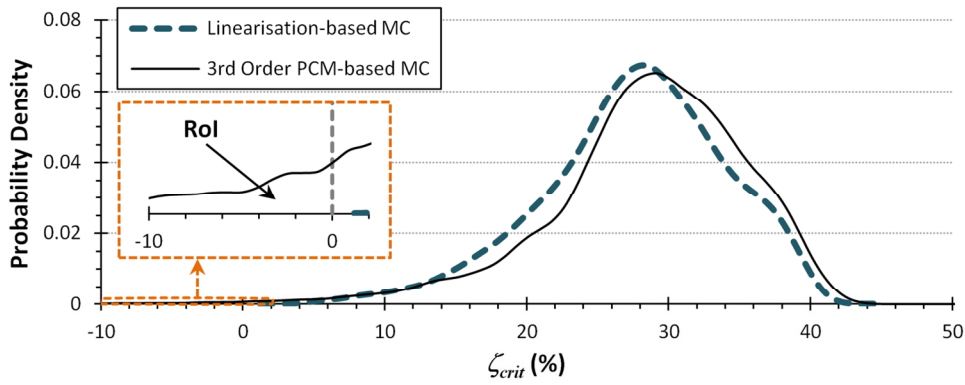


Figure 5-6: Probability distributions for  $\zeta_{crit}$  with PSS-based POD controller installed.

Figure 5-7 shows the predicted PCM-based results ( $\hat{Y}$ ) plotted against the MC linearisation-based results ( $Y$ ) for the same uncertain parameters value sets. Perfect accuracy would result in a straight line ( $\hat{Y} = Y$ ). The 95% confidence ranges for the PCM model estimates of  $\zeta_{crit}$  are resented in Table 5-5. In 95% of estimates, the PCM model is accurate to within the ranges stated within the table. These limits have been provided in terms of the critical mode damping factor values and are measured as a percentage.

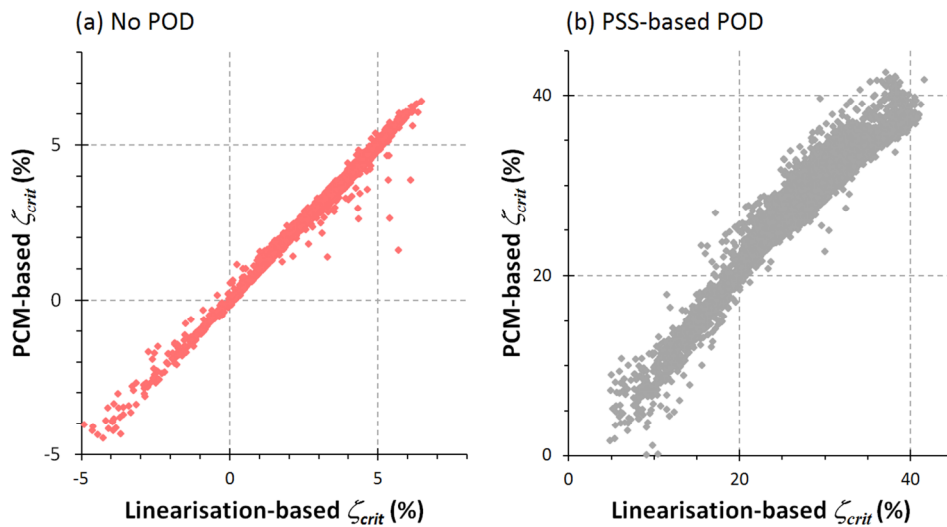


Figure 5-7: Plots of PCM-based  $\zeta_{crit}$  values against linearisation-based  $\zeta_{crit}$  values with (a) no POD controller, and (b) a PSS-based POD controller installed.

Table 5-5: 95% confidence range for the PCM model function estimate of  $\zeta_{crit}$ .

95% Confidence Range for Estimate of $\zeta_{crit}$ (%)	
No POD	PSS-based POD
±0.167	±3.12

Table 5-5 demonstrates that the linear boundaries are much tighter for the system when there is no POD controller installed ( $\pm 0.17\%$  absolute variation), corresponding to the better coherency seen between the produced *pdfs*. With the PSS-based POD controller installed, Figure 5-7(b), the PCM model under-estimates the damping factor, particularly when the true value is low. This in turn skews the produced distribution towards lower estimated damping factors and causes the slight loss of accuracy. For the example presented, this results in a conservative estimate of the probability of instability, with a PCM-based RoI value which is higher than with the full linearisation-based value.

It should also be noted that the POD controller is directly influencing  $\zeta_{crit}$  and is causing it to vary within a much larger range. This controller action may introduce large nonlinearities with respect to the variation of the damping factor with changing operating conditions. The accuracy plot presented in Figure 5-7 above helps to fully understand the results obtained through the use of the PCM.

### 5.3 Reduction in Modelled Uncertainties

The simulation times presented previously in Table 5-4 demonstrate how the PCM can speed up the uncertainty studies and still provide accurate results. This time reduction would be more pronounced in large system studies with more system states, where linearisation and modal analysis would be a greater computational burden. This would however only be true if the PCM models can be produced using significantly fewer simulations than are required to complete the traditional MC uncertainty study.

It is shown in (5.11) that as the system size (and therefore the number of uncertain system parameters) increases, so too does the number of coefficients. This number can grow rapidly, negating the benefit of the PCM approach. A method is therefore required to reduce the number of uncertainties modelled, whilst retaining the accuracy of the results.

#### 5.3.1 Eigenvalue Sensitivity

Ranking based on eigenvalue sensitivity is used within this work to identify the uncertain parameters which have the greatest effect on the critical modes of interest. The rank which was found to be most useful is derived from (4.1) used with the probabilistic evaluation of controller performance in Chapter 4, and is given below as

(5.21). This index  $r_{\lambda_i \gamma_j}$  can be used to identify the sensitivity of the mode  $\lambda_i$  to the uncertain parameter  $\gamma_j$ .

$$r_{\lambda_i \gamma_j} = \left| \frac{\partial \lambda_i}{\partial \gamma_j} \right| \left| \frac{\sigma_{\gamma_j}}{\mu_{\gamma_j}} \right| \quad (5.21)$$

As the damping of the eigenvalue is of interest, the rank index  $r_{\lambda_i \gamma_j}$  is calculated using only the real part  $\sigma_i$  substituted for  $\lambda_i$  in (5.21). Again, care should be taken to distinguish between the eigenvalue real part  $\sigma$  and the uncertain parameter standard deviation  $\sigma_\gamma$ . The first term – the sensitivity measure – is calculated using a 1% change in each parameter value. The second term in (5.21) weights this sensitivity by the expected variation in the uncertain parameter. A numerical example of the similar rank calculation performed in Chapter 4 is included in Appendix B.

Evaluating this expression for each of the uncertain parameters in the set  $\Gamma$  for the case study on the two-area test network provides the following ranked order (with the most significant parameter first):  $P_{dc}$ ,  $L_2$ ,  $G_3$ ,  $G_4$ ,  $L_1$ ,  $G_2$ . The ranked order is the same both with and without the POD controller installed, although the individual rank values differ.

### 5.3.2 The Effect of Parameter Reduction on Model Error

The rank values can be used to assess the number of parameters to include in the reduced set  $\Gamma^{red}$ . Alternatively, due to the short time required to produce PCM models (especially when the total number of uncertainties is small), the option exists to build models with increasing  $n_\gamma$  until the error  $\varepsilon_{RSSR}$  is tolerably small. This has been completed for the case study on the two-area network, using third order PCM models estimating  $\zeta_{crit}$ .

The  $\varepsilon_{RSSR}$  values with increasing numbers of parameters (both with and without the PSS-based POD controller) are shown below in Figure 5-8. Parameter selection is made according to the previously stated ranked order. Figure 5-8 also shows the  $\varepsilon_{RSSR}$  values for the best possible selection of parameters based on an exhaustive search of all possible combinations. This is included in order to demonstrate the validity of using the eigenvalue sensitivity rank as a selection tool for parameters. It is clear that the selection

based on eigenvalue sensitivity rank will often choose the best possible set of parameters. This method therefore provides a very good method of parameter reduction when an exhaustive search is not possible.

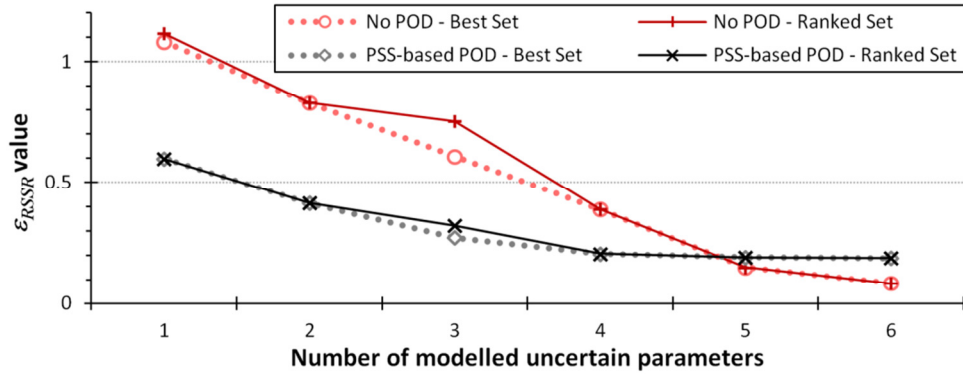


Figure 5-8:  $\varepsilon_{RSSR}$  for increasing numbers of modelled uncertain parameters.

With no POD controller, the error values consistently reduce until all parameters are modelled. Even with five parameters included (all but  $G_2$ )  $\varepsilon_{RSSR}$  is still double its final value which suggests that parameter reduction may not be possible in this case. With the PSS-based POD controller installed, however, the values of  $\varepsilon_{RSSR}$  level off when four parameters have been included in the set  $\Gamma^{red}$ . Using just four parameters in the reduced set  $\Gamma^{red}$  should therefore provide similar accuracy to the full set  $\Gamma$ . The addition of the PSS-POD controller has reduced the effect of  $L_1$  and  $G_2$  on the damping of the critical mode and these parameters can therefore be neglected from the PCM model.

This has been assessed by re-running the MC-based uncertainty study on the test system with the PSS POD controller installed. The PCM model function estimating  $\zeta_{crit}$  is again 3<sup>rd</sup> order, but take only the four uncertain parameters  $\Gamma^{red} = \{G_3, G_4, L_2, P_{dc}\}$  as inputs.

### 5.3.3 Results and Discussion

It is evident from Figure 5-9 that the reduced set of uncertainties can be used to provide results which are as accurate as those obtained by modelling the full set of stochastic system parameters. The two *pdfs* shown in Figure 5-9 overlap with a very high degree of accuracy. This reduction also has a large effect on the number of coefficients to find, lowering it from eighty-four to just thirty-five. In turn this reduces the total time taken to produce the PCM model and complete 10,000 MC runs to just 35.89 s (compared to 81.95 s previously).

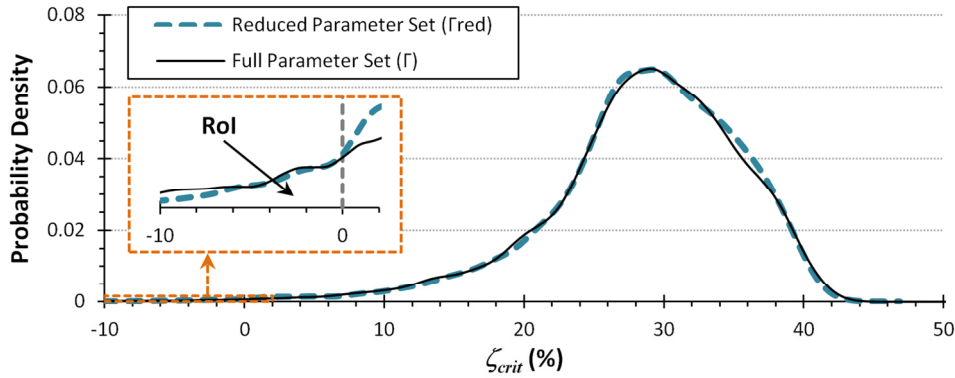


Figure 5-9: Pdfs for  $\zeta_{crit}$  with the full and reduced sets of uncertain parameters.

Reduction in the number of modelled parameters is an effective method of further improving the time gains offered by using PCM with uncertainty studies. It also enables the use of the method with larger power system applications. For example, modelling forty uncertain parameters with a 3<sup>rd</sup> order model would result in 12,341 coefficients to deduce. Parameter reduction is necessary for the probabilistic small-disturbance analysis of large power systems in order to preserve the time benefits associated with the PCM.

The presented case study is a valuable demonstration of the potential benefits of the PCM applied to the probabilistic small-disturbance stability assessment of power systems. The level of parameter reduction is however much greater within larger power systems. The small nature of the two-area network means that all of the uncertain parameters within the system influence the location of the critical inter-area mode, especially when no POD controller is installed. In larger power systems, the behaviour and movement of modes of interest are heavily dominated by a few key loads and generators within the network, resulting in a greater reduction in the number of considered uncertainties.

## 5.4 Case Study on Large Test Network

The PCM has been used with a large test system in order to demonstrate the suitability of the techniques described in the previous sections. A PCM model is designed to provide the distribution of the damping factor of the critical system mode in order to assess the risk of system instability (RoI), and the need for damping improvement by supplementary control.

### 5.4.1 Modifications to the Test Network

This study is completed using the large five-area power system. As in Chapter 4, two VSC-HVDC lines are installed, one from bus 18 to bus 50, and one from bus 41 to bus

40. Nominal operating capacities are set at 400 MW and 300 MW respectively, importing into the NYPS region of the test system. Data and controller settings for the two VSC-HVDC lines are provided in Appendix A.

The damping of the critical system mode is central to the post-disturbance performance of this network. In this large test system, the critical mode is the lowest frequency inter-area mode with a nominal frequency of 0.41 Hz and a damping factor of 4.31%.

### 5.4.2 Uncertain Network Parameters

The system contains a total of fifty-one uncertain parameters: fifteen generators (excluding the slack), two VSC-HVDC lines, and thirty-four loads. The number of simulations required to produce 1<sup>st</sup>, 2<sup>nd</sup>, 3<sup>rd</sup>, and 4<sup>th</sup> order PCM models using the full set of uncertain parameters is 52, 1378, 24,804, and 341,055 respectively. It is clear that unless a first order model is sufficient (and the previous study conducted on the two-area test system suggests it will not be), a reduction in the number of modelled parameters is necessary to make the approach computationally competitive.

Generators and loads are modelled with a normal distribution with 25% range at  $3\sigma_\gamma$  around the mean nominal values  $\mu_\gamma$ . As before, generators are modelled as *PV* buses with constant voltage output with generator G13 the slack bus. Loads are considered to have constant power factor when producing their random parameter values. The VSC-HVDC lines have uniformly distributed operating capacities between 200–500 MW for the DC line 18–50, and between 150–400 MW for the DC line 41–40. Reactive power injection at all converter stations is regulated at zero.

### 5.4.3 Reduced System Uncertainties

Eigenvalue sensitivity analysis is completed using the rank given in (5.21) as previously described. It is found that the full set of fifty-one uncertain network parameters can be reduced to eight whilst maintaining accurate results. The set of eight parameters, consisting of six generators and two loads, is given in (5.22). Values for  $\mu_\gamma$  and  $\sigma_\gamma$  for these normally distributed parameters ( $\gamma_1 \dots \gamma_8$ ) can be found in Table D-3 in Appendix D.

$$\Gamma^{red} = \{G_4, G_5, G_6, G_7, G_{14}, G_{16}, L_{18}, L_{20}\} \quad (5.22)$$

#### 5.4.4 Results and Discussion

It is found that a third order model is required to accurately reproduce the probabilistic distribution of the damping factor of the system's critical oscillatory mode (as seen with the case study on the smaller test system). This requires 165 full system linearisations in order to produce the model. The results obtained from 10,000 MC runs using the full linearisation-based approach and using the PCM model are shown in Figure 5-10.

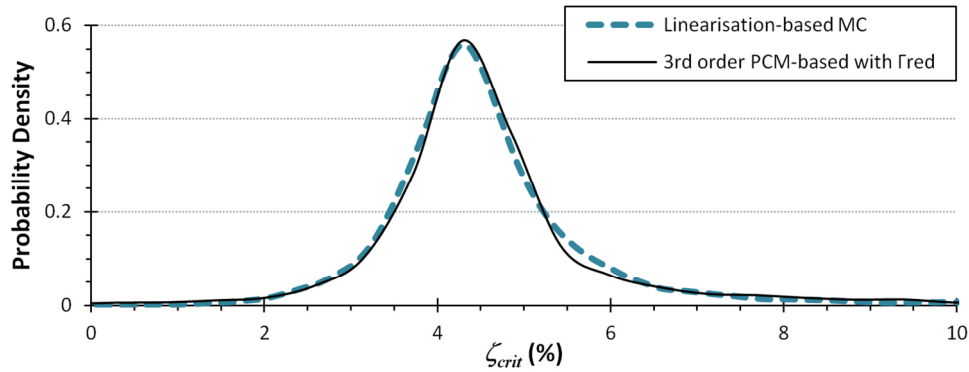


Figure 5-10: *Pdfs* for  $\zeta_{crit}$  with the PCM model using a reduced set of uncertain parameters and the full linearisation-based approach.

Despite the vast reduction in considered uncertainties – from the original fifty-one to eight – the PCM model function is able to accurately reproduce the *pdf* for  $\zeta_{crit}$ . The PCM model correctly provides the RoI as zero,  $P(\zeta_{crit} < 0\%) = 0$ . However, it is clear from the produced *pdfs* in Figure 5-10 that the mode is poorly damped and that it requires the assistance of a supplementary POD controller to avoid persistent post-disturbance oscillations.

The times taken to perform these studies are presented in Table 5-6 below. Again, it can be seen that the PCM approach greatly reduces the computational burden, requiring just 165 linearisations to build the model. Eigenvalue sensitivity-based parameter ranking requires  $n_\gamma + 1$  simulations for a system with  $n_\gamma$  uncertain parameters (a change to each parameter value in turn, and the nominal case for comparison) – fifty-two linearisations in this case. The total time taken with the PCM approach accounts for 2.44% of the time required for the traditional linearisation-based approach. It should also be noted that this dramatic reduction in computational time would still be present if faster methods for system linearisation are used because the PCM fundamentally reduces the number of full system linearisations required.

Table 5-6: Times taken to complete MC uncertainty studies on the five-area system.

<i>Task</i>	<i>PCM-based</i>	<i>Linearisation-based</i>
<i>Uncertain Parameter Ranking</i>	190.30 s	N/A
<i>Generate <math>\Gamma</math> sets</i>	0.21 s	N/A
<i>Identify sets with unique rank</i>	22.19 s	N/A
<i>Run linearisations and build model</i>	450.48 s	N/A
<i>10,000 MC runs</i>	4.1 s	~7 hours 36 minutes
<i>Total time taken</i>	11 minutes 7 s	~7 hours 36 minutes

### 5.4.5 Inclusion of Optimal Power Flow

In the case studies presented within this chapter, it has been assumed that generator output and loading at buses are independent random variables. In practical power systems, the behaviour of various loads and generators can be correlated.

A further investigation has been made into the use of the PCM alongside an Optimal Power Flow (OPF) solution. The same five-area network (as described in Section 5.4.1) has been used with the OPF solver minimising the generation cost based on traditional quadratic cost functions for each generation unit [166]. The details of the generator cost functions and system constraints are given in Appendix A.

Loads and VSC-HVDC lines are still as before, following normal and uniform distributions respectively.

#### 5.4.5.1 Additional Considerations

Additional factors must be considered when applying the PCM to systems using an OPF solution. Generator output power is no longer a random variable and is instead subject to the cost functions and constraints involved in the optimisation. In turn, generator output power cannot be considered to be an uncertain parameter when determining the set of collocation points. If a generator's output power is particularly variable, and therefore has a significant effect on the location of a critical oscillatory mode, it is possible that additional measures would be required in order to include the effects of its variation within the solution.

This brief illustrative case study is presented in order to demonstrate that the PCM can be utilised with OPF solutions in order to reproduce the distribution of critical system modes.

### 5.4.5.2 PCM Model Details

Following a sensitivity analysis including the OPF, it is found that a third order model consisting of eight uncertain parameters is suitable to estimate the damping factor of the critical low frequency mode. It can be seen that the reduced parameter set (5.23) consists of only loads and the two VSC-HVDC operating capacities. Details of the parameter distributions and orthogonal polynomials can be found in Appendix D.

$$\Gamma^{red} = \{P_{dc}^{VSC-1}, P_{dc}^{VSC-2}, L_{28}, L_{29}, L_{41}, L_{42}, L_{47}, L_{48}\} \quad (5.23)$$

### 5.4.5.3 Results and Discussion

The produced distributions for  $\zeta_{crit}$  are given in Figure 5-11. It is evident that good results are achieved, despite the additional complications that the inclusion of the OPF introduces. This brief illustrative study has demonstrated the feasibility of such an approach, however further work is required to thoroughly explore methods to incorporate the variation of the generators. This could perhaps be completed based upon the cost functions for the various generating units. Neglecting this generator output variation has led to slight inaccuracies in the PCM-based *pdf* for  $\zeta_{crit}$ . However, the peak value (the *most probable* value) is very similar to that produced using full system linearisations, and the distribution maintains good accuracy during the critical regions of poorest damping. As with the previous study on the large test system, the PCM model correctly provides the RoI as zero.

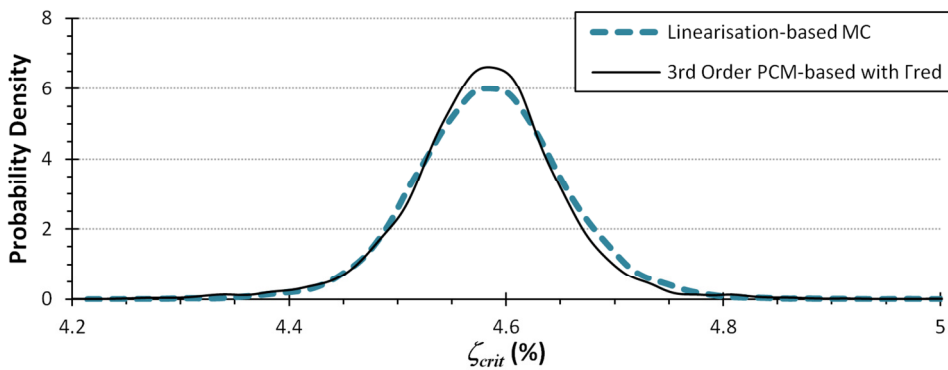


Figure 5-11: Pdfs for  $\zeta_{crit}$  with the PCM model using a reduced set of uncertain parameters and the full linearisation-based approach with an OPF solution.

## 5.5 Summary

This chapter has clearly demonstrated the suitability of the PCM for probabilistic small-disturbance stability studies. This efficient sampling approach significantly reduces the number of full power system linearisations required to produce accurate statistical

distributions for critical system parameters. Operational uncertainties have been incorporated into the small-disturbance analysis of two case study networks in order to calculate the risk of system instability (RoI) index.

For the first time in open literature, a larger number of system uncertainties has been considered simultaneously when applying the PCM to power system studies. More significantly, methods of eigenvalue sensitivity based parameter reduction have been demonstrated to facilitate the application of the PCM on large systems where inclusion of all system uncertainties would not be possible. Large levels of reduction, from fifty-one to just eight modelled uncertainties (i.e., a reduction of approximately 85%), has enabled accurate distributions of critical mode damping factors to be produced in a small fraction of the time required for traditional approaches.

There are, however, also some shortcomings of the method. It is not possible to produce models based on conditional *pdfs* between various network parameters as the orthogonal polynomials cannot be initially defined. However, the illustrative study presented has shown that the method can produce good results when used with an OPF solution. Since it has been demonstrated that accurate results are obtained following significant reduction in the number of parameters, it might be possible to model only a few key uncertainties and neglect others which have distributions that are conditional upon those key values. Further work is required to clarify these issues, though the initial results clearly demonstrated the feasibility and applicability of the PCM to probabilistic small-disturbance stability studies.

This method could be incorporated with probabilistic evaluations such as that presented previously in Chapter 4, and could facilitate a move towards the *online* probabilistic stability assessment of uncertain power systems. The PCM can also provide a means through which probabilistic values of electromechanical modes can be quickly identified as demonstrated in the following chapter.

# 6 Probabilistic Tuning of Damping Controllers

---

This thesis has shown that VSC-HVDC systems can provide a very effective means of damping persistent post-disturbance electromechanical oscillations within power systems, especially when utilising wide area signals. Furthermore, it was clearly demonstrated in Chapter 4 that such controllers do not necessarily display satisfactory levels of performance across the wide ranging operating conditions that will be typical of future power systems. Thorough probabilistic assessment of all supplementary WAMS-based POD controllers for use with VSC-HVDC systems should be completed in order to gain a full understanding of their expected behaviour and to guide mitigation strategies as required.

The previous chapter introduced the PCM as a means through which probabilistic small disturbance studies can be completed using a small fraction of full system linearisations required for traditional MC-based uncertainty studies. This efficient sampling technique was demonstrated to provide accurate results for large test system, and may in turn facilitate a move towards online probabilistic studies. This will enable fast calculation of risk indices based on the future uncertainty in system configuration, generation, and loading.

Within this chapter, probabilistic system representation is introduced as a means to more accurately account for the probabilistic variation in critical system eigenvalues. This represents the sixth original contribution of this thesis. Probabilistic studies are completed to determine the most likely open loop modal positions. The power system can then be represented using modal canonical forms of the power system state space model. This form allows manipulation of the oscillatory eigenvalues to ensure that the probabilistic values can be used during the later controller design process. Furthermore, the PCM can be used to efficiently identify these probabilistic values without the need for vast numbers of full system linearisations. In this way, the probabilistic tuning process can be easily completed.

This approach towards robust probabilistic tuning of damping controllers is presented for a six-node VSC-MTDC grid embedded within the large five-area power system. It is demonstrated that the controller designed using the probabilistic system representation is more robust than a traditionally designed controller which uses the given nominal operating conditions. The PCM is also shown to provide a good estimate of the probabilistic conditions and again provides a more robust controller than would traditionally be designed.

## **6.1 Probabilistic Controller Tuning Methodology**

It has been clearly demonstrated in previous chapters that the locations of electromechanical oscillatory modes will vary as the operating point of a power system changes. System controllers are typically designed for the nominal operating point of the network; however the real operating conditions will be defined by many factors such as load variation, renewable generation availability, and energy market fluctuations. Probabilistic mode locations, as opposed to the mode locations at the nominal operating point, should therefore be used when designing a damping controller. This will ensure that the controller action is targeted at the most likely frequencies which are associated with the modes to be damped.

### **6.1.1 Determining Probabilistic Mode Locations**

Due to the nonlinearities of power systems, the most probable modal locations do not necessarily correspond to the most probable operating conditions. The probability distributions for the open loop locations of the electromechanical modes must be determined using a MC approach and many system linearisations. Alternatively, more

efficient computational techniques can be used such as Latin hypercube, low discrepancy sequences, or the PCM which will be utilised within this chapter [134-137].

As explored in previous chapters, any distribution can be utilised to generate the operating conditions for a power network, including conditional distributions or historical information. For the presented study an optimal power flow solution was not considered, however the methodology presented could be completed using OPF. It was shown in Chapter 5 that the PCM has provided good results when used with OPF, ensuring that this sampling method could still be utilised to improve the efficiency of the proposed robust controller tuning.

Following the establishment of the probability distributions for each electro-mechanical mode, *probabilistic modes* can be defined as the most likely values for the electromechanical modes of interest. The peak values from the probability distributions for both the real and imaginary parts of the modes are selected. The use of these probabilistic modes during the controller design, rather than the nominal modes, leads to a controller which is more robust to the changing operating conditions of the power system.

### 6.1.2 Probabilistic System Representation

As previously described in Chapter 2, the linearised state space model of a power system can be rewritten in the modal canonical form of (2.84)–(2.85), reproduced as (6.1)–(6.2).

$$\dot{\mathbf{z}} = \mathbf{\Lambda}\mathbf{z} + \mathbf{B}_M\Delta\mathbf{u} \quad (6.1)$$

$$\Delta\mathbf{y} = \mathbf{C}_M\mathbf{z} + \mathbf{D}\Delta\mathbf{u} \quad (6.2)$$

The modal transition matrix  $\mathbf{\Lambda}$  is diagonal with the structure (6.3).

$$\mathbf{\Lambda} = \text{diag} \left\{ \left[ \lambda_1 \cdots \lambda_{n_r} \right], \left[ \begin{array}{cc} \sigma_1 & \omega_1 \\ -\omega_1 & \sigma_1 \end{array} \right] \cdots \left[ \begin{array}{cc} \sigma_{n_c} & \omega_{n_c} \\ -\omega_{n_c} & \sigma_{n_c} \end{array} \right] \right\} \quad (6.3)$$

In (6.3),  $\lambda_1 \cdots \lambda_{n_r}$  are the purely real eigenvalues;  $n_r$  is the number of real eigenvalues,

the  $2 \times 2$  block diagonals  $\left[ \begin{array}{cc} \sigma_1 & \omega_1 \\ -\omega_1 & \sigma_1 \end{array} \right] \cdots \left[ \begin{array}{cc} \sigma_{n_c} & \omega_{n_c} \\ -\omega_{n_c} & \sigma_{n_c} \end{array} \right]$  correspond to the complex pairs of

eigenvalues  $\lambda_i = \sigma_i \pm j\omega_i$ , and  $n_c$  is the number of complex eigenvalue pairs. An

example of the modal canonical representation for a simple system is presented in Appendix E.

With the system represented in a diagonal form, the mode locations for the nominal system can be modified to represent the probabilistic modes which have already been determined. Values in  $\Lambda$  are altered for the critical electromechanical modes of interest to represent the probabilistic values. Following this, the control design can be completed using the probabilistic system representation.

## 6.2 Test System Details

As with many of the novel ideas presented within this thesis, the application of the method is best presented using a case study. The robust probabilistic tuning of a damping controller will be completed using a complex study system, utilising the large five-area test network with the inclusion of an embedded VSC-MTDC grid with connected stochastic wind generation.

### 6.2.1 Modifications to the Test Network

The large five-area power system, with an embedded VSC-MTDC grid and a 300 MW wind farm represents a possible future network scenario – particularly for the UK when considering the wind farm connections which will be completed within the North Sea. As in Section 3.4, the inter-area tie-lines 18–49 and 41–40 have been removed. In place of these removed AC lines, a six-bus, seven-line VSC-MTDC grid has been installed, as shown in Figure 6-1 below. A wind farm with a maximum generating capacity of 300 MW is connected to this VSC-MTDC grid via the converter station at node 6. The converter station at MTDC node 1 is the DC *slack* bus. Data and controller settings for the VSC-MTDC grid are provided in Appendix A.

#### 6.2.1.1 VSC-MTDC System Details

Nominal values of active power injection for VSC-MTDC converters 2–5 are set based on previous AC tie line power flows. Active power flow injection at MTDC node 6 is determined by the output of the connected wind farm. Reactive power injection at the MTDC nodes 1–5 is regulated at zero. At MTDC node 6, reactive power is supplied by the converter as required to support the wind farm. At each MTDC node regulating power flow excluding the wind farm (i.e., MTDC nodes 2–5), a supplementary input signal  $\Delta P^{ref}$  is available which can be used to modulate the active power reference set-points for stabilising purposes. This modulation is limited to 10% of rated capacity.

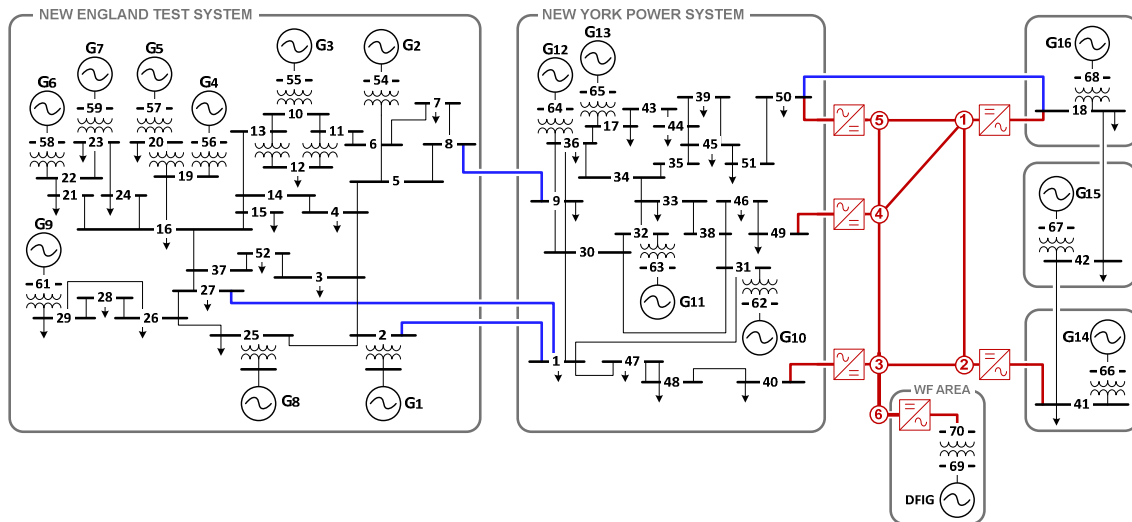


Figure 6-1: Five-area test network with VSC-MTDC and wind generation installed.

### 6.2.1.2 Wind Farm System Details

For the purpose of the studies performed, it has been assumed that power output from the wind farm is constant during the linearisation and analysis of each operating point. MTDC node 6 is connected to the wind farm and operates with *frequency-voltage* control. It is also assumed that the converter is able to maintain a constant AC voltage, so that all power produced by the wind farm is transferred to the VSC-MTDC system. This assumption is valid provided the MTDC system voltage does not deviate considerably. This is an acceptable simplification for studies focussed on the post disturbance stabilisation of the main AC system and controller robustness to variable operating conditions – and not the fast transient performance of the VSC-MTDC grid.

The modelled wind farm consists of 150 Vestas V-80 2 MW turbines [183]. All wake effects are neglected so the total wind farm power produced is calculated from the wind speed and the power curve for the turbine, scaled by the number of turbines.

### 6.2.2 WAMS-Based POD Control

The test system which has been described displays four low frequency modes requiring additional damping. The fast controllability of the VSC-MTDC grid is exploited in order to provide this additional damping through modulation of the active power injection at all MTDC nodes regulating active power flow. The WAMS-based MLQG controller structure described in Section 2.4.2 (and shown to be effective in numerous examples throughout this thesis) is used to provide this POD action.

### 6.2.2.1 Nominal Controller Design

Controller inputs are selected by modal observability as the AC power flows through the following lines:  $y_1^{MLQG} : P_{ac, 45-51}$ ,  $y_2^{MLQG} : P_{ac, 68-18}$ ,  $y_3^{MLQG} : P_{ac, 65-17}$ , and  $y_4^{MLQG} : P_{ac, 67-42}$ . These four wide area signals are subject to delays of 375 ms [20-23]. Controller output signals are assumed to have negligibly small delays representing hard-wired fibre-optic connections to all MTDC converter stations ( $u_1^{MLQG}, \dots, u_4^{MLQG} : \Delta P_{dc, 2}^{ref}, \dots, \Delta P_{dc, 5}^{ref}$ ).

Table 6-1: Inter-area mode details for the five-area network with embedded VSC-MTDC grid and wind farm with and without an MLQG POD controller in place.

Mode	No POD		MLQG POD	
	Frequency (Hz)	Damping Factor (%)	Frequency (Hz)	Damping Factor (%)
Mode 1	0.253	4.47	0.253	12.30
Mode 2	0.427	4.61	0.437	13.11
Mode 3	0.623	4.27	0.623	11.27
Mode 3	0.780	4.81	0.780	11.84

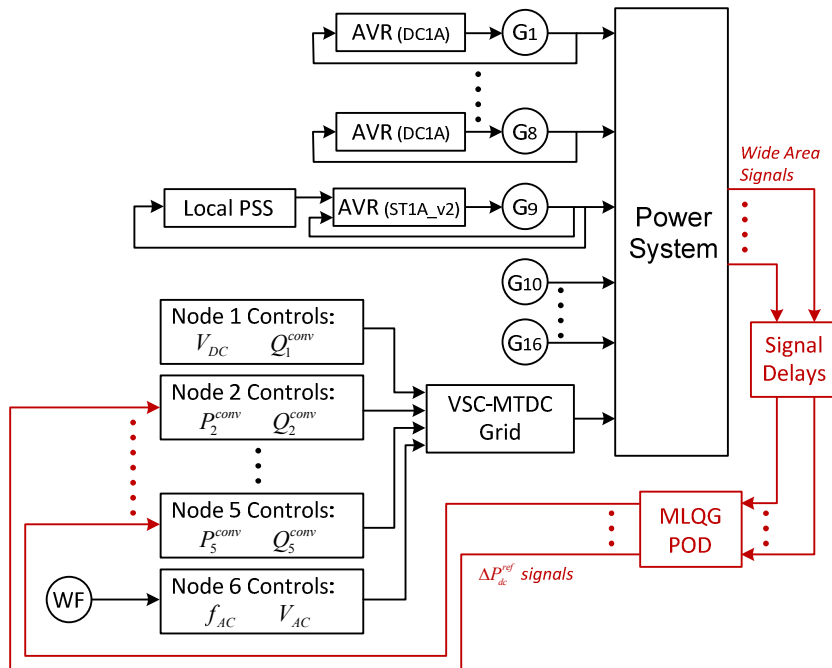


Figure 6-2: Control overview for the five-area network including VSC-MTDC grid and wind farm, with MLQG POD controller.

The full linearised power system model of 235<sup>th</sup> order is used during the controller synthesis. The modal weighting matrix  $\mathbf{Q}_M$  is finely tuned to achieve equal target damping factors of 20% on each of the four low frequency modes. These weights are

then reduced uniformly to limit the gain of the largest singular value of the LQR transfer function to 6dB in order to improve robust stability properties [162]. The final controller is then reduced to lessen the online computational burden of the controller. The bound on the final controller order was set to limit low frequency mode damping factor degradation to no more than 5%, resulting in a 32<sup>nd</sup> order POD controller. The fixed parameters used during the LTR tuning process are included in Appendix A. The low frequency mode details (with no POD, and with this reduced order *nominal controller* installed) are given in Table 6-1. The full system control overview is presented in Figure 6-2 including the POD controller.

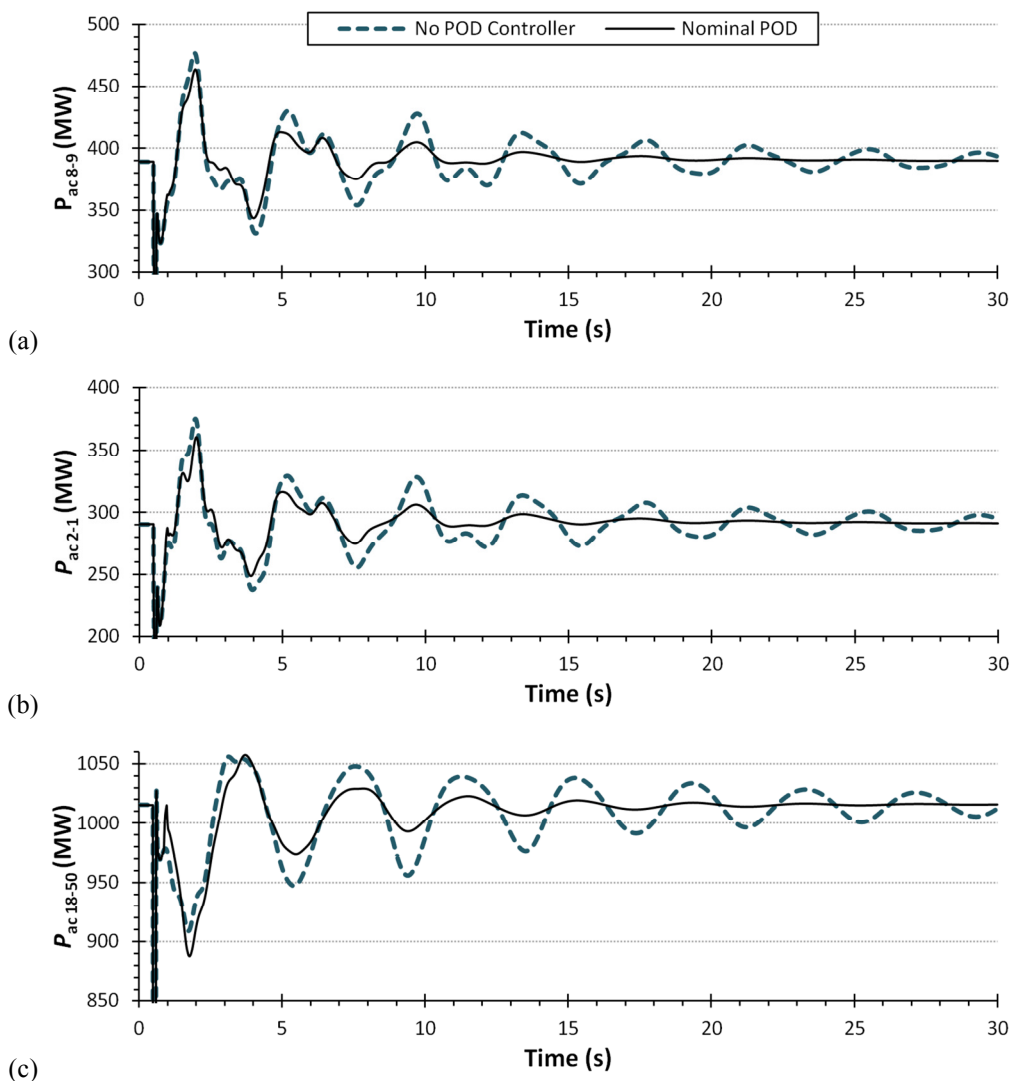


Figure 6-3: Transient performance of the *nominal* controller at the nominal operating point demonstrated by the stabilisation of power flow through (a) line 8–9, (b) line 2–1, and (c) line 18–50.

An example of the transient performance of the system at the nominal operating point is presented in Figure 6-3 where the AC power flow through the three largest inter-area tie-lines (8–9, 2–1, and 18–50) are shown. The final inter-area tie-line transfers only

29.6 MW and the oscillations present on this flow could be easily tolerated in a practical power system. The system is subjected to a 100 ms self-clearing three-phase fault at bus 43 within the NYPS area. The post-disturbance oscillations within the interconnected AC network are effectively damped using the MLQG POD controller.

### 6.3 Application of Probabilistic Controller Tuning

In order to complete the probabilistic controller tuning, the variation of system parameters must be known in order to identify the probabilistic mode locations. Historical or forecast data could be utilised if known. In this case study, generator power output and load demand are assumed to be normally distributed, wind speed follows a Weibull distribution, and VSC-MTDC converter station power injection follows a uniform distribution. Operating conditions are selected by drawing operating points from the specified distributions. Only feasible operating conditions with converged load flows and stable open loop modes are considered. Probabilistic studies are performed using 5000 system simulations, drawing operating parameters from the distributions outlined below.

#### 6.3.1 Variation in System Operating Conditions

Generators are modelled with non-varying voltage and normally distributed active power output. System loads are modelled with constant power factor and normally distributed active power demand. Generators and loads are modelled with a normal distribution with 25% range at  $3\sigma_\gamma$  around the mean nominal values  $\mu_\gamma$ . As in previous studies, generators are modelled as *PV* buses with constant voltage output with generator G13 the slack bus. Loads are considered to have constant power factor when producing their random parameter values.

VSC-MTDC power injection values are set as uniformly distributed around the nominal values. MTDC nodes 2–5 have nominal values of power injection into the AC grid of –600, 400, 350, and 500 MW respectively. The uniform distribution at each node is limited to  $\pm 100$  MW.

The generation capacity of the wind farm is determined by the wind speed  $v$ . For these studies, wind speed is a random variable following a Weibull distribution, as described by (6.4).

$$f(v) = \begin{cases} \frac{k}{\varphi} \left(\frac{v}{\varphi}\right)^{k-1} e^{-(v/\varphi)^k} & v \geq 0, \\ 0 & v < 0, \end{cases} \quad (6.4)$$

In (6.4),  $k$  is the *shape parameter* and  $\varphi$  is the *scale parameter* (commonly signified by  $\lambda$  but called  $\varphi$  here to avoid confusion).

In this study, values for these parameters are adopted from [184] with  $k = 2.2$  and  $\varphi = 11.1$ , implying a mean wind speed of  $\bar{v} = 9.83 \text{ ms}^{-1}$ . This distribution is shown in Figure 6-4 alongside the power curve for a Vestas V-80 turbine [183]. The wind farm consists of 150 of these machines. The total power produced is calculated by randomly selecting a wind speed, calculating the power produced at this speed from the power curve for the V-80 turbine, and finally scaling the individual turbine output to the capacity of the whole wind farm.

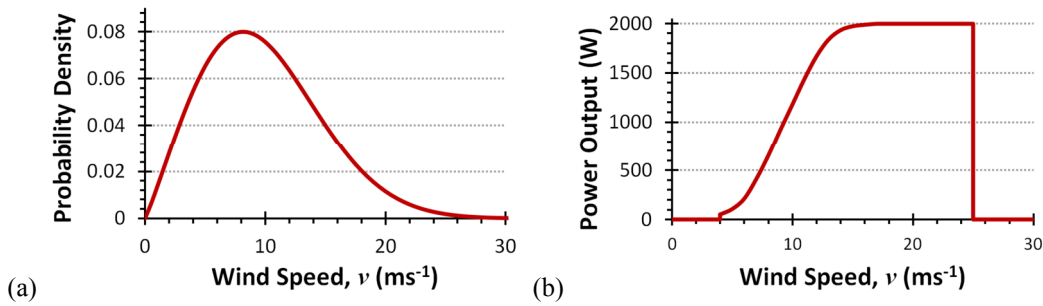


Figure 6-4: (a) Weibull distribution of wind speed, and (b) Vestas V-80 2 MW turbine power curve.

### 6.3.2 Identification of Electromechanical Modes

The robustness of the designed supplementary POD controllers is assessed through small disturbance analysis. As in previous studies with the MLQG POD controller, this requires the use of classification tools to ensure fast and accurate identification of the critical low frequency modes. A Naïve Bayes classifier is again used to identify the necessary modes based on their damping, frequency, and system state modal participation factors.

### 6.3.3 Results and Discussions

The designed nominal controller is tested for the wide ranging operating conditions described. This assessment can identify modes which see poor damping factors and suggest where the probabilistic approach may offer some advantages.

### 6.3.3.1 Performance of the Nominal Controller

The results of subjecting the nominal controller to the variation in operating conditions are presented in Figure 6-5. This plot shows the closed loop locations of the four inter-area modes when the POD controller is installed. The *crescent* shape of the modal spread is similar that originally seen in Chapter 3 when the effects of varying HVDC operating capacity were investigated on the small test system. Clearly for this study a wide variety of parameters are being varied, however the effect of some of these parameters is to cause the same type of variation in modal position.

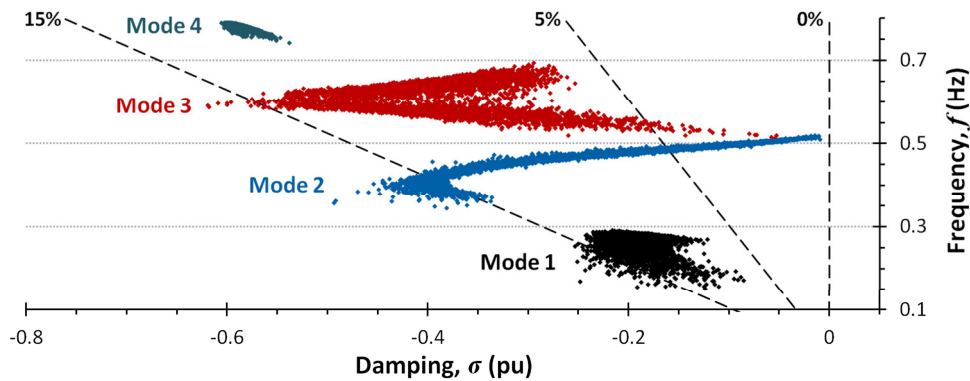


Figure 6-5: Closed loop low frequency model locations with *nominal* controller installed. Dashed lines signify damping factors of 0%, 5%, and 15%.

Modes 1 and 4 maintain damping factors greater than 5% for all operating conditions. This is also true for the vast majority of operating conditions for Mode 3, which sees the damping factor drop below 5% in just 30 of the 5000 tested conditions; i.e.,  $P(\zeta < 5\%) = 0.6\%$ . This low risk of poor damping could be considered tolerable in practical power systems, although it is desirable for  $P(\zeta < 5\%)$  to be zero. Mode 2 is more problematic and does not demonstrate satisfactory performance with  $P(\zeta < 5\%) = 27.1\%$ . Modes 1, 3, and 4 can be considered to have satisfactory damping across all operating conditions but this is not true for Mode 2. The probabilistic tuning method may improve the controller robustness.

### 6.3.3.2 Open Loop Modes

By assessing the position of the open loop low frequency modes, the extent to which the use of probabilistic tuning will improve the controller's robustness can be judged. If the probabilistic modes have the same values as the nominal modes, the final *probabilistic controller* design will be the same as the nominal controller which has already been

tested. Figure 6-6 below displays the spread of open loop mode positions seen due to the variation in operating conditions.

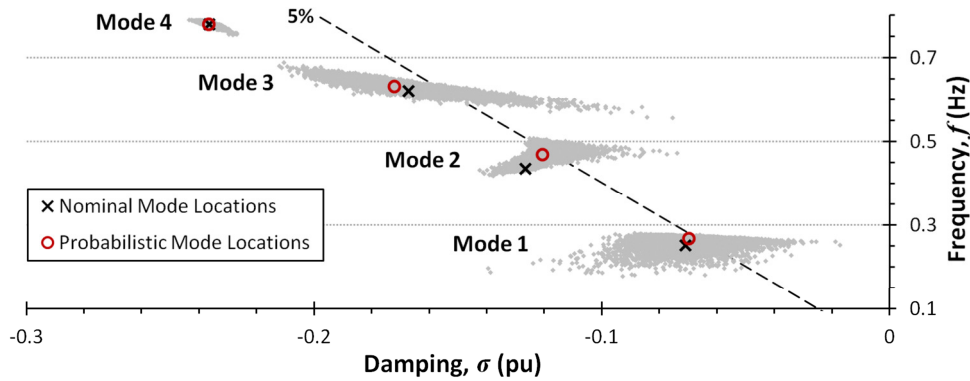


Figure 6-6: Open loop low frequency mode locations, including the nominal and probabilistic values. The dashed line signifies a damping factor 5%.

Figure 6-6 also shows the nominal open loop mode positions and the probabilistic locations based on the modal spread observed. It can be seen that the nominal mode locations are not always representative of the probabilistic values. It is also evident that the greatest disparity between the nominal and probabilistic values is for Mode 2 – the mode experiencing the poorest closed loop performance. Use of the probabilistic values for Mode 2 should improve the controller’s robust performance with respect to the damping of this mode. This will be completed in order to demonstrate the benefits of using the proposed probabilistic system representation.

It should also be noted that this modal spread will be dependent on the variation in operating conditions, and therefore the disparity between the probabilistic and nominal mode locations could be much greater for other systems than those shown in Figure 6-6. This disparity is also clearly dependent on the designation of the nominal operating point, which could further accentuate the variation between the two representative modal locations.

The *pdfs* for the open loop modal damping factors are given in Figure 6-7 below. These have been produced based on the modal spread observed in Figure 6-6. The non-Gaussian variation in the spread of damping factors of these critical low-frequency modes can clearly be seen.

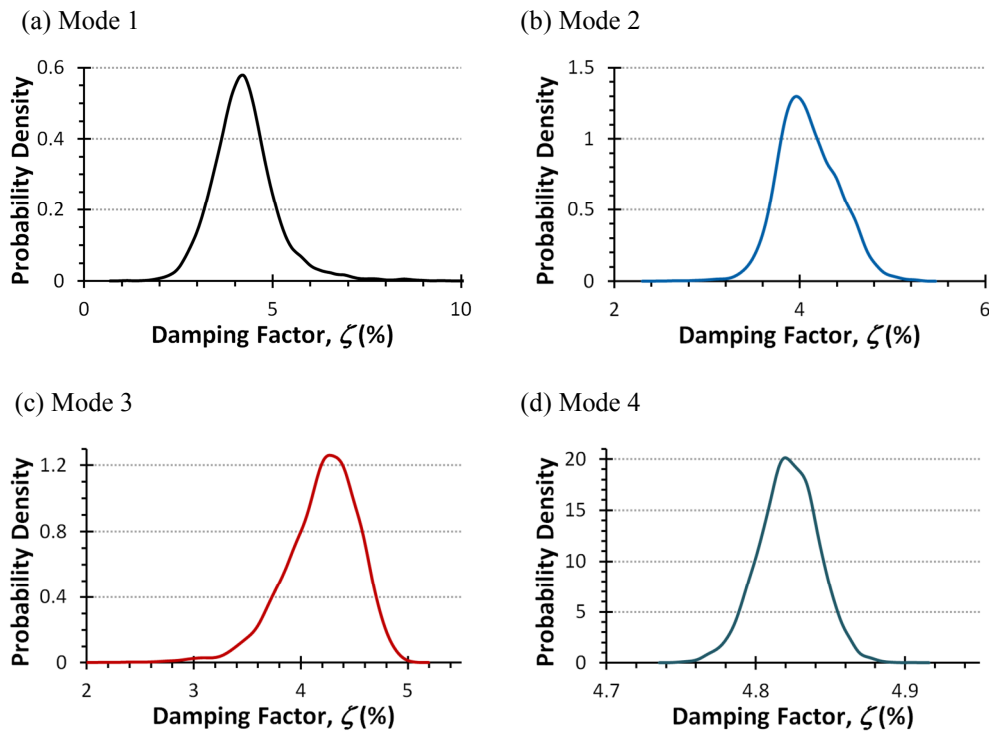


Figure 6-7: Pdfs for the open loop damping factors of the low-frequency modes.

### 6.3.3.3 Performance of the Probabilistic Controller

The process of designing the controller is completed once more using the probabilistic values for Mode 2:  $\lambda_{prob}^{Mode 2} = -0.121 \pm j2.96$  (obtained as described in Section 6.1.1). Standard nominal values are used for the remaining low frequency modes to highlight the benefits made to Mode 2. Again, the target damping is set at 20% per mode, the LQR singular value gain limited to 6dB, and the final controller reduced to 32<sup>nd</sup> order. This probabilistic controller can now be reassessed against the full range of defined operating conditions.

A box and whisker plot is used to compare the results achieved using the nominal and probabilistic controllers, presented as Figure 6-8. The boxes represent the 25<sup>th</sup> and 75<sup>th</sup> percentiles; the bar within the box shows the median, the whiskers show the minimum and maximum values, and the notches on the whiskers display the 2.5<sup>th</sup> and 97.5<sup>th</sup> percentiles (i.e., 95% of the data is contained within these notches).

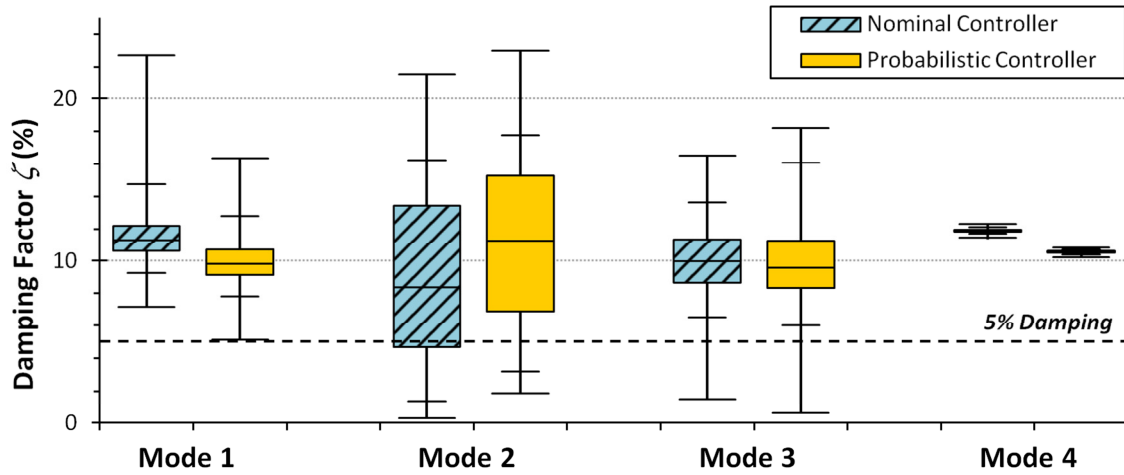


Figure 6-8: Damping factors for the low frequency modes with the *nominal* and *probabilistic* controllers installed.

It is evident from Figure 6-8 that the use of the probabilistic system representation (containing the probabilistic value for Mode 2 only) has improved the robustness of the controller with respect to the damping factor of Mode 2. The damping factor for Mode 3 is largely unchanged, and that of Mode 4 is slightly reduced but remains greater than 10%. Mode 1 also experiences slightly reduced damping but  $P(\zeta < 5\%)$  is still equal to zero. These small changes are due to variations in the weighting factors used during controller synthesis. The main area of interest is Mode 2, which has improved considerably such that  $P(\zeta < 5\%) = 12.3\%$ . This improvement (down from 27.1%) is due to the use of the probabilistic mode location for Mode 2.

It should be acknowledged that achieving  $P(\zeta < 5\%) = 0$  for each mode is not the direct aim of this study, although it would be desirable for optimal system performance with respect to oscillation damping. This study instead illustrates the benefits of using a probabilistic approach to controller tuning. The simple use of the probabilistic modal location for the poorly damped Mode 2, ascertained through simulation of the known variation in operating conditions, results in a more robust damping controller.

#### 6.4 Application of the Probabilistic Collocation Method

It has been shown that the use of a probabilistic system representation resulted in a more robust controller performance with respect to the damping of Mode 2. In order to create this probabilistic system representation, the most probable values of the eigenvalue relating to Mode 2 must be determined. It was shown previously in Chapter 5 that the PCM can be used to accurately produce the distributions of system modes using a small

number of full system linearisations. This can be exploited to provide the probabilistic mode location for Mode 2, which will be used to produce the POD controller. This avoids the need for thousands of full system linearisations and significantly reduces the computational time required to produce the controller.

The case study system (as described in Section 6.2) consists of a set  $\Gamma$  of fifty-four uncertain network parameters: fifteen generators (excluding the slack), thirty-four loads, four VSC-MTDC nodes, and one wind farm (dependent on the wind speed  $v$ ). As previously shown in Chapter 5, the number of coefficients to deduce (and therefore the number of full system linearisations to perform) increases very quickly as the number of system uncertainties rises, as per (5.11). For systems containing large numbers of uncertainties, parameter reduction is required to ensure that a large number of full linearisations are not required – therefore preserving the benefits introduced by the PCM.

#### 6.4.1 Reduction in Modelled Uncertainties

The number of considered system uncertainties is reduced using the eigenvalue sensitivity based ranking index (5.21), introduced previously in Chapter 5. These rank values are calculated for the full set of fifty-four uncertain system parameters with respect to the critical Mode 2. Ranks are determined using a 1% change in the each parameter value. As both damping and frequency are to be calculated from the PCM model, ranking has been completed for each of these outputs in turn, before normalising the results and summing the resulting rank values.

In many cases, it is possible to use the calculated rank values to directly assess which parameters are suitable for inclusion in the reduced set of uncertainties. For this case study, a short analysis is performed to identify parameters which have an  $r_{\lambda_i \gamma_j}$  value which is greater than double the next highest rank value. Such a sharp decline in  $r_{\lambda_i \gamma_j}$  between two parameters suggests a significant reduction in the parameter's importance and influence on the position of the critical mode. Such an interval occurs just four times: between parameters 1–2, 10–11, 52–53, and 53–54. It is highly likely that more than one uncertain parameter will be required, and also that modelling fifty-two or more uncertainties is impractical with the PCM. Therefore, the  $r_{\lambda_i \gamma_j}$  values indicate that the top ten ranked parameters should provide a suitable approximation when concerned with the location of Mode 2.

The reduced set of parameters is given in (6.5) below and consists of the wind speed, three generators, two VSC-MTDC nodes, and four loads. All remaining parameters are modelled as constant at their nominal operating points during production of the PCM model.

$$\Gamma^{red} = \{v, G_{14}, G_{15}, G_{16}, P_{dc}^{MTDC-3}, P_{dc}^{MTDC-4}, L_{18}, L_{41}, L_{42}, L_{50}\} \quad (6.5)$$

#### 6.4.2 Discontinuities in Wind Farm Power Output

The power curve for the Vestas V-80 2 MW turbine, shown in Figure 6-4(b) above, displays discontinuities which must be taken into account when applying the PCM. The wind speed is ranked as the most influential parameter affecting the location of Mode 2, and must be included as a PCM model function input.

The wind speed can be considered as operating in the following three distinct regions:

- (i) At wind speeds when the wind farm produces no power ( $v < 4 \text{ ms}^{-1}$ , or  $v \geq 25 \text{ ms}^{-1}$ ).
- (ii) At wind speeds when power output is curtailed at the maximum wind farm capacity of 300 MW ( $18 \leq v < 25 \text{ ms}^{-1}$ ).
- (iii) At wind speeds when power output is variable ( $4 \leq v < 18 \text{ ms}^{-1}$ ).

For each of these operational regions, a separate PCM model was produced. The models for cases (i) and (ii) do not require any variation of the wind speed  $v$ , as it will not affect the power produced by the wind farm. Therefore, the wind speed can be modelled as constant within the regions defined above. These PCM models take the remaining nine uncertain parameters in  $\Gamma^{red}$  as inputs. The model for case (iii) uses the complete set of ten reduced parameters. The correct model is then later selected during the MC runs of the PCM function, dependent on the randomly selected value of wind speed.

#### 6.4.3 PCM-Based Probabilistic Modal Estimation

The PCM is used to estimate both the damping  $\sigma$  and frequency  $\omega$  of Mode 2 under the presence of the detailed system uncertainty. This is completed using the reduced set of system uncertainties  $\Gamma^{red}$ . From the produced distributions, the PCM-based probabilistic modal location is determined as  $\lambda_{PCM}^{Mode 2} = -0.122 \pm j2.89$ . As only the most probable values are required for the modal tuning (the peaks of the produced

distributions), some accuracy can be sacrificed at the tails of the distributions and 2<sup>nd</sup> order PCM models are sufficient. This further reduces the number of full system linearisations required.

Figure 6-9 presents the probabilistic values for  $\sigma$  and  $\omega$  for Mode 2 determined using increasing numbers of uncertain parameters (according to the ranking order previously established). This figure demonstrates the validity of selecting the top ten ranked parameters as it can be seen that after ten parameters have been modelled there is little further variation in the probabilistic modal values. The plot of the damping value  $\sigma$  shows that the addition of the 6<sup>th</sup> and 7<sup>th</sup> parameters has very little impact upon the probabilistic value obtained. This suggests that the ranking index used is providing a poor ranked parameter order. It should be noted however that the ranking was based upon both damping and frequency, and it can be seen that the addition of the 6<sup>th</sup> and 7<sup>th</sup> parameters has a significant effect on the probabilistic frequency value – justifying the inclusion of these uncertainties.

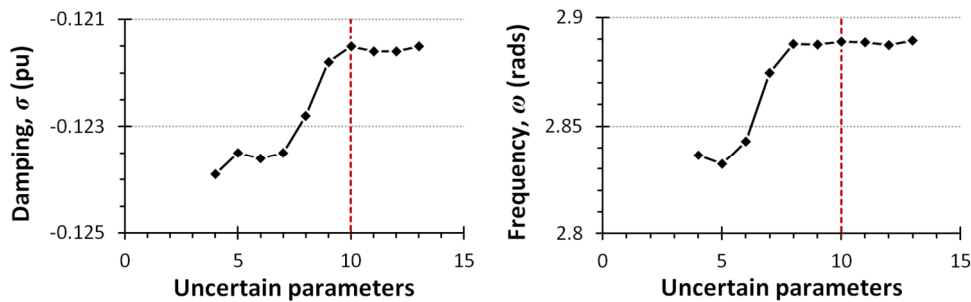


Figure 6-9: PCM-based probabilistic values for Mode 2 with increasing numbers of modelled uncertain parameters.

If the previously calculated  $r_{\lambda_i \gamma_j}$  values do not directly suggest a suitable number of parameters to be included in the reduced set  $\Gamma^{red}$ , then it is possible to create models of increasing order until little variation in the probabilistic mode values is seen – as demonstrated in Figure 6-9. This will require more computational time and full linearisations than making a direct assessment based on the rank values. On the other hand, producing these low order models with small numbers of parameters still requires significantly fewer full linearisations than a traditional MC-based approach and significant savings can still be seen.

An assessment of the PCM-based probabilistic values for Mode 2 shows that this mode location is much closer to that produced from the traditional MC-based approach than the previous nominal location. It is also evident that some discrepancy between the

frequency values remains, due to the approximations of the PCM approach. This may lead to some deterioration in controller robustness and will be investigated further.

#### 6.4.4 Results and Discussions

A new MLQG POD controller is synthesised, this time using the PCM-based probabilistic location of Mode 2. As before, target damping factors of 20% are used for each low frequency mode, the maximum singular value gain is limited to 6dB and the final controller is reduced to 32<sup>nd</sup> order. This PCM-based probabilistic controller is assessed using 5000 simulations across the full range of system conditions.

##### 6.4.4.1 Performance of the PCM-Based Probabilistic Controller

The distributions of the damping factors witnessed with both the traditional MC-based and PCM-based probabilistic controllers installed are compared in Figure 6-10 below. This figures shows that the two controllers perform very similarly, with only a slight reduction seen in the damping of Mode 2. It was anticipated that this may occur, due to the slightly reduced  $\omega$  value produced by the PCM approach compared with the traditional MC approach.

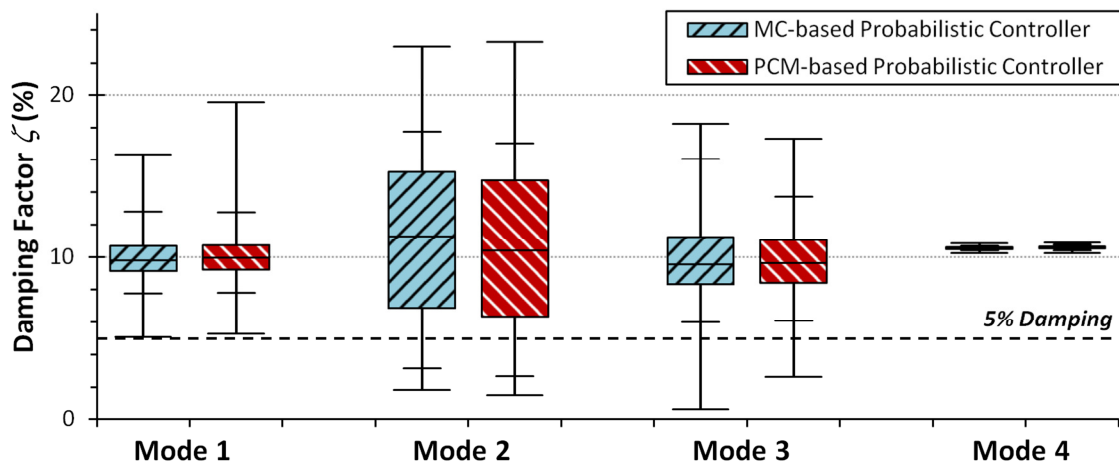


Figure 6-10: Damping factors for the low frequency modes with the MC-based and PCM-based probabilistic controllers installed.

Analysis of the obtained results reveals that  $P(\zeta < 5\%) = 16.1\%$  for Mode 2 when using the PCM-based probabilistic controller. This represents a slight increase when compared with the 12.3% seen using the MC-based probabilistic controller. However, this is a large improvement compared to the initial value of 27.1% achieved using the nominal controller. The risk of poor damping,  $P(\zeta < 5\%)$ , for each low frequency mode with each controller installed is summarised in Table 6-2 below.

Table 6-2: Risk of poor damping for low frequency modes.

Controller	Risk of Poor Damping, $P(\zeta < 5\%)$			
	Mode 1	Mode 2	Mode 3	Mode 4
Nominal	0%	27.1%	0.60%	0%
MC-based Probabilistic	0%	12.3%	1.08%	0%
PCM-based Probabilistic	0%	16.1%	0.96%	0%

Both probabilistic controllers lead to a marked reduction in the risk of poor damping for Mode 2 compared with the nominal controller. Importantly, they do not cause a significant change in the damping of the remaining modes. This is particularly so in the case of Mode 3, for which  $P(\zeta < 5\%)$  remains roughly equal to 1% in all cases.

The *pdfs* for the closed loop damping factor of Mode 2 with each controller installed is presented in Figure 6-11. These *pdfs* have been produced using a kernel density smoothing algorithm and it should be noted that no values of negative damping factor were recorded for any controller (as shown by the previous box plots). The improvement made by the use of the probabilistic controllers is clear. The probability density is reduced for low damping factor values and increased for high damping factors. The PCM-based probabilistic controller displays a very slight reduction in performance compared to the MC-based probabilistic controller. This is caused by the slight error in probabilistic Mode 2 values used for the controller synthesis.

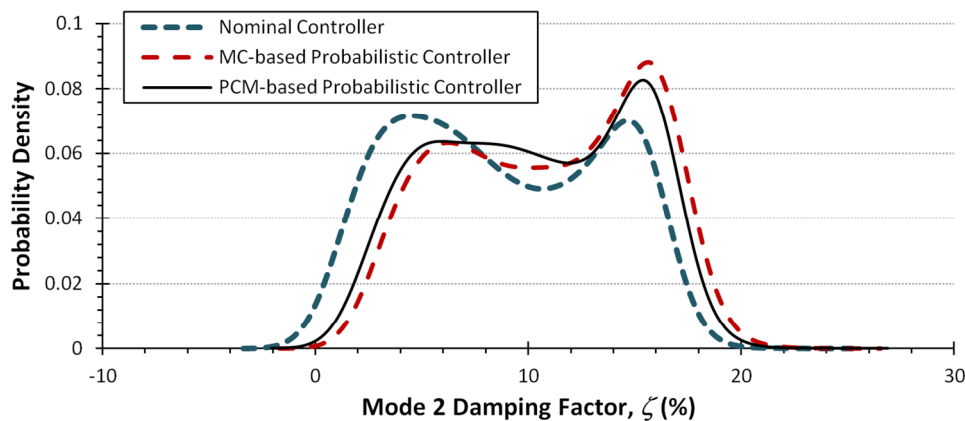


Figure 6-11: *Pdfs* for the damping factor of Mode 2 with different controller designs in place.

Ideally the variation in closed loop damping of Mode 2 would be reduced further in order to guarantee a given value of damping factor for this mode. This is however a problem that is dependent upon the closed loop performance of the controller structure given the uncertainty that is modelled. The probabilistic state representation is able to improve on this by skewing the *pdf* towards the high damping factor regions. A new

controller design based on a different structure and synthesis technique may be required if this performance is not considered acceptable.

#### 6.4.4.2 Computational Savings using the PCM

This chapter has clearly demonstrated that the use of probabilistic system representation results in improved controller robustness and therefore a more stable system, particularly when concerning oscillatory modes which display poor closed loop damping. The necessity to perform a large number of full system linearisations in order to create the probabilistic representation of the power system may however prove prohibitive, especially for large power systems. This case study has demonstrated that the PCM can be exploited to significantly reduce the number of full linearisations required, whilst still achieving improved controller robustness.

The process of parameter ranking based on eigenvalue sensitivity requires  $n_\gamma + 1$  linearisations for a power system with  $n_\gamma$  uncertain parameters; consisting of a change to each parameter in turn and the nominal case for comparison. The number of full simulations required when creating each of the three PCM models for this network is found using (5.11) within Chapter 5. This is equal to fifty-five linearisations for both cases (i) and (ii), and sixty-six for case (iii) – totalling 176 full system linearisations. The total computational times taken to produce the probabilistic values for Mode 2 using the PCM are detailed in Table 6-3.

Table 6-3: Computational process times for the Probabilistic Collocation Method.

<i>Process</i>	<i>Time Taken (s)</i>
Eigenvalue sensitivity analysis (55 full linearisations)	190.3
Identification of operating conditions for PCM model	46.2
Full system linearisation (176 full linearisations)	604.2
5000 MC runs with model function	1.0
<b>Total</b>	<b>841.7</b>

This total time taken, approximately 14 minutes, is just 4.8% of the time taken to perform the traditional MC approach where 5000 linearisations take approximately 17,660 s (almost five hours). The PCM can therefore be used to quickly assess probabilistic modal locations with minimal loss of accuracy in order to enable robust damping controller designs.

Table 6-4: Time taken and probability of poor damping for Mode 2 with each controller design.

<i>Controller Design Approach</i>	<i>Time Taken (s)</i>	<i>Mode 2 <math>P(\zeta &lt; 5\%)</math></i>
Nominal Controller	3.1	27.1%
PCM-based Probabilistic Controller	841.7	16.3%
MC-based Probabilistic Controller	17,660	12.3%

The time taken to complete each controller design and the associated values of risk of poor damping for Mode 2 are collated in Table 6-4. The additional time and effort required in order to improve the final closed loop controller performance is evident. When such controllers are designed, a judgement must be made as to whether the increased design effort can be afforded.

It should be noted that in Chapter 5 the PCM was shown to be an effective tool for the rapid assessment of modal distributions. The combination of fast controller design and efficient testing may facilitate the evaluation of a much greater number of controllers of varying structure and design for a large variety of system conditions and contingency situations. This in turn will lead to the selection of the most robust controllers, ensuring good practical performance.

## 6.5 Summary

Within this chapter, a method to improve the robustness of WAMS-based damping controllers in the presence of operational uncertainties has been presented. The use of a novel probabilistic system representation has been clearly demonstrated to improve the performance of controllers when subjected to uncertainties. The methodology was illustrated using a complex test system representative of possible future transmission systems, incorporating an embedded multi-node VSC-MTDC system as well as stochastic wind generation.

The PCM was effectively utilised to efficiently determine the probabilistic values of critical system eigenvalues which were then used to design the POD controller with improved robustness. The use of this efficient sampling technique vastly reduces the number of full system linearisations required as previously shown. In the example case study provided this resulted in over 95% computational time savings, transforming the approach from potentially prohibitively slow to readily achievable on practical systems.

The proposed approach illustrated within this chapter is not limited by the chosen controller structure, controller synthesis technique, nor the nature of the uncertainties

considered. It could be implemented with any WAMS-based POD controller design which is based on a linearised power system model and with any number and type of uncertainties (both parametric and operational). As such, the proposed technique is widely applicable.

The methodology proposed represents the union of many of the ideas developed throughout this thesis. In Chapter 3, the extensive analysis into the effects of HVDC systems concluded that a large potential exists to exploit the fast controllability of these emerging embedded systems through suitable controllers to improve power system stability. Such controllers were then investigated in Chapter 4, where the need for a thorough assessment of controller robustness to system variations was established. Finally, the PCM was implemented effectively on small and large systems in Chapter 5 to efficiently produce the statistical distributions of critical system modes. Within this chapter, the probabilistic values obtained from the PCM approach have been utilised to create a probabilistic system representation. This has been used to create a WAMS-based POD controller which modulates the power injection from a VSC-MTDC grid to stabilise post-disturbance power system oscillations. Moreover, this controller has been assessed across wide ranging operating conditions and has been proven to be more robust than standard nominal controller designs.

# 7 Conclusions and Future Work

---

## 7.1 Conclusions

This thesis has thoroughly evaluated the improvements to small-disturbance stability that HVDC-based power oscillation damping control can achieve. In completing this research, probabilistic methods have been developed which assess the performance of damping controllers and subsequently design controllers which are more robust to variable operating conditions.

The design of effective and robust POD controllers for HVDC systems is both important and relevant for power system operators. The number of HVDC projects is dramatically rising, whilst traditional AC power lines are increasingly facing limitations caused by power oscillations. Additionally the penetration of intermittent renewable energy sources is resulting in highly variable operating conditions. The combination of these factors means that it is important to exploit the fast controllability of HVDC systems in order to improve system stability, as well as to thoroughly assess any designed controllers to ensure that they perform satisfactorily across all system conditions.

A thorough review of past research surrounding POD control revealed that numerous controller designs and implementation strategies have been previously proposed. Despite the availability of multiple control strategies, and the increasing availability of WAMS-based signals, POD controllers within practical power systems continue to use a traditional PSS-based structure. The review identified that a comprehensive evaluation of a single, readily applicable, WAMS-based controller implemented with HVDC systems is required.

This evaluation has been completed and represents the first original contribution of the thesis. A WAMS-based multi-variable controller structure has been compared with a traditional PSS-based design for a variety of HVDC systems. The MLQG control structure, which has previously only been implemented as an advisory controller for generator PSSs was developed further for application with VSC-HVDC lines in test systems of varying size. This modal design of the LQG control formulation allows targeted action on specified critical oscillatory modes whilst leaving adequately damped locally controlled modes unaffected. The potential to exploit HVDC lines for stabilising purposes was clearly demonstrated, as well as comprehensively establishing the benefits of the complex control structure using wide area signals. The MLQG controller was shown to be more robust to changing operating conditions than the PSS-based design, outperforming the simpler structure on both small and large test systems. This continued to be the case when the WAMS-based signals were subjected to lengthy transmission delays. It was also shown that the MLQG controller is resilient to significant increases of signal transmission delay, and complete signal loss. Further analysis demonstrated that the modulation of reactive power (which is possible with VSC-HVDC systems) offers few additional stabilising benefits when compared with active power modulation, thereby confirming the findings of previous research.

The review of past research revealed that a wide range of modulation capacities have often been considered, with values of up to 40% of rated capacity stated as suitable for short-term overload situations. The second original contribution of this thesis is a study into the effects of limiting the modulation capacity available for POD action. This has shown that system stabilisation is quickest when large capacity is available. It was also demonstrated that clear benefits remain with the MLQG controller when the modulation capacity is limited to just  $\pm 5\%$  – with the five-area test system stabilised in approximately half the time taken if no HVDC-based POD control is installed. An

analysis performed on a commercial HVDC line has shown that there is high availability of spare operational capacity, before overload capabilities have been considered. The results from this research suggest that flexible limits on modulation capacity (dependent on system operating conditions) would enable greater exploitation of the damping capabilities of the HVDC systems.

Despite the widely established view that multi-terminal VSC-HVDC systems will provide vital support to future electricity transmission systems, there has been no work into their use for POD-based stabilising action. All of the available academic research into POD with multi-terminal HVDC (MTDC) systems was completed prior to the advent of VSC-HVDC and was primarily concerned with the complexities of modulating power flow through LCC-MTDC systems – for which steady state power flow control was often prohibitively complicated. This novel research into the use of VSC-MTDC systems for POD control represents the third original contribution of this thesis. The benefits of MTDC-based POD control have been clearly established in this thesis, demonstrating how the use multiple controllable power injection points can ensure effective oscillation damping within the interconnected AC system, with minimal control effort

A large number of WAMS-based multivariable control designs make use of nominally robust controller structures, such as  $H_\infty$  formulations. The inherent mathematical robustness that such designs claim is entirely dependent upon accurate representation of the system and the uncertainties present. Poor formalisation of the system variations may lead to a practical controller which cannot achieve the level of performance expected, yet this is scarcely satisfactorily investigated. The fourth original contribution established within this thesis is a probabilistic methodology to assess the robustness of supplementary system damping controllers with any design structure. This new methodology accounts for the stochastic variation in power system operation as well as key equipment outages. Classification tools are used to improve the accuracy of the technique and to deduce operational areas which have an increased risk of system instability, and can be subsequently avoided through intelligent generator dispatch.

The probabilistic methodology which has been developed to assess controller performance utilises the traditional numerical MC approach and therefore requires vast numbers of full system linearisations. Whilst this ensures accurate results, less computationally intensive methods are desirable – particularly for online system

analysis. Within this research, the Probabilistic Collocation Method has been developed for application with large power systems in order to accurately produce the statistical distributions of critical system eigenvalues using significantly fewer full linearisations than traditional approaches. Previous applications of the PCM for probabilistic small-disturbance analysis have been limited to just one or two system uncertainties. Within this thesis, the parameter reduction methods required to enable application on realistic power system models containing many uncertainties are established and thoroughly explained. Illustrative studies presented on large systems using standard power flow and optimal power flow solutions demonstrate, for the first time, the feasibility and applicability of the PCM for probabilistic small-disturbance analyses. This work represents the fifth original contribution of this thesis.

The sixth and final original contribution of this thesis is the use of a probabilistic system representation during POD controller synthesis to yield designs which are more robust to system uncertainties. Probabilistic studies are completed to determine the most likely locations of critical oscillatory modes which are then incorporated into the linearised system model. This ensures that the probabilistic variation in critical system eigenvalues is more accurately accounted for. Both the traditional MC approach and the efficient sampling of the PCM approach have been used to produce this probabilistic representation for a realistic power system. An evaluation of the performance of these probabilistic controller designs across wide ranging system operating conditions has shown them to be more robust to the system uncertainties than an equivalent WAMS-based controller designed using the standard nominal system representation.

## **7.2 Future Work**

The work presented within this thesis has fulfilled all of the research aims which were initially defined. Nevertheless there are a number of areas where this work could be extended in order to further develop the ideas and methods which have been established.

This thesis has presented a comprehensive analysis of a single WAMS-based controller design – the MLQG structure. The original review of past research in this area revealed a wide range of alternative controller design methods used for POD control. These included sliding mode controls, relative gain array, non-linear optimisation, evolutionary optimisation (such as genetic algorithms), Prony-based adaptive control,  $H_\infty$  designs, Lyapunov energy functions, and fuzzy control amongst others. It would be

desirable to examine the response of these wide ranging control synthesis techniques using the probabilistic methodology developed. This large comparative study would enable these control techniques to be assessed against each other, using the same test systems and variable operating conditions in order to establish their relative performance, robustness, simplicity and scalability to practical power system implementation. Without a study like this it is perhaps unlikely that power systems operators would be willing to select a complex controller structure and move away from the traditional PSS-based design, despite the shortcomings which have been identified.

The research presented within this thesis concerned with supplementary POD control for HVDC systems has implemented this control exclusively with VSC-HVDC systems. The reasons for this have been clearly stated; to begin with it is much simpler to achieve active power modulation without the need for complex reactive power compensation control. VSC-HVDC systems are also becoming increasingly prevalent, and multi-terminal grids will require the use of VSC technology. Nevertheless, the majority of existing HVDC systems in operation use the classic LCC thyristor-based technology, often at much high capacities than VSC-HVDC installations. There is great potential within these high capacity LCC-HVDC lines to stabilise AC networks but this may require the use of additional FACTS devices or active filtering schemes to regulate the reactive power requirements of the converter stations. The MLQG controller structure which has been demonstrated as suitable for VSC-HVDC-based POD control should also be designed and analysed for LCC-HVDC systems.

VSC-MTDC grids have been shown to have high potential to damp oscillations within interconnected AC networks due to the large number of controllable power injection nodes. The studies performed on VSC-MTDC grids within this thesis have assumed the use of an extension of traditional point-to-point links and include a slack DC bus. In practice, such a slack node would not exist and more complex *voltage-droop* characteristics would be implemented in order to achieve more equal power sharing during transient events. Whilst the slack node does not in any way invalidate the results obtained with the VSC-MTDC studies, a practical control implementation strategy should be derived to enable POD damping with VSC-MTDC grids. This may either require the detection of oscillations within the AC systems and a switch in control mode, or the direct application of POD control within the voltage-droop operational control scheme.

The PCM has been developed for implementation on large test systems through the application of parameter reduction methods, providing accurate estimation of the critical mode probability distributions. However, the method is currently unable to account for correlation between uncertain parameters. This should be further investigated in order to ensure the applicability of the PCM for fast assessment of critical risk indices (such as the risk of system instability). The high levels of parameter reduction possible and the good results seen using an OPF solution suggest that provided the key system parameters can be included, further correlated parameters may be neglected with few detrimental effects. The work presented on the PCM could be extended to further facets of system instability risk determination. Such work could incorporate transient instability assessments and the impacts of other new technology such as large scale penetration of renewable generation and FACTS devices.

Throughout this thesis, the stability benefits of using HVDC-based POD control have been clearly demonstrated. It is difficult to quantify these benefits however, particularly in terms of the economic impact on the power system. If these benefits could be assigned a monetary value, then projects such as this would become more attractive and HVDC systems may in turn become more popular. Power system stability issues cause infrequent but catastrophic failures, for example the 10 August 1996 WSCC collapse in the USA which was described in the introduction. Avoiding such events is obviously desirable, but it is difficult to assign an economic value to the prevention of an event which may have never occurred otherwise. Further benefits may be more easily defined, for example the deferral of AC line upgrades if stability improvements facilitate an increase in allowable power transfer capacity. Nevertheless there are many challenges in performing an economic evaluation of the stability improvements made by a supplementary HVDC-based POD controller, and a thorough methodical framework is required.

A final subject for future work following this thesis is the application of a robust WAMS-based HVDC POD controller within a practical power system. The methodologies to establish a probabilistic system representation, design a suitable controller, and subsequently thoroughly test its robustness to the known variations within a power system could be fully utilised. Such a project would require numerous stages, including detailed modelling and perhaps implementation using real-time digital

simulators with PMU data measurements in order to ensure confidence in the controller design.

---

# 8 References

---

- [1] P. Kundur, *Power System Stability and Control*. London: McGraw-Hill, Inc., 1994.
- [2] G. Rogers, *Power System Oscillations*. Norwell: Kluwer Academic Publishers, 2000.
- [3] K. R. Padiyar, *Analysis of Subsynchronous Resonance in Power Systems*. Boston: Kluwer Academic Publishers, 1999.
- [4] S. M. Ustinov, J. V. Milanovic, and V. A. Maslennikov, "Inherent dynamic properties of interconnected power systems," *International Journal of Electrical Power & Energy Systems*, vol. 24, pp. 371-378, 2002.
- [5] P. M. Anderson and A. A. Fouad, *Power System Control and Stability*: IEEE Press, 1994.
- [6] D. N. Kosterev, C. W. Taylor, and W. A. Mittelstadt, "Model validation for the August 10, 1996 WSCC system outage," *IEEE Trans on Power Systems*, vol. 14, pp. 967-979, 1999.
- [7] "1996 System Disturbances: Review of Selected 1996 Electricity System Disturbances in North America," North American Electric Reliability Council: [online] Available at: [www.nerc.com](http://www.nerc.com), August 2002.
- [8] V. Venkatasubramanian and Y. Li, "Analysis of 1996 Western American Electric Blackouts," in *Bulk Power System Dynamics and Control - VI*, Cortina d'Ampezzo, Italy, 2004.
- [9] F. Aboytes, F. Sanchez, A. I. Murcia Cabra, and J. E. Gomez Castro, "Dynamic stability analysis of the interconnected Colombia-Venezuela power system," *IEEE Trans on Power Systems*, vol. 15, pp. 376-381, 2000.
- [10] O. B. Tor, C. Gencoglu, O. Yilmaz, E. Cebeci, and A. N. Guven, "Damping measures against prospective oscillations between Turkish grid and ENTSO-E System," in

- International Conference on Power System Technology (POWERCON)*, Hangzhou, China, 2010.
- [11] E. Martinez and A. R. Messina, "Modal analysis of measured inter-area oscillations in the Mexican Interconnected System: The July 31, 2008 event," in *IEEE Power and Energy Society General Meeting*, Detroit, USA, 2011.
- [12] M. E. Aboul-Ela, A. A. Sallam, J. D. McCalley, and A. A. Fouad, "Damping controller design for power system oscillations using global signals," *IEEE Trans on Power Systems*, vol. 11, pp. 767-773, 1996.
- [13] I. Kamwa, R. Grondin, and Y. Hebert, "Wide-area measurement based stabilizing control of large power systems-a decentralized/hierarchical approach," *IEEE Trans on Power Systems*, vol. 16, pp. 136-153, 2001.
- [14] J. J. Sanchez-Gasca, N. W. Miller, A. Kurita, and S. Horiuchi, "Multivariable control for damping interarea oscillations in power systems," *IEEE Control Systems Magazine*, vol. 9, pp. 28-32, 1989.
- [15] V. Centeno, J. de la Ree, A. G. Phadke, G. Michel, R. J. Murphy, and R. O. Burnett, Jr., "Adaptive out-of-step relaying using phasor measurement techniques," *IEEE Computer Applications in Power*, vol. 6, pp. 12-17, 1993.
- [16] "IEEE Standard for Synchrophasor Measurements for Power Systems," *IEEE Std C37.118.1-2011 (Revision of IEEE Std C37.118-2005)*, pp. 1-61.
- [17] D. M. Lavery, D. J. Morrow, A. McKinley, and M. Cregan, "OpenPMU: Open source platform for Synchrophasor applications and research," in *IEEE Power and Energy Society General Meeting*, Detroit, USA, 2011.
- [18] X. Xiaorong, X. Yaozhong, X. Jinyu, W. Jingtao, and H. Yingdao, "WAMS applications in Chinese power systems," *IEEE Power and Energy Magazine*, vol. 4, pp. 54-63, 2006.
- [19] M. Chenine, Z. Kun, and L. Nordstrom, "Survey on priorities and communication requirements for PMU-based applications in the Nordic Region," in *IEEE PowerTech*, Bucharest, Romania, 2009.
- [20] J. W. Stahlhut, T. J. Browne, G. T. Heydt, and V. Vittal, "Latency Viewed as a Stochastic Process and its Impact on Wide Area Power System Control Signals," *IEEE Trans on Power Systems*, vol. 23, pp. 84-91, 2008.
- [21] V. Madani, A. Vaccaro, D. Villacci, and R. L. King, "Satellite based communication network for large scale power system applications," in *Bulk Power System Dynamics and Control - VII. Revitalizing Operational Reliability*, Charleston, USA, 2007.
- [22] W. Hongxia, K. S. Tsakalis, and G. T. Heydt, "Evaluation of time delay effects to wide-area power system stabilizer design," *IEEE Trans on Power Systems*, vol. 19, pp. 1935-1941, 2004.
- [23] B. Chaudhuri, R. Majumder, and B. C. Pal, "Wide-area measurement-based stabilizing control of power system considering signal transmission delay," *IEEE Trans on Power Systems*, vol. 19, pp. 1971-1979, 2004.
- [24] Z. Yang and A. Bose, "Design of Wide-Area Damping Controllers for Interarea Oscillations," *IEEE Trans on Power Systems*, vol. 23, pp. 1136-1143, 2008.

- 
- [25] H. Zhijian and J. V. Milanovic, "Damping of Inter-area Oscillations by WAM Based Supplementary Controller," in *IEEE Power and Engineering Society General Meeting*, Tampa, USA, 2007.
- [26] H. Zhijian and J. V. Milanovic, "The Effectiveness of WAM Based Adaptive Supervisory Controller for Global Stabilization of Power Systems," in *IEEE PowerTech*, Lausanne, Switzerland, 2007, pp. 1652-1659.
- [27] N. Hui, G. T. Heydt, and L. Mili, "Power system stability agents using robust wide area control," *IEEE Trans on Power Systems*, vol. 17, pp. 1123-1131, 2002.
- [28] D. Dotta, A. S. e Silva, and I. C. Decker, "Wide-Area Measurements-Based Two-Level Control Design Considering Signal Transmission Delay," *IEEE Trans on Power Systems*, vol. 24, pp. 208-216, 2009.
- [29] A. Almutairi, "Enhancement of Power System Stability using Wide Area Measurement System Based Damping Controller," in *School of Electrical and Electronic Engineering*. vol. Ph.D. Manchester: University of Manchester, 2010.
- [30] B. Chaudhuri, B. C. Pal, A. C. Zolotas, I. M. Jaimoukha, and T. C. Green, "Mixed-sensitivity approach to H infinity control of power system oscillations employing multiple FACTS devices," *IEEE Trans on Power Systems*, vol. 18, pp. 1149-1156, 2003.
- [31] B. Chaudhuri and B. C. Pal, "Robust damping of multiple swing modes employing global stabilizing signals with a TCSC," *IEEE Trans on Power Systems*, vol. 19, pp. 499-506, 2004.
- [32] M. Zarghami, M. L. Crow, and S. Jagannathan, "Nonlinear Control of FACTS Controllers for Damping Interarea Oscillations in Power Systems," *IEEE Trans on Power Delivery*, vol. 25, pp. 3113-3121, 2010.
- [33] P. K. Dash, S. Mishra, and G. Panda, "Damping multimodal power system oscillation using a hybrid fuzzy controller for series connected FACTS devices," *IEEE Trans on Power Systems*, vol. 15, pp. 1360-1366, 2000.
- [34] A. C. Zolotas, B. Chaudhuri, I. M. Jaimoukha, and P. Korba, "A Study on LQG/LTR Control for Damping Inter-Area Oscillations in Power Systems," *IEEE Trans on Control Systems Technology*, vol. 15, pp. 151-160, 2007.
- [35] J. He, C. Lu, X. Wu, P. Li, and J. Wu, "Design and experiment of wide area HVDC supplementary damping controller considering time delay in China southern power grid," *Generation, Transmission & Distribution, IET*, vol. 3, pp. 17-25, 2009.
- [36] Y. Li, C. Rehtanz, D. Yang, Ru, x, S. berg, Ha, and U. ger, "Robust high-voltage direct current stabilising control using wide-area measurement and taking transmission time delay into consideration," *Generation, Transmission & Distribution, IET*, vol. 5, pp. 289-297.
- [37] Y. Pipelzadeh, B. Chaudhuri, and T. C. Green, "Control Coordination Within a VSC HVDC Link for Power Oscillation Damping: A Robust Decentralized Approach Using Homotopy," *IEEE Trans on Control Systems Technology*, 2012.
- [38] J. Wang, C. Fu, and Y. Zhang, "Design of WAMS-Based Multiple HVDC Damping Control System," *IEEE Trans on Smart Grid*, vol. 2, pp. 363-374, 2011.

- [39] X. M. Mao, Y. Zhang, L. Guan, X. C. Wu, and N. Zhang, "Improving power system dynamic performance using wide-area high-voltage direct current damping control," *IET Generation, Transmission & Distribution*, vol. 2, pp. 245-251, 2008.
- [40] "ABB Reference Projects," A. AB, Ed.: [online] Available at: <http://www.abb.com/hvdc>, 2009.
- [41] "HVDC Projects Listing Prepared for the DC and Flexible AC Transmission Subcommittee of the IEEE Transmission and Distribution Committee," Working Group on HVDC and FACTS Bibliography and Records, 2011.
- [42] J. Arrillaga, *High Voltage Direct Current Transmission*, 2nd ed. London: The Institute of Electrical Engineers, 1998.
- [43] J. Arrillaga, Y. H. Liu, and N. R. Watson, *Flexible Power Transmission: The HVDC Options*. Chichester: John Wiley & Sons, Ltd, 2007.
- [44] "Siemens AG - HV Direct Current Transmission Systems (HVDC)," [online] Available at: <http://www.energy.siemens.com/hq/en/power-transmission/hvdc/>, 2012.
- [45] "ABB Reference Projects," ABB AB: [online] Available at: <http://www.abb.com/hvdc>, 2012.
- [46] G. Reed, R. Pape, and M. Takeda, "Advantages of voltage sourced converter (VSC) based design concepts for FACTS and HVDC-link applications," in *IEEE Power Engineering Society General Meeting*, 2003, p. 1821 Vol. 3.
- [47] Y. Ming, L. Gengyin, L. Guangkai, L. Haifeng, and Z. Ming, "Modeling of VSC-HVDC and its active power control scheme," in *International Conference on Power System Technology (POWERCON)*, Singapore, 2004, pp. 1351-1355.
- [48] V. Elanders, "It's Time To Connect: Technical description of HVDC Light® technology," ABB AB2008.
- [49] EWEA, "The European offshore wind industry - Key trends and statistics: 1st half 2011," 2011.
- [50] "Offshore Development Information Statement: Future Scenarios Consultation," National Grid Electricity Transmission plc: [online] Available at: <http://www.nationalgrid.com>, February 2011.
- [51] EWEA, "Oceans of Opportunity: Harnessing Europe's largest domestic energy resource," 2009.
- [52] "International Energy Outlook 2011," U.S. Energy Information Administration: [online] Available at: <http://www.eia.gov>, September 2011.
- [53] "Western HVDC Link: Consultation Document," National Grid Electricity Transmission, Scottish Power Transmission: [online] Available at: <http://www.westernhvdcLink.co.uk>, January 2011.
- [54] "Press Release: EIB, Inelfe, RTE and REE sign EUR 350m loan contract to finance construction of France-Spain power interconnector," INELFE, European Investment Bank, Réseau de Transport d'Électricité, RED Eléctrica de España: [online] Available at: [www.inelfe.eu](http://www.inelfe.eu), 6 October 2011.

- 
- [55] R. A. Jabr, B. C. Pal, and N. Martins, "A Sequential Conic Programming Approach for the Coordinated and Robust Design of Power System Stabilizers," *IEEE Trans on Power Systems*, vol. 25, pp. 1627-1637, 2010.
- [56] L. Xianzhang, E. N. Lerch, and D. Povh, "Optimization and coordination of damping controls for improving system dynamic performance," *IEEE Trans on Power Systems*, vol. 16, pp. 473-480, 2001.
- [57] A. L. B. Do Bomfim, G. N. Taranto, and D. M. Falcao, "Simultaneous tuning of power system damping controllers using genetic algorithms," *IEEE Trans on Power Systems*, vol. 15, pp. 163-169, 2000.
- [58] M. A. Abido, "Optimal design of power-system stabilizers using particle swarm optimization," *IEEE Trans on Energy Conversion*, vol. 17, pp. 406-413, 2002.
- [59] Y. L. Abdel-Magid and M. A. Abido, "Optimal multiobjective design of robust power system stabilizers using genetic algorithms," *IEEE Trans on Power Systems*, vol. 18, pp. 1125-1132, 2003.
- [60] Y. L. Abdel-Magid, M. A. Abido, S. Al-Baiyat, and A. H. Mantawy, "Simultaneous stabilization of multimachine power systems via genetic algorithms," *IEEE Trans on Power Systems*, vol. 14, pp. 1428-1439, 1999.
- [61] R. A. Ramos, L. F. C. Alberto, and N. G. Bretas, "A new methodology for the coordinated design of robust decentralized power system damping controllers," *IEEE Trans on Power Systems*, vol. 19, pp. 444-454, 2004.
- [62] D. J. Trudnowski, J. R. Smith, T. A. Short, and D. A. Pierre, "An application of Prony methods in PSS design for multimachine systems," *IEEE Trans on Power Systems*, vol. 6, pp. 118-126, 1991.
- [63] X. Lei, D. Jiang, and D. Retzmann, "Stability improvement in power systems with non-linear TCSC control strategies," *European Trans on Electrical Power*, vol. 10, pp. 339-345, 2000.
- [64] E. N. Lerch, D. Povh, and L. Xu, "Advanced SVC control for damping power system oscillations," *IEEE Trans on Power Systems*, vol. 6, pp. 524-535, 1991.
- [65] G. N. Taranto, J. K. Shiau, J. H. Chow, and H. A. Othman, "Robust decentralised design for multiple FACTS damping controllers," *IEE Generation, Transmission & Distribution*, vol. 144, pp. 61-67, 1997.
- [66] M. Klein, L. X. Le, G. J. Rogers, S. Farrokhpay, and N. J. Balu, "H infinity damping controller design in large power systems," *IEEE Trans on Power Systems*, vol. 10, pp. 158-166, 1995.
- [67] J. J. Sanchez-Gasca and J. H. Chow, "Power system reduction to simplify the design of damping controllers for interarea oscillations," *IEEE Trans on Power Systems*, vol. 11, pp. 1342-1349, 1996.
- [68] M. Noroozian, M. Ghandhari, G. Andersson, J. Gronquist, and I. Hiskens, "A robust control strategy for shunt and series reactive compensators to damp electromechanical oscillations," *IEEE Trans on Power Delivery*, vol. 16, pp. 812-817, 2001.
- [69] M. Ghandhari, G. Andersson, and I. A. Hiskens, "Control Lyapunov functions for controllable series devices," *IEEE Trans on Power Systems*, vol. 16, pp. 689-694, 2001.
-

- 
- [70] N. Yang, Q. Liu, and J. D. McCalley, "TCSC controller design for damping interarea oscillations," *IEEE Trans on Power Systems*, vol. 13, pp. 1304-1310, 1998.
- [71] K. M. Son and J. K. Park, "On the robust LQG control of TCSC for damping power system oscillations," *IEEE Trans on Power Systems*, vol. 15, pp. 1306-1312, 2000.
- [72] A. M. Kulkarni and K. R. Padiyar, "Damping of power swings using series facts controllers," *International Journal of Electrical Power & Energy Systems*, vol. 21, pp. 475-495, 1999.
- [73] E. V. Larsen, J. J. Sanchez-Gasca, and J. H. Chow, "Concepts for design of FACTS controllers to damp power swings," *IEEE Trans on Power Systems*, vol. 10, pp. 948-956, 1995.
- [74] M. M. Farsangi, Y. H. Song, and K. Y. Lee, "Choice of FACTS device control inputs for damping interarea oscillations," *IEEE Trans on Power Systems*, vol. 19, pp. 1135-1143, 2004.
- [75] H. F. Wang, "Selection of robust installing locations and feedback signals of FACTS-based stabilizers in multi-machine power systems," *IEEE Trans on Power Systems*, vol. 14, pp. 569-574, 1999.
- [76] Z. Xiao-Ping, C. Rehtanz, and B. Pal, *Flexible AC Transmission Systems: Modelling and Control*. New York: Springer Inc., 2006.
- [77] D. D. Simfukwe, B. C. Pal, R. A. Jabr, and N. Martins, "Robust and low-order design of flexible ac transmission systems and power system stabilisers for oscillation damping," *IET Generation, Transmission & Distribution*, vol. 6, pp. 445-452, 2012.
- [78] C. Li-Jun and I. Erlich, "Simultaneous coordinated tuning of PSS and FACTS damping controllers in large power systems," *IEEE Trans on Power Systems*, vol. 20, pp. 294-300, 2005.
- [79] P. Pourbeik and M. J. Gibbard, "Simultaneous coordination of power system stabilizers and FACTS device stabilizers in a multimachine power system for enhancing dynamic performance," *IEEE Trans on Power Systems*, vol. 13, pp. 473-479, 1998.
- [80] T. T. Nguyen and R. Gianto, "Optimisation-based control coordination of PSSs and FACTS devices for optimal oscillations damping in multi-machine power system," *IET Generation, Transmission & Distribution*, vol. 1, pp. 564-573, 2007.
- [81] C. Karawita and U. D. Annakkage, "Multi-Infeed HVDC Interaction Studies Using Small-Signal Stability Assessment," *IEEE Trans on Power Delivery*, vol. 24, pp. 910-918, 2009.
- [82] R. K. Pandey, "Stability Analysis of AC/DC System With Multirate Discrete-Time HVDC Converter Model," *IEEE Trans on Power Delivery*, vol. 23, pp. 311-318, 2008.
- [83] C. Osauskas and A. Wood, "Small-signal dynamic modeling of HVDC systems," *IEEE Trans on Power Delivery*, vol. 18, pp. 220-225, 2003.
- [84] S. Arabi, G. J. Rogers, D. Y. Wong, P. Kundur, and M. G. Lauby, "Small signal stability program analysis of SVC and HVDC in AC power systems," *IEEE Trans on Power Systems*, vol. 6, pp. 1147-1153, 1991.
- [85] D. Jovcic, N. Pahalawaththa, and M. Zavahir, "Small signal analysis of HVDC-HVAC interactions," *IEEE Trans on Power Delivery*, vol. 14, pp. 525-530, 1999.
-

- 
- [86] S. Cole and R. Belmans, "A proposal for standard VSC HVDC dynamic models in power system stability studies," *Electric Power Systems Research*, vol. 81, pp. 967-973, 2011.
- [87] V. P. Lukic, A. Prole, and S. Gruber, "Perturbation approach to optimal connection of HVDC to AC power systems," *International Journal of Electrical Power & Energy Systems*, vol. 4, pp. 100-110, 1982.
- [88] V. P. Lukic and A. Prole, "Optimal connection of controlled HVDC to AC power system," *International Journal of Electrical Power & Energy Systems*, vol. 6, pp. 150-160, 1984.
- [89] H. S. Ramadan, H. Siguerdidjane, M. Petit, and R. Kaczmarek, "Performance enhancement and robustness assessment of VSC-HVDC transmission systems controllers under uncertainties," *International Journal of Electrical Power & Energy Systems*, vol. 35, pp. 34-46, 2012.
- [90] H. Weng and Z. Xu, "WAMS based robust HVDC control considering model imprecision for AC/DC power systems using sliding mode control," *Electric Power Systems Research*, vol. 95, pp. 38-46.
- [91] R. L. Cresap and W. A. Mittelstadt, "Small-signal modulation of the Pacific HVDC inertia," *IEEE Trans on Power Apparatus and Systems*, vol. 95, pp. 536-541, 1976.
- [92] R. L. Cresap, W. A. Mittelstadt, D. N. Scott, and C. W. Taylor, "Operating Experience with Modulation of the Pacific HVDC Intertia," *IEEE Trans on Power Apparatus and Systems*, vol. PAS-97, pp. 1053-1059, 1978.
- [93] H. J. C. Peiris, U. D. Annakkage, and N. C. Pahalawaththa, "Frequency regulation of rectifier side AC system of an HVDC scheme using coordinated fuzzy logic control," *Electric Power Systems Research*, vol. 48, pp. 89-95, 1998.
- [94] P. K. Dash, A. C. Liew, and A. Routray, "Design of robust controllers for HVDC links in AC-DC power systems," *Electric Power Systems Research*, vol. 33, pp. 201-209, 1995.
- [95] H. Cai, Z. Qu, and D. Gan, "A nonlinear robust HVDC control for a parallel AC/DC power system," *Computers & Electrical Engineering*, vol. 29, pp. 135-150, 2003.
- [96] T. Smed and G. Andersson, "Utilizing HVDC to damp power oscillations," *IEEE Trans on Power Delivery*, vol. 8, pp. 620-627, 1993.
- [97] Y. Pipelzadeh, B. Chaudhuri, and T. C. Green, "Wide-area power oscillation damping control through HVDC: A case study on Australian equivalent system," in *IEEE Power & Energy Society General Meeting*, Minneapolis, USA, 2010.
- [98] G. Liu, Z. Xu, Y. Huang, and W. Pan, "Analysis of inter-area oscillations in the South China Interconnected Power System," *Electric Power Systems Research*, vol. 70, pp. 38-45, 2004.
- [99] J. He, C. Lu, X. Wu, P. Li, and J. Wu, "Design and experiment of wide area HVDC supplementary damping controller considering time delay in China southern power grid," *IET Generation, Transmission & Distribution*, vol. 3, pp. 17-25, 2009.
-

- 
- [100] X. M. Mao, Y. Zhang, L. Guan, and X. C. Wu, "Coordinated control of interarea oscillation in the China Southern power grid," *IEEE Trans on Power Systems*, vol. 21, pp. 845-852, 2006.
- [101] H. Jingbo, L. Chao, W. Xiaochen, W. Jingtao, and T. S. Bi, "Design and experiment of heuristic adaptive HVDC supplementary damping controller based on online Prony analysis," in *IEEE Power Engineering Society General Meeting*, 2007.
- [102] R. Eriksson and L. Soder, "Coordinated control design of multiple HVDC links based on model identification," *Computers & Mathematics with Applications*, vol. 60, pp. 944-953, 2010.
- [103] R. Eriksson and L. Soder, "On the coordinated control of multiple HVDC links using input-output exact linearization in large power systems," *International Journal of Electrical Power & Energy Systems*, vol. 43, pp. 118-125, 2012.
- [104] A. Fuchs, S. Mariethoz, M. Larsson, and M. Morari, "Grid stabilization through VSC-HVDC using wide area measurements," in *IEEE PowerTech*, Trondheim, Norway, 2011.
- [105] H. F. Latorre, M. Ghandhari, and L. Soder, "Active and reactive power control of a VSC-HVdc," *Electric Power Systems Research*, vol. 78, pp. 1756-1763, 2008.
- [106] H. F. Latorre, M. Ghandhari, and L. Soder, "Use of local and remote information in POD control of a VSC-HVdc," in *IEEE PowerTech*, Bucharest, Romania, 2009.
- [107] Y. Li, C. Rehtanz, D. Yang, S. Ruberg, and U. Hager, "Robust high-voltage direct current stabilising control using wide-area measurement and taking transmission time delay into consideration," *IET Generation, Transmission & Distribution*, vol. 5, pp. 289-297, 2011.
- [108] H. F. Latorre and M. Ghandhari, "Improvement of power system stability by using a VSC-HVdc," *International Journal of Electrical Power & Energy Systems*, vol. 33, pp. 332-339, 2011.
- [109] E. M. Carlini, V. G. Lopez, and M. Muller-Mienack, "Future challenges for European TSOs: a pan-European supergrid," in *Cigre International Symposium on The Electric Power System of the Future*, Bologna, Italy, 2011.
- [110] G. Fulli, A. Purvins, S. Ruberg, A. L'Abbate, and G. Migliavacca, "Evolutions and challenges towards a potential Pan-European HVAC/HVDC SuperGrid," in *Cigre International Symposium on The Electric Power System of the Future*, Bologna, Italy, 2011.
- [111] P. K. Dash, M. A. Rahman, and P. C. Panda, "Dynamic Analysis of Power Systems with Multiterminal HVDC Links and Static Compensators," *IEEE Power Engineering Review*, vol. PER-2, pp. 23-24, 1982.
- [112] M. A. Rahman and P. K. Dash, "Stabilization of an AC-DC power system using a controlled multiterminal HVDC link," *Electric Power Systems Research*, vol. 4, pp. 135-146, 1981.
- [113] D. B. Petkovski and M. Athans, "Robust decentralized control of multiterminal DC/AC power systems," *Electric Power Systems Research*, vol. 9, pp. 253-262, 1985.

- 
- [114] A. Hamzei-Nejad and C. M. Ong, "Coordinating the DC Power Injections of a Multiterminal HVDC System for Dynamic Control of AC Line Flows," *IEEE Trans on Power Systems*, vol. 1, pp. 146-152, 1986.
- [115] J. Beerten, S. Cole, and R. Belmans, "Generalized Steady-State VSC MTDC Model for Sequential AC/DC Power Flow Algorithms," *IEEE Trans on Power Systems*, vol. 27, pp. 821-829, 2011.
- [116] G. O. Kalcon, G. P. Adam, O. Anaya-Lara, S. Lo, and K. Uhlen, "Small-Signal Stability Analysis of Multi-Terminal VSC-Based DC Transmission Systems," *IEEE Trans on Power Systems*, vol. 27, pp. 1818-1830, 2012.
- [117] S. Cole, J. Beerten, and R. Belmans, "Generalized Dynamic VSC MTDC Model for Power System Stability Studies," *IEEE Trans on Power Systems*, vol. 25, pp. 1655-1662, 2010.
- [118] N. R. Chaudhuri, R. Majumder, B. Chaudhuri, and J. Pan, "Stability Analysis of VSC MTDC Grids Connected to Multimachine AC Systems," *IEEE Trans on Power Delivery*, vol. 26, pp. 2774-2784, 2011.
- [119] X. Lie, Y. Liangzhong, M. Bazargan, and W. Yi, "The Role of Multiterminal HVDC for Wind Power Transmission and AC Network Support," in *Asia-Pacific Power and Energy Engineering Conference (APPEEC)*, 2010.
- [120] J. H. Chow, J. J. Sanchez-Gasca, R. Haoxing, and W. Shaopeng, "Power system damping controller design-using multiple input signals," *IEEE Control Systems Magazine*, vol. 20, pp. 82-90, 2000.
- [121] T. Zabaiou, F. Okou, L. A. Dessaint, and O. Akhrif, "Time-delay compensation of a wide-area measurements-based hierarchical voltage and speed regulator," *Canadian Journal of Electrical and Computer Engineering*, vol. 33, pp. 77-85, 2008.
- [122] R. Majumder, B. Chaudhuri, B. C. Pal, and Z. Qing-Chang, "A unified Smith predictor approach for power system damping control design using remote signals," *IEEE Trans on Control Systems Technology*, vol. 13, pp. 1063-1068, 2005.
- [123] B. Mirkin and P. O. Gutman, "Robust Output-Feedback Model Reference Adaptive Control of SISO Plants With Multiple Uncertain, Time-Varying State Delays," *IEEE Trans on Automatic Control*, vol. 53, pp. 2414-2419, 2008.
- [124] N. R. Chaudhuri, S. Ray, R. Majumder, and B. Chaudhuri, "A New Approach to Continuous Latency Compensation With Adaptive Phasor Power Oscillation Damping Controller (POD)," *IEEE Trans on Power Systems*, vol. 25, pp. 939-946, 2010.
- [125] R. N. Allan, B. Borkowska, and C. H. Grigg, "Probabilistic analysis of power flows," *Proceedings of the Institution of Electrical Engineers*, vol. 121, pp. 1551-1556, 1974.
- [126] B. Borkowska, "Probabilistic Load Flow," *IEEE Trans on Power Apparatus and Systems*, vol. PAS-93, pp. 752-759, 1974.
- [127] J. L. Rueda, D. G. Colome, and I. Erlich, "Assessment and Enhancement of Small Signal Stability Considering Uncertainties," *IEEE Trans on Power Systems*, vol. 24, pp. 198-207, 2009.

- 
- [128] J. L. Rueda and D. G. Colome, "Probabilistic performance indexes for small signal stability enhancement in weak wind-hydro-thermal power systems," *IET Generation, Transmission & Distribution*, vol. 3, pp. 733-747, 2009.
- [129] R. C. Burchett and G. T. Heydt, "Probabilistic Methods For Power System Dynamic Stability Studies," *IEEE Trans on Power Apparatus and Systems*, vol. PAS-97, pp. 695-702, 1978.
- [130] C. K. Pang, Z. Y. Dong, P. Zhang, and X. Yin, "Probabilistic analysis of power system small signal stability region," in *International Conference on Control and Automation (ICCA)*, 2005, pp. 503-509.
- [131] F. B. Alhasawi and J. V. Milanovic, "Correlation between uncertainties in system model parameters and distribution of critical electromechanical modes," in *7th Mediterranean Conference on Power Generation, Transmission and Distribution (MedPower)*, Agia Napa, Cyprus, 2010.
- [132] K. W. Wang, C. Y. Chung, C. T. Tse, and K. M. Tsang, "Improved probabilistic method for power system dynamic stability studies," *IEE Generation, Transmission & Distribution*, vol. 147, pp. 37-43, 2000.
- [133] X. Xialing, L. Tao, and Z. Xiaoming, "Probabilistic analysis of small signal stability of microgrid using point estimate method," in *International Conference on Sustainable Power Generation and Supply (SUPERGEN)*, Nanjing, China, 2009.
- [134] A. A. Alabduljabbar, J. V. Milanovic, and E. M. Al-Eid, "Low Discrepancy Sequences Based Optimization Algorithm for Tuning PSSs," in *International Conference on Probabilistic Methods Applied to Power Systems (PMAPS)*, Puerto Rico, 2008.
- [135] V. A. Maslennikov, J. V. Milanovic, and S. M. Ustinov, "Robust ranking of loads by using sensitivity factors and limited number of points from a hyperspace of uncertain parameters," *IEEE Trans on Power Systems*, vol. 17, pp. 565-570, 2002.
- [136] H. Yu, C. Y. Chung, K. P. Wong, H. W. Lee, and J. H. Zhang, "Probabilistic Load Flow Evaluation With Hybrid Latin Hypercube Sampling and Cholesky Decomposition," *IEEE Trans on Power Systems*, vol. 24, pp. 661-667, 2009.
- [137] J. R. Hockenberry and B. C. Lesieutre, "Evaluation of Uncertainty in Dynamic Simulations of Power System Models: The Probabilistic Collocation Method," *IEEE Trans on Power Systems*, vol. 19, pp. 1483-1491, 2004.
- [138] D. Han and J. Ma, "Effect of Uncertainties in Parameters of Load Model on Dynamic Stability Based on Probabilistic Collocation Method," in *IEEE PowerTech*, Lausanne, Switzerland, 2007, pp. 1100-1104.
- [139] M. Li, J. Ma, and Z. Y. Dong, "Uncertainty analysis of load models in small signal stability," in *International Conference on Sustainable Power Generation and Supply (SUPERGEN)*, Nanjing, China, 2009, pp. 1-6.
- [140] J. Machowski, J. W. Bialek, and J. R. Bumby, *Power System Dynamics and Stability*. Chichester: John Wiley & Sons, Inc., 1997.
- [141] P. W. Sauer and M. A. Pai, *Power System Dynamics and Stability*. Upper Saddle River: Prentice Hall, Inc., 1998.

- 
- [142] "IEEE Recommended Practice for Excitation System Models for Power System Stability Studies," *IEEE Std 421.5-2005 (Revision of IEEE Std 421.5-1992)*, 2006.
- [143] E. V. Larsen and D. A. Swann, "Applying Power System Stabilizers Parts I, II and III," *IEEE Trans on Power Apparatus and Systems*, vol. 100, pp. 3017-3046, 1981.
- [144] "Load representation for dynamic performance analysis [of power systems]," in *Power Systems, IEEE Transactions on*. vol. 8 IEEE Task Force on Load Representation for Dynamic Performance, 1993, pp. vol. 9, no. 2, pp. 472-482.
- [145] C. Concordia and S. Ihara, "Load Representation in Power System Stability Studies," *IEEE Trans on Power Apparatus and Systems*, vol. 101, pp. 969-977, 1982.
- [146] J. Lam, "Model reduction of delay systems using Pade approximants," *International Journal of Control*, vol. 57, pp. 377 - 391, 1993.
- [147] H. F. Latorre, M. Ghandhari, and L. Söder, "Active and reactive power control of a VSC-HVdc," *Electric Power Systems Research*, vol. 78, pp. 1756-1763, 2008.
- [148] J. Arrillaga and N. R. Watson, *Computer Modelling of Electrical Power Systems*, 2nd ed. Chichester: John Wiley & Sons, Ltd, 2001.
- [149] C. Feltes, H. Wrede, F. W. Koch, and I. Erlich, "Enhanced Fault Ride-Through Method for Wind Farms Connected to the Grid Through VSC-Based HVDC Transmission," *IEEE Trans on Power Systems*, vol. 24, pp. 1537-1546, 2009.
- [150] P. E. Bjorklund, K. Srivastava, and W. Quaintance, "Hvdc Light Modeling for Dynamic Performance Analysis," in *Power Systems Conference and Exposition (PSCE)*, Atlanta, USA, 2006, pp. 871-876.
- [151] J. Beerten, D. V. Hertem, and R. Belmens, "VSC MTDC Systems with a Distributed Voltage Control - A Power Flow Approach," in *IEEE PowerTech*, Trondheim, Norway, 2011.
- [152] A. M. Lyapunov, *Stability of Motion (English Translation)*. London: Academic Press, Inc, 1967.
- [153] C. Zheng, X. Zhou, and L. Ruomei, "Dynamic Modeling and Transient Simulation for VSC based HVDC in Multi-Machine System," in *International Conference on Power System Technology (PowerCon)*, Chongqing, China, 2006, pp. 1-7.
- [154] D. V. Hertem, R. Eriksson, L. Soder, and M. Ghandhari, "Coordination of Multiple Power Flow Controlling Devices in Transmission Systems," in *IET ACDC*, London, UK, 2010.
- [155] J. V. Milanovic and S. K. Yee, "Roadmap for tuning power system controllers," in *3rd IASTED International Conference on Power and Energy Systems*, Marbella, Spain, September 2-4, 2003, pp. 763-770.
- [156] F. L. Pagola, I. J. Perez-Arriaga, and G. C. Verghese, "On Sensitivities, Residues and Participations. Applications to Oscillatory Stability Analysis and Control," *IEEE Power Engineering Review*, vol. 9, pp. 61-61, 1989.
- [157] L. Rouco and F. L. Pagola, "An eigenvalue sensitivity approach to location and controller design of controllable series capacitors for damping power system oscillations," *IEEE Trans on Power Systems*, vol. 12, pp. 1660-1666, 1997.

- 
- [158] K. Ogata, *Modern Control Engineering*, 4th ed. Minnesota: Prentice Hall, 2002.
- [159] N. S. Nise, *Control Systems Engineering*, 3rd ed. California: John Wiley & Sons, 2000.
- [160] T. Michigami, M. Terasaki, N. Sasazima, K. Hayashi, and T. Okamoto, "Development of a new adaptive LQG system generator for high-speed damping control techniques of power system oscillation," *Electrical Engineering in Japan*, vol. 142, pp. 30-40, 2003.
- [161] A. M. D. Ferreira, J. A. L. Barreiros, J. W. Barra, and J. R. Brito-de-Souza, "A robust adaptive LQG/LTR TCSC controller applied to damp power system oscillations," *Electric Power Systems Research*, vol. 77, pp. 956-964, 2007.
- [162] S. Skogestad and I. Postlethwaite, *Multivariable Feedback Control: Analysis and Design*. Chichester: John Wiley & Sons, 1996.
- [163] G. H. Golub and C. F. V. Loan, *Matrix Computations*. Baltimore: The John Hopkins University Press, 1989.
- [164] M. G. Safonov and R. Y. Chiang, "A Schur method for balanced-truncation model reduction," *IEEE Trans on Automatic Control*, vol. 34, pp. 729-733, 1989.
- [165] B. Pal and B. Chaudhuri, *Robust Control in Power Systems*. New York: Springer Inc., 2005.
- [166] R. D. Zimmerman, C. E. Murillo-Sanchez, and R. J. Thomas, "MATPOWER: Steady-State Operations, Planning, and Analysis Tools for Power Systems Research and Education," *IEEE Trans on Power Systems*, vol. 26, pp. 12-19, 2011.
- [167] P. L. Francos, S. S. Verdugo, H. F. Alvarez, S. Guyomarch, and J. Loncle, "INELFE - Europe's first integrated onshore HVDC interconnection," in *IEEE Power & Energy Society General Meeting*, San Diego, USA, 2012.
- [168] "Metered half-hourly electricity demands: July - December 2011," National Grid Transmission: [online] Available at: [www.nationalgrid.com](http://www.nationalgrid.com), 2011.
- [169] J. Doyle, "Guaranteed margins for LQG regulators," *IEEE Trans on Automatic Control*, vol. 23, pp. 756-757, 1978.
- [170] J. V. Milanovic, I. A. Hiskens, and V. A. Maslennikov, "Ranking loads in power systems-comparison of different approaches," *IEEE Trans on Power Systems*, vol. 14, pp. 614-619, 1999.
- [171] T. M. Mitchell, *Machine Learning*. New York: McGraw Hill, 1997.
- [172] W. J. Conover, *Practical Nonparametric Statistics*, 3rd ed. New York: John Wiley & Sons, Inc., 1999.
- [173] L. Breiman, J. Friedman, R. Olshen, and C. Stone, *Classification and Regression Trees*. Boca Raton, Florida: CRC Press, 1984.
- [174] J. Gama, "Functional Trees," *Machine Learning*, vol. 55, pp. 219-250, 2004.
- [175] N. Landwehr, M. Hall, and E. Frank, "Logistic Model Trees," *Machine Learning*, vol. 59, pp. 161-205, 2005.
- [176] M. D. Webster, M. A. Tatang, and G. J. McRae, "Application of Probabilistic Collocation Method for Uncertainty Analysis of a Simple Ocean Model," Massachusetts Institute of Technology, MIT Joint Program on the Science & Policy of Global Change Report Series 4, 1996.

- 
- [177] M. A. Tatang, "Direct incorporation of uncertainty in chemical and environmental systems," in *Department of Chemical Engineering*. vol. Ph.D. Cambridge: Massachusetts Institute of Technology, 1995.
- [178] P. Beckmann, *Orthogonal Polynomials for Engineers and Physicists*. Boulder, CO: Golem Press, 1973.
- [179] P. J. Davis and P. Rabinowitz, *Methods of Numerical Integration*. New York: Academic Press, 1975.
- [180] G. Gautschi, "Algorithm 726: ORTHPOL - a package of routines for generating orthogonal polynomials and Gauss-type quadrature rules," *ACM Trans on Mathematical Software*, vol. 20, pp. 21-62, 1994.
- [181] D. Fowler, "The Binomial Coefficient Function," *The American Mathematical Monthly*, vol. 103, pp. 1-17, 1996.
- [182] A. W. Bowman and A. Azzalini, *Applied Smoothing Techniques for Data Analysis*. New York: Oxford University Press, 1997.
- [183] "V80-2.0 MW: Unsurpassed reliability and performance at high-wind sites in North America," Vestas Americas Inc.: [online] Available at [www.vestas.com](http://www.vestas.com), 2012.
- [184] J. P. Coelingh, A. J. M. van Wijk, and A. A. M. Holtslag, "Analysis of wind speed observations over the North Sea," *Journal of Wind Engineering and Industrial Aerodynamics*, vol. 61, pp. 51-69, 1996.
- [185] T. B. Nguyen and M. A. Pai, "Dynamic security-constrained rescheduling of power systems using trajectory sensitivities," *IEEE Trans on Power Systems*, vol. 18, pp. 848-854, 2003.

# Appendix A: Network Data

This appendix will provide the data required in order to perform dynamic studies on the test systems used throughout this thesis. In all cases a system base of 100 MVA is used.

## A.1 Two-Area Test Network Data

All original data is adopted from [1].

### 8.1.1 Line Impedances

The line impedance data for the network is presented in Table A-1.

Table A-1: Line data for the Kundur two area test network.

From Bus	To Bus	R (pu)	X (pu)	B (pu)
1	5	0	0.15 / 9	0
2	6	0	0.15 / 9	0
3	11	0	0.15 / 9	0
4	10	0	0.15 / 9	0
5	6	$25 \times 0.0001$	$25 \times 0.001$	$25 \times 0.00175$
10	11	$25 \times 0.0001$	$25 \times 0.001$	$25 \times 0.00175$
6	7	$10 \times 0.0001$	$10 \times 0.001$	$10 \times 0.00175$
9	10	$10 \times 0.0001$	$10 \times 0.001$	$10 \times 0.00175$
7	8	$110 \times 0.0001$	$110 \times 0.001$	$110 \times 0.00175$
7	8	$110 \times 0.0001$	$110 \times 0.001$	$110 \times 0.00175$
8	9	$110 \times 0.0001$	$110 \times 0.001$	$110 \times 0.00175$
8	9	$110 \times 0.0001$	$110 \times 0.001$	$110 \times 0.00175$

### A.1.1 Load Flow Data

Data required to complete load flow is included in Table A-2, bus 1 is the slack.

Table A-2: Load flow data for the Kundur two area test network.

Bus	$V$ (pu)	$\theta$ (°)	$P_G$ (MW)	$P_L$ (MW)	$Q_L$ (MVar)	$Q_C$ (MW)
1	1.03	0	–	–	–	–
2	1.01	–	700	–	–	–
3	1.03	–	719	–	–	–
4	1.01	–	700	–	–	–
7	–	–	–	967	100	200
9	–	–	–	1767	100	350

## A.1.2 Generator Dynamic Data

The generator dynamic presented is given in Table A-3 on the machine base.

Table A-3: Generator dynamic data for the Kundur two area test network.

Gen	Rating (MVA)	$X_d$ (pu)	$X'_d$ (pu)	$X''_d$ (pu)	$T'_{d0}$ (s)	$T''_{d0}$ (s)	$X'_q$ (pu)	$X''_q$ (pu)	$T'_{q0}$ (s)	$T''_{q0}$ (s)	$H$ (s)
G1	900	1.8	0.3	0.25	8	0.03	1.7	0.25	0.4	0.05	6.5
G2	900	1.8	0.3	0.25	8	0.03	1.7	0.25	0.4	0.05	6.5
G3	900	1.8	0.3	0.25	8	0.03	1.7	0.25	0.4	0.05	6.175
G4	900	1.8	0.3	0.25	8	0.03	1.7	0.25	0.4	0.05	6.175

All generators use the same AVR settings, given below:

$$K_A^{ex} = 200, T_A^{ex} = 0.01, T_B^{TGR} = 10, T_C^{TGR} = 1, E_{fd}^{min} = -5.5, E_{fd}^{max} = 5.5.$$

Similarly, PSS settings on all generators are identical, and given below:

$$T_W^{PSS} = 10, T_1^{PSS} = 0.05, T_2^{PSS} = 0.02, T_3^{PSS} = 3, T_4^{PSS} = 5.4, K_{PSS} = 20, E_{PSS}^{min} = -0.1, E_{PSS}^{max} = 0.1.$$

## A.2 NETS-NYPS Test Network Data

Full system details, generator and exciter parameters are adopted from [165] with PSS settings for G9 sourced from [2].

### A.2.1 Line Impedances

The line impedance data for the network is presented in Table A-4, including transformer off-nominal turns ratio (*ONR*) where applicable.

Table A-4: Line data for the NETS-NYPS test network.

From Bus	To Bus	$R$ (pu)	$X$ (pu)	$B$ (pu)	<i>ONR</i>	From Bus	To Bus	$R$ (pu)	$X$ (pu)	$B$ (pu)	<i>ONR</i>
2	53	0	0.0181	0	1.025	33	34	0.0011	0.0157	0.202	–
6	54	0	0.025	0	1.07	35	34	0.0001	0.0074	0	0.946
10	55	0	0.02	0	1.07	34	36	0.0033	0.0111	1.45	–
19	56	0.0007	0.0142	0	1.07	9	36	0.0022	0.0196	0.34	–
20	57	0.0009	0.018	0	1.009	9	36	0.0022	0.0196	0.34	–
22	58	0	0.0143	0	1.025	16	37	0.0007	0.0089	0.1342	–
23	59	0.0005	0.0272	0	1	31	38	0.0011	0.0147	0.247	–

From Bus	To Bus	R (pu)	X (pu)	B (pu)	ONR
25	60	0.0006	0.0232	0	1.025
29	61	0.0008	0.0156	0	1.025
31	62	0	0.026	0	1.04
32	63	0	0.013	0	1.04
36	64	0	0.0075	0	1.04
17	65	0	0.0033	0	1.04
41	66	0	0.0015	0	1
42	67	0	0.0015	0	1
18	68	0	0.003	0	1
36	17	0.0005	0.0045	0.32	–
49	18	0.0076	0.1141	1.16	–
16	19	0.0016	0.0195	0.304	–
19	20	0.0007	0.0138	0	1.06
16	21	0.0008	0.0135	0.2548	–
21	22	0.0008	0.014	0.2565	–
22	23	0.0006	0.0096	0.1846	–
23	24	0.0022	0.035	0.361	–
16	24	0.0003	0.0059	0.068	–
2	25	0.007	0.0086	0.146	–
25	26	0.0032	0.0323	0.531	–
37	27	0.0013	0.0173	0.3216	–
26	27	0.0014	0.0147	0.2396	–
26	28	0.0043	0.0474	0.7802	–
26	29	0.0057	0.0625	1.029	–
28	29	0.0014	0.0151	0.249	–
1	30	0.0008	0.0074	0.48	–
9	30	0.0019	0.0183	0.29	–
9	30	0.0019	0.0183	0.29	–
30	31	0.0013	0.0187	0.333	–
1	31	0.0016	0.0163	0.25	–
30	32	0.0024	0.0288	0.488	–
32	33	0.0008	0.0099	0.168	–
4	14	0.0008	0.0129	0.1382	–
13	14	0.0009	0.0101	0.1723	–
14	15	0.0018	0.0217	0.366	–
15	16	0.0009	0.0094	0.171	–

From Bus	To Bus	R (pu)	X (pu)	B (pu)	ONR
33	38	0.0036	0.0444	0.693	–
41	40	0.006	0.084	3.15	–
48	40	0.002	0.022	1.28	–
42	41	0.004	0.06	2.25	–
18	42	0.004	0.06	2.25	–
17	43	0.0005	0.0276	0	–
39	44	0	0.0411	0	–
43	44	0.0001	0.0011	0	–
35	45	0.0007	0.0175	1.39	–
39	45	0	0.0839	0	–
44	45	0.0025	0.073	0	–
38	46	0.0022	0.0284	0.43	–
1	47	0.0013	0.0188	1.31	–
47	48	0.0025	0.0268	0.4	–
47	48	0.0025	0.0268	0.4	–
46	49	0.0018	0.0274	0.27	–
45	51	0.0004	0.0105	0.72	–
50	51	0.0009	0.0221	1.62	–
37	52	0.0007	0.0082	0.1319	–
3	52	0.0011	0.0133	0.2138	–
1	2	0.0035	0.0411	0.6987	–
2	3	0.0013	0.0151	0.2572	–
3	4	0.0013	0.0213	0.2214	–
4	5	0.0008	0.0128	0.1342	–
5	6	0.0002	0.0026	0.0434	–
6	7	0.0006	0.0092	0.113	–
5	8	0.0008	0.0112	0.1476	–
7	8	0.0004	0.0046	0.078	–
8	9	0.0023	0.0363	0.3804	–
6	11	0.0007	0.0082	0.1389	–
10	11	0.0004	0.0043	0.0729	–
12	11	0.0016	0.0435	0	1.06
10	13	0.0004	0.0043	0.0729	–
12	13	0.0016	0.0435	0	1.06
1	27	0.032	0.32	0.41	–
50	18	0.0012	0.0288	2.06	–

## A.2.2 Load Flow Data

Data required to complete load flow is included in Table A-5, G13 connected to bus 65 is the slack.

Table A-5: Load flow data for the NETS-NYPS test network.

<i>Bus</i>	<i>V</i> (pu)	$\theta$ (°)	$P_G$ (MW)	$P_L$ (MW)	$Q_L$ (MVar)	<i>Bus</i>	<i>V</i> (pu)	$\theta$ (°)	$P_G$ (MW)	$P_L$ (MW)	$Q_L$ (MVar)
1	–	–	–	252.7	118.56	44	–	–	–	267.55	4.84
3	–	–	–	322	2	45	–	–	–	208	21
4	–	–	–	200	73.6	46	–	–	–	150.7	28.5
7	–	–	–	234	84	47	–	–	–	203.12	32.59
8	–	–	–	208.8	70.8	48	–	–	–	241.2	2.2
9	–	–	–	104	125	49	–	–	–	164	29
12	–	–	–	9	88	50	–	–	–	100	-147
15	–	–	–	320	153	51	–	–	–	337	-122
16	–	–	–	329	32	52	–	–	–	158	30
17	–	–	–	6000	300	53	1.045	–	250	–	–
18	–	–	–	2470	123	54	0.98	–	545	–	–
20	–	–	–	680	103	55	0.983	–	650	–	–
21	–	–	–	274	115	56	0.997	–	632	–	–
23	–	–	–	248	85	57	1.011	–	505	–	–
24	–	–	–	309	-92	58	1.05	–	700	–	–
25	–	–	–	224	47	59	1.063	–	560	–	–
26	–	–	–	139	17	60	1.03	–	540	–	–
27	–	–	–	281	76	61	1.025	–	800	–	–
28	–	–	–	206	28	62	1.01	–	500	–	–
29	–	–	–	284	27	63	1	–	1000	–	–
33	–	–	–	112	0	64	1.0156	–	1350	–	–
36	–	–	–	102	-19.46	65	1.011	0	–	–	–
39	–	–	–	267	12.6	66	1	–	1785	–	–
40	–	–	–	65.63	23.53	67	1	–	1000	–	–
41	–	–	–	1000	250	68	1	–	4000	–	–
42	–	–	–	1150	250						

### A.2.3 Generator Dynamic Data

The generator dynamic presented is given in Table A-6 and Table A-7, scaled to the given machine base.

Table A-6: Generator dynamic data for the NETS-NYPS test network (1).

<i>Gen</i>	<i>Bus</i>	<i>Rating (MVA)</i>	$X_{ik}$ (pu)	$X_d$ (pu)	$X'_d$ (pu)	$X''_d$ (pu)	$T'_{d0}$ (s)	$T''_{d0}$ (s)
G1	53	100	0.0125	0.1	0.031	0.025	10.2	0.05
G2	54	100	0.035	0.295	0.0697	0.05	6.56	0.05
G3	55	100	0.0304	0.2495	0.0531	0.045	5.7	0.05
G4	56	100	0.0295	0.262	0.0436	0.035	5.69	0.05
G5	57	100	0.027	0.33	0.066	0.05	5.4	0.05
G6	58	100	0.0224	0.254	0.05	0.04	7.3	0.05
G7	59	100	0.0322	0.295	0.049	0.04	5.66	0.05
G8	60	100	0.028	0.29	0.057	0.045	6.7	0.05
G9	61	100	0.0298	0.2106	0.057	0.045	4.79	0.05
G10	62	100	0.0199	0.169	0.0457	0.04	9.37	0.05
G11	63	100	0.0103	0.128	0.018	0.012	4.1	0.05
G12	64	100	0.022	0.101	0.031	0.025	7.4	0.05
G13	65	200	0.003	0.0296	0.0055	0.004	5.9	0.05
G14	66	100	0.0017	0.018	0.00285	0.0023	4.1	0.05
G15	67	100	0.0017	0.018	0.00285	0.0023	4.1	0.05
G16	68	200	0.0041	0.0356	0.0071	0.0055	7.8	0.05

Table A-7: Generator dynamic data for the NETS-NYPS test network (2).

<i>Gen</i>	<i>Bus</i>	<i>Rating (MVA)</i>	$X_q$ (pu)	$X'_q$ (pu)	$X''_q$ (pu)	$T'_{q0}$ (s)	$T''_{q0}$ (s)	<i>H</i> (s)	<i>D</i>
G1	53	100	0.069	0.028	0.025	1.5	0.035	42	4
G2	54	100	0.282	0.06	0.05	1.5	0.035	30.2	9.75
G3	55	100	0.237	0.05	0.045	1.5	0.035	35.8	10
G4	56	100	0.258	0.04	0.035	1.5	0.035	28.6	10
G5	57	100	0.31	0.06	0.05	0.44	0.035	26	3
G6	58	100	0.241	0.045	0.04	0.4	0.035	34.8	10
G7	59	100	0.292	0.045	0.04	1.5	0.035	26.4	8
G8	60	100	0.28	0.05	0.045	0.41	0.035	24.3	9
G9	61	100	0.205	0.05	0.045	1.96	0.035	34.5	14
G10	62	100	0.115	0.045	0.04	1.5	0.035	31	5.56
G11	63	100	0.123	0.015	0.012	1.5	0.035	28.2	13.6
G12	64	100	0.095	0.028	0.025	1.5	0.035	92.3	13.5
G13	65	200	0.0286	0.005	0.004	1.5	0.035	248	33
G14	66	100	0.0173	0.0025	0.0023	1.5	0.035	300	100
G15	67	100	0.0173	0.0025	0.0023	1.5	0.035	300	100
G16	68	200	0.0334	0.006	0.0055	1.5	0.035	225	50

Generators G1-G8 all use type DC1A exciters, with the following parameters:

$$T_R = 0.01, K_A^{ex} = 40, T_A^{ex} = 0.02, E_{ex}^{min} = -10, E_{ex}^{max} = 10, T_E^{ex} = 0.785, K_E^{ex} = 1, \\ A_E^{ex} = 0.07, B_E^{ex} = 0.91.$$

Generator G9 uses a type ST1A\_v2 exciter, with the following parameters:

$$T_R = 0.01, K_A^{ex} = 200, E_{fd}^{min} = -5, E_{fd}^{max} = 5.$$

Generator G9 is also fitted with a PSS with the following settings:

$$T_W^{PSS} = 10, T_1^{PSS} = 0.05, T_2^{PSS} = 0.01, T_3^{PSS} = 0.05, T_4^{PSS} = 0.02, K_{PSS} = 10, \\ E_{PSS}^{min} = -0.5, E_{PSS}^{max} = 0.5.$$

### A.3 HVDC System Details

Details are provided for the HVDC system parameters used for various case studies throughout this thesis.

#### A.3.1 LCC-HVDC Line Embedded in Two-Area Network (Section 3.1)

LCC-HVDC line parameters (on 400 MW HVDC base with  $V_{dc}^{base} = 200$  kV):

$$R_{dc} = 0.022, L_{dc} = 2.48 \times 10^{-3}, C_{dc} = 1.08 \times 10^{-3}.$$

LCC-HVDC controller parameters:

$$K_P^{Idc,rect} = K_P^{Idc,inv} = 45, K_I^{Vdc,inv} = 65, K_I^{Idc,rect} = K_I^{Idc,inv} = 1000, K_I^{Vdc,inv} = 2000, \\ \gamma^{min} = 15^\circ.$$

#### A.3.2 VSC-HVDC Line Embedded in Two-Area Network (Section 3.1)

VSC-HVDC line parameters (on 400 MW HVDC base with  $V_{dc}^{base} = 200$  kV):

$$R_{dc} = 0.044, L_{dc} = 2.8 \times 10^{-4}, C_{dc} = 3.715 \times 10^{-3}.$$

VSC-HVDC controller parameters:

$$K_P^{Vdc} = 3, K_I^{Vdc} = 40, K_I^{Pdc} = K_I^{Qdc} = 20.$$

### A.3.3 VSC-HVDC Line Embedded in Two-Area Network (Section 3.2)

VSC-HVDC line parameters (on 400 MW HVDC base with  $V_{dc}^{base} = 200$  kV):

$$R_{dc} = 0.044, L_{dc} = 2.8 \times 10^{-4}, C_{dc} = 3.715 \times 10^{-3}.$$

VSC-HVDC controller parameters:

$$K_p^{Vdc} = 3, K_I^{Vdc} = 40, K_I^{Pdc} = K_I^{Qdc} = 20.$$

PSS-based POD controller parameters (on 100 MVA base):

$$T_W^{POD} = 10, T_1^{POD} = T_3^{POD} = 0.5503, T_2^{POD} = T_4^{POD} = 0.1994, K_{POD} = 0.35.$$

Fixed parameters during MLQG LTR tuning:

$$\Gamma = I, W_o = 0.1 \times I, \Theta = 0.001 \times I, \text{ and } V_o = 0.001 \times I.$$

### A.3.4 VSC-HVDC Line Embedded in Five-Area Network (Section 3.3)

VSC-HVDC line parameters (on 600 MW HVDC base with  $V_{dc}^{base} = 300$  kV):

$$R_{dc} = 0.04, L_{dc} = 2 \times 10^{-4}, C_{dc} = 3.5 \times 10^{-3}.$$

VSC-HVDC controller parameters:

$$K_p^{Vdc} = 20, K_I^{Vdc} = 60, K_I^{Pdc} = K_I^{Qdc} = 20.$$

PSS-based POD controller parameters (on 100 MVA base):

$$T_W^{POD} = 10, T_1^{POD} = T_3^{POD} = 0.9161, T_2^{POD} = T_4^{POD} = 0.1728, K_{POD} = 0.22.$$

Fixed parameters during MLQG LTR tuning:

$$\Gamma = I, W_o = 0.1 \times I, \Theta = 0.001 \times I, \text{ and } V_o = 0.001 \times I.$$

### A.3.5 VSC-MTDC Grid Embedded in Five-Area Network (Section 3.4)

All data provided is based on a 100 MW HVDC base (with  $V_{DC}^{base} = 500$  kV).

VSC-MTDC line parameters are given in Table A-8. All converter stations also cause active power flow losses of 1%.

Table A-8: VSC-MTDC line data

From Node	To Node	$R_{dc}$ (pu)	$L_{dc}$ (pu)
1	2	0.01	$2.0 \times 10^{-4}$
1	4	0.007	$1.4 \times 10^{-4}$
1	5	0.005	$1.0 \times 10^{-4}$
2	3	0.005	$1.0 \times 10^{-4}$
3	4	0.008	$1.6 \times 10^{-4}$
4	5	0.006	$1.2 \times 10^{-4}$

VSC-MTDC converter capacitance values (at nodes 1–5) are given below in pu:

$$C_{dc} = \{0.275, 0.1875, 0.1625, 0.2625, 0.1375\}.$$

VSC-MTDC controller parameters:

$$K_P^{Vdc} = 20, K_I^{Vdc} = 200, K_I^{Pdc} = 50, K_I^{Qdc} = 20.$$

### A.3.6 Two VSC-HVDC Lines Embedded in Five-Area Network (Section 4.2)

VSC-HVDC-1 line parameters (on 600 MW HVDC base with  $V_{dc}^{base} = 300$  kV):

$$R_{dc} = 0.045, L_{dc} = 2.8 \times 10^{-4}, C_{dc} = 3.715 \times 10^{-3}.$$

VSC-HVDC-2 line parameters (on 500 MW HVDC base with  $V_{dc}^{base} = 250$  kV):

$$R_{dc} = 0.045, L_{dc} = 2.8 \times 10^{-4}, C_{dc} = 3.715 \times 10^{-3}.$$

Both VSC-HVDC controller parameters:

$$K_P^{Vdc} = 3, K_I^{Vdc} = 40, K_I^{Pdc} = K_I^{Qdc} = 20.$$

Fixed parameters during MLQG LTR tuning for all supplementary controllers:

$$\Gamma = I, W_o = 0.1 \times I, \Theta = 0.001 \times I, \text{ and } V_o = 0.001 \times I.$$

### A.3.7 VSC-HVDC Line Embedded in Two-Area Network (Section 5.2)

VSC-HVDC line parameters (on 400 MW HVDC base with  $V_{dc}^{base} = 200$  kV):

$$R_{dc} = 0.045, L_{dc} = 2 \times 10^{-4}, C_{dc} = 3.5 \times 10^{-3}.$$

VSC-HVDC controller parameters:

$$K_P^{Vdc} = 3, K_I^{Vdc} = 40, K_I^{Pdc} = K_I^{Qdc} = 20.$$

### A.3.7.1 POD Controller Settings (Section 5.2.5)

PSS-based POD controller parameters (on 100 MVA base):

$$T_W^{POD} = 10, T_1^{POD} = T_3^{POD} = 0.6726, T_2^{POD} = T_4^{POD} = 0.1088, K_{POD} = 0.12.$$

### A.3.8 VSC-MTDC Grid Embedded in Five-Area Network with Additional Wind Farm (Section 6.2)

All data provided is based on a 100 MW HVDC base (with  $V_{DC}^{base} = 500$  kV).

VSC-MTDC line parameters are given in Table A-10. All converter stations also cause active power flow losses of 1%.

Table A-9: VSC-MTDC line data

From Node	To Node	$R_{dc}$ (pu)	$L_{dc}$ (pu)
1	2	0.01	$2.0 \times 10^{-4}$
1	4	0.007	$1.4 \times 10^{-4}$
1	5	0.005	$1.0 \times 10^{-4}$
2	3	0.005	$1.0 \times 10^{-4}$
3	4	0.008	$1.6 \times 10^{-4}$
4	5	0.006	$1.2 \times 10^{-4}$
3	6	0.001	$1.2 \times 10^{-4}$

VSC-MTDC converter capacitance values (at nodes 1–6) are given below in pu:

$$C_{dc} = \{0.275, 0.1875, 0.1625, 0.2625, 0.1375, 0.0750\}.$$

VSC-MTDC controller parameters:

$$K_P^{Vdc} = 20, K_I^{Vdc} = 200, K_I^{Pdc} = 50, K_I^{Qdc} = 20.$$

Fixed parameters during MLQG LTR tuning for all supplementary controllers:

$$\Gamma = I, W_o = 0.1 \times I, \Theta = 0.001 \times I, \text{ and } V_o = 0.001 \times I.$$

## A.4 Data for Optimal Power Flow

In Section 5.4.5, an optimal power flow solution is incorporated with the five-area test network. The optimisation minimises the total cost of generation for the given loading scenario, where each generator is subject to the standard cost function (A.1).

$$\text{Cost} = c_0 + c_1 P_e + c_2 P_e^2 \text{ \$/hour} \quad (\text{A.1})$$

The coefficient values for each generator are given in Table A-10. For generators G1–9, these are adopted from [185], for the remaining generators G10–16, these have been derived to achieve nominal generator outputs close to the standard power flow solution. Also included in Table A-10 are the constraints on active and reactive power for each generating unit.  $P^{max}$  values have been selected as 1.5 times the nominal active power output from the standard power flow solution for G1–10 and 1.25 times for the larger generators G11–16. Also note that all bus voltages are constrained to between 0.9 and 1.1 pu.

Table A-10: Data for optimal power flow solution with five-area test network.

Generator	Bus	$c_0$	$c_1$	$c_2$	$P^{max}$ (MW)	$P^{min}$ (MW)	$Q^{min}$ (MVar)
G1	53	0	6.9	0.0193	375	100	–100
G2	54	0	3.7	0.0111	817.5	100	–100
G3	55	0	2.8	0.0104	975	100	–100
G4	56	0	4.7	0.0088	948	100	–100
G5	57	0	2.8	0.0128	757.5	100	–100
G6	58	0	3.7	0.0094	1050	100	–100
G7	59	0	4.8	0.0099	840	100	–100
G8	60	0	3.6	0.0113	810	100	–100
G9	61	0	3.7	0.0071	1200	100	–100
G10	62	0	3.9	0.0090	750	100	–100
G11	63	0	4.0	0.0050	1250	500	–100
G12	64	0	2.9	0.0040	1687.5	500	–100
G13	65	0	2.5	0.0019	4488.8	2000	–100
G14	66	0	3.3	0.0033	2231.3	500	–100
G15	67	0	3.8	0.0050	1250	500	–100
G16	68	0	3.5	0.0014	5000	3000	–100

# Appendix B: Eigenvalue Sensitivity Rank Values

This appendix will detail the rank values calculated based on eigenvalue sensitivity.

## B.1 Numerical Example of Rank Calculation

The rank equation (4.1) is used in this example, repeated as (B.1) below.

$$\text{Rank} = \left| \frac{\partial \lambda_i}{\partial \gamma_j} \right| \left| \frac{\gamma_j}{\lambda_i} \right| \left| \frac{\sigma_{\gamma_j}}{\mu_{\gamma_j}} \right| \quad (\text{B.1})$$

The example is presented to establish the rank value corresponding to the eigenvalue sensitivity of Mode 1 to variations of G16 within the five-area network.

The nominal value for this generator power output  $\mu_{\gamma_{G16}} = 4000$  MW. The standard deviation of the distribution for G16 for the study presented in Chapter 4 is equal to 25% of nominal values at  $3\sigma_{\gamma}$ . Therefore  $\sigma_{\gamma_{G16}} = 333.33$  MW.

As stated in Chapter 4, the rank is calculated using only the real part  $\sigma_i$  substituted for  $\lambda_i$  in (B.1). This is equal to  $-0.1119$  for the nominal operating point. Following a 1% increase in the power output of G16, this changes to  $-0.1131$ , therefore  $\delta\sigma_{\text{Mode 1}} = -0.0012$ .

The rank value can now be calculated as in (B.2), with all calculated values normalised for comparison.

$$\text{Rank} = \left| \frac{-0.0012}{40} \right| \left| \frac{4000}{-0.1119} \right| \left| \frac{333.33}{4000} \right| = 8.936 \times 10^{-3} \quad (\text{B.2})$$

## B.2 Five-Area Test Network (Section 4.3)

The normalised rank values for with the centralised controller in place are shown in Table B-1, and with the decentralised controller in Table B-2.

Table B-1: Normalised rank values with the centralised controller installed.

<i>Parameter</i>	<i>Rank Value</i>	<i>Parameter</i>	<i>Rank Value</i>
G16	1.000	L27	0.066
G14	0.787	G1	0.065
L18	0.507	L47	0.053
G15	0.354	L28	0.052
L42	0.349	G12	0.051
L41	0.337	HVDC2	0.050
G6	0.330	HVDC1	0.049
G4	0.275	L25	0.048
G7	0.248	L4	0.041
G9	0.240	L7	0.039
G5	0.239	L52	0.038
L20	0.219	L1	0.036
G3	0.204	L26	0.033
G8	0.160	L8	0.033
G2	0.158	L51	0.030
L17	0.148	L40	0.028
G11	0.124	L49	0.027
G10	0.088	L50	0.025
L16	0.088	L46	0.022
L15	0.082	L45	0.016
L24	0.082	L39	0.012
L48	0.081	L33	0.011
L21	0.081	L44	0.010
L23	0.077	L12	0.005
L29	0.072	L36	0.005
L3	0.069		

Table B-2: Normalised rank values with the decentralised controller installed.

<i>Parameter</i>	<i>Rank Value</i>	<i>Parameter</i>	<i>Rank Value</i>
G16	1.000	G11	0.033
L18	0.407	HVDC1	0.033
G14	0.355	L3	0.033
G15	0.203	L27	0.032
L42	0.198	HVDC2	0.031
G6	0.174	G1	0.030
L41	0.167	G10	0.028
G4	0.145	L28	0.025
G5	0.137	L25	0.023
L20	0.133	L4	0.019
G7	0.132	L47	0.018
G9	0.101	L52	0.018
L17	0.098	L7	0.017
G3	0.097	L26	0.016
G2	0.075	L8	0.014
G8	0.075	L40	0.012
L51	0.059	L49	0.011
G12	0.051	L1	0.009
L16	0.045	L46	0.008
L21	0.044	L45	0.006
L50	0.044	L33	0.005
L23	0.044	L39	0.004
L15	0.043	L44	0.004
L24	0.041	L12	0.003
L29	0.035	L36	0.003
L48	0.035		

### B.3 Two-Area Test Network (Section 5.3)

The normalised rank values for the two-area test network are given in Table B-3.

Table B-3: Normalised rank values with and without the PSS-based POD controller.

<i>No POD Controller</i>		<i>PSS-based POD Controller</i>	
<i>Parameter</i>	<i>Rank Value</i>	<i>Parameter</i>	<i>Rank Value</i>
HVDC	1.000	HVDC	1.000
L2	0.713	L2	0.243
G3	0.670	G3	0.146
G4	0.537	G4	0.141
L1	0.243	L1	0.042
G2	0.089	G2	0.013

# Appendix C: PCM Model Functions

The mathematical description of the PCM model function  $g(\Gamma)$  up to fourth order are presented as (C.1)–(C.4) below; where  $\mathbf{K}$  is the set of coefficients,  $\gamma_i$  is the  $i^{\text{th}}$  uncertain parameter in the set  $\Gamma$ ,  $n_\gamma$  is the number of modelled uncertain parameters, and  $H_o(\gamma_i)$  is the  $o^{\text{th}}$  order orthogonal polynomial of  $\gamma_i$ .

$$g_1(\Gamma) = \left[ \sum_{i=1}^{n_\gamma} H_1(\gamma_i) \right] \mathbf{K} \quad (\text{C.1})$$

$$g_2(\Gamma) = \left[ \sum_{i=1}^{n_\gamma} H_1(\gamma_i) + \sum_{i=1}^{n_\gamma} H_2(\gamma_i) + \sum_{i=1}^{n_\gamma-1} \sum_{j=i+1}^{n_\gamma} H_1(\gamma_i) H_1(\gamma_j) \right] \mathbf{K} \quad (\text{C.2})$$

$$g_3(\Gamma) = \left[ \sum_{i=1}^{n_\gamma} H_1(\gamma_i) + \sum_{i=1}^{n_\gamma} H_2(\gamma_i) + \sum_{i=1}^{n_\gamma-1} \sum_{j=i+1}^{n_\gamma} H_1(\gamma_i) H_1(\gamma_j) \right. \\ \left. + \sum_{i=1}^{n_\gamma} H_3(\gamma_i) + \sum_{i=1}^{n_\gamma} \sum_{j=1, j \neq i}^{n_\gamma} H_2(\gamma_i) H_1(\gamma_j) + \sum_{i=1}^{n_\gamma-2} \sum_{j=i+1}^{n_\gamma-1} \sum_{k=j+1}^{n_\gamma} H_1(\gamma_i) H_1(\gamma_j) H_1(\gamma_k) \right] \mathbf{K} \quad (\text{C.3})$$

$$g_4(\Gamma) = \left[ \sum_{i=1}^{n_\gamma} H_1(\gamma_i) + \sum_{i=1}^{n_\gamma} H_2(\gamma_i) + \sum_{i=1}^{n_\gamma-1} \sum_{j=i+1}^{n_\gamma} H_1(\gamma_i) H_1(\gamma_j) \right. \\ \left. + \sum_{i=1}^{n_\gamma} H_3(\gamma_i) + \sum_{i=1}^{n_\gamma} \sum_{j=1, j \neq i}^{n_\gamma} H_2(\gamma_i) H_1(\gamma_j) + \sum_{i=1}^{n_\gamma-2} \sum_{j=i+1}^{n_\gamma-1} \sum_{k=j+1}^{n_\gamma} H_1(\gamma_i) H_1(\gamma_j) H_1(\gamma_k) \right. \\ \left. + \sum_{i=1}^{n_\gamma} H_4(\gamma_i) + \sum_{i=1}^{n_\gamma} \sum_{j=1, j \neq i}^{n_\gamma} H_3(\gamma_i) H_1(\gamma_j) + \sum_{i=1}^{n_\gamma-1} \sum_{j=i+1}^{n_\gamma} H_2(\gamma_i) H_2(\gamma_j) \right. \\ \left. + \sum_{i=1}^{n_\gamma} \sum_{j=1, j \neq i}^{n_\gamma-1} \sum_{k=j+1}^{n_\gamma} H_2(\gamma_i) H_1(\gamma_j) H_1(\gamma_k) \right. \\ \left. + \sum_{i=1}^{n_\gamma-3} \sum_{j=i+1}^{n_\gamma-2} \sum_{k=j+1}^{n_\gamma-1} \sum_{l=k+1}^{n_\gamma} H_1(\gamma_i) H_1(\gamma_j) H_1(\gamma_k) H_1(\gamma_l) \right] \mathbf{K} \quad (\text{C.4})$$

# Appendix D: PCM Model Uncertain Parameter Details

This appendix provides the details for the uncertain system parameters which have been used to produce Probabilistic Collocation Method functions within this thesis.

## D.1 Two-Area Test Network (Section 5.2)

### D.1.1 Normally Distributed Parameters

Details for the normally distributed uncertain parameters within the two-area test network are provided in Table D-1.

Table D-1: Normal distribution details for uncertain parameters in the Kundur two area network.

	$\gamma_1 : G_2$	$\gamma_2 : G_3$	$\gamma_3 : G_4$	$\gamma_4 : L_1$	$\gamma_5 : L_2$
$\mu_\gamma$ (MW)	700	719	700	967	1767
$\sigma_\gamma$ (MW)	46.67	47.93	46.67	64.47	117.8

### D.1.2 Uniformly Distributed Parameters

The VSC-HVDC power flow  $P_{DC}$  follows a uniform distribution. Recursive coefficients have been determined as presented in Table D-2.

Table D-2: Recursive coefficients for orthogonal polynomials representing the uniform distribution of the VSC-HVDC line power flow.

Orthogonal Polynomial Order, $o$	Recursive coefficients	
	$a$	$b$
1	200	40,000
2	200	3,333.50
3	200	2,666.80
4	200	2,571.56
5	200	2,539.81

## D.2 Five-Area Test Network with Standard Power Flow Solution (Section 5.4)

### D.2.1 Normally Distributed Parameters

Details for the normally distributed uncertain parameters within the five-area test network when a standard power flow solution is used are provided in Table D-3.

Table D-3: Normal distribution details for uncertain parameters in the five-area network with standard PF solution.

	$\gamma_1 : G_4$	$\gamma_2 : G_5$	$\gamma_3 : G_6$	$\gamma_4 : G_7$	$\gamma_5 : G_{14}$	$\gamma_6 : G_{16}$	$\gamma_7 : L_{18}$	$\gamma_8 : L_{20}$
$\mu_\gamma$ (MW)	632	505	700	560	1785	4000	2470	680
$\sigma_\gamma$ (MW)	52.67	42.08	58.33	46.67	148.75	333.33	205.83	56.67

## D.3 Five-Area Test Network with Optimal Power Flow Solution (Section 5.4.5)

### D.3.1 Normally Distributed Parameters

Details for the normally distributed uncertain parameters within the five-area test network when an optimal power flow solution is used are provided in Table D-4.

Table D-4: Normal distribution details for uncertain parameters in the five-area network with OPF solution.

	$\gamma_3 : L_{28}$	$\gamma_4 : L_{29}$	$\gamma_5 : L_{41}$	$\gamma_6 : L_{42}$	$\gamma_7 : L_{47}$	$\gamma_8 : L_{48}$
$\mu_\gamma$ (MW)	206	284	1000	1150	203.12	241.2
$\sigma_\gamma$ (MW)	17.17	23.67	83.33	95.83	16.93	20.10

### D.3.2 Uniformly Distributed Parameters

The operating capacities of VSC-HVDC-1 and VSC-HVDC-2 ( $P_{dc}^{VSC-1}$  and  $P_{dc}^{VSC-2}$ ) follow uniform distributions. Recursive coefficients have been determined as presented in Table D-5.

Table D-5: Recursive coefficients for orthogonal polynomials representing the uniform distributions of  $P_{dc}^{VSC-1}$  and  $P_{dc}^{VSC-2}$ .

Orthogonal Polynomial Order, $o$	$P_{dc}^{VSC-1}$		$P_{dc}^{VSC-2}$	
	$a$	$b$	$a$	$b$
1	350	1.003	275	1.004
2	350	7550.00	275	5250.00
3	350	6039.80	275	4199.80
4	350	5823.77	275	4049.49
5	350	5751.43	275	3999.05

These coefficients result in the monic orthogonal polynomials (D.1)–(D.5) representing  $\gamma_1 : P_{dc}^{VSC-1}$  and (D.6)–(D.10) representing  $\gamma_2 : P_{dc}^{VSC-2}$ .

$$H_1(\gamma_1) = \gamma_1 - 350 \tag{D.1}$$

$$H_2(\gamma_1) = \gamma_1^2 - 700\gamma_1 + 1.150 \times 10^5 \tag{D.2}$$

$$H_3(\gamma_1) = \gamma_1^3 - 1050\gamma_1^2 + 3.539 \times 10^5 \gamma_1 - 3.812 \times 10^7 \tag{D.3}$$

$$H_4(\gamma_1) = \gamma_1^4 - 1400\gamma_1^3 + 7.156 \times 10^5 \gamma_1^2 - 1.579 \times 10^8 \gamma_1 + 1.267 \times 10^{10} \tag{D.4}$$

$$H_5(\gamma_1) = \gamma_1^5 - 1750\gamma_1^4 + 1.200 \times 10^6 \gamma_1^3 - 4.023 \times 10^8 \gamma_1^2 + 6.591 \times 10^{10} \gamma_1 - 4.216 \times 10^{12} \tag{D.5}$$

$$H_1(\gamma_2) = \gamma_2 - 275 \tag{D.6}$$

$$H_2(\gamma_2) = \gamma_2^2 - 550\gamma_2 + 7.038 \times 10^4 \tag{D.7}$$

$$H_3(\gamma_2) = \gamma_2^3 - 825\gamma_2^2 + 2.174 \times 10^5 \gamma_2 - 1.820 \times 10^7 \tag{D.8}$$

$$H_4(\gamma_2) = \gamma_2^4 - 1100\gamma_2^3 + 4.403 \times 10^5 \gamma_2^2 - 7.576 \times 10^7 \gamma_2 + 4.720 \times 10^9 \tag{D.9}$$

$$H_5(\gamma_2) = \gamma_2^5 - 1375\gamma_2^4 + 7.388 \times 10^5 \gamma_2^3 - 1.935 \times 10^8 \gamma_2^2 + 2.469 \times 10^{10} \gamma_2 - 1.225 \times 10^{12} \tag{D.10}$$

# Appendix E: Modal System Representation

This appendix presents an example of the modal canonical form of a state space system representation. The example presented is of a sixth order generator model with no associated controllers.

The standard system representation as per the form (E.1) and (E.2) is given by (E.3)–(E.6).

$$\Delta \dot{\mathbf{x}} = \mathbf{A}\Delta \mathbf{x} + \mathbf{B}\Delta \mathbf{u} \quad (\text{E.1})$$

$$\Delta \mathbf{y} = \mathbf{C}\Delta \mathbf{x} + \mathbf{D}\Delta \mathbf{u} \quad (\text{E.2})$$

$$\mathbf{A} = \begin{bmatrix} -0.142 & 0 & 0.044 & 0 & 0 & 0 \\ 0 & 0.777 & 0 & 0.110 & 0 & 0 \\ 20 & 0 & -20 & 0 & 0 & 0 \\ 0 & -28.571 & 0 & -28.571 & 0 & 0 \\ 0 & 0 & 0 & 0 & 0 & 314.159 \\ -0.083 & 0.121 & -0.020 & -0.015 & 0 & 0 \end{bmatrix} \quad (\text{E.3})$$

$$\mathbf{B} = \begin{bmatrix} 0.004 & 0 & 0.098 & 0 & 0 & 0 \\ 0 & 0.020 & 0 & 0 & 0 & 0 \\ 0.496 & 0 & 0 & 0 & 0 & 0 \\ 0 & 0.638 & 0 & 0 & 0 & 0 \\ 0 & 0 & 0 & 0 & 0 & -314.159 \\ 0 & 0 & 0 & 0.010 & -0.010 & 0 \end{bmatrix} \quad (\text{E.4})$$

$$\mathbf{C} = \begin{bmatrix} 1 & 0 & 0 & 0 & 0 & 0 \\ 0 & 1 & 0 & 0 & 0 & 0 \\ 0 & 0 & 1 & 0 & 0 & 0 \\ 0 & 0 & 0 & 1 & 0 & 0 \\ 0 & 0 & 0 & 0 & 1 & 0 \\ 0 & 0 & 0 & 0 & 0 & 1 \end{bmatrix} \quad (\text{E.5})$$

$$\mathbf{D} = \begin{bmatrix} 0 & 0 & 0 & 0 & 0 & 0 \\ 0 & 0 & 0 & 0 & 0 & 0 \\ 0 & 0 & 0 & 0 & 0 & 0 \\ 0 & 0 & 0 & 0 & 0 & 0 \\ 0 & 0 & 0 & 0 & 0 & 0 \\ 0 & 0 & 0 & 0 & 0 & 0 \end{bmatrix} \quad (\text{E.6})$$

This state-space representation can be transformed to the modal canonical form as per (E.7) and (E.8) using the modal transformation matrix  $\mathbf{M}$ , where  $\mathbf{z} = \mathbf{M}\Delta\mathbf{x}$ .

$$\dot{\mathbf{z}} = \mathbf{\Lambda}\mathbf{z} + \mathbf{B}_M\Delta\mathbf{u} \quad (\text{E.7})$$

$$\Delta\mathbf{y} = \mathbf{C}_M\mathbf{z} + \mathbf{D}\Delta\mathbf{u} \quad (\text{E.8})$$

The new modal state matrices are given as (E.9)–(E.11).

$$\mathbf{\Lambda} = \begin{bmatrix} -0.098 & 0 & 0 & 0 & 0 & 0 \\ 0 & -20.044 & 0 & 0 & 0 & 0 \\ 0 & 0 & 0.669 & 0 & 0 & 0 \\ 0 & 0 & 0 & -28.464 & 0 & 0 \\ 0 & 0 & 0 & 0 & 0 & 0.005 \\ 0 & 0 & 0 & 0 & 0 & 0 \end{bmatrix} \quad (\text{E.9})$$

$$\mathbf{B}_M = \begin{bmatrix} 0.044 & 0 & 0.784 & 0 & 0 & 0 \\ -0.245 & 0 & 0.049 & 0 & 0 & 0 \\ 0 & -0.359 & 0 & 0 & 0 & 0 \\ 0 & 0.661 & 0 & 0 & 0 & 0 \\ 0 & 0 & 0 & 0 & 0 & -9.818 \\ 0 & 0 & 0 & 19.948 & -19.948 & 0 \end{bmatrix} \quad (\text{E.10})$$

$$\mathbf{C}_M = \begin{bmatrix} 0 & 0 & 0 & 0 & 0 & 0 \\ 0 & 0 & -0.062 & -0.004 & 0 & 0 \\ 0.125 & -1.999 & 0 & 0 & 0 & 0 \\ 0 & 0 & 0.061 & 0.998 & 0 & 0 \\ 0 & 0 & 0 & 0 & 32 & 0 \\ 0 & 0 & 0 & 0 & 0 & 0.001 \end{bmatrix} \quad (\text{E.11})$$

# Appendix F: Publications from the Thesis

---

## F.1 International Journal Publications

- [F1] **R. Preece**, J. V. Milanović, A. M. Almutairi, and O. Marjanovic, “Probabilistic Evaluation of Damping Controller in Networks With Multiple VSC-HVDC Lines”, *Accepted for publication in the IEEE Transactions on Power Systems*, 2012.
- [F2] **R. Preece**, J. V. Milanović, A. M. Almutairi, and O. Marjanovic, “Damping of Inter-Area Oscillations in Mixed AC/DC Networks using WAMS Based Supplementary Controller”, *Accepted for publication in the IEEE Transactions on Power Systems*, 2012, **Invited journal paper**.
- [F3] **R. Preece**, N. C. Woolley, J. V. Milanović, “The Probabilistic Collocation Method for Power System Damping and Voltage Collapse Studies in the Presence of Uncertainties”, *Accepted for publication in the IEEE Transactions on Power Systems*, 2012.

## F.2 Submitted International Journal Publications

- [F4] **R. Preece**, J. V. Milanović, “Tuning of a Damping Controller for Multi-terminal VSC-HVDC Grids using the Probabilistic Collocation Method”, *Submitted to the IEEE Transactions on Power Delivery Special Issue on “HVDC Systems and Technologies”*, October 2012.

## F.3 International Conference Publications

- [F5] **R. Preece** and J. V. Milanović, “Comparison of Dynamic Performance of Meshed Networks with Different Types of HVDC Lines”, *IET ACDC 2010*, London, UK, 19-21 October 2010.
- [F6] **R. Preece**, A. M. Almutairi, O. Marjanovic, and J. V. Milanović, “Damping of Electromechanical Oscillations Using WAMS Based Supplementary MLQG Controller Installed at VSC based HVDC Line”, *IEEE PowerTech 2011*, Trondheim, Norway, 19-23 June 2011.
- [F7] **R. Preece**, A. M. Almutairi, O. Marjanovic, and J. V. Milanović, “Damping of Electromechanical Oscillations by VSC-HVDC Active Power Modulation with Supplementary WAMS Based Modal LQG Controller”, *IEEE Power & Energy Society General Meeting*, Detroit, USA, 24-29 July 2011.

- [F8] **R. Preece**, A. M. Almutairi, O. Marjanovic, and J. V. Milanović, “Effectiveness of a Supplementary MLQG Power Oscillation Damping Controller Installed at an HVDC Line within a Meshed Network”, *Cigré International Symposium: The Electric Power System of the Future*, Bologna, Italy, 13-15 September 2011.
- [F9] **R. Preece**, J.V. Milanović, “The Probabilistic Collocation Method for Dealing with Uncertainties in Power System Small Disturbance Studies”, *IEEE Power & Energy Society General Meeting*, San Diego, USA, 22-26 July 2012.
- [F10] **R. Preece**, J. V. Milanović, “Power Oscillation Damping using VSC-MTDC Grids”, *8<sup>th</sup> IFAC Power Plant and Power Systems Control Symposium*, Toulouse, France, 2-5 September 2012.